



Max-Planck-Institut  
für Plasmaphysik

# Microwave Heating and Diagnostic of Suprathermal Electrons in an Overdense Stellarator Plasma

vorgelegt von  
Dipl.-Phys.  
Torsten Stange  
aus Blankenburg

von der Fakultät II - Mathematik und Naturwissenschaften  
der Technischen Universität Berlin  
zur Erlangung des akademischen Grades

Doktor der Naturwissenschaften  
- Dr. rer. nat. -

**Genehmigte Dissertation**

Promotionsausschuss:

Vorsitzender: Prof. Dr. Mario Dähne  
Berichter: Prof. Dr. Dieter Breitschwerdt  
Berichter: Prof. Dr. Robert Wolf  
Berichter: PD Dr. Heinrich Peter Laqua

Tag der wissenschaftlichen Aussprache: 17.10.2013

Berlin 2014  
D 83



*Für die lieben Menschen, die mit mir gebangt haben.*

„MÖGE DIE LORENTZ-KRAFT MIT DIR SEIN!“



---

## Abstract

The resonant coupling of microwaves into a magnetically confined plasma is one of the fundamental methods for the heating of such plasmas. Identifying and understanding the processes of the heating of overdense plasmas, in which the wave propagation is generally not possible because the wave frequency is below the plasma frequency, is becoming increasingly important for high density fusion plasmas. This work focuses on the heating of overdense plasmas in the WEGA stellarator. The excitation of electron Bernstein waves, utilizing the OXB-conversion process, provides a mechanism for the wave to reach the otherwise not accessible resonant absorption layer.

In WEGA these OXB-heated plasmas exhibit a suprathermal electron component with energies up to 80 keV. The fast electrons are located in the plasma center and have a Maxwellian energy distribution function within the soft X-ray related energy range. The corresponding averaged energy is a few keV.

The OXB-discharges are accompanied by a broadband microwave radiation spectrum with radiation temperatures of the order of keV. Its source was identified as a parametric decay of the heating wave and has no connection to the suprathermal electron component. For the detailed investigation of the microwave emission, a quasioptical mirror system, optimized for the OX-conversion, has been installed. Based on the measurement of the broadband microwave stray radiation of the decay process, the OX-conversion efficiency has been determined to 0.56 being in good agreement with full-wave calculations.

In plasmas without an electron cyclotron resonance, corresponding to the wave frequency used, non-resonant heating mechanisms have been identified in the overdense plasma regions. Whistler waves or R-like waves are the only propagable wave types within the overdense plasmas. The analysis of the heating efficiency in dependence on the magnetic flux density leads to tunneling as the most probable coupling mechanism.

For the determination of the heating efficiencies of the different heating scenarios (overdense non-resonant heating, underdense and overdense resonant heating) a variety of diagnostic methods have been used. Based on heat wave experiments and measuring the response of the total plasma radiation, an estimate of the absorbed heating power and the energy confinement time has been achieved with an accuracy of  $\pm 10\%$  dependent on the measurement accuracy of the radiated power.

## Zusammenfassung

Eine der Hauptmethoden zur Heizung eines magnetisch eingeschlossenen Plasmas basiert auf der resonanten Einkopplung von Mikrowellen. Von wachsender Bedeutung für Fusionsplasmen hoher Dichte ist die Identifizierung und das Verständnis der Mechanismen zur Heizung von überdichten Plasmen, in denen eine Wellenpropagation im Allgemeinen nicht möglich ist, da die Plasmafrequenz höher als die Heizfrequenz ist. Das Hauptthema in der vorliegenden Arbeit ist die Heizung von überdichten Plasmen am Stellarator WEGA. Die Anregung von Elektron-Bernsteinwellen über den OXB-Konversionsprozess bietet eine Möglichkeit die andernfalls nicht zugängliche resonante Absorptionsschicht im Plasma zu erreichen.

Im speziellen Fall von WEGA wird während der OXB-Heizung eine überthermische Elektronenkomponente mit Energien bis zu 80 keV erzeugt. Die schnellen Elektronen sind im Plasmazentrum lokalisiert und weisen innerhalb des weichen Röntgenbereiches eine Maxwell'sche Verteilung auf. Die entsprechende mittlere Energie liegt im Bereich von einigen keV.

Die OXB-Entladungen sind zusätzlich begleitet von einem breitbandigen Mikrowellenspektrum mit Strahlungstemperaturen von ebenfalls einigen keV. Die Quelle der Strahlung konnte als parametrischer Zerfall der Heizwelle identifiziert werden ohne eine Verbindung zur überthermischen Elektronenkomponente. Zur detaillierten Untersuchung der Mikrowellenemission wurde ein quasioptisches Spiegelsystem aufgebaut, das auf die OX-Konversion optimiert ist. Mit Hilfe der breitbandigen Streustrahlung des Zerfallsprozess konnte die OX-Konversionseffizienz mit 0.56 bestimmt werden, das in guter Übereinstimmung mit dem theoretischen Wert ist.

Darüber hinaus wurde bei Plasmen ohne eine Elektronen-Zyklotron-Resonanz bezüglich der Heizwelle ein überdichter nicht-resonanter Heizprozess untersucht. Whistler-Wellen oder allgemeiner Wellen mit einer rechtsdrehenden Polarisation sind die einzigen ausbreitungsfähigen Wellen innerhalb der untersuchten stark überdichten Plasmen. Durch Analyse der Heizeffizienz in Abhängigkeit von der magnetischen Flussdichte in der Umgebung der Reflexionsschicht lässt sich auf die Tunnelung als wahrscheinlichster Kopplungsmechanismus schließen.

Zur Bestimmung der Heizeffizienz für die verschiedenen Heizszenarien (überdichte nicht-resonante Heizung sowie unterdichte und überdichte resonante Heizung) wurde eine Vielzahl von Diagnostik-Methoden angewendet. Im Fall von Wärmewellenexperimenten wurden unter anderem die Zeitabhängigkeit der Plasmastrahlung genutzt um zu einer Abschätzung der Heizleistung sowie der Energieeinschlusszeit zu kommen. Die Genauigkeit der Methode kann auf  $\pm 10\%$  abgeschätzt werden abhängig von der Messgenauigkeit der Strahlungsmessung.

# Contents

<b>1</b>	<b>Introduction</b>	<b>1</b>
1.1	WEGA Stellarator . . . . .	3
1.1.1	Magnetic Field Configuration . . . . .	3
1.1.2	Plasma Parameters . . . . .	5
1.2	Thesis Outline . . . . .	6
<b>2</b>	<b>Wave Propagation Theory</b>	<b>7</b>
2.1	Wave Description in Magnetized Plasmas . . . . .	7
2.1.1	Cold Plasmas . . . . .	8
2.1.2	Warm Plasmas (Finite Plasma Temperature) . . . . .	12
2.2	Wave Propagation and Absorption within Magnetized Plasmas . . . . .	16
2.2.1	Electron Cyclotron Interaction . . . . .	17
2.2.2	Collisional Interaction . . . . .	19
2.2.3	Electron Bernstein Wave Interaction . . . . .	20
2.3	Wave Description outside the Plasma . . . . .	27
2.3.1	Free-space Propagation . . . . .	27
2.3.2	Imaging of Gaussian Beams . . . . .	29
2.3.3	Waveguide Propagation . . . . .	30
2.3.4	Calculation Methods . . . . .	31
<b>3</b>	<b>General Experimental Setup</b>	<b>33</b>
3.1	Heating Systems . . . . .	33
3.1.1	28 GHz Heating System . . . . .	33
3.1.2	2.45 GHz Heating System . . . . .	42
3.2	Standard Diagnostics . . . . .	44
3.2.1	Machine Control . . . . .	44
3.2.2	Stray Radiation Detector (Sniffer Probe) . . . . .	45
3.2.3	Microwave Interferometer . . . . .	45
3.2.4	Microwave Radiometer . . . . .	46
3.2.5	Bolometer . . . . .	48
3.2.6	X-ray Diagnostics . . . . .	49
3.2.7	Magnetic Diagnostics . . . . .	56
3.2.8	Langmuir Probe . . . . .	57
<b>4</b>	<b>Development of Quasioptical Microwave Detection System</b>	<b>59</b>
4.1	Mirror System . . . . .	60
4.2	Corrugated Feed Horn . . . . .	65
4.3	Transmission Line . . . . .	67
4.3.1	Bragg-Reflector . . . . .	68
4.3.2	Circular Polarizer . . . . .	69

<b>5</b>	<b>Experimental Results</b>	<b>73</b>
5.1	Heating Scenarios in Comparison . . . . .	73
5.1.1	X2-Heating . . . . .	74
5.1.2	Non-resonant Heating . . . . .	87
5.1.3	OXB-Heating . . . . .	103
5.2	Generation of suprathermal particles . . . . .	109
5.2.1	Energy distribution in OXB-heated discharges . . . . .	109
5.2.2	Spatially resolved measurements during OXB-heated discharges . . . . .	113
5.2.3	Temporally resolved measurements during OXB-heated discharges . . . . .	117
5.2.4	Maximum Energy of Relativistic Electrons in SLA-discharges . . . . .	119
5.3	Source of high intensity microwave radiation during OXB-heating . . . . .	123
5.3.1	Distribution in the torus . . . . .	125
5.3.2	Generation Mechanism . . . . .	129
5.4	Investigation of OX-Conversion Process . . . . .	134
5.4.1	Invasive Diagnostic Technique . . . . .	134
5.4.2	Non-invasive Diagnostic Technique . . . . .	137
<b>6</b>	<b>Conclusions and Summary</b>	<b>141</b>
<b>A</b>	<b>Appendices</b>	<b>145</b>
A.1	Lead Filter Method . . . . .	145
	<b>Bibliography</b>	<b>149</b>
	<b>Danksagung</b>	<b>159</b>
	<b>Selbständigkeitserklärung</b>	<b>161</b>

# 1 Chapter 1

---

## Introduction

The visible universe consists almost exclusively of plasma. The most prominent example is the sun, which generates its radiated power by means of fusion of hydrogen to helium [HG13].

In connection with aerospace a second well known example is the plasma generated during the atmospheric entry of a space vehicle. Its high speed on the order of the escape velocity leads to aerodynamic heating of the passing air. The gas is ionized with a resultant plasma temperature<sup>1</sup> on the order of 1 eV [Ste13]. During this time, radio communication with the base station on the earth is not possible, because plasma screens the shuttle against electromagnetic waves up to a certain frequency depending on the electron density  $n_e$ . The electrons follow the alternating electric field of the radio wave which leads to a reflection by the evanescent plasma layer. The resultant oscillation of the electrons against the inertial ion background has a maximum frequency called *plasma frequency*  $\omega_{pe} = \sqrt{n_e e^2 / (\epsilon_0 m_e)}$ . The plasma is called *overdense* when the frequency of the incident electromagnetic (EM) wave is lower than the plasma frequency. The reflection of the wave can be suppressed by use of a magnetic field with magnetic flux density  $B$  around the shuttle hull [TRM<sup>+</sup>09]. The electrons and ions gyrate around the magnetic field lines with the so called *electron* and *ion cyclotron frequency*  $\omega_{pe} = eB/m_e$  leading to an anisotropy of the possible oscillations of both particle species [HW65]. *Tunneling* processes of an incident EM-wave are possible depending on the wave polarization and its propagation direction in relation to the magnetic field vector. Furthermore, the *gradient length*  $L_n$  of the electron density is an important determinant for the *tunneling efficiency* [Bud61]. In the case of a space shuttle, a perpendicular magnetic field in relation to the hall surface allows a tunneling of a so called *Whistler* wave, whose name originates from the first observations of radio waves propagating along the earth's magnetic field in the ionosphere. Detection with a radio receiver produces a whistling sound because higher frequencies propagate faster than lower ones [Str11]. Furthermore, Whistler waves are commonly used for the heating of overdense laboratory plasmas confined within a linear magnetic field configuration. The investigation of the propagation properties of Whistler waves remains a topic of contemporary research.

---

<sup>1</sup>In plasma physics the temperature is usually given in energy units. Under the condition of a Boltzmann distribution in the thermal equilibrium 1 eV corresponds to 11604 K.

The same problem regarding the coupling an electromagnetic wave into an overdense magnetically confined plasma appears in fusion research which aims at realizing the fusion reactions of the hydrogen isotopes deuterium and tritium to helium. The goal is the commercial generation of energy that necessitates ion temperatures on the order of 10 keV and ion densities of  $10^{20} \text{ m}^{-3}$ . If the frequency of the incident microwave beam is equal to the electron cyclotron frequency or higher harmonics<sup>2</sup>, underdense plasmas can be efficiently heated by what is termed *electron cyclotron resonance heating* (ECRH). Efficient heating of overdense plasmas is still being investigated.

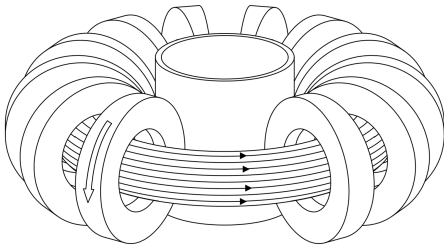


Figure 1.1: *Toroidal field component for the confinement of hot plasmas in fusion research*

In contrast to linear devices, the magnetic field lines in fusion experiments are in the shape of a closed loop within a torus shaped vacuum chamber, as is shown in Figure 1.2. A direct tunneling of whistler waves parallel to the magnetic field lines is not possible, however, special *conversion processes* between different plasma wave modes in the vicinity of the density gradient of the plasma allow the coupling of an incident heating beam to an overdense high temperature plasma. In contrast to the tunneling process, an electromagnetic wave within the plasma can be converted into an electrostatic wave based on a coherent *gyro motion* of the electrons around the magnetic field lines. The latter one is called *electron Bernstein wave* (EBW), and has no upper density limit, but a lower one. For this reason, the efficient application of the mentioned conversion processes is the topic of the most current research. Furthermore, the inverse process can be used as temperature diagnostic for the electrons. Their gyration constitutes an accelerated movement leading to the generation of electromagnetic waves, or electrostatic EBWs. The former process is commonly used in fusion research for the determination of the *electron temperature*  $T_e$  of underdense plasmas, and is referred to as *electron cyclotron emission diagnostic* (ECE-diagnostic) [HG13]. On the other hand, the emission of EBWs allows for the possibility of performing the same measurements for overdense plasmas, called *electron Bernstein emission diagnostic* (EBE-diagnostic) [VL03].

The diagnostic as well as the heating via EBWs are not yet commonly used in fusion research due to the higher technical effort. Instead, smaller experiments with lower temperatures but with fusion relevant magnetic field configurations are better suited for the development of new concepts because of their higher flexibility. Investigation of the introduced conversion as well as tunneling processes is currently underway at the WEGA *stellarator* located in the Max-Planck-Institute for Plasma Physics in Greifswald. The following section gives a brief description of the confinement concept, the resultant magnetic field configuration and the achievable plasma parameters which are compared with modern fusion experiments. This is followed by an outline of the thesis.

---

<sup>2</sup>Heating efficiency is dependent on the incidence direction with respect to the magnetic field lines and the polarization of the heating beam. The highest absorption is achieved for the first and the second harmonic of the electron cyclotron frequency. Details are given in chapter 2.2.1.

## 1.1 WEGA Stellarator

A solely toroidal magnetic field, as shown in Figure 1.1, is not sufficient to confine a plasma. The curvature of the magnetic field lines as well as the radial gradient of the magnetic flux density  $B$  leads to a charge separation of the plasma particles on a vertical axis. The resultant vertical electric field within the plasma causes a so called  $\mathbf{E} \times \mathbf{B}$  – drift to the *low field side* (LFS) of the torus. For this reason, a twist of the magnetic field lines is introduced by use of an additional poloidal magnetic field which has the direction of the current of the toroidal field coils shown in Figure 1.1. The result is a short circuit of the vertical charge separation.

### 1.1.1 Magnetic Field Configuration

A classical stellarator like WEGA generates the additional poloidal magnetic field by helical field coils which wind themselves around the torus. A sketch of the WEGA coil system is shown in Figure 1.3, and an illustration of the used coordinate system in Figure 1.2. After two toroidal turns, each coil has encircled the torus five times in the poloidal direction. Thus, the geometrical position of the helical field coils at a certain poloidal cross section repeats itself after a change of the toroidal angle of  $\Delta\phi = 72^\circ$ , leading to a five-fold symmetry.

The strength of the field line twist is dependent on the ratio of the helical to the toroidal field current whose square is proportional to the so called *rotational transform*  $\nu$ . This value corresponds to the average poloidal angle which a field line undergoes during one toroidal orbit.

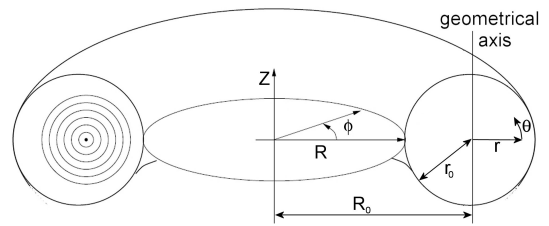


Figure 1.2: The two used coordinate systems  $(R, \phi, z)$  and  $(r, \phi, \theta)$  with the major radius  $R$ , the minor radius  $r$ , the toroidal angle  $\phi$  and the poloidal angle  $\theta$ .

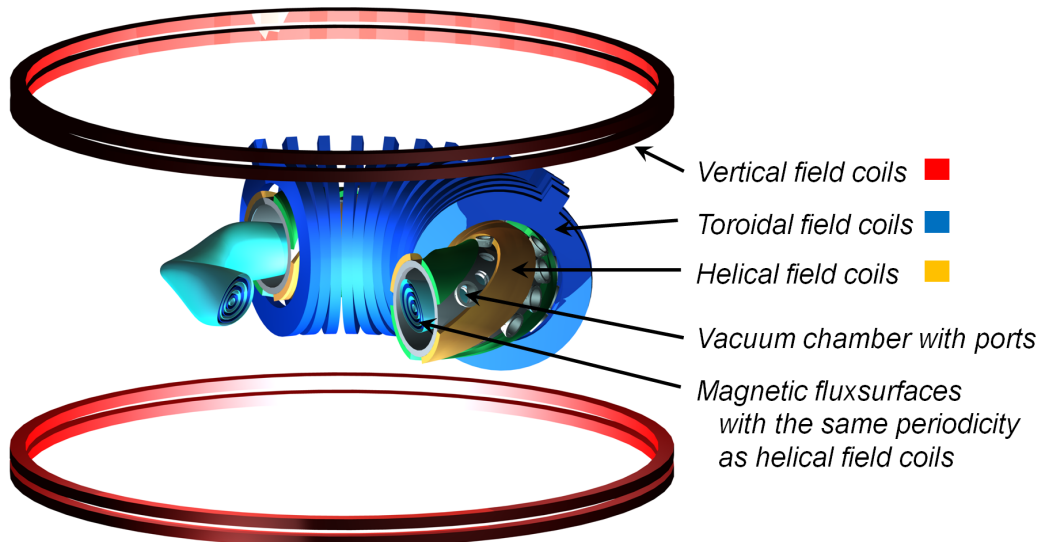


Figure 1.3: Magnetic field coil system of the WEGA stellarator with a half cut view of the toroidal vacuum chamber. One fifth of the vacuum flux surfaces are faded out. The vertical field coils can be used to increase or decrease the major radius of the magnetic axis.

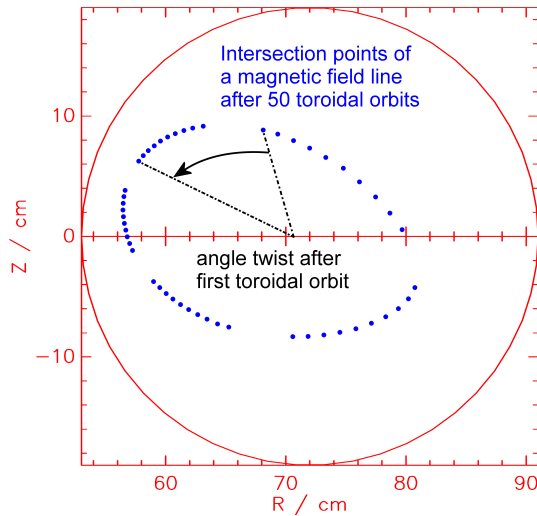


Figure 1.4: *Intersection points of one twisted magnetic field line with a poloidal cross section of the torus. The rotational transform  $t$  characterizes the angle twist after one toroidal orbit.*

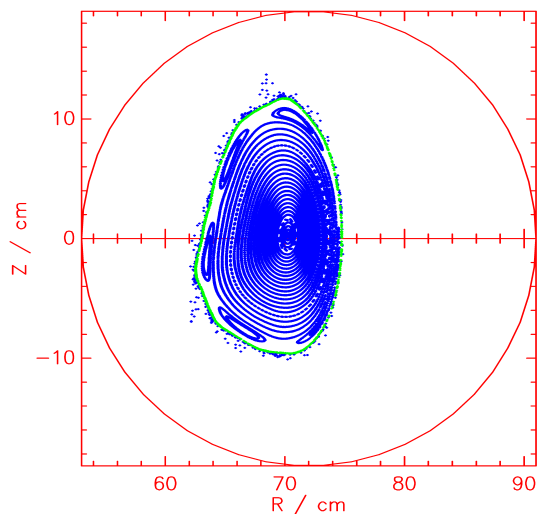


Figure 1.5: *Poincaré plot at a symmetry plane with the so called standing ellipse. The flux surface shape on both sides are mirror-images of one another with respect to this poloidal plane. The green line indicates the last closed flux surface.*

surface. The magnetic axis is characterized by  $r_{\text{eff}} = 0$ . The perpendicular transport of particles and energy from the axis to the last closed flux surfaces leads to a finite *particle and energy confinement time* which increases with increased magnetic field strength. The magnetic flux density at WEGA is limited to  $B_0 = 0.5$  T at the magnetic axis limiting the

Figure 1.4 shows as an example the intersection points of one magnetic field line at an arbitrary poloidal cross section after 50 toroidal orbits<sup>3</sup>. If the normalized rotational transform is an irrational number, the magnetic field line will not close after an infinite number of circles. The result is a so called *closed magnetic flux surface* on which the particles are confined. The representation as intersection points on a poloidal cross section, as shown in Figure 1.4, is called a Poincaré-plot.

The rotational transform of each flux surface increases with increasing minor radius  $r$  because of the lower distance to the helical field coils being responsible for the field line twist. WEGA has a major radius of  $R_0 = 72$  cm and a minor radius of  $r_0 = 19$  cm. Figure 1.5 shows a typical magnetic field configuration at a symmetry plane. The diameter of the magnetically confined plasmas is approximately 20 cm and dependent on the rotational transform. An excessively high value leads to stochastic magnetic field lines such that no closed flux surfaces are possible. The result is the existence of a *last closed flux surface* (LCFS) defining the plasma cross section. A confinement beyond the LCFS is not given.

Particle transport parallel to the magnetic field is approximately six magnitudes higher than transport perpendicular to the flux surfaces. For this reason, the latter ones constitute isosurfaces regarding temperature and density. Each poloidal cross section within one fifth of the torus has another shape of the flux surfaces. For better comparison of different poloidal cross sections, the plasma parameters are given in terms of a normalized minor radius called *effective radius*  $r_{\text{eff}}$ . It corresponds to the minor radius of a torus with the same volume as the relevant flux

<sup>3</sup>The calculation is made with the aid of the w7-code which is able to trace a particle within a magnetic field. The latter one is constructed from current filaments by use of the Biot-Savart law [Wer08].

particle confinement time to the order of  $\tau_P \approx 10$  ms. For the energy confinement time  $\tau_E$  a lower value must be expected because it is limited by transport and radiation losses. These losses are defined by the temperature and the density of the plasma and are discussed in detail in the first part of the experimental results in chapter 5.

### 1.1.2 Plasma Parameters

The typical electron temperatures of the investigated overdense plasmas are on the order of ten eV. This is in contrast to modern fusion experiments which obtain up to 10 keV. The density of the investigated plasmas, however, achieves fusion relevant values with  $n_e \approx 10^{19} \text{ m}^{-3}$ , although overdense plasmas are only possible with use of helium or argon as discharge gas. The reason can be found in the relatively low available heating power and the high power losses which do not allow an overdense hydrogen plasma. A further important plasma parameter for the analysis of the heating efficiency is the stored energy  $W$ , being a volume integration of the averaged particle energy  $\varepsilon_s = \frac{3}{2}k_B T_s$  of each particle species  $s$  multiplied with the particular local density  $n_s$ . The temperature of the ions is typically much less than 1 eV so that the stored energy is mainly defined by the electrons:

$$W = \sum_s \int_V n_s \varepsilon_s d^3x \approx \int_V n_e \frac{3}{2} k_B T_e d^3x = 4\pi^2 R \int_{r=0}^a n_e \varepsilon_e r dr = 6\pi^2 R k_B \int_{r=0}^a n_e T_e r dr. \quad (1.1)$$

The stored energy of the thermal electrons, called bulk electrons, is on the order of 1 J in comparison to more than some MJ in modern fusion experiments. The energy amount of a possible suprathermal component, however, is not included and must be added. The energy range of the suprathermal electrons in WEGA plasmas can be anywhere from around ten keV up to one MeV. Even though the corresponding density is only a fractional amount of the bulk densities, the investigation of the acceleration process is of great interest. Higher particle energies can lead to higher electrical currents within the plasma which are important for the confinement concept of the *tokamak*. In contrast to the stellarator, the poloidal field component for the rotational transform is generated by internal plasma currents which are induced with the aid of a transformer using the plasma as secondary winding. This process is limited by the maximum current on the primary side leading to pulsed operation of a tokamak. For this reason, efficient non-inductive current drive scenarios would allow the envisaged continuous operation of a future tokamak-like power plant. In contrast, the stellarator is an intrinsically steady state device.

## 1.2 Thesis Outline

The actual thesis is mainly dedicated to the investigation of overdense plasma heating by means of electrostatic electron Bernstein waves (EBW) at the WEGA stellarator. For this purpose, the incident microwave beam must be converted with the aid of the so called OXB-conversion process. The second chapter starts with a brief description of the electromagnetic wave types in cold plasmas as well as electrostatic plasma waves in consideration of a finite plasma temperature. This is followed by an overview of the main conditions required to use electromagnetic and electrostatic waves for plasma heating as well as diagnostics by means of the microwave emission from the plasma. The following section explains the propagation properties of microwave beams outside the plasma that are important for the proper design of the coupling optics used in the microwave emission diagnostic system as well as the 28 GHz heating system. The used frequency corresponds to heating at the second harmonic of the electron cyclotron frequency which is defined by the magnetic flux density of  $B_0 = 0.5$  T. A more detailed description of the used heating systems is given in the first part of chapter 3. It is followed by a brief description of the most important diagnostics used for the analysis of the heating processes. This section also includes a more detailed description of the upgrades of the X-ray diagnostic systems put into place with the goal of obtaining a spatially resolved measurement of a suprathreshold electron component that appears during EBW-heating.

Chapter 4 deals with the development of a quasioptic antenna as well as a broadband polarizer for the microwave emission diagnostic to investigate the expected electron Bernstein wave emission as well as the efficiency of the OXB-conversion process. The experimental results discussed in chapter 5 begin with a comparison between the standard underdense ECRH-method and the overdense heating scenarios which are possible at the WEGA stellarator. In this context, a second overdense discharge scenario is discussed based on the tunneling of whistler waves by use of the 2.45 GHz heating system. This is followed by a detailed investigation of the suprathreshold electron components appearing in the different discharge scenarios at WEGA. Furthermore, a high intensity microwave emission can be observed during EBW-heating. The underlying generation mechanism is explained in section 5.3. Chapter 5 concludes with the experimental results regarding the efficiency of the OXB-conversion process. For this purpose, both an invasive method with the aid of the heating beam itself, and a non-invasive method with aid of the developed microwave emission diagnostic, were used.

# 2 Chapter 2

---

## Wave Propagation Theory

„Waves in plasmas” is a very broad field that has been investigated for more than 100 years and is still a topic of current research. This chapter contains only a brief overview to give the reader an understanding of the relevant vocabulary. A detailed introduction can be found in the forthcoming book by Hartfuß and Geist [HG13], which comprehensively illustrates the theoretical background important for fusion physics in its diagnostic applications. Also greatly advisable is the classic book by Heald and Wharton concerning theoretical and applied plasma diagnostics with microwaves [HW65]. In spite of the solely theoretical presentation, the standard works for waves in plasmas are the books by Stix [Sti92] and by Swanson [Swa03]. A good German introduction with sufficient depth and specific reference to overdense plasma heating can be found in Stroth’s book [Str11].

### 2.1 Wave Description in Magnetized Plasmas

The propagation properties of an electromagnetic wave with angular frequency  $\omega$  are changed with respect to the vacuum, if the propagation medium is electrically or magnetically polarizable. In the case of a plasma, the electrons follow the wave electric field  $\mathbf{E}(\mathbf{r}, t) = \mathbf{E}(\mathbf{r}) \exp(-i\omega t)$  and the ions are typically treated as a fixed background because of their much higher mass. The resultant oscillation of the electrons against the ion background has a maximum frequency called plasma frequency  $\omega_{pe} = \sqrt{n_e e^2 / (\epsilon_0 m_e)}$ . For this reason, only electromagnetic waves above the plasma frequency are able to propagate through a non-magnetized plasma. Waves with a lower frequency are in the so called *cutoff*. The electron density, corresponding to  $\omega = \omega_{pe}$ , is called *critical* or *cutoff density*  $n_c$ .

The magnetic field, however, introduces an additional anisotropy of electron movement leading to different oscillation properties dependent on the direction of the electric field vector of the wave. The simplest approach assumes cold electrons with an electron temperature  $T_e = 0$  as a good description for the coupling of electromagnetic waves into the plasma [HG13]. On the other hand, a finite thermal velocity allows the propagation of local charge accumulations like the introduced plasma oscillation. The resultant propagating electric fields are called electrostatic waves, whose different types are treated in subsection 2.1.2.

### 2.1.1 Cold Plasmas

A wave in a plasma can be characterized by a temporally harmonic perturbation of the equilibrium plasma parameters [Str11]. For instance, the perturbed electric field can be expressed as  $\tilde{\mathbf{E}}(\mathbf{r}, t) = \tilde{\mathbf{E}}(\mathbf{r}) \exp(-i\omega t)$ . Because of small perturbations, the Maxwell equations in their linearized form are the basis for the treatment of electrostatic, magnetostatic or electromagnetic waves. The wave propagation is described by the induction law and Ampere's law from which the wave equation can be deduced:

$$\nabla \times (\nabla \times \tilde{\mathbf{E}}(\mathbf{r})) = \frac{\omega^2}{c^2} \left( \tilde{\mathbf{E}}(\mathbf{r}) + \frac{i}{\epsilon_0 \omega} \tilde{\mathbf{j}}_e(\mathbf{r}) \right) = \frac{\omega^2}{c^2} \epsilon \tilde{\mathbf{E}}(\mathbf{r}). \quad (2.1)$$

The free charge carriers of the plasma react to the electromagnetic alternating field by a directed current density which is added to the displacement current density  $i\omega\tilde{\mathbf{E}}/c^2$  of the vacuum leading to a dielectric tensor  $\epsilon$  different from unity. The more inertial ion movement was neglected compared to the electron current density  $\tilde{\mathbf{j}}_e(\mathbf{r})$ . The latter one depends on the local electron density  $n_e$  that is typically assumed to be constant for the basic analysis. In this case the spatial evolution of the wave is also harmonic with a constant wave vector  $\mathbf{k}$ . With  $\tilde{\mathbf{E}}(\mathbf{r}) = \tilde{\mathbf{E}} \exp(i\mathbf{k}\mathbf{r})$  the left hand side of equation (2.1) can be simplified to  $\nabla \times (\nabla \times \tilde{\mathbf{E}}(\mathbf{r})) = -\mathbf{k} \times (\mathbf{k} \times \tilde{\mathbf{E}})$ . The electron current density  $\tilde{\mathbf{j}}_e = -en_e\tilde{\mathbf{v}}_e$  arises from the linearized equation of motion of the electrons in a homogenous magnetic field:

$$-i\omega m_e n_e \tilde{\mathbf{v}}_e = -en_e \left( \tilde{\mathbf{E}} + \tilde{\mathbf{v}}_e \times \mathbf{B} \right) - m_e n_e \nu \tilde{\mathbf{v}}_e - i\mathbf{k}\tilde{\mathbf{p}}. \quad (2.2)$$

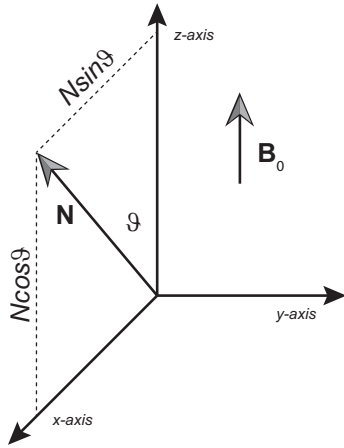


Figure 2.1: *Used coordinate system with the homogenous magnetic flux density  $\mathbf{B} = (0, 0, B_z)$  in  $z$ -direction and the refractive index  $\mathbf{N} = \mathbf{k}c/\omega$  in the  $x$ - $z$ -plane under an angle  $\vartheta$  to the  $z$ -axis*

In a cold plasma the electron temperature can be set to zero and the pressure term  $-i\mathbf{k}\tilde{\mathbf{p}}$  vanishes. This approximation describes the essential properties of electromagnetic waves in high temperature fusion plasmas very well [HG13]. Because collisions cannot be completely neglected, a friction force  $m_e\nu\tilde{\mathbf{v}}_e$  with a collision frequency  $\nu$  is added in the force balance. Elastic collisions of the electrons with the ions leads to an impulse transfer and a decrease of the electric conductivity. Furthermore, the electrons are redirected by collisions among themselves leading to an equipartition of the electron velocity parallel and perpendicular to the magnetic field lines. Therefore, the reaction of the electrons to the electric alternating field is shifted in the phase relation leading to a dissipative damping. The collision frequency  $\nu$  is defined as the inverse of the average time after which a particle has lost its energy of the particular direction of motion. For this reason, the decelerating force acts parallel and needs to be treated only as a vector  $\nu$ . For electron-ion collisions the components are distinguished between an effective collision frequency parallel  $\nu_{\parallel}$  and perpendicular  $\nu_{\perp}$  to the magnetic field vector  $\mathbf{B}$  [Swa03]. The calculation of each component will be treated in section 2.2.2. Without loss of generality the coordinate system can be

chosen in such a way that the magnetic field vector  $\mathbf{B} = (0, 0, B_z)$  points in  $z$ -direction and the wave propagation takes place in the  $x$ - $z$ -plane. For this reason, the dielectric tensor of the wave equation (2.1) in combination with equation (2.2) can be simplified to

$$\epsilon = \begin{pmatrix} S & -iD & 0 \\ iD & S & 0 \\ 0 & 0 & P \end{pmatrix} \text{ with} \quad (2.3)$$

$$S = 1 - \frac{X_{\perp}}{1 - Y^2} \quad D = -\frac{X_{\perp}Y}{1 - Y^2} \quad P = 1 - X_{\parallel} \quad (2.4)$$

The quantities  $X$  and  $Y$  have their usual definitions as a dimensionless electron density  $n_e$  and dimensionless electron cyclotron frequency  $\omega_{ce}$  but in the case of  $X$  with the introduced parallel and perpendicular collision frequencies:

$$X_{\perp} = \frac{\omega_{pe}^2}{\omega^2} \left( \frac{1}{1 + i\frac{\nu_{\perp}}{\omega}} \right) = \frac{n_e}{n_c} \left( \frac{1}{1 + i\frac{\nu_{\perp}}{\omega}} \right), \quad X_{\parallel} = \frac{\omega_{pe}^2}{\omega^2} \left( \frac{1}{1 + i\frac{\nu_{\parallel}}{\omega}} \right), \quad Y = \frac{\omega_{ce}}{\omega + i\nu_{\perp}}. \quad (2.5)$$

For the investigation of the wave propagation the wave vector  $\mathbf{k}$  can be expressed in terms of the refractive index  $N$  and the angle  $\vartheta$  between the propagation direction and the magnetic field

$$\frac{\mathbf{k}c}{\omega} = \mathbf{N} = \begin{pmatrix} N \sin \vartheta \\ 0 \\ N \cos \vartheta \end{pmatrix}. \quad (2.6)$$

Figure 2.1 illustrates the used coordinate system. After insertion of equation (2.3) and (2.6) in (2.1) and solving of the double vector product, the wave equation can be written as [Swa03]:

$$\begin{pmatrix} S - N^2 \cos^2 \vartheta & -iD & N^2 \cos \vartheta \sin \vartheta \\ iD & S - N^2 & 0 \\ N^2 \cos \vartheta \sin \vartheta & 0 & P - N^2 \sin^2 \vartheta \end{pmatrix} \begin{pmatrix} E_x \\ E_y \\ E_z \end{pmatrix} = 0 \quad (2.7)$$

The solutions are determined by a vanishing matrix determinant. This conditional equation is named cold dispersion relation or Altar-Appleton<sup>1</sup> equation:

$$AN^4 - BN^2 + C = 0 \text{ with the coefficients} \quad (2.8)$$

$$\begin{aligned} A &= S \sin^2 \vartheta + P \cos^2 \vartheta \\ B &= (S + D)(S - D) \sin^2 \vartheta + PS(1 + \cos^2 \vartheta) \\ C &= P(S + D)(S - D) \end{aligned} \quad (2.9)$$

The solution of equation (2.8) leads to

$$N^2 = \frac{B \pm \sqrt{B^2 - 4AC}}{2A}. \quad (2.10)$$

Because of the different signs, two different propagating wave types can occur, called *ordinary* and *extraordinary* mode, but a general solution in the form  $\omega(k)$  cannot be derived. For the analytical study the problem is typically reduced to the propagation perpendicular ( $\vartheta = 90^\circ$ ) and parallel ( $\vartheta = 0^\circ$ ) to the magnetic field. The two possible modes in each case are historically termed with different names. For the parallel propagation the so called R- and L-waves are derived from the right hand and left hand circularly polarized fundamental modes.

<sup>1</sup>The name Appleton-Hartree dispersion relation is also often used although Hartree only influenced the publication and Wilhelm Altar first calculated the dispersion relation during his collaboration with Hartree in 1926 [Swa03].

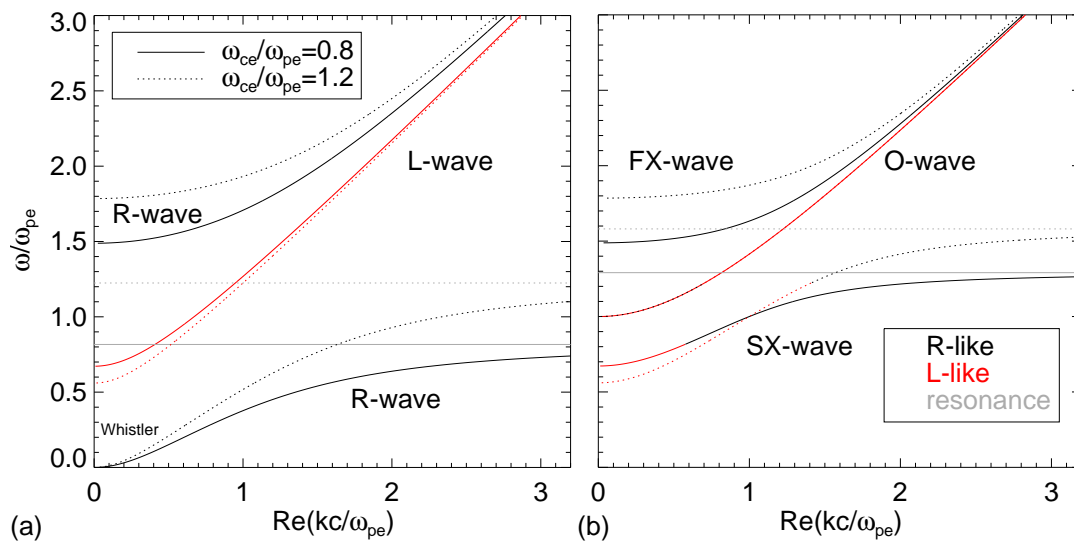


Figure 2.2: Dispersion relation of the cold plasma with the wave frequency  $\omega$  dependent on the wave vector  $k$  (both related to the plasma frequency  $\omega_{pe}$ ) for the two special propagation directions  $\vartheta = 0^\circ$  (a) and  $\vartheta = 90^\circ$  (b). The fundamental wave modes are plotted for  $\omega_{ce}/\omega_{pe} = 0.8$  and  $\omega_{ce}/\omega_{pe} = 1.2$ , respectively.

For the perpendicular propagation the names ordinary or O-wave and extraordinary or X-wave are used. The former one has a linear polarization parallel to magnetic field vector and the latter one perpendicular to that. With the transition from  $\vartheta = 90^\circ$  to  $\vartheta = 0^\circ$  the linear polarization of both fundamental modes becomes more and more elliptical with opposite senses of rotation and polarization ellipses perpendicular on each other. For  $\omega > \omega_{ce}$  the ordinary mode corresponds to the L-wave and the extraordinary mode to the R-wave. Therefore, the oblique modes only should be distinguished in L-like and R-like waves, even though the ellipticity is zero near  $\vartheta = 90^\circ$ <sup>2</sup>. This classification becomes apparent in Figure 2.2 that shows the dispersion relation  $\omega(k)$  for the special cases of propagation. For  $\vartheta = 90^\circ$  the so called fast X-wave (FX-wave) evolves from the upper branch of the R-wave and the O-wave from the L-wave. But in the vicinity of resonances the wavelength tends to zero and the polarization is modified becoming more parallel to the magnetic field. This also explains why the slow X-wave (SX) does not evolve from the lower branch of the R-wave but from a split-up of the L-wave. If R- and L-like waves exist in parallel, the cut-off-frequency of the former one will be higher, but it is only dependent on the plasma parameters. The general analytical solution of the cut-off-frequencies is

$$\omega_{\text{cut}} = \frac{1}{2} \sqrt{\omega_{ce}^2 + 4\omega_{pe}^2} \pm \frac{\omega_{ce}}{2}. \quad (2.11)$$

The first one is called Upper-X- or R-cut-off and the second one Lower-X- or L-Cut-Off. The third one arises from the general plasma cut-off-frequency. In contrast, the resonance frequencies depend on the direction of propagation and can be calculated by

<sup>2</sup>A much more sophisticated classification into quasi-transversal and quasi-longitudinal modes is possible but needs lengthy explanations and would be confusing. Especially in the vicinity of resonances a special treatment is necessary.

$$\omega_{\text{res}}^2 = \frac{1}{2}\omega_{\text{uh}}^2 \pm \frac{1}{2}\sqrt{\omega_{\text{uh}}^4 - 4\omega_{\text{pe}}^2\omega_{\text{ce}}^2 \cos^2 \vartheta}. \quad (2.12)$$

The historically termed Upper-Hybrid-frequency  $\omega_{\text{uh}}^2 = \omega_{\text{ce}}^2 + \omega_{\text{pe}}^2$  is the resonance frequency of the so called slow X-wave in the case of perpendicular propagation. For the parallel propagation there are two resonances: the electron cyclotron frequency of the R-wave and the plasma frequency that cannot be identified with a propagating wave. To get a feeling how the different wave modes are related to each other in a bounded plasma Figure 2.3 shows a density dependent representation of the squared refractive index for two different magnetic fields in relation to the propagation frequency. Typically a ratio lower 1 is used for the heating of magnetically confined plasmas because of resonant absorption at the fundamental and higher harmonics of the electron cyclotron frequency. An introduction as well as references will be given in section 2.2.1. Both cases of Figure 2.2 can be understood as boundaries of the areas in Figure 2.3 where a wave propagation is possible. The so called overdense area applies for  $n_e/n_c > 1$  where only the slow X-mode is able to propagate. But the excitation from the vacuum is only possible with a fast wave mode. Because of the density gradient, an obliquely incident wave would be deflected that leads to a continuous change of the propagation angle and split-up into the particular actually valid fundamental modes. Under certain conditions a full conversion will happen. The evolution of the squared refractive index is shown in Figure 2.9 of subsection 2.2.3.1. At the resonance the slow X-wave can excite electrostatic electron Bernstein waves that are the preferred wave type for overdense plasma heating and will be introduced in the next section. But this wave type cannot exist for  $\omega_{\text{ce}}/\omega > 1$ . The electromagnetic R-like waves are able to propagate in the overdense region, however, and are known as Whistler waves in the case of nearly parallel propagation to the magnetic field lines [Str11]. The research of this wave type was initiated by the astrophysicist who investigated the wave propagation along the earth magnetic field lines in the ionosphere<sup>3</sup>. His results can be transferred to WEGA and give the basis for the modeling of the overdense non-resonant heating in subsection 5.1.2.4.

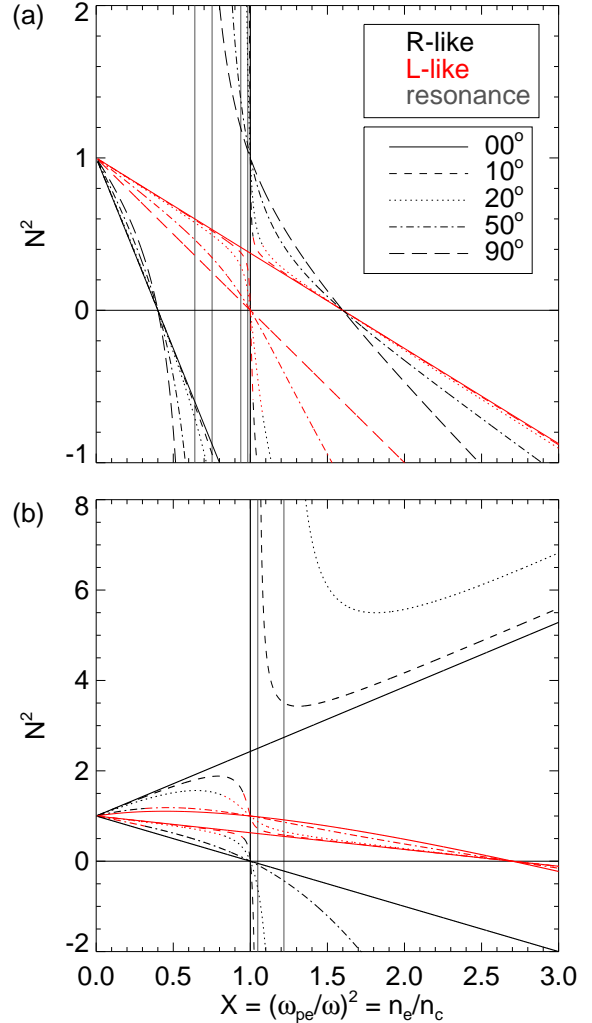


Figure 2.3: Squared refractive index  $N^2$  at various propagation angles  $\vartheta$  dependent on the normed electron density  $X$  for a normed magnetic field of (a)  $Y = 0.6$  and (b)  $Y = 1.7$ .

<sup>3</sup>At low frequencies the phase velocity increases with higher frequency which leads to a whistling sound of a radio wave propagating from one earth pole to the other (see dispersion relation of lower R wave branch in Figure 2.2a).

### 2.1.2 Warm Plasmas (Finite Plasma Temperature)

The plasma pressure  $\tilde{p}$  within the equation of motion (2.2) cannot be ignored for a finite plasma temperature. A density disturbance of electrons or ions leads to electric fields which can propagate through the plasma because of the finite velocity of the particle species. The result are additional wave types called electrostatic waves with an electric field vector along the wave vector  $\mathbf{k}$ . In contrast to electromagnetic waves, propagation in a vacuum is not possible because the plasma is needed to act as a propagation medium.

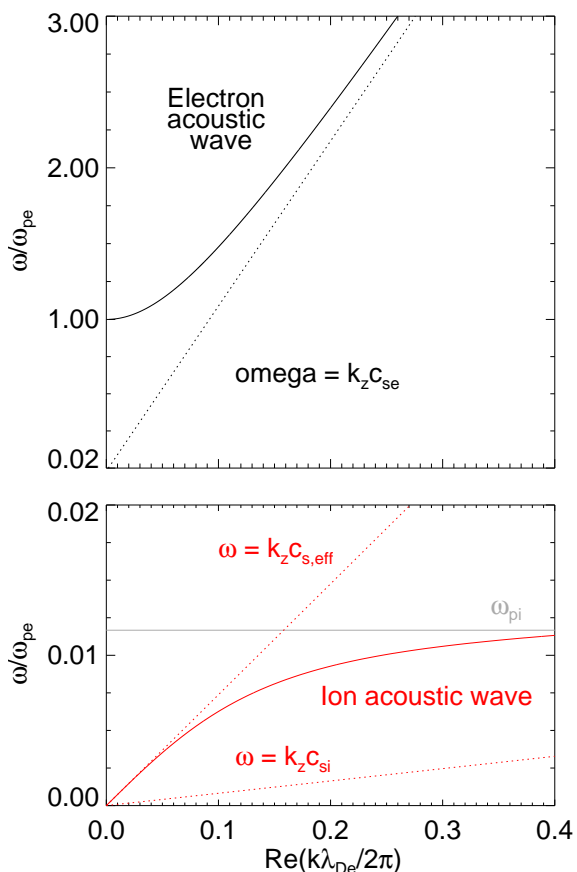


Figure 2.4: Dispersion relation of warm plasma with the normalized wave frequency  $\omega$  dependent on the wave vector  $k$  related to the Debye length of  $\lambda_{De} \approx 6 \mu\text{m}$  for a singly ionized helium plasma with an electron temperature  $T_e = 6 \text{ eV}$ , an ion temperature  $T_i = 25 \text{ meV}$  and an electron density  $n_e = 8 \cdot 10^{18} \text{ m}^{-3}$ .

Analysis necessitates the consideration of the equation of state  $p/n^\gamma = \text{const}$  which specifies the temperature equalization within gases by means of the adiabatic coefficient  $\gamma$  [Str11]. If the considered process is much faster than the thermalization time, an adiabatic coefficient of  $\gamma = 3$  must be used for one dimension. On the other hand,  $\gamma = 1$  is valid for isothermal processes. The linearization of pressure ( $p = p_0 + \tilde{p}$ ) and of density ( $n = n_0 + \tilde{n}$ ) leads to a disturbed pressure  $\tilde{p} = \gamma p_0 \tilde{n}/n_0$  for each species. A change in pressure is related to a density perturbation  $\tilde{n}$  whose propagation is defined by the continuity equation by means of equalization flows. As was mentioned in the previous subsection, a harmonic ansatz is used for the density  $n(\mathbf{r}) = n_0(\mathbf{r}) + \tilde{n} \exp(i\mathbf{k}\mathbf{r})$  as well as for the particle velocity  $\mathbf{v}(\mathbf{r}) = \tilde{\mathbf{v}} \exp(i\mathbf{k}\mathbf{r})$ . The resultant density perturbation  $\tilde{n} = \mathbf{k}\tilde{\mathbf{v}}n_0/\omega$  is dependent on the velocity perturbation  $\tilde{\mathbf{v}}$  which also determines the pressure perturbation  $\tilde{p}$ . The latter one is inserted in the equation of motion (2.2) for each particle species [Str11].

The simplest solution can be obtained for propagation in the  $z$ -direction because the magnetic field has no influence on the movement of the charged particles. The resultant current density of electrons and ions is inserted into the wave equation (2.1) so that the corresponding dielectric constant can be written as

$$\epsilon_z = 1 - \frac{\omega_{pi}^2}{\omega^2 - k_z^2 c_{si}^2} - \frac{\omega_{pe}^2}{\omega^2 - k_z^2 c_{se}^2} = 0. \quad (2.13)$$

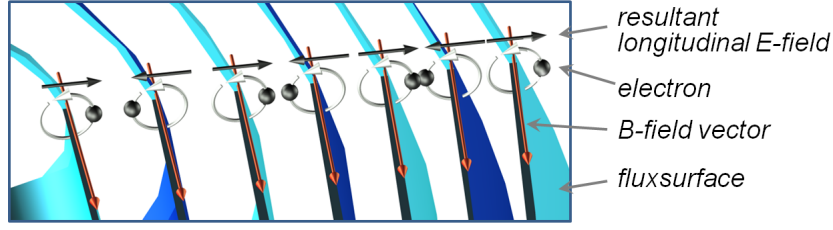


Figure 2.5: Simplified illustration of an electron Bernstein wave based upon the coherent motion of the electrons around the magnetic field lines.

The displacement current by the temporally alternating electric field is directly compensated by parallel plasma currents so that no magnetic field appears as the reason for the vanishing left side of equation (2.1). The characteristic velocities are the *electron speed of sound*  $c_{se} = \sqrt{\gamma_e T_{e,\parallel}/m_e}$  and the *ion speed of sound*  $c_{si} = \sqrt{\gamma_i T_{i,\parallel}/m_i}$ . If  $\omega^2 \geq k_z^2 c_{se}^2$ , the last term of equation (2.13) dominates and the second term can be ignored. This leads to the dispersion relation of *electron acoustic waves* (or *Bohm-Gross waves*)

$$\omega = \sqrt{\omega_{pe}^2 + k_z^2 c_{se}^2}. \quad (2.14)$$

Their wavelength  $\lambda_{BG} = 2\pi/k_z$  is of the order of the *Debye length*  $\lambda_{De}$ , which defines the screening of a charge by the surrounding charged particles. The electric field generated by the charge is decreased to  $1/e$  at the distance of the Debye length. The behavior is similar to the electromagnetic O-mode, as shown in Figure 2.4, but with a smaller phase velocity  $v_{ph} \gtrsim c_{se}$ .

A second solution of equation (2.13) exists for much smaller frequencies of the order of the ion plasma frequency  $\omega_{pi} \ll \omega_{pe}$ . The dispersion of this so called *ion acoustic wave* is shown in the bottom graph of Figure 2.4, which has an enlarged vertical scale. For small ion temperatures  $T_{i,\parallel} \rightarrow 0$ , a resonance appears at the ion plasma frequency so that the behavior can be compared with the electromagnetic R-wave. The dispersion relation for  $\omega < \omega_{pi}$  can be approximated by [Str11]

$$\omega = \sqrt{c_{se}^2 \frac{m_e}{m_i} + c_{si}^2} k_z = c_{s,\text{eff}} k_z = \sqrt{\frac{T_{e,\parallel} + 3T_{i,\parallel}}{m_i}} k_z. \quad (2.15)$$

The wave is carried by both particle species, but the inertia of the system is defined by the ion mass.

The ion and electron acoustic waves for propagation in the  $z$  – direction are not influenced by the magnetic field. For perpendicular propagation with respect to the magnetic field lines, the gyro motion of the charged particles determines the dispersion relation of the corresponding electrostatic waves. Figure 2.5 shows a simplified example of the gyrating electrons with the *Larmor radius*  $r_{L,e} = v_{\perp}/\omega_{ce} = v_{\perp} m_e/eB$ . A coherent motion leads to an alternating electric field with propagation quasi-perpendicular to the magnetic field. In contrast to the acoustic modes, a finite Larmor radius is required for the existence of the so called electron Bernstein waves, which in turn necessitates a finite electron temperature.

For the derivation of the corresponding dispersion relation, the hot dielectric tensor  $\epsilon^{(h)}$  must be considered that has only non-vanishing diagonal components in contrast to the cold dielectric tensor in equation (2.3). Each component is dependent on, amongst others, at least two components of the refractive index  $\mathbf{N} = kc/\omega \cdot (\sin \vartheta, 0, \cos \vartheta)$ . Dependence on the wave vector perpendicular to the magnetic field vector,  $k_{\perp} = \sqrt{k_x^2 + k_y^2}$ , is expressed in terms of the so called finite Larmor parameter  $\mu = 1/2k_{\perp}^2 r_{L,e}^2$ , as a normalization of the Larmor radius to the wavelength. For perpendicular propagation ( $\vartheta = 90^\circ \Rightarrow N_z = 0$ ), as is shown in Figure 2.5, the dielectric tensor<sup>4</sup> takes on the same principal aspect as equation (2.3), with the following elements:

$$\epsilon_{xx}^{(h)} = \epsilon_{yy}^{(h)} = 1 - \frac{1}{\mu} \cdot F(\mu) = 1 - \frac{1}{\mu} \cdot 2X \exp(-\mu) \sum_{n=1}^{\infty} \frac{n^2 I_n(\mu)}{1 - n^2 Y^2} \quad (2.16)$$

$$\epsilon_{xy}^{(h)} = -\epsilon_{yx}^{(h)} = -i \frac{X}{Y} \exp(-\mu) \left\{ I_1(\mu) - I_0(\mu) + \sum_{n=1}^{\infty} \frac{I_{n-1}(\mu) - 2I_n(\mu) + I_{n+1}(\mu)}{1 - n^2 Y^2} \right\} \quad (2.17)$$

The summation of the Bessel functions  $I_n$  is executed over the number  $n$  of cyclotron harmonics. Depending on the considered wave frequency  $\omega$  the series can be limited to a few elements. The component  $\epsilon_{zz}^{(h)}$  is not given because it only leads to a generalization of the O-mode introduced in the previous subsection.

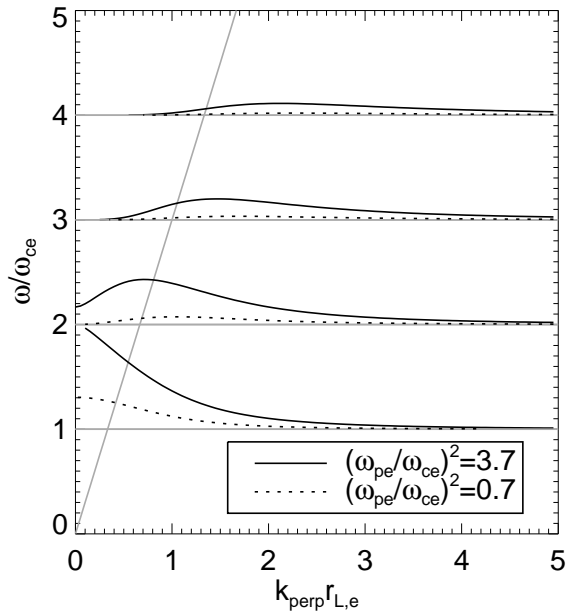


Figure 2.6: Dispersion relation of warm plasma with the normalized wave frequency  $\omega$  dependent on the wave vector  $k$ , which is related to the Larmor radius  $r_{L,e}$  for an electron temperature of  $T_e = 7 \text{ eV}$ .

If the electric field vector of the electrostatic electron Bernstein wave is assumed to only be in propagation direction ( $x$ -direction), the dispersion relation arises from  $\epsilon_{xx}^{(h)} = 0$  and can be expressed as

$$\mu = k_{\perp}^2 \frac{r_{L,e}^2}{2} = F(\mu) \quad (2.18)$$

with a multitude of solutions. This assumption is valid for small wavelengths ( $k_{\perp}^2 r_{L,e}^2 > 3n$ ) because the non diagonal elements vanish and all possible modes are fully decoupled [Vol03]. At higher wavelengths, however, the EBW gets an electric field component in  $y$ -direction, which constitutes a coupling to the slow X-mode (SX) also introduced in the previous subsection. The common dispersion relation is shown in Figure 2.6 and was deduced from

$$N^2 = \frac{\epsilon_{xx}^{(h)} \epsilon_{yy}^{(h)} + (\epsilon_{xy}^{(h)})^2}{\epsilon_{xx}^{(h)}}. \quad (2.19)$$

<sup>4</sup>The hot dielectric tensor also contains the plasma dispersion function, which was not introduced because it vanishes for perpendicular propagation.

The left side of the diagonal line corresponds to a SX-mode which has resonance around the Upper-Hybrid-frequency  $\omega_{\text{uh}}^2 = \omega_{\text{ce}}^2 + \omega_{\text{pe}}^2$  as shown in Figure 2.2b. Therefore, its refractive index becomes large and the electric field component in  $x$ -direction dominates. The phase velocity of the SX-wave is simultaneously reduced and becomes of the order of the thermal velocity of the electrons. The SX-mode gains an electrostatic character and is transformed into a fully electrostatic EBW given by equation (2.18). Because of a vanishing imaginary part  $\Im(k_{\perp})$  of the solutions, the perpendicular propagation of EBWs is not dampened, but has resonance at each cyclotron harmonic. This allows a specific heating of the plasma at a certain radial position within the toroidal magnetic field. A great advantage of EBWs in relation to the electromagnetic modes is the lack of a cutoff. There is, however, a lower density limit whose corresponding plasma frequency is defined by the upper hybrid frequency. Therefore, a direct coupling from the vacuum is not possible. The excitation of EBWs with the aid of slow X-waves will be described in subsection 2.2.3.

A further result of the finite Larmor radius  $r_{L,e}$  is the possibility of heating the electrons with the aid of electromagnetic waves also at higher harmonics of the electron cyclotron frequency. In contrast, the absorption at the first harmonic already appears in the imaginary solution  $\Im(k)$  of the cold dispersion relation. The details will be explained in the next section, in relation to the conditions for efficient plasma heating.

## 2.2 Wave Propagation and Absorption within Magnetized Plasmas

If an electromagnetic or electrostatic microwave<sup>5</sup> of certain frequency  $\omega$  propagates through a magnetized plasma, its intensity is either reduced by local absorption or increased by local emission. The case of local emission is not relevant for the analysis of plasma heating, but it should be mentioned in order to explain the basics of an electron cyclotron emission (ECE) and an electron Bernstein wave emission (EBE) diagnostic. The crucial equation for heating results as special case through ignoring any emission from the plasma.

The radiation transport of microwaves in a plasma is characterized by an interplay of emission and absorption processes. The change of local intensity  $I$  along the propagation path length  $s$  is given by the local emission coefficient  $j$  and the absorption coefficient  $\alpha$  multiplied by  $I$ :

$$\frac{dI(\omega, \mathbf{K}, n_e, T_e)}{ds} = j(\omega, \mathbf{K}, n_e, T_e) - \alpha(\omega, \mathbf{K}, n_e, T_e) \cdot I(\omega, \mathbf{K}, n_e, T_e). \quad (2.20)$$

Absorption and emission are generally dependent on the electron temperature  $T_e$  and density  $n_e$ , as well as on the considered frequency and the propagation direction of the wave in relation to the magnetic field vector. The integration of equation (2.20) along the propagation path leads to intensity  $I_R$  at an arbitrary point  $R$  within or outside the plasma:

$$I_R(\omega, \mathbf{K}, n_e, T_e) = I_Q(\omega, \mathbf{K}, n_e, T_e) \cdot \exp(-\tau_{Q \rightarrow R}) + \frac{j(\omega, \mathbf{K}, n_e, T_e)}{\alpha(\omega, \mathbf{K}, n_e, T_e)} [1 - \exp(-\tau_{Q \rightarrow R})]. \quad (2.21)$$

The so called *optical depth*  $\tau_{Q \rightarrow R}$  is the line integration of the absorption coefficient along the propagation path from the source at point  $Q$  to the observation point  $R$ :

$$\tau_{Q \rightarrow R} = \int_Q^R \alpha(\omega, \mathbf{K}, n_e, T_e) ds. \quad (2.22)$$

In the case of thermal equilibrium<sup>6</sup>, Kirchhoff's law is valid and the ratio of emission and absorption coefficient is equal to the radiated intensity  $B(\omega, T)$  of a black body of the temperature  $T$  [DGLR94]. Planck's law can be approximated in the microwave frequency range by the Rayleigh-Jeans law so that a direct proportionality of the intensity  $B(\omega, T)$  on the temperature follows. For this reason, the intensity observed by a microwave emission diagnostic is proportional to the electron temperature  $T_e$  and is referred to as radiation temperature  $T_{\text{rad}}$ . Ignoring a source  $I_Q(\omega, \mathbf{K}, n_e, T_e)$  outside the plasma in equation (2.21), the radiation temperature is given by

$$T_{\text{rad}} = T_e [1 - \exp(-\tau_{Q \rightarrow R})]. \quad (2.23)$$

In the case of plasma heating, emission can be neglected and the heating power not absorbed after the first penetration path through the plasma can be calculated by

$$P_1 = P_0 \exp(-\tau_{Q \rightarrow R}). \quad (2.24)$$

Full absorption is achieved by *optically thick* plasmas corresponding to  $\tau \gtrsim 3$ .

---

<sup>5</sup>Only the electron cyclotron frequency range and higher harmonics are of interest. The spectrum ranges from 10 GHz up to 300 GHz for typical fusion experiments. This allows for the assumption of a finite microwave beam, which is explained in section 2.3.1.

<sup>6</sup>A more detailed treatment can be found in the author's diploma thesis [Sta08] as well as [HG13].

### 2.2.1 Electron Cyclotron Interaction

Only the absorption and emission of electromagnetic waves are typically referred to as electron cyclotron interaction. Even though electron Bernstein waves (EBW) are also based on electron cyclotron movement, absorption and emission of EBWs is referred to as electron Bernstein wave interaction.

#### 2.2.1.1 Heating

Electrons absorb an electromagnetic wave, if its frequency  $\omega$  is equal to the cyclotron frequency  $\omega_{ce}$  or higher harmonics  $n\omega_{ce}$ . A finite absorption for the latter case is only possible for a finite Larmor radius  $r_{L,e}$ . Figure 2.7 shows a simplified sketch of how the acceleration takes place. An electron in an inhomogeneous alternating electric field is more strongly accelerated on the side with the higher electric field, than decelerated on the side with the lower electric field. The result is a net energy gain.

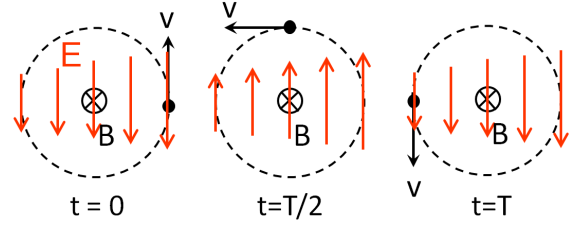


Figure 2.7: A finite Larmor radius and the electric field gradient of the heating wave are the conditions necessary for the acceleration of an electron at the second harmonic of the cyclotron frequency.

For perpendicular incidence, the first harmonic O-mode and the second harmonic X-mode have the highest absorption coefficient dependent on the electron temperature and density<sup>7</sup>. For a finite magnetic field the heating at the second harmonic allows for an electron density that is four times higher because of the square dependence of the critical density on the plasma frequency. Considering an inhomogeneous magnetic field, integration of the absorption coefficient  $\alpha_{X2}$  leads to an optical depth of [Sta08; BCDBE83]

$$\tau_{X2} = \pi \frac{\omega_{pe}^2}{\omega_{ce} c} \frac{k_B T_e}{m_e c^2} \frac{B_0}{\left| \frac{dB_0}{dR} \right|} \approx \pi^2 \left( \frac{\omega_{pe}}{\omega_{ce}} \right)^2 \frac{k_B T_e}{m_e c^2} \frac{R_0}{\lambda}. \quad (2.25)$$

The higher the magnetic field gradient, the thinner the resonant layer and the smaller the optical depth. Optically thick plasmas ( $\tau > 3$ ) are achieved for electron temperatures in the range of 1 keV and densities of  $n_e = 10^{19} \text{ m}^{-3}$ . For smaller values, an incident heating beam hits the inner wall, which does not fully reflect the non absorbed heating power. Its absorption is on the order of 1%, which means that modern fusion experiments with up to 1 MW beam power in an area of  $100 \text{ cm}^2$  should achieve at least 80% single path absorption. Otherwise, the beam can cause serious damage to the wall on the high field side (HFS).

<sup>7</sup>A detailed review on electron cyclotron absorption and emission can be found in [BCDBE83].

### 2.2.1.2 Emission

The observation of electron cyclotron emission by an ECE-diagnostic is based upon emission and reabsorption by the electrons. Intensity is measured with an absolutely calibrated detector which allows the direct determination of the electron temperature  $T_e$  for the case of an optically thick plasma ( $\tau > 3$ ). The effective emission location of a certain frequency  $\omega$  is dependent on the major radius  $R$  because of the decreasing magnetic field along the unit vector  $\mathbf{e}_R$ . The spatial resolution of an ECE-diagnostic is limited due to relativistic and Doppler broadening<sup>8</sup>. Furthermore, the low emission power necessitates an integrated measurement over a finite frequency range. Assuming a viewing area of about  $100 \text{ cm}^2$ , the detectable power around 28 GHz is limited by the Rayleigh-Jeans law to a few  $\text{nW}/(\text{eV} \cdot \text{MHz})$ .

For optical thin plasmas ( $\tau \ll 1$ ), the density must be known to determine recursively the proportional factor of equation (2.23). For this reason, the second harmonic X-mode is generally used for ECE detection in order to obtain the highest possible absorption and the highest possible cutoff-frequency defined by the Upper X-cutoff-frequency. In some scenarios of modern stellarators or spherical tokamaks the condition  $\omega > \omega_{\text{cut}}$  is not fulfilled, so that the temperature diagnostic with the aid of ECE is not possible. Electron Bernstein wave emission, however, is not limited by the upper electron density, but necessitates the conversion to electromagnetic waves for observation from outside the plasma. The physical conditions will be explained in subsection 2.2.3.

### 2.2.1.3 TRAVIS-Code

The incident electromagnetic beam used for plasma heating has a finite width because of physical and technical limitations that will be explained in section 2.3. On the other hand, the temperature and density profiles can vary greatly around the resonance position so that the optical depth, given by equation (2.22), changes over the beam radius. Furthermore, the beam undergoes diffraction within the plasma that can lead to broadening of the deposition profile. For this reason, a three dimensional calculation of propagation and absorption is necessary, and can be realized with the aid of the ray-tracing code TRAVIS developed by IPP [MEH<sup>+</sup>06].

The beam is divided into concentric rings, each with a variable number of rays. If the wavelength  $\lambda = 2\pi/k$  is much less than the density gradient within the plasma<sup>9</sup>, the diffraction of the whole beam can be calculated by the so called ray-tracing technique. The actual gradient of the Hamiltonian as well as its change in the direction of the wave vector  $\mathbf{k}_{\text{ray}}$  is calculated for each ray, defining the change of the ray position and its direction. The Hamiltonian is defined by the local refractive index of the plasma calculated from the electron temperature and density profiles given by the following profile function

$$f = P_1 \left\{ P_4 - P_5 + (1 + P_5 - P_4) \left[ 1 - \left( \frac{r_{\text{eff}}}{a_0} \right)^{P_2} \right]^{P_3} + P_5 \left[ 1 - \exp \left( - \left( \frac{r_{\text{eff}}}{a_0 P_6} \right)^2 \right) \right] \right\} \quad (2.26)$$

---

<sup>8</sup>A detailed description can be found in[HG13] or in the author's diploma thesis using the example of the WEGA stellarator [Sta08].

<sup>9</sup>WKB-approximation can be used.

The profiles are assigned to the flux surface data of the magnetic field configuration used in the experiment resulting in a three dimensional plasma model. The polarization of the considered beam can be one of the two fundamental modes: ordinary and extraordinary. This convention is used along the whole path of the beam for the calculation of absorption and diffraction, even though the angle of the incident beam with respect to the magnetic field lines changes during propagation. The reason can be found in the conservation of the certain electromagnetic mode, if the refractive indexes of the propagable modes vary markedly. For example, an oblique incident beam with  $\vartheta = 56^\circ$  and R-like polarization propagates towards a density cutoff with its normal vector perpendicular to the magnetic field lines. The corresponding refractive index decreases as shown in Figure 2.3a. Furthermore, the beam is deflected leading to a smaller angle  $\vartheta$  and a change of the corresponding polarization ellipse of the actual fundamental plasma mode. The cross polarized fundamental mode (L-like), however, has a much higher refractive index at the same normalized density so that a split into the two actual fundamental plasma modes does not happen in the first order. The polarization is repositioned and the reflected wave also leaves the plasma as an R-like wave without reversal of rotation as is expected from reflection by a mirror<sup>10</sup>.

### 2.2.2 Collisional Interaction

Elastic collisions of the electrons with ions or uncharged particles leads to an additional phase shift in the reaction of the electrons on the alternating electric field. The result is a decrease in electric conductivity as well as dissipative damping of a propagating electromagnetic wave. Furthermore, the electrons are also redirected by collisions among themselves, leading to equipartition of the electron velocity parallel and perpendicular to the magnetic field lines.

Collisions have already been considered in the dispersion relation of cold plasma. For this purpose, a viscous damping term  $m_e \nu \tilde{\mathbf{v}}_e$  with the collision frequency  $\nu$  was introduced in the equation of motion (2.2). This formalism is known as the Krook-model and is only valid when the collision frequency is not dependent on the electron velocity [Swa03]. Strictly speaking, it can only be used for collisions of the electrons with the neutral background gas.

A velocity dependent collision frequency can be taken into account by use of an effective collision frequency which must be determined by averaging over the velocity distribution function. A detailed treatment of this concept can be found in [HW65] with the resultant calculation formula for the effective electron-ion collision frequency

$$\nu_{ei,eff} \approx 3.6 \cdot 10^{-6} Z \frac{n_e}{T_e^{3/2}} \ln \Lambda. \quad (2.27)$$

The ions with the charge number  $Z$  are assumed to be cold with  $T_i = 0$ . The integration over the Maxwellian distributed electron velocities is given by the *Coulomb logarithm*<sup>11</sup>

$$\ln \Lambda = \ln \left( 0.45 \frac{\omega_{pe}}{\omega} \right) + \ln \left( 1.24 \cdot 10^{-9} \frac{T_e^{3/2}}{Z \sqrt{n_e}} \right). \quad (2.28)$$

<sup>10</sup>Elliptical polarizations with respect to the magnetic field vector are in general denoted as R-like or L-like waves. If the polarization is given in respect to the propagation direction, this will be separately denoted.

<sup>11</sup>The Coulomb logarithm is given in the high frequency limit. The formula within the brackets of the second term is known as the *Spitzer parameter*.

Furthermore, different collision frequencies can be assigned for parallel and perpendicular propagation with respect to the magnetic field vector. For  $\omega/\nu_{ei} \gg 1$  the parallel collision frequency can be approximated with  $\nu_{ei,\parallel} \approx 0.5\nu_{ei,\perp} = 0.5\nu_{ei,\text{eff}}$  [Swa03]. Putting these quantities into equation (2.5), the resultant local absorption coefficient of collisional heating can be calculated by the imaginary solution of equation (2.10) [Bek66]

$$\alpha_{\text{coll}} = 2\Im(k). \quad (2.29)$$

A further consequence of collisions is an increase of the *skin depth*  $\delta$  which corresponds to the penetration depth of an electromagnetic wave into an overdense plasma area ( $X = \omega_{pe}^2/\omega^2 > 1$ ). The exact value is dependent on  $X$  and the density gradient  $\partial X/\partial r$ , but the increase of  $\delta$  is limited to a factor of 2.

### 2.2.3 Electron Bernstein Wave Interaction

The coherent gyro motion of the electrons forms an electron Bernstein wave, if densities exist on the order of the *upper hybrid density*  $n_{\text{uh}} = (\omega^2 - \omega_{ce}^2)\epsilon_0 m_e/e^2$  or above. A power transport by the EBW is not possible for lower densities because the group velocity tends to be zero as shown in Figure 2.6. For long wavelengths ( $k_{\perp}^2 r_{L,e}^2 \ll 3n$ ), however, the electrostatic Bernstein wave couples to the electromagnetic SX-wave. The left side of the diagonal line in Figure 2.6 corresponds to the transient area. An X-wave incident perpendicularly to the plasma from the magnetic low field side (LFS) corresponds to a FX-wave. This wave mode is reflected at the lower X-cutoff, as shown in Figure 2.3a, and has no direct access to the overdense plasma region. A conversion of an incident electromagnetic wave into a SX-wave and subsequently into an EBW is only possible under certain conditions explained in the following subsection.

#### 2.2.3.1 Conversion Processes

There are two possible conversion processes to excite a slow extraordinary wave by an electromagnetic wave incident from the LFS. The first one is based on the tunneling of an FX-wave through the evanescent plasma layer and is called FX-SX-conversion<sup>12</sup>. It can be compared with the tunneling of a proton through the Coulomb barrier to another proton. In contrast, the second process bases on the direct coupling of an obliquely incident ordinary wave (L-like) to an extraordinary wave (R-like) within the overdense plasma region. Full conversion can only be achieved for a certain incidence angle  $\vartheta_{\text{opt}}$  with respect to the magnetic field lines. A similar process can be found in optics. A ray of light is fully transmitted through a boundary between two media with different refractive indexes, if the incidence angle of the ray is equal to the so called Brewster angle and the polarization of the wave is parallel to the incidence plane. The corresponding conversion process in plasma physics is called OX-conversion, even though a name like LR-conversion would better convey the required elliptical polarization of the involved wave modes.

---

<sup>12</sup>The conversion between two wave modes must be distinguished between the direct mode coupling and a tunneling which is the result of a finite skin depth.

**FX-SX-conversion** In contrast to the oblique incidence of wave in the OX-conversion, the tunneling to the slow extraordinary wave is most efficient for perpendicular incidence ( $\vartheta = 90^\circ$ ). For this propagation direction, the normalized distance  $\Delta X$  between the upper X-cutoff and the resonance is minimum as apparent in Figure 2.3a. Furthermore, the wave is not deflected because the propagation direction is along the density gradient. For this reason, the FX-wave with perpendicular polarization to the magnetic field lines has the highest tunneling probability. The tunneling is encouraged by the upper hybrid resonance as border to the propagation area of the SX-wave. Budden first described such a tunneling process of electromagnetic waves propagating along the magnetic field lines ( $\vartheta = 0^\circ$ ) in the ionosphere with a simple model known as 'Budden-Tunneling' or the 'Budden problem' [Bud61; MjØ87]. Figure 2.3b shows the dispersion relation along a density gradient for  $Y > 1$ . A R-like wave or rather a R-wave for  $\vartheta = 0^\circ$  is able to tunnel through the cutoff at  $X = 1$  into the overdense area. The transmitted power splits into an absorption at the resonance as well as an excitation of an R-like wave in the overdense area which is called Whistler wave [MjØ87]. This process is physically related to the FX-SX-conversion because of the similar dispersion relation, even though the SX-wave has a further cutoff in the overdense area. The excited SX-wave is reflected at the lower X-cutoff and propagates back to the UHR-layer where the SX-wave is converted into an electron Bernstein wave. The solutions shown in Figure 2.3 for an homogenous plasma, are not valid for both tunneling processes because the ansatz  $\tilde{\mathbf{E}}(\mathbf{r}) = \tilde{\mathbf{E}} \exp(i\mathbf{k}\mathbf{r})$ , with a constant wave vector  $\mathbf{k}$ , was used in section 2.1.1. Especially in the vicinity of singularities, a full wave solution must be sought. Assuming an only linear polarized X-wave (perpendicular propagation), the wave equation (2.1) in combination with the dielectric tensor (2.3) can be reduced to

$$\partial_{xx}\tilde{E}_y(x) + \frac{\omega^2}{c^2} \left( S - \frac{D^2}{S} \right) \tilde{E}_y(x) = \partial_{xx}\tilde{E}_y(x) + \frac{\omega^2}{c^2} Q(x)\tilde{E}_y(x) = 0. \quad (2.30)$$

The modeling of the function  $Q(x)$ , which can be interpreted as a scatter potential [RS00], leads to a differential equation that was solved in [FRS<sup>+</sup>95]. In consideration of the conversion to an EBW in the cutoff-resonance-cutoff resonator, the total conversion efficiency can be deduced [RS00]:

$$C_{\text{SX-FX-B}} = 4 \exp(-\pi\eta) [1 - \exp(-\pi\eta)] \cos^2 \left( \frac{\varphi_{\text{SX-SX}}}{2} + \varphi_\Gamma \right). \quad (2.31)$$

The  $\cos^2$ -factor introduces only a modulation of the maximum conversion efficiency  $C_{\text{SX-FX-B, max}} = 4 \exp(-\pi\eta) [1 - \exp(-\pi\eta)]$  which is dependent on the phase difference between the SX-wave propagating towards the lower X-cutoff and the reflected component. The second quantity  $\varphi_\Gamma$  is the phase of the gamma-function  $\Gamma = (-i\eta/2)$ . The Budden-parameter  $\eta$  determines the maximum conversion efficiency  $C_{\text{SX-FX-B, max}}$  and is given for a slightly changing magnetic flux density ( $L_B \gg L_n$ ) by [RS00]

$$\eta = \frac{\omega_{ce} L_n}{c\alpha} \left[ \sqrt{1 + \alpha^2} - 1 \right]^{1/2}. \quad (2.32)$$

A dependence on the wave frequency  $\omega$  is given by the parameter  $\alpha = (\omega_{pe}/\omega_{ce})|_{\text{UHR}}$  being the ratio of plasma frequency and electron cyclotron frequency at the corresponding UHR-layer. Figure 2.8 shows the expected envelope of the conversion efficiency for an typical overdense WEGA discharge with a magnetic flux density of about half a Tesla. The plasma was heated with 28 GHz microwaves corresponding to the second harmonic of the electron cyclotron frequency. The relatively high density gradient allows no appreciable conversion around 28 GHz. In contrast, a one magnitude lower gradient length would allow almost full conversion. For frequencies lower 13 GHz there is no UHR within the plasma so that an excitation of electron Bernstein waves is in general not possible. As obvious in Figure 2.6, perpendicularly propagating electron Bernstein waves cannot exist for frequencies  $\omega$  lower than the local electron cyclotron frequency  $\omega_{ce}$ .

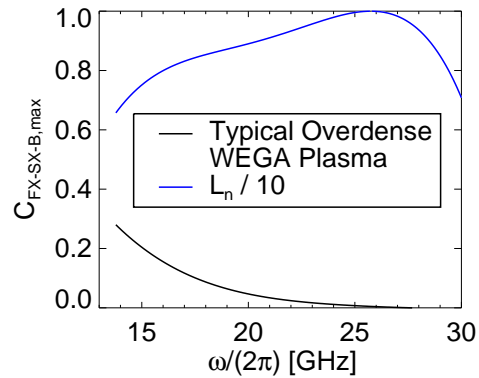


Figure 2.8: *Envelope of the efficiency of the FX-SX-B-conversion given by equation (2.31) and (2.32). A density gradient length of the order  $L_n = 2$  cm was used being a typical value for an overdense WEGA discharge. This is compared with the efficiency for a ten times higher gradient length.*

**O-X-conversion (L-R-conversion)** The direct mode coupling of an ordinary to an extraordinary mode along a density gradient can be derived from the dispersion relation (2.10). The two different signs indicate both modes which must have the same refractive index for full conversion. For this reason, the expression  $B^2 - 4AC$  must vanish which is fulfilled for  $X = 1$  and  $\vartheta = 0^\circ$ . In this case, the perpendicular wave vector is zero and equation (2.10) gives the optimal parallel refractive index for a conversion

$$N_z^2 = N_{z,\text{opt}}^2 = \frac{Y|_{X=1}}{Y|_{X=1} + 1}. \quad (2.33)$$

If a wave propagates obliquely towards the density gradient of an overdense plasma, only the perpendicular wave vector goes to zero at the cutoff layer and the parallel wave vector remains unchanged. In the vacuum, the total refractive index fulfills the geometrical relation  $N^2 = 1 = N_x^2 + N_z^2$  (with  $N_\perp = N_x$  and  $N_\parallel = N_z$ ) so that the wave must be launched under an angle of  $\vartheta_{\text{OX}} = \arccos(N_{z,\text{opt}})$  for full OX-conversion.

If the wavelength is assumed much smaller than the density gradient length of a plasma slab ( $\lambda \ll L_n$ ), the evolution of the perpendicular refractive index of an obliquely incident wave can be calculated by [PK73]

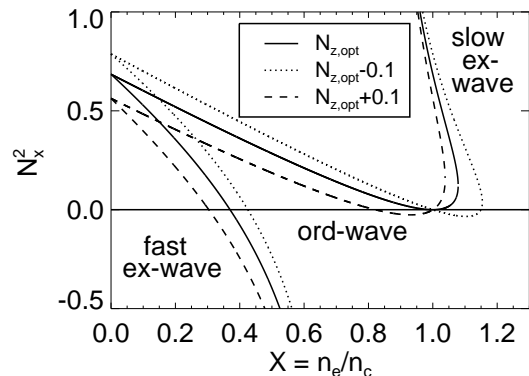


Figure 2.9: *Perpendicular refractive index  $N_x^2$  as a function of the normalized density  $X$  for an ordinary wave obliquely incident on an inhomogeneous plasma slab. In the case of a normalized magnetic field with  $Y = B/B_{\text{res}} = 0.46$ , full conversion to a slow extraordinary mode is obtained for  $N_{z,\text{opt}} = 0.56$  corresponding to  $\vartheta_{\text{OX}} = 56^\circ$ .*

$$N_x^2 = 1 - N_z^2 - X - \frac{XY}{2(1 - X - Y^2)} \left\{ Y(1 + N_z^2) \mp \left[ Y^2(1 - N_z^2)^2 + 4N_z^2(1 - X) \right]^{1/2} \right\}. \quad (2.34)$$

Figure 2.9 shows  $N_x^2$  in dependence on the normalized density  $X$  for three different parallel refractive indexes  $N_z$ . The deviation from the optimal value  $N_{z,\text{opt}}$  leads to a thin evanescent plasma layer. The result is a partial reflection of the ordinary wave with only a partial OX-conversion. The theoretically expected transmission in dependence on  $N_z$  can be expressed by [Mj084]

$$T_{\text{Mj084}} = \exp \left\{ -\pi k_0 L_n \sqrt{\frac{Y}{2}} \left[ 2(1 + Y)(N_z - N_{z,\text{opt}})^2 + N_y^2 \right] \right\}. \quad (2.35)$$

The Gaussian like function defines a transmission window around the optimal incidence angle  $\vartheta_{\text{OX}}$ . The lower the product of the density gradient length and the vacuum wave vector, the broader the acceptance window. The typical WEGA gradient length  $L_n \approx 2$  cm leads to a full width half maximum (FWHM) of  $15^\circ$  for a 28 GHz wave. A basic requirement for the conversion is the correct polarization of the incident ordinary wave, which is given by the complex ratio of the perpendicular and parallel electric field components:

$$\frac{E_\perp}{E_\parallel} = -\frac{i}{2N_z} \left[ \frac{YN_x^2}{1 - X} \mp \left( \frac{Y^2N_x^4}{(1 - X)^2} + 4N_z^2 \right)^{1/2} \right]. \quad (2.36)$$

As explained in subsection 2.2.1.3, the polarization of the wave will be changed by the plasma, when the direction of the wave vector is changed by diffraction. After conversion of the L-like wave (ordinary) to the R-like wave (extraordinary) in the vicinity of the cutoff-layer ( $X = 1$ ), the R-like wave propagates back into the underdense plasma area as shown in Figure 2.9. Similar to the FX-SX-B-conversion, the R-like wave (slow extraordinary) is converted into an electron Bernstein wave at the UHR-layer, but the parallel refractive index remains unchanged. The result is an obliquely propagating EBW which can transfer a finite impulse to the resonantly absorbing electrons. A more detailed explanation of absorption and current drive is given in the next subsection.

### 2.2.3.2 Heating and Emission

The propagation of an electron Bernstein wave is damped by resonant absorption as well as elastic and inelastic collisions of the electrons with other particle species. If the wave reaches a cyclotron resonance, the phase velocity goes to zero, as is shown in Figure 2.6. The wavelength is decreased to the thermal electron Larmor radius and the electric field resonantly accelerates the gyrating electrons.

The absorption coefficient of an perpendicularly propagating EBW at the first harmonic is typically a few magnitudes higher compared to the electromagnetic X2-mode under consideration of similar fusion relevant plasma parameters<sup>13</sup> [Vol03]. For this reason, the power is sharply deposited around the resonance. This behavior is more strongly emphasized for lower temperatures because of an inverse dependence of the absorption coefficient on the temperature [Vol03].

<sup>13</sup>A direct comparison of the same harmonic is not possible because both wave types cannot exist at the same density.

As an example, the absorption coefficient  $\alpha_{\omega}^{\text{B1}}$  for the first harmonic EBW has a  $XT^{-3/2}$ -dependence whereas the absorption coefficient  $\alpha_{\omega}^{\text{X2}}$  for the second harmonic extraordinary mode has a  $XT^{1/2}$ -dependence [Laq07]. Thus, full absorption can be easier achieved in low temperature plasmas. A more detailed treatment of electron Bernstein wave absorption can be found in [Vol03].

In subsection 2.1.2 the propagation direction of an EBW was assumed to be only perpendicular to the magnetic field lines ( $N_{\parallel} = 0$ ). As explained in the previous subsection, the conversion process can introduce a finite parallel component that necessitates the consideration of a possible Doppler shifted absorption. The resonance condition for electron Bernstein wave absorption is given by

$$1 - \frac{n\omega_{ce}}{\omega\gamma} - N_z \frac{v_z}{c} = 0 \quad \text{with } \gamma = \frac{1}{\sqrt{1 - (\frac{v}{c})^2}}. \quad (2.37)$$

The parallel refractive index at the resonance position, however, can be completely different from the initial one during the excitation of the EBW. Its propagation path within an inhomogeneous plasma is strongly dependent on the magnetic field configuration as well as the temperature and density profile. An analysis of propagation and absorption is only possible by ray tracing whose basics were explained in subsection 2.2.1.3 in the example of TRAVIS. For electron Bernstein waves the so called AMR-code must be used which is explained in the next subsection.

The typical launch scenarios for stellarators have the goal to reduce current drive so that the initial parallel refractive index introduced by the OXB-conversion must be minimized. Because of the three-dimensional magnetic field configuration of stellarators, the change of the incidence position to another poloidal plane with a different cross section can result in a significantly different parallel refractive index at the resonance position. On the other hand, the launch scenario can be optimized to a maximum parallel refractive index to increase the current drive for the compensation of internal plasma currents.

Regarding Kirchhoff's law, the high absorption coefficient of electron Bernstein waves also results in a high emission coefficient at the resonance frequency. The consequence is a thermal electron Bernstein wave emission with a radiation temperature equal to electron temperature. The generated EBWs can be converted into electromagnetic waves by the BXO-conversion process being the inverse OXB-conversion process. For this reason, the electron Bernstein wave emission (EBE) can be detected under the same optimal angle  $\vartheta_{\text{OX}}$  with respect to the magnetic field lines. The use of EBE as a replacement for an ECE-diagnostic for the case of an overdense plasma is still under investigation in fusion research. A very detailed description of its successful application at the stellarator Wendelstein 7-AS can be found in [Vol03]. Furthermore, the use of EBE as an edge current diagnostic at the spherical tokamak MAST is another important example for the diagnostic potential of electron Bernstein waves [SDBF<sup>+</sup>11].

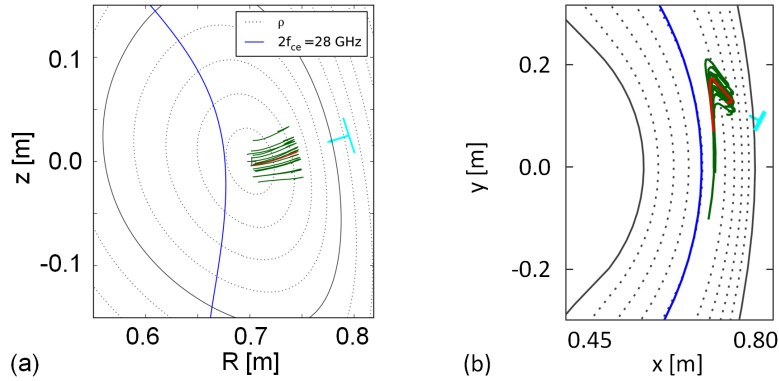


Figure 2.10: AMR-calculation of the electron Bernstein wave propagation projected on a poloidal plane around the incidence position (a) and on the equatorial plane at  $z = 0$  (b). The direction of the incident ordinary microwave beam is indicated by the cyan arrow.

### 2.2.3.3 AMR-code

The power deposition of electron Bernstein wave heating, as well as the expected emission by the electrons via EBWs, can be calculated with the AMR-code developed by IPP-Prague [Urb08]. The abbreviation stands for Antenna (A), mode conversion (M) and ray-tracing (R). Similar to the TRAVIS-code, the incident microwave beam of the antenna is divided into individual rays that are traced to its individual intersection points with the O-mode cutoff layer. The O-X-conversion efficiency is calculated for each ray by a one-dimensional full-wave code.

The electrostatic ray-tracing starts with the slow extraordinary mode by use of the real part of the non-relativistic dielectric tensor. The absorption is calculated by the imaginary part of the non-relativistic, weakly-relativistic, or fully-relativistic dielectric tensor. The resultant power deposition or the electron Bernstein wave emission is finally calculated by solving the radiative transfer equation. The density and temperature profiles, necessary for the calculation, are given by the following profile function<sup>14</sup>

$$f = (P_1 - P_4) \exp\left(-\left|\frac{r_{\text{eff}} - P_5}{a_0 P_2}\right|^{P_3}\right) + P_4. \quad (2.38)$$

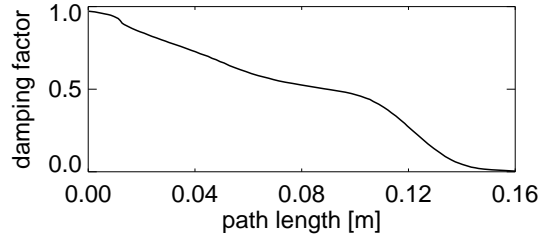


Figure 2.11: Damping factor of the central ray of Figure 2.10 during its propagation to the plasma center.

<sup>14</sup>The profiles are given in relation to the effective radius  $a_0$  of the LCFS which is defined in the flux surface data. The parameter  $P_1$  corresponds to the maximum density and temperature with  $P_4$  as offset value. The width of the profile is adjusted with the parameter  $P_2$ . A double peaked profile can be achieved with a shift of the maximum by the value  $P_5$ . The gradient length of the profile can be changed by the parameter  $P_3$ .

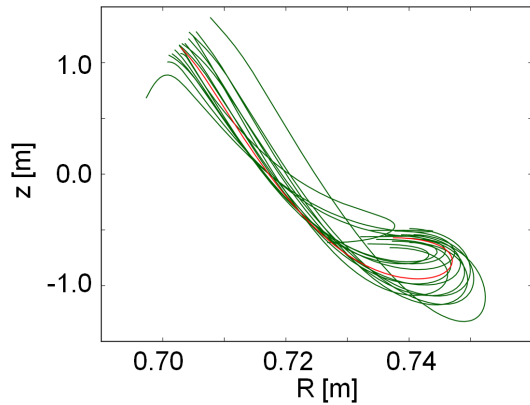


Figure 2.12: *Parallel refractive index of the EBW propagation of Figure 2.10 in dependence on the major radius coordinate.*

parallel refractive index changes sign and the wave changes its propagation direction to the magnetic field vector. Furthermore, the resonance condition (2.37) is fulfilled and the wave is resonantly absorbed with a peak power deposition in the plasma center. As shown in Figure 2.12, the parallel refractive index can reach values greater than one because of the generally high refractive index of electrostatic waves. For this reason, electron Bernstein waves can be also used for current drive.

Figure 2.10 shows an example of the calculated EBW-propagation using a typical launch scenario at WEGA in a poloidal and equatorial cut through the flux surfaces. The launch direction of the ordinary mode is given by the cyan colored arrow. The end of the green lines in the plasma center indicate the full absorption of the beam, but part of the power is also absorbed by collisional damping along the whole path. Figure 2.11 shows the damping factor versus the path length of the central ray, which is indicated in Figure 2.10 by a red line. Almost half of the power is absorbed until the beam reaches the plasma center. This part corresponds to the straight ray path in Figure 2.10b with the same propagation direction as the incident ordinary mode. In the plasma center, the

## 2.3 Wave Description outside the Plasma

The AMR- and TRAVIS-codes use a so called *Gaussian beam* for the description of an incident wave which is different to geometrical optics. The propagation of an electromagnetic beam in the microwave frequency range is defined by the wave nature of the light due to the non-vanishing wavelength compared to the beam width. If the imaging optical components are comparatively large relative to the wavelength, a so called *quasioptical* description with paraxial spherical waves<sup>15</sup> is possible [Gol98].

### 2.3.1 Free-space Propagation

With the assumption of an initial Gaussian electric field distribution  $\mathbf{E}(r, 0) = \mathbf{A} \exp[-r^2/w_0^2] = \mathbf{A} \exp[-(x^2 + y^2)/w_0^2]$  at  $z = 0$ , every point  $(x, y)$  can be considered as the source of a spherical wave according to the Huygens-Fresnel principle. The *waist*  $w_0$  is characterized by a decrease of the electrical field to  $\mathbf{A}/e$  in relation to the value on the  $z$ -axis. The superposition of the partial waves with the aid of the Huygens-Fresnel integral again leads to a Gaussian field distribution<sup>16</sup> [Gol98]:

$$\mathbf{E}(r, z) = \frac{w_0}{w(z)} \mathbf{A} \exp[-ikz] \exp\left[-i\left(\frac{\pi r^2}{\lambda R_c(z)} - \arctan\left(\frac{\lambda z}{\pi w_0^2}\right)\right)\right] \exp\left[-\frac{r^2}{w(z)^2}\right]. \quad (2.39)$$

Because of the divergence of the partial waves, the so called *beam radius*  $w$  of the  $1/e$ -decrease of the last exponential term increases with an increase in  $|z|$  and is described by

$$w(z) = w_0 \sqrt{1 + \left(\frac{z}{z_c}\right)^2}. \quad (2.40)$$

If  $z$  is higher than the *confocal parameter*  $z_c = \pi w_0^2/\lambda$ , the broadening of the beam will dominate and can be compared with a spherical wave. For  $z < z_c$  the propagation behaves as a beam or a plane wave given by the first imaginary exponential factor. The resultant deformation of the phase caused by the broadening, is described by the second exponential factor producing a curvature of the phase front for  $z \neq 0$  with a *curvature radius* of

$$R_c(z) = z + \frac{z_c^2}{z}. \quad (2.41)$$

The depth of field results in  $z = -z_c \dots z_c$  around the beam waist  $w_0$  of the Gaussian beam. The third imaginary exponential factor is called the *Guoy-phase* but has no practical relevance<sup>17</sup>.

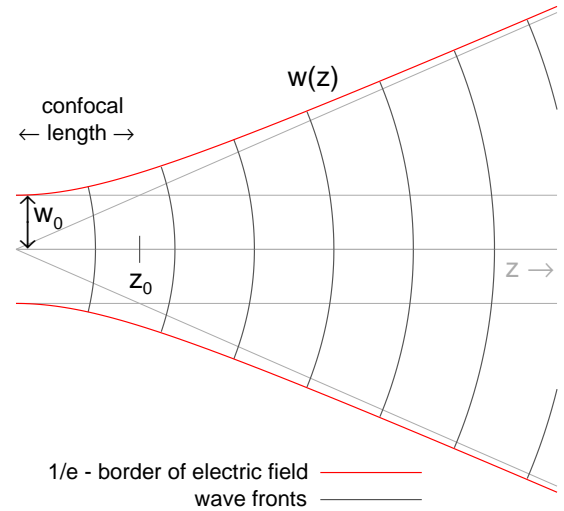


Figure 2.13: Divergence of a Gaussian beam propagating in  $z$ -direction.

<sup>15</sup>Beam divergence is lower than  $30^\circ$  so that the electromagnetic field is concentrated around the propagation axis  $z$  and can be approximated with  $z \gg x, y$  in the spherical wave equation.

<sup>16</sup> $|\mathbf{A}| = \sqrt{2/\pi}/w_0$  for a normalized beam power of 1

<sup>17</sup>The Guoy-phase characterizes a delay of the wave fronts in comparison to a plane wave that most grows within the confocal distance with  $\partial_z \phi \approx \pi/4z_c$  and converges to  $\phi = \pi/2$  for  $z \rightarrow \infty$ .

The value for the total power  $F_{\text{edge}}(r)$  within an arbitrary radius arises out of the so called edge taper  $T_{\text{edge}}(r)$ , corresponding to the normalized intensity at the radius  $r$  relative to the particular value on the axis

$$F_{\text{edge}}(r) = \frac{2}{\pi w(z)^2} \int_0^{r_{\text{edge}}} 2\pi r \exp\left[-\frac{2r^2}{w(z)^2}\right] dr = 1 - \exp\left[-\frac{2r^2}{w(z)^2}\right] = 1 - T_{\text{edge}}(r). \quad (2.42)$$

In the case of a finite aperture with a diameter of  $d_{\text{ap}} = 2r = 2w(z)$ , only 86% of the power is within the beam cross section. Diffraction at the aperture edges leads to an intensity ripple in the beam profile whose amplitude can be limited to 1 % of the beam power for  $d_{\text{ap}} = 3w(z)$  [Gol98]. In the far field approximation  $z \gg z_c$ , the radius of a certain total power  $F_{\text{edge}}(r)$  can be described by an opening angle  $\theta_{F_e}$  that is inversely proportional to the beam waist  $w_0$ :

$$\theta_{F_e} = \arctan \frac{\lambda}{\pi w_0} \sqrt{\frac{1}{2} \ln \left( \frac{1}{1 - F_e} \right)}. \quad (2.43)$$

For a more detailed examination of the dependence of the propagation on the solid angle, a time-independent monochromatic<sup>18</sup> wave field  $E(x, y, z)$  at the plane  $z = z_0$  can be Fourier transformed in spatial partial waves  $\exp[ik_i r_i]$  [CCTF08]:

$$E(x, y, z_0) = \int_{-\infty}^{\infty} \int_{-\infty}^{\infty} \tilde{E}(k_x, k_y, k_z) \exp[i(k_x x + k_y y + k_z z_0)] dk_x dk_y \quad (2.44)$$

The angle spectrum  $\tilde{E}(k_x, k_y, k_z)$  gives the relative part of the emission which depends on the direction in space, because the components  $k_i$  of the wave vector  $k$  are directly connected with the respective directional cosine  $i(k_x x + k_y y + k_z z) = ik(x \cos \alpha + y \cos \beta + z \cos \gamma)$ . After inverse Fourier transformation of the electric field  $E(x, y, z_0)$ , the respective angle spectrum is:

$$\tilde{E}(k_x, k_y, z_0) \exp[ik_z z_0] = \frac{1}{(2\pi)^2} \int_{-\infty}^{\infty} \int_{-\infty}^{\infty} E(x, y, z_0) \exp[-i(k_x x + k_y y)] dx dy. \quad (2.45)$$

The double integral can be separated after the insertion of the initial Gaussian beam profile  $E(x, y, z_0) = E_0 \exp[-(x^2 + y^2)/w^2]$ . Expansion of the exponent by

$$\frac{r_i^2}{w^2} + ik_i r_i = \frac{1}{w^2} \left[ \left( r_i + i \frac{w^2 k_i}{2} \right)^2 - \left( i \frac{w^2 k_i}{2} \right)^2 \right]$$

and integration by the stationary phase method [Jah01] leads to the angle spectrum depending on the angle  $\gamma$  to the main propagation direction

$$\tilde{E}(k_x, k_y, z_0) = \text{const} \cdot \frac{E_0 \exp[-ik_z z_0 \cos \gamma]}{(2\pi)^2} \exp \left[ -\frac{k^2 (1 - \cos^2 \gamma)}{\left(\frac{2}{w}\right)^2} \right].$$

The width is defined by  $1/w$  so that the ability for resolution of an angle-dependent absorption and emission can both be increased by the use of broader beams.

<sup>18</sup>Wave vector  $k = \omega/c = 2\pi/\lambda = \sqrt{k_x^2 + k_y^2 + k_z^2}$  splits in to its components.

### 2.3.2 Imaging of Gaussian Beams

The transformation of a given beam width  $w_{0,1}$  to the desired  $w_{0,2}$  can be realized with the aid of elliptical or parabolic metallic mirrors [Gol98]. An example of an elliptical mirror is shown in Figure 2.14. The rotation of the elliptical shape around the main axis  $a$  constitutes the mirror surface, and can be described by

$$1 = \frac{x^2}{a^2} + \frac{y^2 + z^2}{b^2}. \quad (2.46)$$

The main axis  $a = (R_1 + R_2)/2$  and the minor axis  $b = \sqrt{R_1 R_2 \cos \vartheta_{\text{mirror}}}$  are related to the distances  $R_1$  and  $R_2$  between the two focal points and the reflection point  $P_{\text{mirror}}$  on the mirror surface. The distance between the

focal points is given by  $A_0 = 2ea$  with the so called eccentricity  $e = \sqrt{1 - (b/a)^2}$  of the mirror. In contrast to geometrical optics, the image of a point source at  $F_1$  is not refocused in another point source at  $F_2$  because of the divergence of the beam. The widths  $w_{0,1}$  and  $w_{0,2}$  have a lower distance  $d_1$  and  $d_2$  from the mirror surface so that the curvatures  $R_{c,1}$  and  $R_{c,2}$  of the incident and the transformed Gaussian beam, given by equation (2.41), can fit within the distances  $R_1$  and  $R_2$ . If a beam is incident along a connection line  $\overline{F_1 P_{\text{mirror}}}$ , the  $\vartheta_{\text{mirror}}$  dependent focal distance  $f_{\text{mirror}}$  of the mirror will be described by the well known formula

$$\frac{1}{f_{\text{mirror}}} = \frac{1}{R_1} + \frac{1}{R_2}. \quad (2.47)$$

Using matrix optics (ABCD formalism), the parameter of the beam image can be calculated by

$$d_2 = f_{\text{mirror}} + \frac{d_1 - f_{\text{mirror}}}{\left(\frac{d_1}{f_{\text{mirror}}} - 1\right)^2 + \left(\frac{z_C}{f_{\text{mirror}}}\right)^2} \quad (2.48)$$

and

$$w_{0,2} = \frac{w_{0,1}}{\sqrt{\left(\frac{d_1}{f_{\text{mirror}}} - 1\right)^2 + \left(\frac{z_C}{f_{\text{mirror}}}\right)^2}}. \quad (2.49)$$

The imaging by elliptical mirrors, however, leads to a distortion of the beam. Even though the curvatures of the mirror and the beams are identical, off axis incidence ( $\vartheta_{\text{mirror}} \neq 0$ ) implies a deviation from the central beam line. The fundamental Gaussian mode TEM<sub>00</sub> with a power  $P_0$  is partly transformed into higher order Gaussian modes whose power  $P_{\text{dist}} = P_0 U^2$  is given by the square of the *distortion parameter*

$$U = \frac{w_{\text{mirror}} \tan \vartheta_{\text{mirror}}}{2\sqrt{2}f_{\text{mirror}}}. \quad (2.50)$$

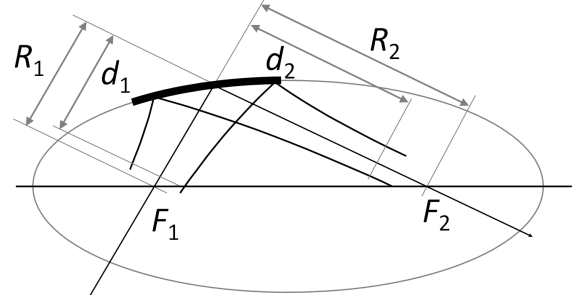


Figure 2.14: Transformation of a Gaussian beam with width  $w_{0,1}$  into a beam with width  $w_{0,2}$  with the aid of an elliptical mirror whose surface is described by a rotation of the shown elliptical shape around the main axis  $a$ . (adapted from [HG13])

The higher the beam width  $w_{\text{mirror}}$  on the mirror, the higher the mismatch of the curvature radius at the beam edge because of the finite angle  $\vartheta_{\text{mirror}}$ . Furthermore, a part of the incident beam is reflected into the cross polarization with a power of  $P_{\text{cross}} = 2U^2$ .

A multitude of examples regarding the design of quasioptical imaging systems can be found in Goldsmith's book [Gol98], or in a paper from Bern university [KM08] which is essentially a German translation of the former book.

### 2.3.3 Waveguide Propagation

A quasioptical system must be fed by an open waveguide or a horn antenna. The open waveguide consists of a hollow metallic tube that conducts microwaves with small losses dependent on the particular waveguide cross-section. The shape and the dimensions of the metallic wall define the minimum propagable frequency. Furthermore, the Maxwell equations together with the boundary conditions allow only discrete solutions of the generated electric and magnetic field pattern, which are also called modes. A detailed introduction to waveguide propagation can be found in the previously referenced book by Hartfuß and Geist [HG13] or the book by Baden Fuller [BF79].

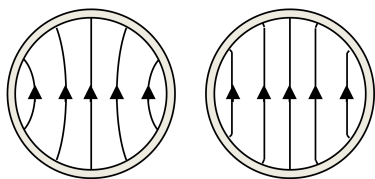


Figure 2.15: *Principal transverse electric field component of the  $TE_{11}$ -mode in a circular waveguide (left) and the  $HE_{11}$ -mode in a corrugated circular waveguide (right).*

In contrast to free-space propagation no transversal electro-magnetic (TEM) waves can exist within a hollow waveguide [HG13]. Either the magnetic or the electric field must have a component in propagation direction so that transversal electric (TE) or transversal magnetic modes (TM) can be excited in a waveguide. Analytic solutions can be obtained for a rectangular and circular waveguide cross section. Both waveguide types are used in this work and in most other microwave applications. The fundamental mode of a circular waveguide is the  $TE_{11}$ -mode, whose principal electric field distribution is shown in Figure 2.15. The first index  $p$  corresponds to the order of the Bessel function  $J_p$ , as well as to its derivative  $J'_p$ , both of which are part of the analytical solution for the circular waveguide. The second index

$m$  indicates the number of the zero  $\chi_{pm}^{\text{TM}}$  of the particular Bessel function or the zero  $\chi'_{pm} = x_{pm}^{\text{TE}}$  of its derivative<sup>19</sup>. The former defines the boundary condition of  $TM_{pm}$ -modes, and the latter that of  $TE_{pm}$ -modes. In general, the index  $p$  indicates the periods of the particular transverse field in azimuthal direction and the index  $m$  indicates the number of field maxima in radial direction.

Depending on the *waveguide radius*  $a_0$ , the propagation of higher order modes is possible such as  $TM_{01}$ ,  $TE_{21}$ ,  $TE_{01}$ ,  $TM_{11}$  and so on. The order corresponds to their accordant *cutoff-wavelength*, which is given by [HG13]

$$\lambda_c^{\text{TM,TE}} = \frac{2\pi a_0}{x_{pm}^{\text{TM,TE}}} \quad (2.51)$$

<sup>19</sup>The typical denotation in the literature is  $TE_{mn}$  and  $TM_{mn}$  but subsection 4.3.2 will treat the coupling between different modes in the case of a small change in the waveguide cross section. The corresponding coupling coefficients are specified in [Doa86] as conversion between  $T_{\dots pm}$ - and  $T_{\dots qn}$ -modes.

The cutoff-wavelength determines the wavelength along the waveguide axis<sup>20</sup>, which is called *waveguide wavelength* and can be calculated by

$$\lambda_w = \frac{\lambda}{\sqrt{1 - \left(\frac{\lambda}{\lambda_c}\right)^2}}. \quad (2.52)$$

Typically, the fundamental TE<sub>11</sub>-mode is used for power transfer in circular waveguides. The attenuation of a monomode waveguide is of the order of some dB/m, and is inversely proportional to the waveguide radius  $a_0$ . The increase of the waveguide radius by up to one magnitude allows a reduction up to 1%/m, dependent on the wave frequency [HG13]. This so called oversized waveguide allows a multitude of different modes, such that a sudden change of the waveguide geometry can lead to a scattering of the fundamental mode into higher order modes. If necessary, the waveguide radius should be changed only smoothly in propagation direction. For example, a horn antenna can be considered to be smooth impedance matching of the free-space to a waveguide.

In contrast to the undesired scattering within a highly oversized waveguide, a periodical change of the waveguide radius through the use of grooves can be used to realize an anisotropic waveguide impedance in azimuthal and propagation direction. The number of these *corrugations* per wavelength is much higher than 1, so that axial currents in the waveguide wall, and thus the particular exciting azimuthal magnetic field  $H_\phi$ , will be suppressed. Furthermore, if the corrugation depth is equal to a half wavelength, the waveguide constitutes a short-circuited stub with a vanishing azimuthal electric field  $E_\phi = 0$ . The resultant field pattern has a linear polarization of up to 100%. It is a combination of a TE<sub>11</sub>- and TM<sub>11</sub>-mode, as their phase velocities are the same for the above mentioned conditions of the corrugations. Therefore, it is denoted as hybrid mode HE<sub>11</sub> with both an electric and a magnetic field component in propagation direction. The main advantage of the HE<sub>11</sub>-mode is a coupling of 98% to the fundamental Gaussian mode TEM<sub>00</sub> by use of a corrugated waveguide or horn antenna. Furthermore, the excited beam has a symmetric cross section with a cross polarization of less than -20 dB.

### 2.3.4 Calculation Methods

The mirrors used in the this work were basically designed using the formulas of subsection 2.3.2. The generated beam pattern of the final setup was compared with a numerical calculation done by Georg Michel [Mic10] whose *Optical Structure Simulation Interface* (OSSI) allows for visualization of the full electric field pattern in the imaging process. A full description of the calculation method, called *plane wave decomposition*, can be found in the corresponding PhD-thesis [Mic98]. The initial electric field distribution is split in the Gaussian modes, which propagate with their corresponding wave vectors and are summed up at the desired position. If enough modes are considered, the calculation constitutes the full solution of the Helmholtz equation. A constant amplitude is assumed on the mirror surface, however, so that the result is only valid for thin lenses or large mirror curvatures.

<sup>20</sup>Only a certain propagation angle in relation to the waveguide axis is possible for a certain free-space wavelength in order to fulfill the boundary condition of a vanishing electric field at the waveguide wall. The superposition of the multiply reflected free-space waves at the inner metallic waveguide wall leads to an effective *waveguide wavelength* along the waveguide axis.

The feeding horn antennas as well as other waveguide components were designed with the aid of the commercial software ANSYS® HFSS (High Frequency Structure Simulator), which uses the *finite element method* to calculate the full electromagnetic wave solution within a limited structure. The code divides the considered volume into thousands of tetrahedra whose vertices define the grid of the calculated field quantities used for the interpolation within the respective tetrahedron. Therefore, the Maxwell equations can be expressed by matrix expressions subsequently solved by numerical techniques [SAS11]. The mesh is iteratively refined in critical regions until the solution converges. The size of the structure should only be on the order of the considered wavelength so that a standard PC is able to accomplish a simulation.

In addition, the results of HFSS were compared with numerical calculations executed by Dietmar Wagner [Wag10], which are based on the *scattering matrix formalism*. Each discontinuity of the waveguide radius leads to scattering into other modes including the particular cross polarization. The scattering matrix constitutes the power transfer between both sides of the discontinuity and can be calculated analytically with the aid of the *mode matching* technique. The details of the technique can be found in the corresponding PhD-thesis [Wag96].

# 3 Chapter 3

---

## General Experimental Setup

The initial operation of the WEGA stellarator began with a 2.45 GHz heating system because of its simple handling. Electron cyclotron resonance heating (ECRH) at the first harmonic O-mode (O1) allows a maximum electron density of only  $n_c = 7.45 \cdot 10^{16} \text{ m}^{-3}$  with a resonant magnetic flux density of  $B \approx 87.5 \text{ mT}$ . For this reason, a detailed investigation of electron Bernstein wave heating (EBWH) via OXB-conversion at the first harmonic followed in the years from 2003 to 2006 [Pod06]. In 2006 WEGA was equipped with a 28 GHz gyrotron and the research was henceforth focused on the so called *high field* operation at  $B_0 \approx 0.5 \text{ T}$  [WLA<sup>+</sup>06] corresponding to ECRH or EBWH at the second harmonic. In mid 2008 the first overdense OXB-heated plasma was realized by H.P. Laqua that lead to subsequent studies [LAM<sup>+</sup>08]. This chapter gives a brief overview of the hardware used, concentrating on the important aspects necessary for interpretation of the experimental data. Section 3.1 explains the two available heating systems, and in section 3.2 all important diagnostics are summarized with cross reference to the particular diploma theses concerned with their installation.

### 3.1 Heating Systems

The solo operation as well as the combined use of both heating system established the investigation and development of different heating scenarios, which are the topic of this thesis. Section 3.1.1 starts with the 28 GHz heating system and includes a more detailed description of the configurations of the quasioptic antenna. This is followed by a description of the 2.45 GHz system with the directivity patterns of the different waveguide antennas.

#### 3.1.1 28 GHz Heating System

The hardware setup of the 28 GHz heating system consists of a 10 kW continuous wave (CW) gyrotron whose circular waveguide output is connected with a circular waveguide transmission line that guides the 28 GHz electromagnetic wave into the toroidal vacuum vessel. Furthermore, the electric field pattern and the polarization of the generated gyrotron mode are properly converted, the process of which will be described in the following subsection. The emission of the open ended waveguide of the transmission line is refocused onto the plasma by two curved metallic mirrors located within the torus.

The main emission frequency of the gyrotron is fixed by its resonator and an underlying magnetic field. More precisely, the exact frequency is 27.94 GHz, but in the following it will be referred to as a 28 GHz wave, although the exact frequency is used in calculations. Additional *parasitic resonances* can be excited at other frequencies depending on the combination of the *gyrotron magnetic coil current*  $I_{\text{GYT}}$  and the *acceleration voltage*  $U_{\text{HV}}$ . This is of great importance for the microwave emission diagnostic, which is extremely sensitive to the parasitic gyrotron emission at other frequencies. A detailed description of the working principle of gyrotrons can be found in [Edg93].

The voltage supply of the gyrotron is equipped with a *fast high voltage transistor switch* HTS 361-03-LC HFS connecting an adjustable ceramic resistor  $R_{\text{HV}}$  in series to the gyrotron and reducing the effective acceleration voltage. The turn-off and turn-on rise times are less than  $1 \mu\text{s}$  [Beh13] and are thus much faster than the typical energy confinement time of 1 ms. This allows a rapid modulation of the forward power up to a modulation frequency of  $f_{\text{mod}} = 10 \text{ kHz}$ . The available resistors were used in different combinations of serial and parallel connections to realize different power levels during the turn-off period. The typical modulation amplitudes used for heat wave propagation experiments are up to 50%. To discriminate between gyrotron emission and plasma emission the modulation of the full power was necessary as well<sup>1</sup>.

#### 3.1.1.1 Transmission Line

The forward power and reflected power are measured at the output of the gyrotron with the aid of directional couplers and standard waveguide diodes. Figure 3.1 shows the following components of the transmission line necessary for the conversion of the electromagnetic  $\text{TE}_{02}$ -mode of the gyrotron to a linear or elliptical polarized  $\text{HE}_{11}$ -mode. The particular electric field configurations are also shown in the waveguide cross section. The first goal is the achievement of a linear polarized  $\text{TE}_{11}$ -mode, being the aforementioned fundamental mode of the circular waveguide. A summary of mode conversion relevant for gyrotron applications is given in [Edg93].

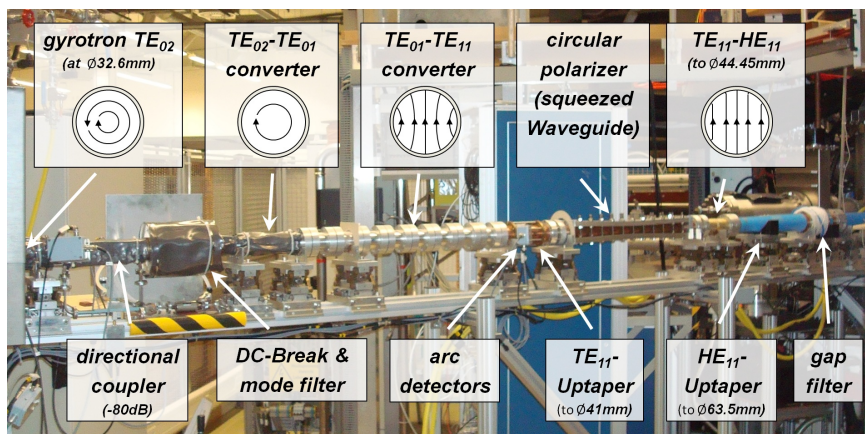


Figure 3.1: Oversized transmission line to the WEGA torus with the necessary mode conversion from the  $\text{TE}_{02}$ -mode of the gyrotron to  $\text{HE}_{11}$ -mode with arbitrary adjustable polarization.

<sup>1</sup>The acceleration voltage must be reduced from  $U_{\text{HV}} = 32.5 \text{ kV}$  to about  $U_{\text{HV}} = 25 \text{ kV}$ , requiring a resistance of at least  $R_{\text{HV}} = 7 \text{ k}\Omega$ .

The linear polarized  $TE_{11}$ -mode can be easily converted into a circular polarization by a  $\lambda/4$ -phase shifter realized by an elliptical waveguide. A wave with a polarization along the major axis of the elliptical cross-section has a larger wavelength than the wave component along the minor axis, as it is the fundamental mode of the elliptical waveguide<sup>2</sup>. If the incident polarization is between its axes of symmetry, the wave can be separated in two equal parts along the axes. The wave polarized along the major axis experiences a negative phase shift against the other one, as is illustrated in Figure 3.2. The resultant polarization for the configuration shown would be right hand circularly polarized with view in propagation direction. In contrast, the rotational direction of waves in plasmas is given with respect to the magnetic field vector. If the circular waveguide between two plates is smoothly squeezed by two plates into an elliptical cross section, the conversion from linear polarization into elliptical polarization will happen without reflections or mode conversions into *spurious modes* (higher order modes). A detailed description of the calculation and fabrication of a *circular polarizer* will follow in subsection 4.3.2 within the context of a microwave detection system, which has been designed in the frame of this work.

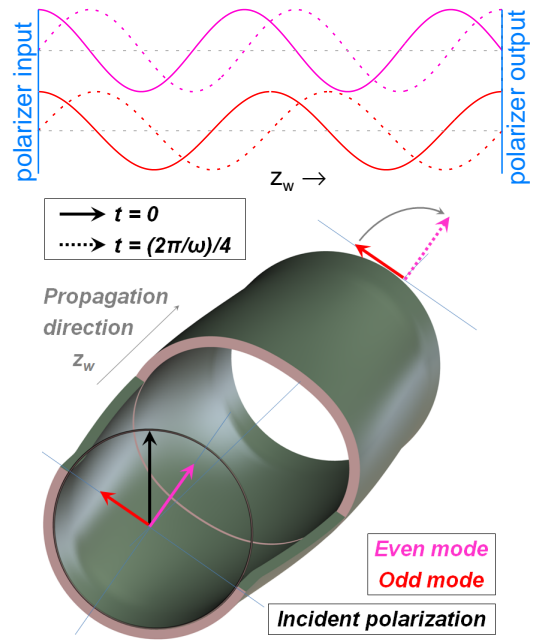


Figure 3.2: *Split of an incident linear polarized wave into two equal parts along the axes of the elliptical cross section of a partially flattened waveguide (one third is cut in the above view). If the phase difference of both independently propagating waves is  $90^\circ$  at the polarizer output, a right hand circular polarization will be generated.*

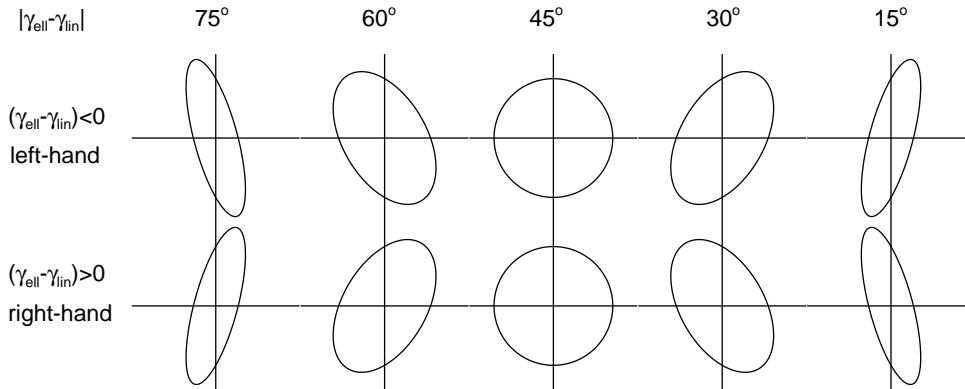


Figure 3.3: *Polarization ellipse and rotation direction dependent on  $\gamma_{ell} - \gamma_{tin}$  from the viewpoint of the propagation direction of the heating wave.*

<sup>2</sup>The set of Bessel functions introduced in subsection 2.3.3 as part of the analytical solution of the electric field within a circular waveguide splits into two new sets of radial eigenfunctions which are called even (fundamental mode) and odd Mathieu functions [HG13]. The cutoff wavelength of the  $TE_{11}^{even}$ -mode, given by equation (2.51), is only slightly decreased in contrast to the  $TE_{11}^{odd}$ -mode.

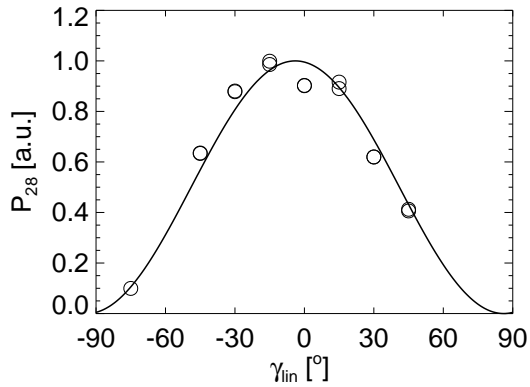


Figure 3.4: Power of the detected vertical polarized part of the emitted  $TE_{11}$ -mode dependent on the tilt angle  $\gamma_{lin}$  of the  $TE_{11}$ -converter.  $\cos^2 \gamma_{lin}$  - fit with maximum at  $\gamma_{lin} = -4^\circ$ .

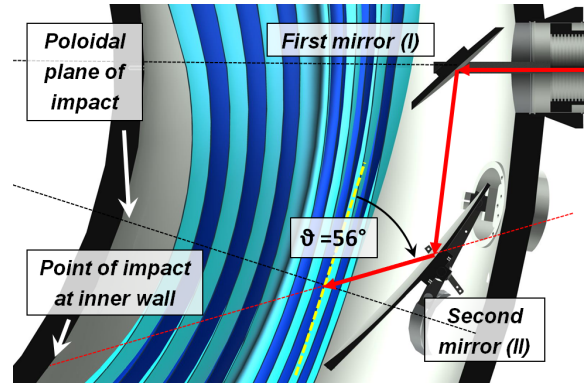


Figure 3.5: ECRH mirror system in a equatorial cut view through  $z = 0$  for OXB-configuration number 0. Figure 1.5 shows the Poincaré plot at the poloidal plane of impact.

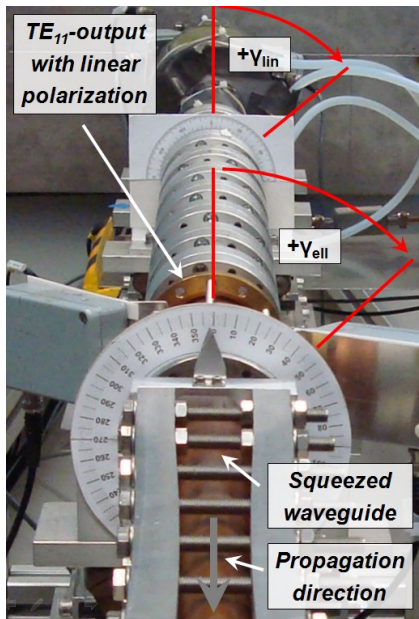


Figure 3.6: Angle convention for the incident linear polarization and the circular polarizer.

must be tilted by  $-\gamma_{lin}$  from the viewpoint of the propagation direction of the heating wave.

Afterwards, the  $TE_{11}$ -mode is converted into an  $HE_{11}$ -mode and the waveguide diameter of the transmission line is increased to the final value of  $d_{28} = 63.5$  mm. The circularly symmetric beam, emitted by the open ended waveguide within the torus, feeds a quasioptic mirror system described in the next subsection. To have the choice between each possible polarization, the  $TE_{11}$ -converter and the circular polarizer can be arbitrarily rotated around their axes. The convention of the adjustable angles is illustrated in Figure 3.6. The linear polarization in the vertical direction was checked by the detection of 20 ms short power pulses with the aid of a standard rectangular  $Ka$ -band (22 – 40 GHz<sup>3</sup>) horn antenna. Figure 3.4 shows good agreement of the measured power with the expected  $\cos^2 \gamma_{lin}$  dependence. If the angle  $\gamma_{ell}$  of the circular polarizer is not equal to the angle  $\gamma_{lin}$  of the linear polarized  $TE_{11}$ -mode, the resultant wave will have an elliptical polarization. For increased comprehension, Figure 3.3 shows the resultant polarization ellipse dependent on the angle  $\gamma_{ell}$  for an incident vertical polarized  $TE_{11}$ -mode with  $\gamma_{lin} = 0^\circ$ . For other angles  $\gamma_{lin}$  the pictured configuration for  $\gamma_{ell} = \gamma_{lin}$

<sup>3</sup>Officially defined as 26.5 – 40 GHz, but the waveguide cutoff is not until 21.08 GHz.

### 3.1.1.2 Quasioptic Mirror System

The OX-conversion takes place over a finite distance within the plasma so that the angle condition must be stable in the range of a wavelength. Furthermore, the  $\mathbf{k}$ -spectrum of a Gaussian beam is narrower the wider the beam waist is (as explained at the end of subsection 2.3.1). With a greater distance to the waist position the  $\mathbf{k}$ -spectrum of a Gaussian beam becomes wider so that it only partially fulfills the angle condition of the OX-conversion. For this reason, the waist of the incident beam should be located in the vicinity of the O-mode-cutoff and must be maximized<sup>4</sup>. As point of impact on the plasma, a toroidal position with compressed flux surfaces at the edge was chosen to achieve the highest possible density gradient and therefore a more desirably high OX-conversion efficiency, as was introduced in subsection 2.2.3.1. Figure 1.5 shows the most useful magnetic field configuration<sup>5</sup>. In the toroidal direction the curvature radius of the flux surfaces is much greater than in the poloidal direction. Therefore, the local poloidal beam radius  $w$  must be limited to about 20 mm so that the flux surface curvature has minimal effect. On the other hand, the toroidal elongation can be increased to at least 30 mm.

The open ended corrugated waveguide of the transmission line produces a circular symmetric Gaussian beam with a waist of

$$w_{0,28} = 0.644 \frac{d_{28}}{2} = 20.45 \text{ mm.}$$

The above formula is a general law for the emission of the HE11-Mode [Gol98]. A quasioptical mirror system refocuses the diverging beam to the desired plane with the required angle of  $\vartheta = 56^\circ$  to the magnetic field lines. An equatorial cut through the WEGA module with the two elliptical mirrors used<sup>6</sup> is shown in Figure 3.5. In contrast to the described imaging in subsection 2.3.2, the beam incidence on the mirrors is not along the focal points of the ellipsoid. Therefore, the focal length in, both the horizontal and the vertical direction<sup>7</sup>, diverge, and an astigmatic Gaussian beam is produced with its waist at different positions in propagation direction in order to achieve the toroidally stronger elongated beam spot at the point of impact on the plasma.

Nowadays the imaging of Gaussian beams is calculated with numerical methods evaluating the full electric field of the propagation. For this reason, the inability to use the idealized formulas of subsection 2.3.2 does not pose a problem. To analyze an astigmatic imaging system without the necessity of a full numerical evaluation, a simple calculation method has been used that allows the use of the quasioptical formulas. The idea behind is to interpolate the cutting line of the ellipsoidal cross section at the equatorial plane by another ellipse with the focal points at the real incident beam line. The necessary condition is the convergence of both curvature radii at the incidence point of the central ray. The curvature radius  $\rho$  of an

<sup>4</sup>The matching of the curvature radii of the Gaussian beam and the cutoff flux surface will further increase the OX-conversion efficiency [KCH<sup>+</sup>08] that is taken into consideration for the design of the microwave detection mirror system in chapter 4.

<sup>5</sup>At the toroidal angle of  $\phi_{\text{OXB0}} = 198^\circ$

<sup>6</sup>All quasioptical systems used at WEGA consist of a waveguide like structure and two imaging mirrors that will be described by roman numerals for an easier discrimination between the output waist  $w_{0,[\text{roman numeral}]}$  and the beam size  $w_{[\text{roman numeral}]}$  at a certain position behind the mirror. The particular mirror which is used as first mirror (I) or second mirror (II) is described by Latin numerals. Three different elliptical mirrors are available.

<sup>7</sup>The description 'toroidal' and 'poloidal' should be used only in direct connection with the plasma so that 'horizontal' and 'vertical' is used for the description of the properties of mirrors as well as the associated imaging process outside the plasma.

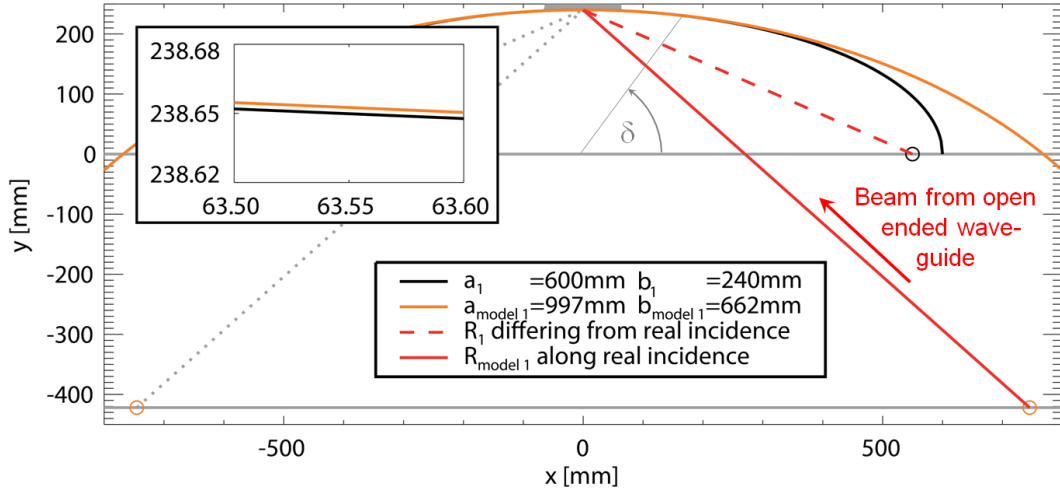


Figure 3.7: Comparison of the real equatorial cutting line of the mirror 1 (black) with the model ellipse (orange) used for the imaging calculation. The size of the mirror is illustrated by a gray hatching at the top of the Figure. The small deviation of both ellipses is shown in an expanded view on the left side.

ellipse with major and minor axis  $a$  and  $b$  dependent on the angle  $\delta$  can be calculated by the following parameter representation [Zei13]:

$$\frac{[(a \sin \delta)^2 + (b \cos \delta)^2]^{3/2}}{ab} = \rho(\delta) \doteq \rho_{\text{model}}(\delta) = \frac{[(a_{\text{model}} \sin \delta)^2 + (b_{\text{model}} \cos \delta)^2]^{3/2}}{a_{\text{model}} b_{\text{model}}}. \quad (3.1)$$

The equation for  $\rho(\delta)$  was already combined with the curvature radius  $\rho_{\text{model}}(\delta)$  of the sought-after model ellipse. The conditions for the focal points of the model ellipse must be used for the definition of the major radius  $a_{\text{model}} = (R_{\text{model, in}} + R_{\text{model, out}})/2$  and the minor radius  $b_{\text{model}} = \sqrt{R_{\text{model, in}} R_{\text{model, out}}} \cos \vartheta_{\text{model}}$  as illustrated in Figure 3.7 for the example of the first mirror. A simple solution for  $\rho_{\text{real}}(\delta) = \rho_{\text{model}}(\delta)$  can be found for the actual symmetric incidence<sup>8</sup>  $R_{\text{model, in}} = R_{\text{model, out}} = R_{\text{model}}$  at  $\delta = 90^\circ$ :

$$a_{\text{model}} = R_{\text{model}} = \frac{a^2}{b} \cos \vartheta_{\text{model}}, \quad b_{\text{model}} = \frac{a^2}{b} \cos^2 \vartheta_{\text{model}}.$$

Table 3.1: Final beam radius in vertical and horizontal direction at the WEGA coordinates  $(R, \phi, z) = (760 \text{ mm}, 198^\circ, 0)$  obtained with different calculation procedures.

Calculation type	$w_{\text{ver}}$ [mm]	$w_{\text{hor}}$ [mm]
Simple model	15.8	31.5
Numerical calculation	13.4	27.5

The calculation of the beam path with the aid of the quasioptical formulas of subsection 2.3.2 is straightforward. The resultant horizontal and vertical beam radii at the expected O-cutoff-position within the plasma are compared in Table 3.1 with a numerical calculation, with the aid of OSSI introduced in subsection 2.3.4. The values of the beam radius obtained with the simple model are 15 % higher compared with the numerical calculation.

The deviation of the model ellipse to the real cutting line is shown in

<sup>8</sup>With additional conditions a solution for  $\delta \neq 90^\circ$  can also be found.

Figure 3.7 in an expanded view and is too small to be the reason for the discrepancy of both calculations. The curvature radius of the mirrors, however, is relatively high for the use of the idealized calculation formulas. The distortion parameter given by equation (2.50) is approximately  $U_{\text{model II}} = 0.2$  for the second mirror so that up to 4% of the power is reflected as higher order Gaussian modes, leading to a distortion of the Gaussian beam shape. The finite mirror size in the numerical calculation probably produces a truncation and therefore a shift of the boundary with 86% power of the beam. In spite of the aforementioned discrepancies, the ratios of the horizontal to the vertical beam radius are in very good agreement, demonstrating the applicability of the suggested model even in extreme situations.

The explained setup subsequently will be referred to as OXB-configuration number 0 ('OXB-config 0') and is characterized by a symmetric incidence on the flux surfaces in poloidal direction. In the summer of 2009 the second mirror was upgraded with a wire rope mechanism to change the toroidal incidence angle on the plasma by a linear vacuum feedthrough<sup>9</sup> and to investigate the angle dependence of the OX-conversion. An exact calculation of the incidence angle is necessary to analyze the heating process. Therefore, the quasioptic mirror system including the support structure was implemented in the WEGA Inventor model to calculate the beam path through the plasma<sup>10</sup>.

As a result of the collaboration with the IPP-Prague a higher current drive in the plasma was predicted for an asymmetric poloidal incidence. For this reason, two further mirror configurations with incidence at another poloidal cross section were investigated. An additional third elliptical mirror, formerly used for X2-heating [OLM<sup>+</sup>06], has a smaller dimension in the horizontal direction than the second mirror of OXB-config 0 (mirror 2)<sup>11</sup>, and can therefore be used as a replacement for mirror 2 to realize the necessary  $\vartheta = 56^\circ$  incidence in the opposite toroidal direction<sup>12</sup>. The poloidal cross section in the vicinity of the expected OX-conversion is shown in Figure 3.8. The relative angle  $\Theta_{\text{rel}}$  between the central wave vector and the flux surface tangent must be perpendicular for maximum OX-conversion efficiency.

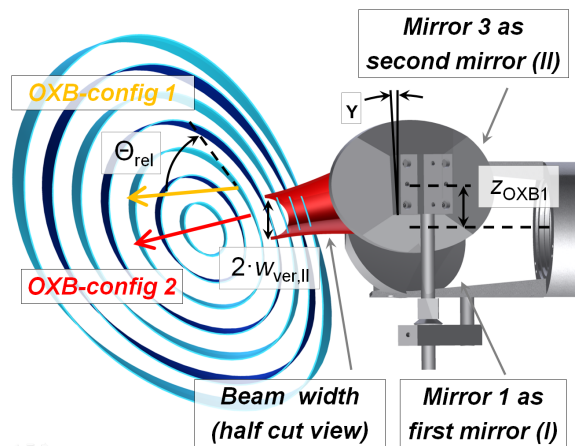


Figure 3.8: Mirror system in OXB-config 2 with the illustrated launch angles of OXB-config 1 and 2.

<sup>9</sup>The rotation of the second mirror occurs around an vertical axis 16 mm off the incidence position on the mirror, leading to a small change of the final beam imaging.

<sup>10</sup>The assembly of the mirrors was also adjusted with the aid of an axial laser beam coupled into the corrugated waveguide. The laser point at the inner torus wall is compared with the Inventor calculation to identify the corresponding beam path. Their coordinates within the torus were used to calculate the incidence angles on the plasma surface with the aid of TRAVIS that allows the use of different magnetic field configurations.

<sup>11</sup>The name 'second mirror' is generally used for the actual second mirror in the quasioptic heating system regardless of whether it is mirror 2 with the parameters  $a_2 = 300$  mm and  $b_2 = 130$  mm or mirror 3 with the parameters  $a_3 = 248$  mm and  $b_3 = 176$  mm.

<sup>12</sup>Impact position around the toroidal angle of  $\phi_{\text{OXB1}} = \phi_{\text{OXB2}} = 208^\circ$

For this purpose the second mirror must be located at a higher  $z$ -position in accordance with a tilt of the whole plane of ray propagation going from the first mirror (mirror I) to the point of impact on the plasma. In the so called 'OXB-config 1' the second mirror (mirror II) was set to  $z_{\text{OXB1}} = 20$  mm with an inclination angle of  $\Upsilon = 10^\circ$  (see Figure 3.8). The resultant relative angle of  $\Theta_{\text{rel, OXB1}} = 67^\circ$  allows an estimation of the poloidal angle dependence in combination with the later used  $\Theta_{\text{rel, OXB2}} = 90^\circ$  of OXB-config 2. The previous mentioned simple calculation of the beam parameters at the same used flux surface leads to beam widths of  $w_{\text{ver,II}} = 13.4$  mm and  $w_{\text{hor,II}} = 26.3$  mm valid for OXB-config 1 and 2.

#### 3.1.1.3 Distribution on the Mirrors

To ensure the proper beam imaging, the beam shape for OXB-config 0 was measured in a joint project involving almost all WEGA team members<sup>13</sup>. For the visualization of a high power microwave beam, a well absorbing target such as PVC must be included in the optical path. Dependent on the local electric field intensity, the PVC-target is heated up and shows the power distribution of the beam. Figure 3.9 shows the measurement on the second mirror<sup>14</sup> as well as the position of the expected central ray in agreement with the maximum intensity. The measured intensity from the left to right side of the picture, however, belongs to an increasing distance of the local beam radius to the first mirror. Therefore, the local beam radius increases from the left to the right side of the visualized beam, but the absolute intensity decreases and the resultant center of the projected beam boundary seems to be shifted to the left. Numerical calculations with the aid of OSSl [Mic10] show the same behavior, as is shown in more detail for the designed observation system in subsection 4.1. This effect is not critical at the inner wall of the torus, the power distribution of which is shown in Figure 3.10 for two different incidence angles. The simultaneously determined position of the laser spot is in good agreement with the averaged center of the beam shape. In the case of  $\vartheta = 51^\circ$ , the same problem with the shifted projection of the beam shape is obvious as described for Figure 3.9.

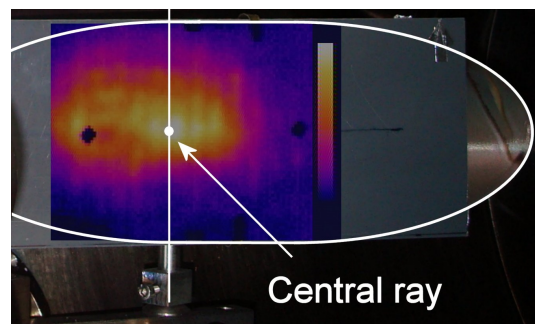


Figure 3.9: *Measurement of the projected power distribution with a PVC-target on the second mirror for the OXB-config 0.*

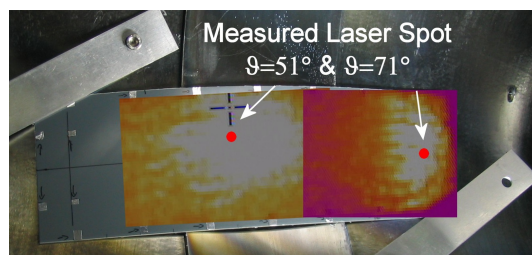


Figure 3.10: *Measurement of the projected power distribution on the inner wall of the torus for the OXB-config 0.*

<sup>13</sup>Special thanks to Peter Drewelow who was responsible for the design of the 'Pfannenwender' (spatula) allowing visualization around the corner on the second mirror. The WEGA ports are too small to directly observe components on the low field side with the thermo camera.

<sup>14</sup>The back of the PVC-target must be covered with aluminum foil to reduce the interference with the reflected pattern of the mirror.

### 3.1.1.4 Beam Propagation through the Plasma

When launching an electromagnetic wave at the second harmonic of the cyclotron frequency the highest absorption is reached for X-Polarization, introduced in subsection 2.2.1 and described in general as X2-heating. This is also valid for low temperatures and densities of typical WEGA plasmas with a resultant absorption of a few per cent. In this case the heating beam is reflected many times between the torus walls before being completely absorbed by the plasma and the stainless steel wall. These so called *multipaths* are shown in Figure 3.11 for a slightly oblique launch. The fundamental modes of propagation are given in this case by a left and right hand elliptically polarized wave. Because of the high reflection coefficient  $\Gamma_{\text{wall}} > 0.99$  of steel, the overall absorption requires up to 100 reflections, but this can no longer be characterized by a propagation of individual beams.

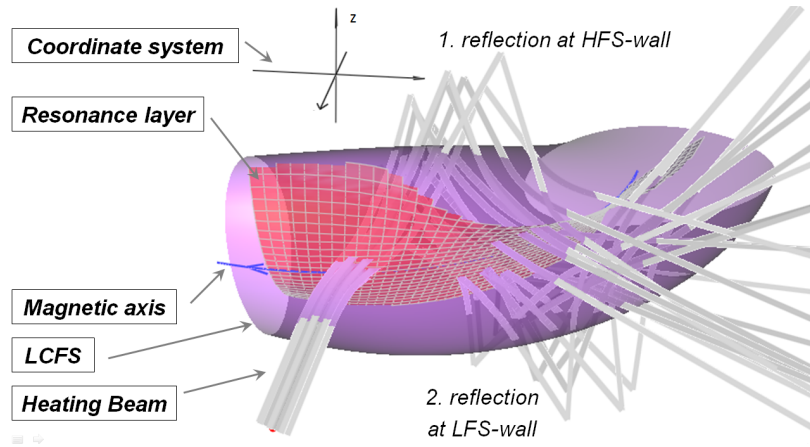


Figure 3.11: *Propagation of the 28 GHz beam through an X2-heated plasma for an oblique launch. In this TRAVIS-calculation the beam is divided into a central ray and 2 circles with 8 rays each.*

The electromagnetic field is more or less uniformly distributed in the torus with many different wave vectors in relation to the magnetic field vector. The X2-mode still has the highest absorption and takes place at the resonant layer shown by the red shaded plane in Figure 3.11. Even though the beam or rather the propagating microwave pattern is characterized by a mix of different polarizations after some wall reflections, only the extraordinary part is absorbed. This is the reason why underdense heating in the following is called X2-heating. The multipath absorption  $\zeta_{\text{multi}}$  can be expressed with the aid of an infinite geometrical series taking into account the cascaded absorption and reflection [Vow88]. With an averaged optical depth  $\tau_{\text{path}} \leq 0.05$  per path, the total absorbed power  $P_{\text{abs}}$  results to:

$$P_{\text{abs}} = P_0 \frac{1 - \exp(-\tau_{\text{path}})}{1 - \Gamma_{\text{wall}} \exp(-\tau_{\text{path}})} = P_0 \zeta_{\text{multi}}. \quad (3.2)$$

### 3.1.2 2.45 GHz Heating System

There are two different transmission systems for the operation with 2.45 GHz. One of them is used with a continuous wave (CW) 20 kW magnetron and the other one with a CW or a modulatable 6 kW magnetron. The latter one cannot be controlled remotely and is only used for special purposes. Both transmission lines connect the magnetron with an antenna in the evacuated torus via mono mode waveguides of different cross sections. A detailed description of the components can be found in [Pod06]. This section is mainly dedicated to the used antennas having direct influence on the coupling to the plasma. But first of all the location of the antennas in the torus as well as an overview of the transmission lines is given in the following subsection.

#### 3.1.2.1 General Setup

The antennas of both heating systems get access to the torus via equatorial ports with a diameter of  $D_A = 91$  mm. Figure 3.12 shows the setup of the transmission lines as well as the corresponding antenna position in relation to the flux surfaces<sup>15</sup>. The 6 kW system is equipped with a slot antenna, and the 20 kW transmission line with a standard slightly curved waveguide. In both systems the matching of the used antenna is realized by a stub tuner transforming the waveguide impedance to the end of the transmission line or rather the antenna.

#### 3.1.2.2 Antenna Directivity

The functionality of the slot antenna can be explained by the geometrical optic approximation considering the wave field between two conducting parallel plates with a certain distance by a superposition of plane waves. To fulfill the boundary conditions of a vanishing electric field at the wall, plane waves of a certain wavelength can only propagate under a defined angle to the waveguide wall [BF79]. For this reason, the emission angle of a slotted waveguide is only given by the frequency and the waveguide dimensions. To reduce the reflection and fit the WEGA boundary conditions, the design ends in a double slot antenna with a slot size of  $100 \text{ mm} \times 52 \text{ mm}$ , respectively [Pod06]. The resultant emission pattern, calculated with HFSS, is shown in Figure 3.13a and b for the empty torus. There are two emission lobes at an angle of  $\Phi_{\text{Slot}} = (90 \pm 37)^\circ$ . The intrinsic reflection because of differing impedance of waveguide and antenna is under 1 %. In the presence of an overdense, badly absorbing plasma in front of the antenna this value is increased by up to 5 % because the part of the emission with a direction perpendicular to the flux surfaces is reflected into the waveguide.

The emission pattern of the bend antenna is basically defined by the waveguide diameter and the surface normal of the antenna mouth. For this reason, the emission angle of the resultant Gaussian beam is at  $\Phi_{\text{Bend}} = (90 + 18)^\circ$ . The direction of the antenna in relation to the toroidal angle  $\phi$  can be changed from anticlockwise, as shown in Figure 3.12, to clockwise. This is an important feature to check the influence of the antenna spectrum on the current drive efficiency.

---

<sup>15</sup>A full overview is shown in Figure 3.14 with the both antennas at the toroidal positions  $\phi_{6\text{kW}} = 288^\circ$  and  $\phi_{20\text{kW}} = 324^\circ$ .

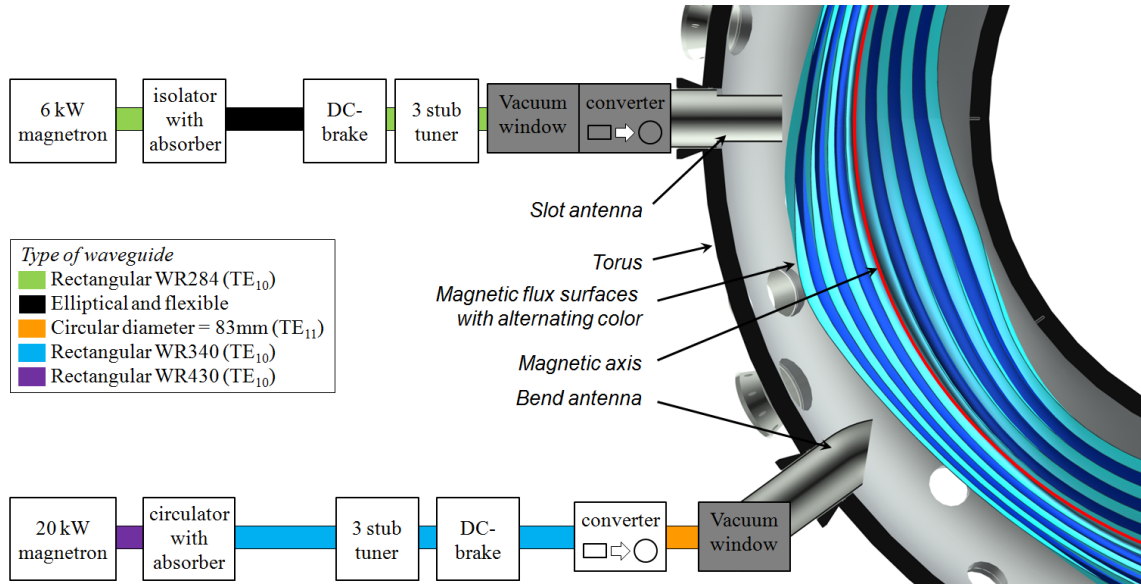


Figure 3.12: *Equatorial cut of WEGA at  $z = 0$  mm with the both magnetron antennas in relation to flux surfaces. The adjacent transmission lines are sketched in a component view.*

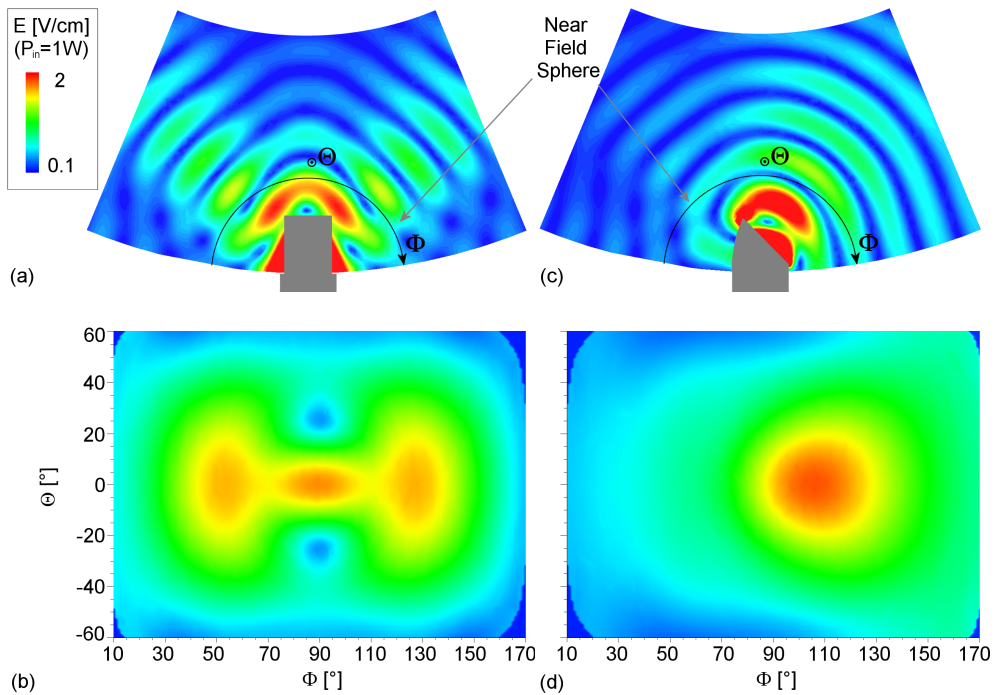


Figure 3.13: *Electric field strength, calculated with HFSS, in the equatorial plane  $z = 0$  mm for the slot antenna of the 6 kW system (a) and the bend antenna of the 20 kW system (c) in the case of ordinary mode feed. The same quantity is shown in the Figures (b) and (d) in dependence on the equatorial and vertical emission angles  $\Theta$  and  $\Phi$  for the depicted near field sphere. The last closed flux surface, however, is within the near field sphere as obvious in Figure 3.12. The color coding is based on a linear scale.*

## 3.2 Standard Diagnostics

An overview of the used diagnostics is shown in Figure 3.14. Almost all diagnostics explained in this section are standard diagnostics and can generate at least relative values of plasma parameters without any further effort. The determination of profiles of the plasma parameters by the bolometer, microwave radiometer, soft X-ray and Langmuir probe especially necessitates the consideration of the magnetic field configuration as well as individual settings of the diagnostics. Important aspects for the evaluation of the experimental results are summarized in the following section. WEGA discharges are highly reproducible when using the same control parameters so that temperature and density profiles of other experiments, for example, can also be used for the interpretation. Small changes in the profiles are hardly resolvable considering the typical minimum error of 10 % of plasma parameter measurements.

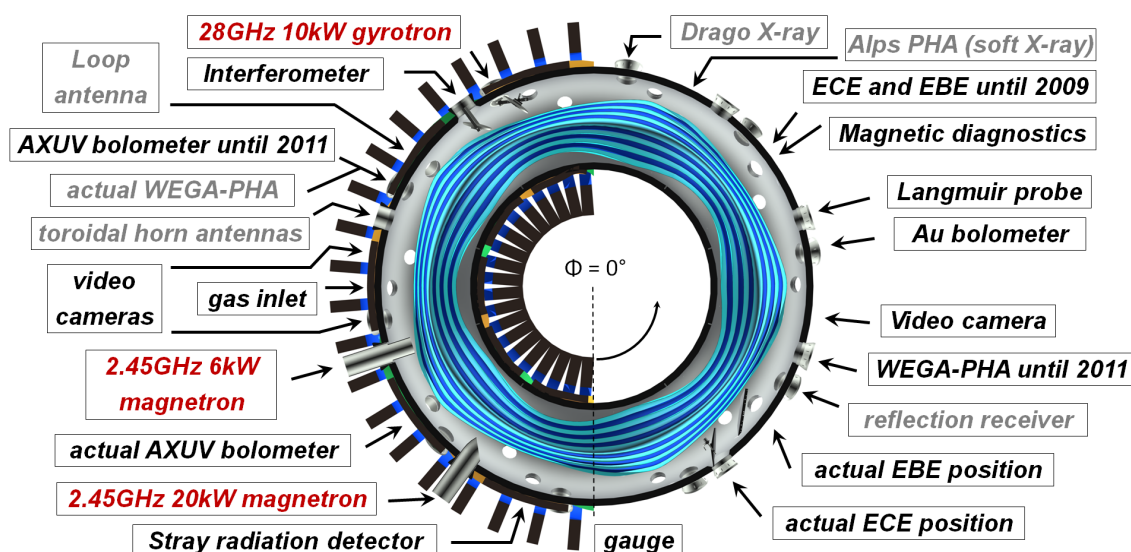


Figure 3.14: *Equatorial cut of the WEGA torus with the positions of the heating systems (red) and of the diagnostics (black & gray). Non-standard diagnostics are gray colored and explained later in chapter 5. The counting of the toroidal angle  $\phi$  is anti-clockwise starting at the indicated dashed line.*

### 3.2.1 Machine Control

Plasma operation at WEGA uses a dedicated control system. The coil currents are measured by shunt resistors as well as Rogowski coils and the gas inlet is controlled by a mass flow controller. The gas pressure is measured by a Pfeiffer Compact FullRange™ Gauge PKR 261, that is located sufficiently far away from the magnetic field coils. Depending on the gas used and the envisaged pressure, a correction factor<sup>16</sup> must be used, which is given in Figure 3.15.

<sup>16</sup>The time dependent pressure signals are evaluated by the following polynomials of 7. order:

He:  $p(x) = -921.19 - 1540.44x - 1074.853x^2 - 405.5478x^3 - 89.3426x^4 - 11.51048x^5 - 0.804632x^6 - 0.0235906x^7$

Ar:  $p(x) = 36.7561 + 16.9337x - 14.5626x^2 - 13.9535x^3 - 4.65048x^4 - 0.772301x^5 - 0.0644413x^6 - 0.00215812x^7$

with  $x = \log(p_{\text{indicated}})$  in the range  $10^{-7} \text{ mbar} \leq p_{\text{indicated}} \leq 10^{-3} \text{ mbar}$ .

### 3.2.2 Stray Radiation Detector (Sniffer Probe)

Sniffer probes measure the stray radiation which results from the non-absorbed microwave radiation. It can be compared with an integrating sphere known as Ulbricht sphere. Inside the sphere the radiation is reflected many times at the inner wall so that the incoming microwave power is smeared out to a more or less homogenous radiation level in each propagation direction. The detection of the stray radiation signal is achieved with a monomode waveguide detector flush-mounted in the wall of the sphere. The monomode waveguide has a broad antenna characteristic so that remaining inhomogeneities of the standing wave pattern within the sphere are almost compensated. The connection of the sniffer probe to the torus is realized by an oversized transmission line allowing a high number of propagable waveguide modes. Therefore, the acceptance angle for multimode stray radiation within the torus is increased [GCH<sup>+</sup>01]<sup>17</sup>. The toroidal position of the sniffer probe in the torus is as far as possible away from the gyrotron to make sure that as many as possible reflections of the heating beam take place before the radiation enters the sphere.

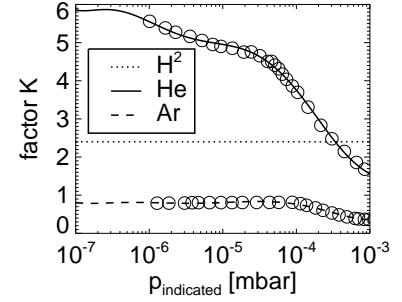


Figure 3.15: Pressure and gas dependent correction factor [PFE02] with the used correction function.

### 3.2.3 Microwave Interferometer

The optical path length of a microwave beam within a plasma is increased in relation to the corresponding vacuum propagation due to the decreasing refractive index  $N$  having a higher electron density  $n_e$ . The O-mode polarization is only affected by the electron density so that a measurement of the phase shift  $\Delta \varphi$  of the probing beam with respect to the vacuum propagation ( $N_{\text{vac}} = 1$ ) allows to determine of the line integrated electron density denoted as  $ndl$ . For high probing frequencies in relation to the plasma frequency ( $X = \omega_{\text{pe}}^2/\omega^2 = n_e/n_c \ll 1$ ), a linear dependence arises for the refractive index [HG13]:

$$N_{\text{O}} = \sqrt{1 - \frac{n_e}{n_c}} \approx 1 - \frac{1}{2} \frac{n_e}{n_c}. \quad (3.3)$$

Therefore, the phase shift gets a linear dependence on the line integrated electron density

$$\Delta \varphi = \frac{2\pi}{\lambda} \int_{z_1}^{z_2} (N_{\text{O}}(z) - N_{\text{vac}}) dz \approx -\frac{\pi}{\lambda n_c} \int_{z_1}^{z_2} n_e dz = -\frac{\pi}{\lambda n_c} ndl = -2.818e^{-15} \lambda ndl. \quad (3.4)$$

<sup>17</sup>A broader description can be found in [SL10] with actual diagnostic improvements, e.g. a mechanical modulator in the copper sphere mixes the modes so that the temporal integration of the detected power level over one modulation period constitutes the averaged value of remaining inhomogeneities in the angle distribution.



Figure 3.16: Sniffer sphere.

The vertical sightline of the probing beam with a frequency of 80.6 GHz is depicted in Figure 3.34b in subsection 3.2.8 which describes the absolute density calibration of the Langmuir profile measurements with the aid of the interferometer<sup>18</sup>.

### 3.2.4 Microwave Radiometer

As introduced in subsection 2.2.1.2 the X2 plasma emission is routinely used in fusion research for determining the electron temperature. The author's diploma thesis was dedicated to building up an electron cyclotron emission diagnostic for the Ka-band (22 – 40 GHz<sup>19</sup>), even though only optical thin plasmas can be generated in WEGA [Sta08; SHH<sup>+</sup>09]. For this reason, the obtained signals correspond to a radiation temperature  $T_{\text{rad}}$  given by equation (2.23). A subsequent calculation of the real electron temperature  $T_e$  of underdense plasmas necessitates more effort because of the multipath emission and reabsorption of microwave radiation, similar to the calculation of the absorbed heating power by equation (3.2). A detailed analysis for an X2 heated plasma will follow in subsection 5.1.1.2.

#### 3.2.4.1 Signal Processing

The principal setup of the whole multichannel radiometer diagnostic is shown in Figure 3.17<sup>20</sup>. The radiation spectrum is received by a horn antenna and pre-amplified by a Low-Noise-Amplifier (LNA). The signal is split by means of power dividers and band-pass filters in 12 continuous frequency bands of some hundreds MHz width and is measured power-proportionally [FH01a; FH01b]. Seven of the twelve channels are within the expected electron cyclotron frequency range of the second harmonic emission between 25 GHz and 35 GHz. For the protection of the sensitive amplifiers a notch filter is necessary for the rejection of the 28 GHz stray radiation.

In the course of the thesis, the diagnostic was rebuilt around the toroidal position  $\phi_{\text{ECE}} = 36^\circ$  to increase the distance to the gyrotron and to have enough space for the setup of a quasi optical mirror system similar to the gyrotron mirror setup. The goal is the investigation of electron Bernstein wave emission (EBE) of overdense plasmas. Furthermore, the OX-conversion efficiency can be measured with the aid of a non-invasive probing beam. The adapted redesign of the antenna and the front end will be the topic of chapter 4. The radiometer bank and the post-amplifiers could remain untouched.

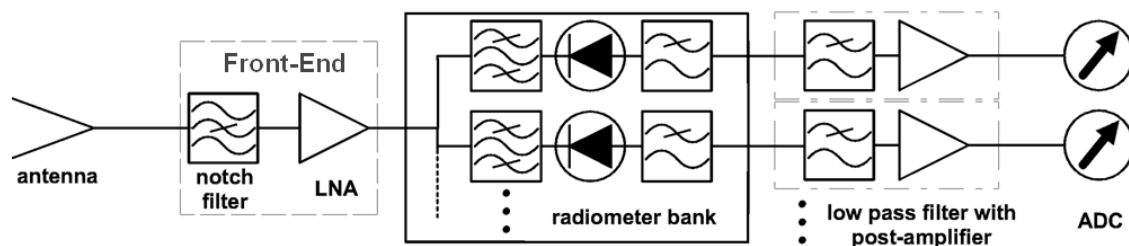


Figure 3.17: Component representation of the whole multichannel radiometer diagnostic.

<sup>18</sup>A detailed description of the electrical signal processing can be found in [GW97; GWH97].

<sup>19</sup>Officially defined as 26.5 – 40 GHz, but the waveguide cutoff is not until 21.08 GHz.

<sup>20</sup>Please find a very detailed description of all components in the author's diploma thesis [Sta08].

The sensitivity calibration of the whole radiometer system is obtained with the aid of the hot-cold-technique using two black body radiation sources at room temperature and liquid nitrogen temperature. For this reason, the power level of the detected emission is expressed in terms of the radiation temperature  $T_{\text{rad}}$  of a black body which has the same emission level [HG13]. In addition, the pre-amplified signal of the radiometer bank can be analyzed with a spectrum analyzer ANRITSU MS2668C allowing the measurement of a continuous spectrum between 21 – 40 GHz. Therefore, a continuous plasma emission can be distinguished from additional resonances of the gyrotron. Besides its design frequency of 28 GHz, the gyrotron resonator is able to excite parasitic resonances at other discrete frequencies whose power level is of the order of the expected plasma emission.

### 3.2.4.2 Horn Antenna Setup

In the years 2009 to 2011, standard rectangular Ka-band horn antennas were used for the initial measurements during the overdense OXB-discharges as well as the other presented discharge types. A viewing angle of  $\vartheta = 56^\circ$  with respect to the magnetic field lines was chosen to maximize the reception of the expected EBE by BXO-conversion. The achieved results are not separately described in the following because of the more detailed investigation with the developed quasioptical antenna system. Furthermore, a second horn antenna configuration with perpendicular observation to the magnetic field lines was implemented to allow quickly switching between the optimal observation direction for EBE and ECE. The vertical observation sightline of the ECE configuration is shown in Figure 3.18 and is preferred for optically thin ECE emission measurements to increase the optical thickness by increase of the optical path length along a constant magnetic field.

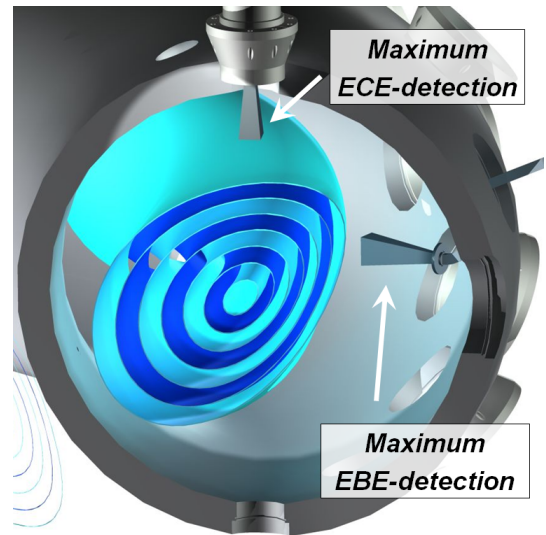


Figure 3.18: *Vertical sightline of the second usable horn antenna.*

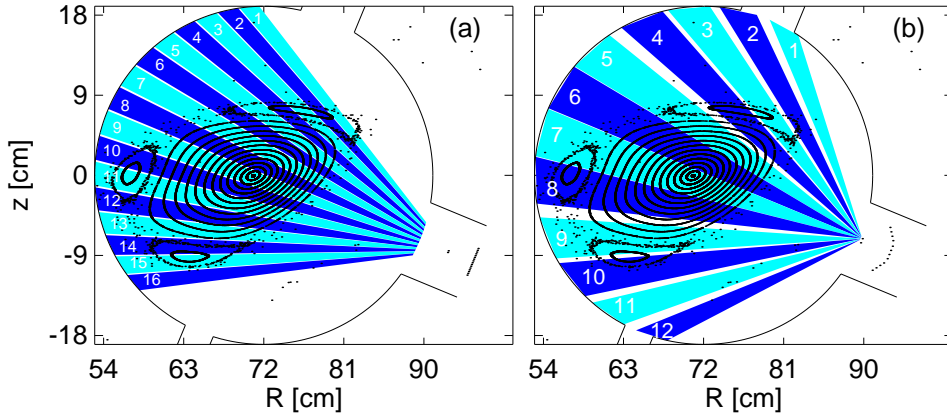


Figure 3.19: *Poloidal cross section of (a) the 16 sightlines of the AXUV-bolometer at  $\phi_{AXUV} = 243^\circ$  and (b) the 12 sightlines of the Au-bolometer at  $\phi_{Au} = 27^\circ$ . Both cases are in relation to a magnetic field configuration with  $\iota = 0.275$ .*

### 3.2.5 Bolometer

Two different bolometric power meters are available to detect the visible and ultraviolet plasma emission. The so called Au-bolometer uses the temperature increase of a gold foil by the absorbed electromagnetic radiation to determine its intensity. A gold resistor is thermally connected to the irradiated gold foil and experiences the same warming. The associated change of its ohmic resistance in relation to a reference resistor is measured with the aid of a Wheatstone bridge. The time constant of warming and cooling of the foil is about 100 ms [Gla10] so that the Au-bolometer is not used for the systematic investigation of the discharges in this thesis. For this purpose, the so called AXUV-bolometer with silicon p-n-junction photodiodes is used. Electron-hole pairs are created by the inner photoelectric effect and separated by the electric field of the p-n junction. The resultant current is proportional to the radiation power in short-circuited operation [IRD13]. The time constant is much lower with about  $0.5 \mu\text{s}$  necessary for experiments with a fast modulation of the gyrotron forward power.

Both bolometers are multichannel systems. The resolution of the sightlines is defined by a pinhole and the distance of the particular bolometer array to it. The optimization of

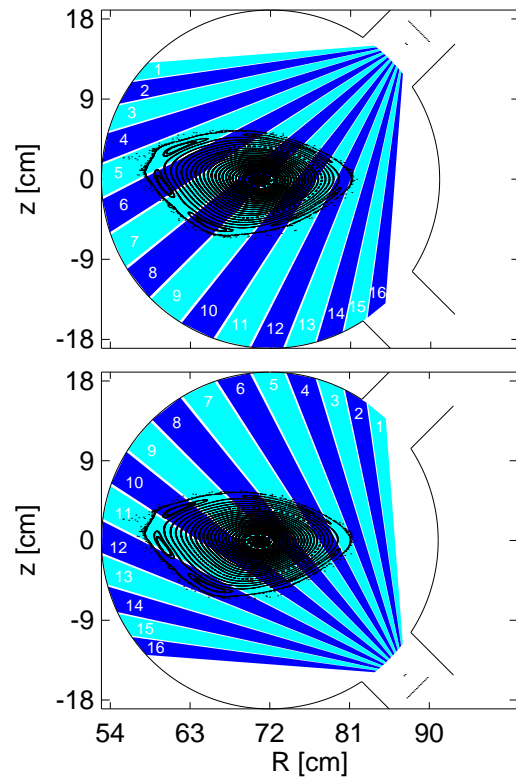


Figure 3.20: *Poloidal cross section of the AXUV-bolometer sightlines at  $\phi_{AXUV} = 306^\circ$ . The sightlines are denoted with 'A' for the upper and 'B' for the lower camera. The magnetic field configuration with  $\iota = 0.36$  is typically used in OXB-discharges.*

both diagnostics, as well as the application to WEGA plasmas, was part of a diploma thesis [Gla10]. Figure 3.19 shows the sightlines of both diagnostics over the plasma cross section. Each detector has finite spatial extent and the colored areas only correspond to the viewing range of the central point of a detector surface. The total sight area of a detector surface has double the width. For the calculation of the time dependent total emitted power, the channel values are added up weighted by their particular sight area [Gla10]. The resulting integrated value of the AXUV-bolometer must be scaled to the integrated value of the Au-bolometer during a steady state phase of the particular discharge. The main advantage of the Au-bolometer is their absolute calibration by the manufacturer allowing the determination of the total radiated power.

In 2011, the AXUV-bolometer was upgraded with a identically constructed second detector array allowing a dual view on the plasma. Figure 3.20 shows the local resolution of both arrays looking under an angle of  $90^\circ$  to each other onto the same plasma cross-section.

### 3.2.6 X-ray Diagnostics

Suprathermal electrons with energies of keV and higher can be analyzed indirectly with the aid of their emitted Bremsstrahlung in the Coulomb field of a heavy charged particle. This is valid for collisions with the ions of a plasma and collisions with the torus wall or other components. The resultant continuous spectrum of such free-free (ff) transitions is typically superimposed by characteristic lines. In contrast to this, bound-bound (bb) transitions a free electron can recombine with an ion in a so called free-bound (fb) transition producing a continuous energy dependent emission. In the case of a Maxwellian energy distribution the ff- and fb-transitions have a strong exponential dependence on the electron temperature [Hut94]. A brief overview of X-ray diagnostic principles with application to fusion plasmas can be found in the book of Hutchinson [Hut94] and a more detailed treatment in the book of Attwood [Att99].

#### 3.2.6.1 Soft X-rays with WEGA-PHA

The energy range of soft X-rays typically spans 200 eV to 8 keV [Att99] but the boundaries are fluent. Energy resolved spectra can be measured by the pulse height analysis (PHA) whose installation at WEGA was part of a diploma thesis [Göt05]. A soft-X photon incident on the semiconductor detector<sup>21</sup> is converted into a voltage pulse proportional to the photon energy. A multichannel-analyzer (MCA) classifies each pulse with regard to its pulse height and the number of counts dependent on the channel energy finally represents the energy spectrum<sup>22</sup>. The maximum count rate of the MCA is on the order of ten thousand counts per second so that the measurement time for a Maxwellian energy spectrum with up to 2048 channels is on the order of seconds to get enough counts in each channel. Furthermore, the voltage pulses are time-dependently detected with the aid of a single channel analysis<sup>23</sup>. This allows the time dependent measurement of soft-X photons within a variable energy range.

<sup>21</sup>The Si(Li) detector (INTERTECHNIQUE ESLX 12) with a sensitive area of  $0.12 \text{ cm}^2$  and a layer thickness of 4 mm is operated in reverse direction with a voltage of  $-800 \text{ V}$  and must be cooled with liquid nitrogen.

<sup>22</sup>This tasks were performed by an integrated unit, Digital Spectrum Analyzer DSA-1000 of CANBERRA, in combination with a standard PC operating the control software Genie-2000.

<sup>23</sup>The single channel analysis consists of the amplifier INTERTECHNIQUE 3567 and the Single Channel Analyzer ORTEC 550 with window filter.

### 3 General Experimental Setup

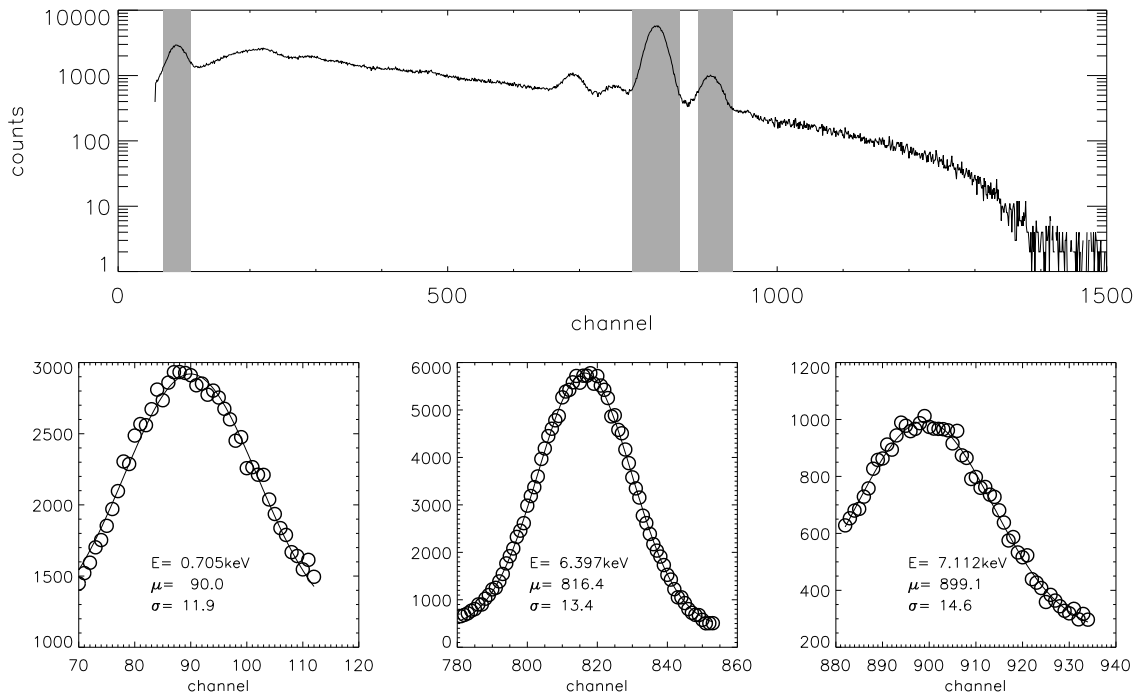


Figure 3.21: *Bremsstrahlung spectrum of the iron target in the energy calibration unit detected with a coarse gain of 320. The position of the known lines  $L_{\alpha}$ ,  $K_{\alpha}$  and  $K_{\beta}$  are fitted with a standard Gaussian function.*

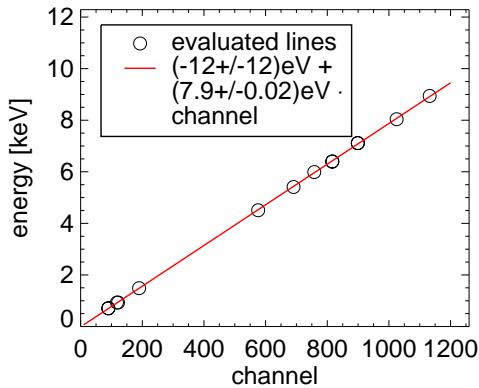


Figure 3.22: *Final calibration for a coarse gain of 320 with the aid of the determined line positions of the targets Cu, CrCu, Al, Ti and Fe.*

The energy assignment of the MCA-channels, however, must be calibrated with the aid of characteristic X-ray line emission of known energy. For this purpose, an energy calibration unit (ECU) similar to a standard X-ray tube is mounted in front of the detector. The anode of the X-ray tube must be slid into the detector viewing range for the energy calibration. By bombardment of the anode with electrons up to an energy of 10 keV, the resultant Bremsstrahlung spectrum is superimposed by the characteristic lines of the particular anode element. Furthermore, different elements can be used as anode so that a multitude of characteristic lines can be used for the energy calibration. Figure 3.21 shows the spectrum of the iron target as an example. The determined values of all elements are used in Figure 3.22 for a linear fit of the calibration that is especially

important for extrapolated calibrations to energies much higher 10 keV. The PHA-diagnostic can also be used for measurements up to energies of 100 keV and higher even though the detection efficiency decreases for energies higher than 20 keV as shown in Figure 3.23. The measured energy spectra are in general corrected with the energy dependent efficiency as well as the transmission of the  $5 \mu\text{m}$  Be-window used in front of the detector. The Be-window protects the detector against visible light and defines the minimum detectable photon energy of approximately 0.5 keV.

The original PHA setup was optimized in two steps with regard to the temporal sensitivity as well as the enabling for spatially resolved measurements. Figure 3.24 shows the first iteration finished in November 2010 (PHA1). The main change in the hardware setup was the reduction of the distance of the detector to the plasma axis from 129 cm to 94 cm. Furthermore, the setup of the optical path was supplemented with a feedthrough with a vertically movable pinhole (diameter 5 mm) defining the viewing area of the detector in the plasma. The screen is with a width of 7 mm much thicker than the pinhole with 3.1 mm, allowing a spatially resolved measurement of photons up to 50 keV. Because of the limited space in the feedthrough module, the viewing area can only be varied in the range above the equatorial plane including the magnetic axis. The upper position is illustrated in Figure 3.24 by a red cone, and the outer flux surface of the expected overdense region of the OXB-heated plasmas is displayed green colored. Additionally, Figure 3.25 shows a poloidal cut view of the maximum lower and upper position. Considering the vacuum flux surfaces, the central ray of the viewing area can be related to a tangentially touched flux surface, whose effective radius  $r_{\text{eff}}$  is declared as impact radius  $r_{\text{imp}}$ .

The exact assignment was determined by a combination of a graphic construction and a calibration measurement with the aid of two LEDs at the inner torus wall. The detector is also sensitive to visible light after removing the Be-window in front of the detector. Figure 3.26 shows the measured count rate in dependence on the used feedthrough position as well as the resultant fit with a double Gaussian distribution. The different count levels of both distributions are caused by use two different LEDs. The resultant two feedthrough positions of the maxima are used for the absolute calibration of the moveable pinhole in the Inventor model of the PHA setup. The poloidal cut of the flux surfaces, shown in Figure 3.25, is used for the assignment of their  $r_{\text{eff}}$ -values with respect to the feedthrough position<sup>24</sup>.

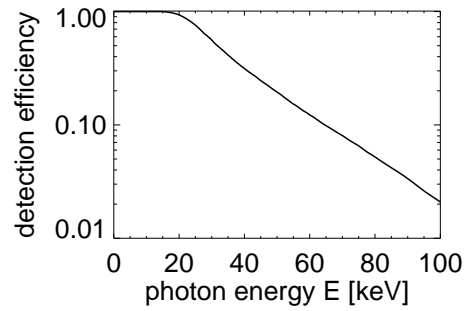


Figure 3.23: Efficiency of a 4 mm thick *Si(Li)*-detector for the detection of an incident photon with energy  $E$ . (interpolated from the data of a 3 mm and 5 mm thick layer [ORT10])

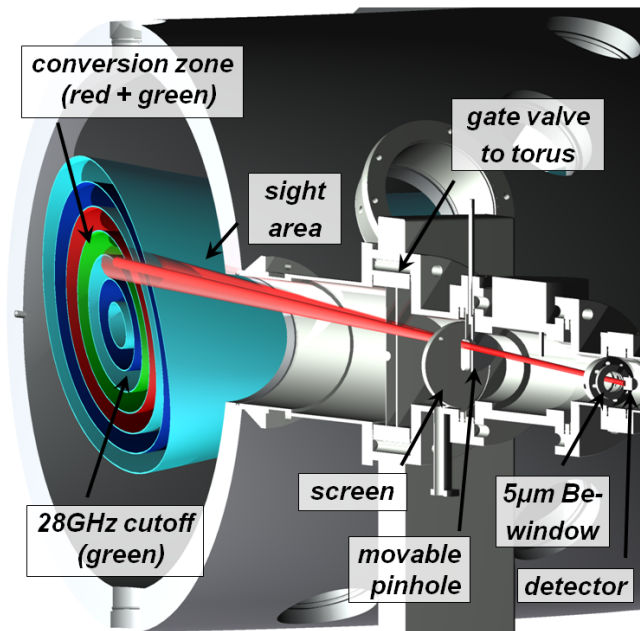


Figure 3.24: First optimized setup of the PHA-diagnostic (PHA1) with a movable pinhole for spatially resolved measurements and a screen made of stainless steel.

<sup>24</sup>The feedthrough position is adjusted by means of turns. The impact radius is given by  $r_{\text{imp}}(\text{turn}) = 51.98 \text{ mm} - 3.48 \frac{\text{mm}}{\text{turn}} \cdot \text{turn} + 0.01 \frac{\text{mm}}{\text{turn}^2} \cdot \text{turn}^2$  for PHA1.

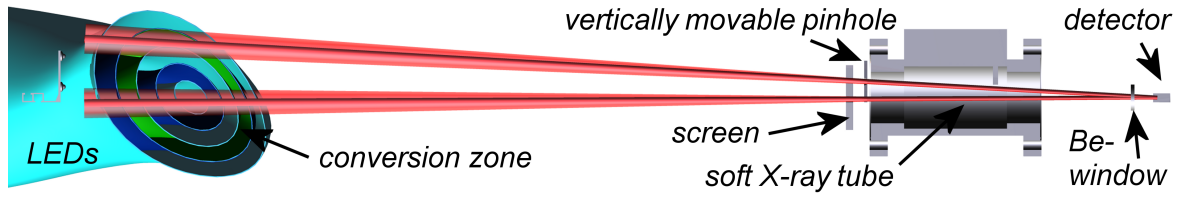


Figure 3.25: Poloidal cut view of the scale setup of PHA1. The red cones illustrate the maximum upper and lower sight area of the detector.

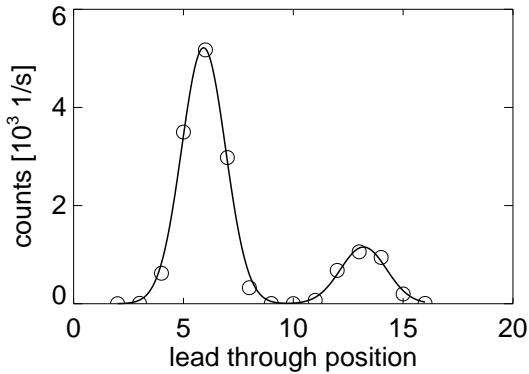


Figure 3.26: Detected visible emission of a blue and white LED mounted at the torus wall on the HFS in dependence on the feedthrough position.

Even though the X-ray emission, spatially resolved in  $z$ -direction, can be assigned to a certain vacuum flux surface, the trajectory of suprathreshold electrons can differ from the vacuum case depending on the particle energy and the movement direction with respect to the magnetic field vector. The resultant drift surfaces can be shifted in radial direction. Furthermore, the particles can be trapped on the low field side of the torus because the increase of the magnetic flux density to the inner side of the torus leads to a magnetic mirror. To also obtain a spatial resolution in radial direction and to extend the temporal sensitivity, the improved PHA (PHA2) comprises the integration of the movable pinhole between the plasma and the gate valve so that the space between the coils is effectively used. The calibration unit was

skipped because the measurements with PHA1 showed only a small change of the energy sensitivity when using the same adjustments. Therefore, the distance of the detector to the plasma axis was reduced to 54 cm allowing a full view over the plasma cross section.

Figure 3.27 shows the final assembly at the WEGA torus with a considerably thicker stainless steel screening which allows the resolution of a spatial X-ray distribution with energies up to 300keV. The 'pinhole' has a rectangular shape with a variable slit height to increase the

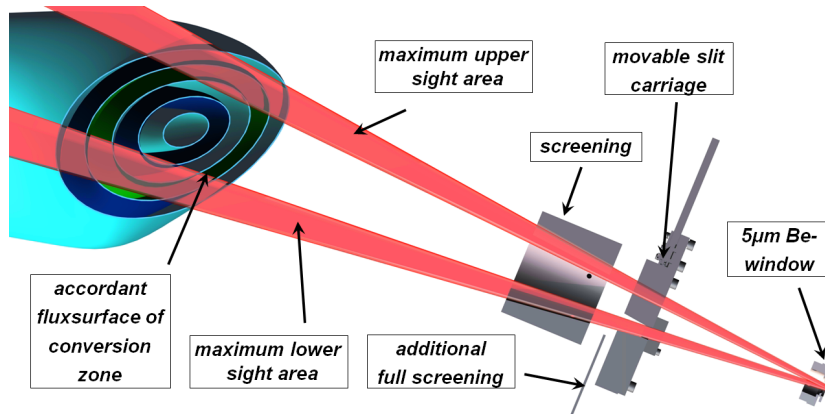


Figure 3.27: Poloidal cut view of the scale sightline setup of PHA2 with a movable slit carriage for spatially resolved measurements.

spatial resolution. Figure 3.27 shows the used setup with the maximum slit height of 10 mm to achieve the maximum count rate<sup>25</sup>. The resultant height of the sight area, captured by the whole detector area, is 25 mm around  $R = 72$  cm. The viewing angle in toroidal direction is  $10^\circ$  with 90 mm sight area width around  $R = 72$  cm<sup>26</sup>.

### 3.2.6.2 Soft X-rays with Alps-PHA

For a more detailed study of the suprathreshold electron component and to confirm the measured data, a collaboration was started with the IPP group Astrophysics and Laboratory-Plasma-Studies (ALPS) in Garching. In a common experimental campaign two new silicon drift detectors (SDD), manufactured by PNSensor GmbH at the Semiconductor Laboratory of the Max-Planck-Society (MPI-HLL), were tested at WEGA in April 2010. The first one is referred to as SDD1 and was only used for the detection up to 17 keV because of its finite thickness<sup>27</sup>. SDD1 has an almost full view of the WEGA cross section, as shown in Figure 3.28. The diagnostic was operated by PhD-students Bernhard Huber and Jaydeep Belapure. The details of the electronic data processing can be found in [Bel13]<sup>28</sup>. The MCA uses 8192 channels but the energy resolution is generally reduced by binning. The energy calibration is described in a preliminary report by Belapure [Bel10] and in contrast to the WEGA-PHA uses the typical characteristic lines during a discharge<sup>29</sup>. In the meantime, this system is used routinely for soft X-ray measurements at the tokamak ASDEX Upgrade in Garching [WHB<sup>+</sup>11] demonstrating its reliability.

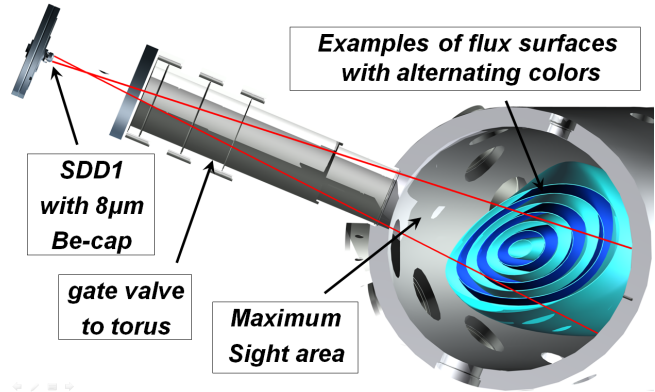


Figure 3.28: Hardware setup of the silicon drift detector (SDD1) at  $\phi_{SDD1} = 153^\circ$ .

In contrast, the second detector called SDD3 has a CsI(Tl) scintillator crystal on top stopping photons with energies up to MeV by creating electron-hole pairs. The subsequent de-excitation produce optical photons detected by the SDD [Bel10]. The system was mounted outside WEGA for the measurement of hard X- and gamma rays and was operated by PhD-student Dieter Michael Schlosser. These measurements led to subsequent studies, with the aid of an SDD-array, to obtain a two dimensional resolution that is described in the next subsection.

<sup>25</sup>Additionally, a full screening with 1 mm thick stainless steel can be shifted in the viewing range of the detector to increase the count rate ratio of high and low energy events.

<sup>26</sup>The slit position is adjusted again by means of turns, but the scale of the used feedthrough allows for a direct assignment of a half turn to the scale position. For this reason, the spatial calibration is given in dependence on the readable position and arises to  $r_{\text{imp}}(\text{pos}) = 323.13 \text{ mm} - 4.87 \frac{\text{mm}}{\text{pos}} \cdot \text{pos} + 0.01 \frac{\text{mm}}{\text{pos}^2} \cdot \text{pos}^2$  for PHA2.

<sup>27</sup>Both detectors have a diameter of 2.4 mm and a thickness of 0.45 mm. SDD1 is equipped with a 30 nm Al-layer as well as an  $8 \mu\text{m}$  Be-window [BH10; OBC<sup>+</sup>10].

<sup>28</sup>The basic principle is similar to the PHA of WEGA.

<sup>29</sup>The  $K_\alpha$  of Ar (2.957 keV), Cr (5.410 keV) and Fe (6.397 keV) [Att99] appear typically in the discharges, even though no argon is let in.

### 3.2.6.3 Hard X-rays with Drago-Array

. In collaboration with Dieter Michael Schlosser a prototype detector array with 77 quadratically arranged single SDDs was tested at WEGA that is shown in Figure 3.29 and is announced as Drago system. The conversion of the incident photons to visible light necessitates a complex backward calculation to identify the initial energy as well as position of the source photon. Details can be found in [FGP<sup>+</sup>10] and references therein. In combination with a pinhole a 2D-image of the plasma emission can be obtained with a resolution of up to 9 channels in poloidal and toroidal direction<sup>30</sup>. The Drago system is integrated in a bulky aluminum box with a plastic window in front of the detector. For this reason, only the positioning in front of a vacuum window is possible.

Figure 3.30 shows the whole setup at WEGA. The pinhole cone<sup>31</sup> is mounted in a fixed position relative to the port adapter that contains an extension of the angular aperture. A fitting piece is clamped on the Drago box, thus aligning the detector array with the pinhole.

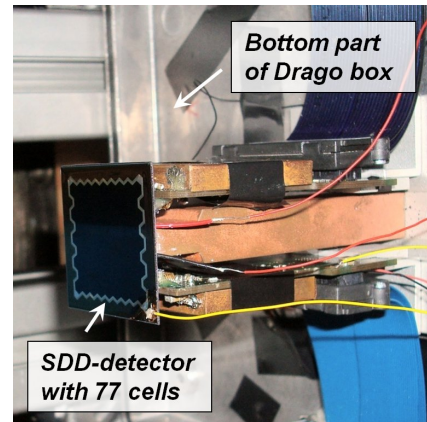


Figure 3.29: *Drago detector array of the PNSensor GmbH without the CsI(Tl) scintillator crystal*

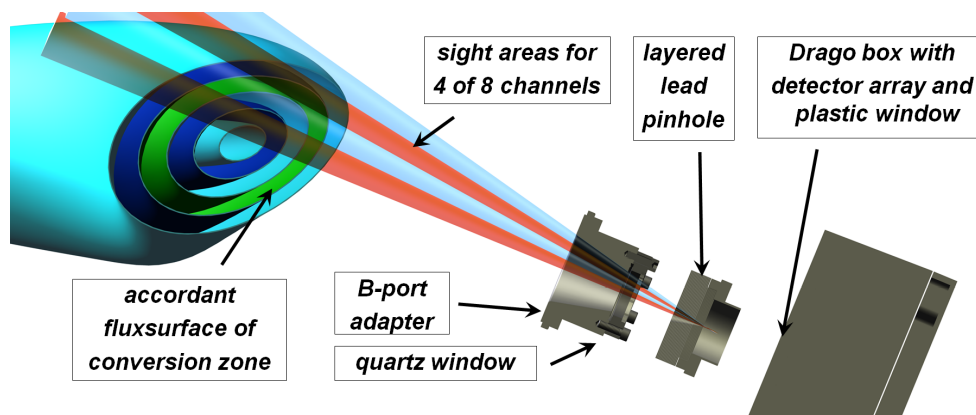


Figure 3.30: *Poloidal cut view of the scale sightline setup of the Drago detector array. Shown are the sight areas of the upper 4 channels of a row with 8 channels. For a 9 channel row the sight areas are displaced by a half of the single detector width.*

<sup>30</sup>The rows of the array alternate between 9 and 8 channels.

<sup>31</sup>The pinhole cone has an angular aperture of 26° with a minimal diameter of 0.8 mm and a thickness of 20 mm. It was realized by twenty 1 mm lead layers that are drilled with the particular diameter of the cone.

### 3.2.6.4 Gamma rays with Gamma-Scout®

The 3 cm thick stainless steel wall of the WEGA torus effectively screens only photons with energies up to circa 100 keV. For this reason, a radiation monitoring by a simple Geiger-Müller type counter outside WEGA gives a quick indication of suprathermal electrons in the hard X- and gamma ray energy range. For the case of small particle densities synchrotron like magnetic field configurations like WEGA allow the generation of so called runaway electrons with the aid of a loop voltage of some volts. Their energy is of the order MeV demanding a continuous monitoring because of safety reasons. The used commercial radiation detector Gamma-Scout® consists of an end-window counting tube<sup>32</sup> with a neon halogen filling [Mir10]. It only allows an integrated measurement of all photon energies with an energy dependent sensitivity as shown in Figure 3.31. The sensitivity at a photon energy of approximately 0.06 MeV is five times higher compared to the reference energy at 0.6 MeV.

For the quantitative analysis of the count rates with regard to the detected photon energy, the expected energy dependent X-ray emission spectrum must be multiplied with the overall transfer factor

$$T_{[\text{config}]}(E_{\text{ph}}) = S_{\text{Gamma}}(E_{\text{ph}})Tr_{[\text{config}]}(E_{\text{ph}}). \quad (3.5)$$

The sensitivity  $S_{\text{Gamma}}(E_{\text{ph}})$  results from Figure 3.31 by normalization and the energy dependent total transmission  $Tr_{[\text{config}]}$  of the particular sightline configuration between the source and the counting tube must be calculated by

$$Tr_{[\text{config}]}(E_{\text{ph}}) = \sum_i \left( \frac{\mu}{\rho} \right)_i \rho_i d_i. \quad (3.6)$$

The mass attenuation coefficient  $\mu/\rho$  as well as the mass density  $\rho$  of the different materials within the sightline are available in standard libraries [HS04]. The considered sightlines and the resultant thickness  $d$  of the stainless steel<sup>33</sup> of the torus as well as the copper of the magnetic field coils will be described in combination with the results. With the aid of additional lead layers in front of the counting tube, the energy of relativistic electrons can be estimated similar to the so called filter method [Hut94].

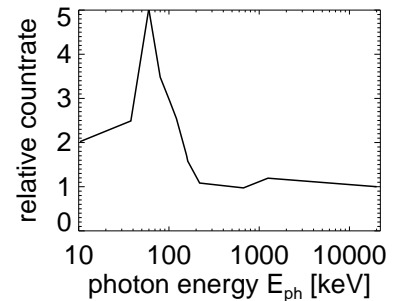


Figure 3.31: *Energy response (relative to CS-137) of a similar radiation detector PRM-8000 (Mazur Instruments) with an identically constructed counting tube for observation of hard X- and gamma rays through the entrance window (adapted from the calibration measurement in [Pea11])*

<sup>32</sup>ZP1401 of the company Centronic

<sup>33</sup>The assumed steel alloy is X5CrNi18-10 (1.4301 or V2A) with the additional parts  $w_{\text{C}} = 0.05\%$  carbon,  $w_{\text{Cr}} = 18\%$  chromium and  $w_{\text{Ni}} = 10\%$  nickel. The mass attenuation coefficient of alloys must be calculated by  $(\mu/\rho)_i = \sum_j w_j (\mu/\rho)_j$ .

### 3.2.7 Magnetic Diagnostics

The change of a current within the plasma can be determined with a loop by use of Faraday's law of induction. The change of the corresponding magnetic flux through the area enclosed by the loop generates a loop voltage whose temporal integration is proportional to the current. If the confining magnetic field is not constant during the change of the plasma current, an additional compensation loop is necessary that only detects the magnetic flux of the confining magnetic field.

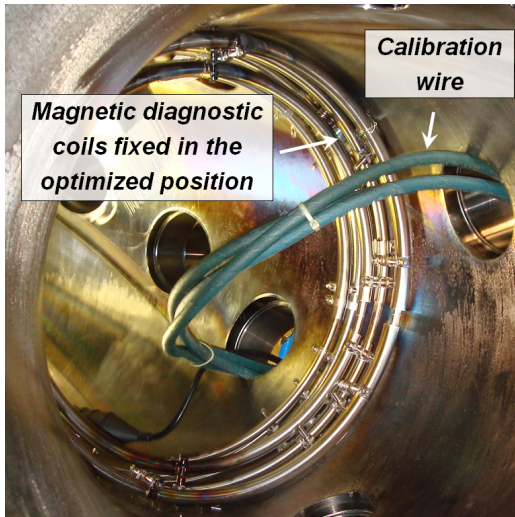


Figure 3.32: *In-vessel coil system of the magnetic diagnostics at  $\phi_{magnetics} = 126^\circ$ . The coil windings must be protected from the plasma and the stray radiation with a preferably thin stainless steel covering.*

The plasma currents must be distinguished into two different types. The driven toroidal plasma current is measured by the exclusive detection of the poloidal magnetic field. This is achieved by a wire wound around a preferably thick, isolated pipe in poloidal direction along the inner wall of the torus and is led the same way back to avoid an induced toroidal magnetic field. Such a setup is called a *Rogowski coil*. On the other hand, a gradient in the *plasma pressure*  $p = nk_B T$  generates a poloidal diamagnetic current that produces an additional toroidal magnetic field oppositely to the toroidal magnetic field. A so called *diamagnetic loop* encircling the plasma cross-section in poloidal direction is able to measure the corresponding magnetic flux change through the enclosed area of the loop and therefore the plasma energy given by equation (1.1). The *plasma beta*, being the ratio of plasma pressure and magnetic pressure, in WEGA is of the order  $\beta \approx 0.001\%$ , necessitating a very accurate compensation measurement of the toroidal magnetic field. The remaining noise,

however, is higher than the signal caused by the plasma and allows only a verification of the plasma pressure from the temperature and density profiles. The determination of the latter ones with the aid of a Langmuir probe is described in the next subsection. The resolution of the Rogowski coil is about 1 Amp. Figure 3.32 shows the in-vessel components of the diamagnetic coil systems as well as the inner Rogowski coil for the current measurement. A detailed description of the hardware setup is given in the accordant diploma thesis [Ch110].

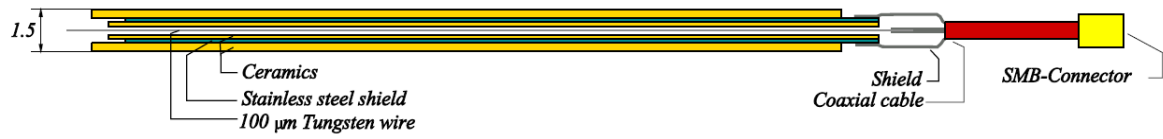


Figure 3.33: Setup of a Langmuir probe. (Adapted from [Mar08])

### 3.2.8 Langmuir Probe

The overview of available diagnostics at WEGA is complemented by one of the oldest techniques to measure plasma parameters. The Langmuir probe consists of a biased tungsten wire, surrounded by metallic shielding that is covered by a ceramic isolation at the inner and outer sides. Because of the thermal load by the plasma, the probe tip consists of graphite having a diameter of 0.9 mm. By sweeping the bias voltage from negative to zero in relation to the reference torus potential, the current on the probe changes from ion to electron dominated. Because of the low ion mobility, the current carried by the ions saturates for strongly negative bias voltages<sup>34</sup>. The ion saturation current can be related to the electron density under certain assumptions [Hut94]. When the bias voltage approaches the so called floating potential the current is more and more influenced by the electrons which is called the electron starting range. Assuming a Maxwellian energy distribution, the probe can be used to determine the electron temperature. The electron current collected should be at least one magnitude smaller than the typical plasma currents to limit the distortion by the measurement and to protect the probe itself.

The setup of the diagnostic as well as the technical design of the probes was developed by Stefan Marsen as part of his PhD-thesis, where a brief summary of probe theory can be found for the special case of WEGA [Mar08]. The high density discharges do not show a saturation of the ion current. The reason can be found in sheath formation around the probe tip or fast electrons collected by the probe even at strongly negative bias voltages. The lower the bias voltage, the higher the sheath thickness and the higher the ion collecting area around the probe. For this reason, the Poisson equation must be solved for the determination of the local sheath potential around the probe. Simplified equations for the consideration of sheath effects were provided by Allen, Boyd and Reynolds [Hut94]. This so called ABR-Theory leads to good fit results for the obtained probe characteristics, even though the sheath effects are of moderate importance for the thick probes. Taking into account that the quality of the fit itself is not a guarantee for the accuracy of the absolute value of calculated parameters, it remains a necessary condition. The determined temperature is practically unaffected by the used theory, however, the absolute value of the calculated density is. The relative values of the ion saturation current, however, are more reliable so that the relative shape of the density profiles can be obtained by the Langmuir probe measurements. The probe penetrates through half of the plasma cross section and back in 200 ms. An example of the measurement as well as the distortion of the probe itself is discussed at the beginning of subsection 5.2.2.

<sup>34</sup>Typically, an ion saturation current of the order 200 mA is measured at  $U_{\text{bias}} = -200$  V.

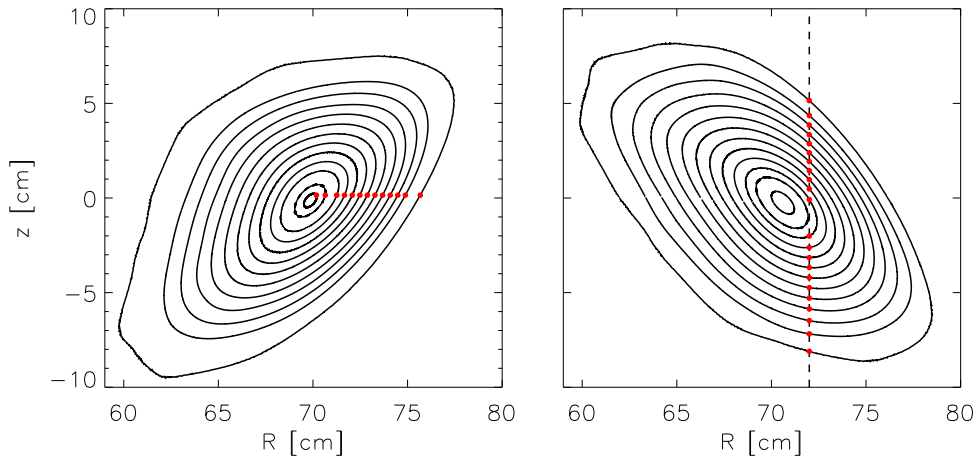


Figure 3.34: The radial probe position  $R_{lang}$  is mapped to the effective radius  $r_{eff}$  of the calculated flux surfaces at the toroidal position  $\phi_{langmuir} = 108^\circ$  (left) that can be assigned to the  $z$  position of the interferometer sightline at  $\phi_{ndl} = 216^\circ$  (right). The shown flux surfaces correspond to the typically used magnetic field configuration with  $\tau = 0.36$ .

The final absolute calibrated electron density profiles are obtained by integration of the relative Langmuir profiles and compared with the measured line integrated density by the microwave interferometer. Figure 3.34 illustrates the mapping process that necessitates a calculation of the magnetic field configuration with the aid of the w7-code. The relative density measured at each major radius of the toroidal position  $\phi_{langmuir} = 108^\circ$  is then translated to the effective radius that is used to define a relative density profile along the vertical interferometer sightline at  $\phi_{ndl} = 216^\circ$ . The high electron densities of the overdense discharges, however, are in contradiction to the approximation in equation (3.3) so that the resultant calculated phase shift is adapted iteratively to the measured phase shift.

# 4 Chapter 4

---

## 4 Development of Quasioptical Microwave Detection System

The detection of electron cyclotron emission (ECE) or electron Bernstein wave emission (EBE) is possible with the aid of a multichannel microwave radiometer which was introduced in subsection 3.2.4. The horn antenna of the diagnostic setup so far, however, cannot be used for an angle dependent measurement of EBE necessary for the investigation of the OX-conversion process. For this reason, a quasioptical antenna was developed which has a similar basic setup as the antenna of the 28 GHz heating system shown in Figure 3.5. In contrast to the heating system, the radiometer antenna must be designed for the whole Ka-band frequency range of about 22 – 40 GHz<sup>1</sup>.

The result is a broadband corrugated horn antenna which feeds a mirror system consisting of two curved metallic mirrors. The second mirror (II) in front of the plasma is steerable and allows an angle dependent measurement<sup>2</sup>. The denotation of both mirrors as first (I) and second (II) mirror is the same as for the heating system, because the final calculation of the beam imaging is based on consideration of an emission system. A result of the so called reciprocity law is that the frequency dependent transformation by a passive two-port is equal for a forward and backward traveling wave. For this reason, the resultant antenna characteristic is generally measured by scanning the emission microwave pattern.

The next two sections describe the design of the steerable mirror system and the corrugated horn antenna. The following section 4.3 explains the transmission line which includes a so called *Bragg reflector* for the rejection of 28 GHz stray radiation and a broadband circular polarizer for transformation of the received elliptical polarized wave to a linear polarized wave which can be detected by the Low Noise Amplifier (LNA). The LNA feeds the radiometer bank so that the described parts finally replace 'antenna' and 'front end' in Figure 3.17.

---

<sup>1</sup>Officially defined as 26.5 – 40 GHz, but the waveguide cutoff is not until 21.08 GHz.

<sup>2</sup>All quasioptical systems used at WEGA consist of a waveguide like structure and two imaging mirrors that will be described by roman numerals for an easier discrimination between the output waist  $w_{0,[roman numeral]}$  and the beam size  $w_{[roman numeral]}$  at a certain position behind the mirror. The particular mirror which is used as first mirror (I) or second mirror (II) is described by Latin numerals. Three different elliptical mirrors are available.

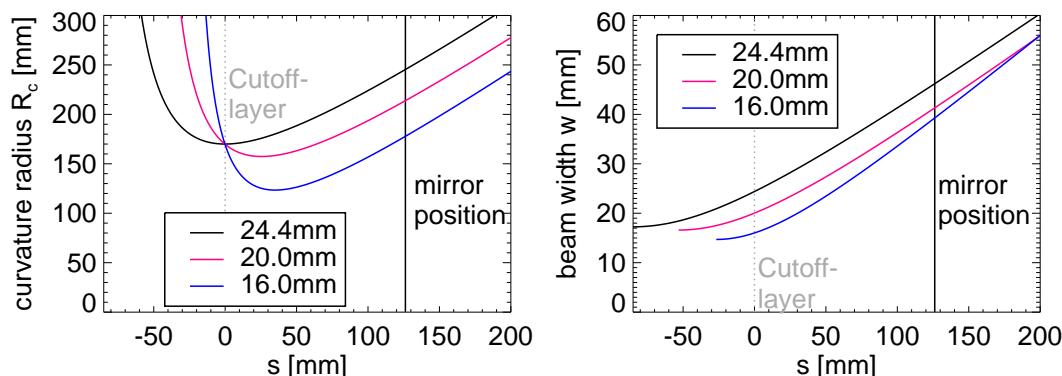


Figure 4.1: Evolution of the curvature radius  $R_c$  of a Gaussian Beam for different beam widths  $w$  at the position  $s = 0$  (left). The position of the beam waist  $w_0$  is adjusted in such a way that the curvature radius is matched to the fluxsurface curvature in vertical direction. The result is a beam width of around  $w_{ver} \approx 50$  mm at the mirror (II) (right).

## 4.1 Mirror System

The best strategy in designing a broadband quasioptic imaging system is first the analysis of the imaging properties by the mirrors. The limited space within the torus defines the realizable width of the Gaussian beam. The beam waist at the input of the mirror system gives the boundary conditions for the feeding horn antenna whose broadband design is a more challenging task than the optimization of the mirror parameters. For this reason, the fabrication and measurement of the horn antenna is the next step after the rough dimensioning of the imaging system. With knowledge of the parameter of the resultant horn antenna a redesign of the mirrors can follow which can be built with higher precision.

A detailed description of the design procedure is beyond the scope of this work hence only the main design criteria shall be explained. The main goal of the optimized imaging system is the maximization of the OX-conversion efficiency in consideration of an emission system<sup>3</sup>. Furthermore, the antenna system should be able to resolve an angle-dependent emission or absorption. The OX-conversion efficiency is generally reduced due to the finite beam size of the incident microwave beam [KCH<sup>+</sup>08]. As explained in subsection 2.3.4, the reason can be found in the finite  $\mathbf{k}$ -spectrum since it only partially fulfills the condition of equation (2.33). For this reason, the width of the Gaussian beam should be as large as possible around the conversion layer. The envisaged beam parameters for the antenna system are derived from the results of full wave simulations given in [KCH<sup>+</sup>08] which contains an extensive collection of calculated OX-conversion efficiencies for different beam widths and plasma geometries. The beam width should be at least twice as high as the vacuum wavelength  $\lambda_0$ . In this case, the conversion efficiency is of the order of  $C_{OX} \approx 0.7$  on the assumption of a slab geometry<sup>4</sup> [KCH<sup>+</sup>08]. The cutoff-fluxsurface, however, has a finite curvature in toroidal and poloidal direction leading to a further decrease of the OX-conversion efficiency of the order of 10%<sup>5</sup>.

<sup>3</sup>The antenna system, however, should also be used as transmitter to determine the OX-conversion efficiency with the aid of a reflection measurement. For this purpose, an additional receiving antenna must be installed in the direction of the reflected part of the probing microwave beam.

<sup>4</sup>Furthermore, the conversion efficiency is dependent on the density gradient length which is of the order of  $L_n \approx 3$  cm in the case of a probing frequency around 28 GHz. Smaller normalized density gradient lengths  $k_0 L_n$  can be obtained for lower probing frequencies.

<sup>5</sup>This effect can be neglected for  $w \leq 2\lambda_0$  but in this case the conversion efficiency is already decreased to less than 30% because of the small beam width.

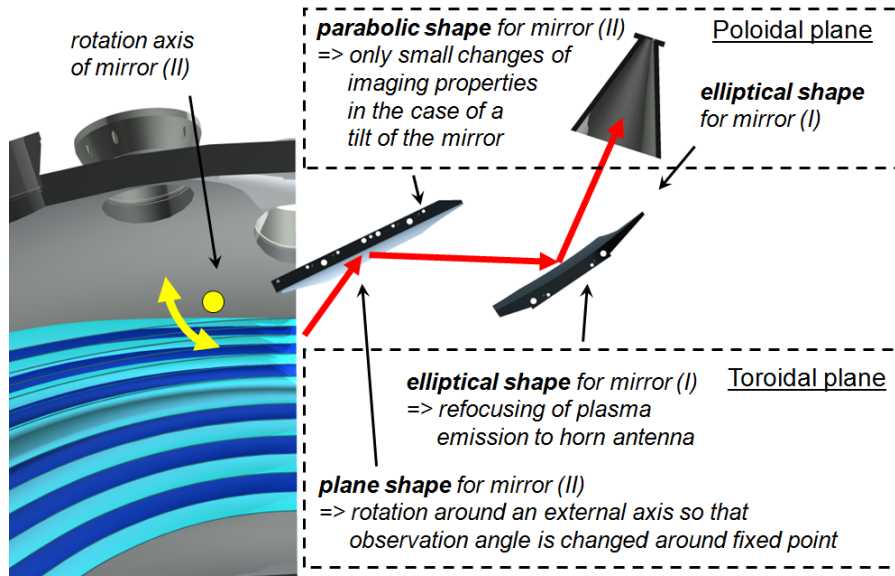


Figure 4.2: *Principal design considerations of the quasioptic mirror system to realize an astigmatic imaging of the plasma emission. The imaging properties in the vertical and horizontal plane are treated separately.*

This effect can be minimized by matching the phase front of the considered Gaussian beam to the curvature of the fluxsurface. As point of impact on the plasma, the same poloidal cross-section as for OXB-config 0 was chosen<sup>6</sup> which is shown in Figure 1.5. In this case, the Gaussian beam curvature in the vertical direction must be  $R_{c,ver} = 170$  mm. The necessary horizontal curvature with approximately  $R_{c,hor} = 900$  mm can be only achieved around the waist of the Gaussian beam, where the beam properties can be compared with a plane wave. The evolution of the curvature radius and the beam width is compared in Figure 4.1 for different beam waists  $w_0$ . The used frequency of 27.2 GHz ( $\lambda_0 = 11$  mm) is the mid-frequency of a radiometer channel whose frequency range corresponds to a central second harmonic electron Bernstein wave emission. The relevant cutoff-layer should be located around  $s = 0$  and the waist of the beam is positioned in a way such that its curvature radius is matched to the fluxsurface curvature in vertical direction<sup>7</sup>. The maximum beam width at the cutoff-layer is approximately  $w_{ver,c} \approx 2.3\lambda_0$  with around  $w_{ver} \approx 50$  mm at the position of the second mirror. It has to be recalled that the beam width indicates only the beam boundary that contains 86 % of the beam power. For transmission of almost the full beam power, a mirror or other apertures must be dimensioned to double the beam width  $w$ . This limits also the horizontal beam width to around  $w_{hor,c} \approx 4\lambda_0$  because the mirror (II) must be steerable in the horizontal plane to resolve the angle dependent emission or absorption around the desired observation angle of  $\vartheta \approx 56^\circ$ . Because of the three dimensional magnetic field configuration, however, the beam impact on the cutoff-layer should be unchanged during a tilt of the mirror.

To fulfill the different conditions in vertical and horizontal direction, an astigmatic Gaussian beam must be considered. The imaging of the beam in the vertical and horizontal plane can be treated separately, as already applied in subsection 3.1.1.2 for the calculation of the gyrotron mirrors. Figure 4.2 gives an overview of the used optical elements and their influence on the beam imaging. The best way to resolve the plasma emission around a fixed point is

<sup>6</sup>The compressed fluxsurfaces at the plasma edge lead to a small density gradient length  $L_n$ .

<sup>7</sup>The matching is only possible within the confocal length  $z_c$ , otherwise the beam width would be too large for the realizable mirror size within the torus.

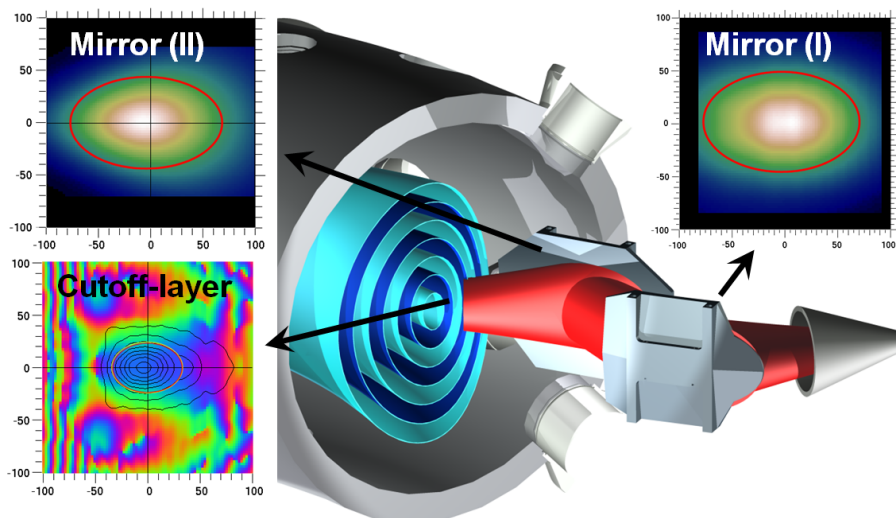


Figure 4.3: Imaging of the plasma emission by the designed mirror system. The red shape indicates the beam width  $w$  (86 % of the power) of the astigmatic Gaussian beam. The shown electric field distribution on the mirrors and on the cutoff-layer was calculated with the aid of OSSI [Mic10].

to tilt a plane mirror around a vertical axis within the plasma. Furthermore, the imaging of the beam is not changed in this case and is only given by the elliptical mirror in front of the horn antenna. In the vertical plane, a refocusing of the plasma emission by mirror (II) is necessary otherwise the beam expansion would be too large for an exclusive refocusing by mirror (I). A parabolic curvature was assumed for the vertical direction of mirror (II) to image the plasma emission to infinity. In this case, the change of the imaging properties by a tilt of the mirror can be minimized. The optimal elliptical curvature radius of mirror (I) in vertical direction, however, differs from the optimal one in horizontal direction. A possibility to merge the curvature radius of both directions is given in [WGGPR07]. The idea is to rotate the desired horizontal elliptical mirror shape not around its major axis but around the major axis of the desired vertical elliptical mirror shape.

Amongst the above principal design considerations, the detailed analysis of the imaging properties had the goal to minimize the distortion parameter (2.50) and to realize an almost full power transmission by the mirrors. The result is a beam width of  $w_{\text{ver,c}} \approx 2.3\lambda_0 = 25$  mm in vertical direction and  $w_{\text{hor,c}} \approx 3.1\lambda_0 = 34$  mm in horizontal direction at a major radius of  $R = 740$  mm. For this case, the resultant OX-conversion efficiency is given to  $C_{\text{OX}} \approx 0.5$  for  $k_0 L_n = 30$  [KCH<sup>+</sup>08]. The horn antenna must generate an emission which corresponds to a Gaussian beam with a waist of  $w_{0,\text{horn}} = 16$  mm at a frequency of 27.2 GHz.

The imaging properties of the designed system were verified by a numerical calculation with the aid of OSSI [Mic10]. For this purpose, the desired Gaussian beam waist was assumed at the position of the horn antenna. The resultant beam shape on the surface of both mirrors and on the cutoff-layer is shown in Figure 4.3. The red curve corresponds to the desired beam shape which is in good agreement with the calculated shape. The color coding corresponds to the phase of the wave indicating the desired converging beam in vertical direction. One cycle of the color change blue-green-red corresponds to a phase delay of  $180^\circ$ .

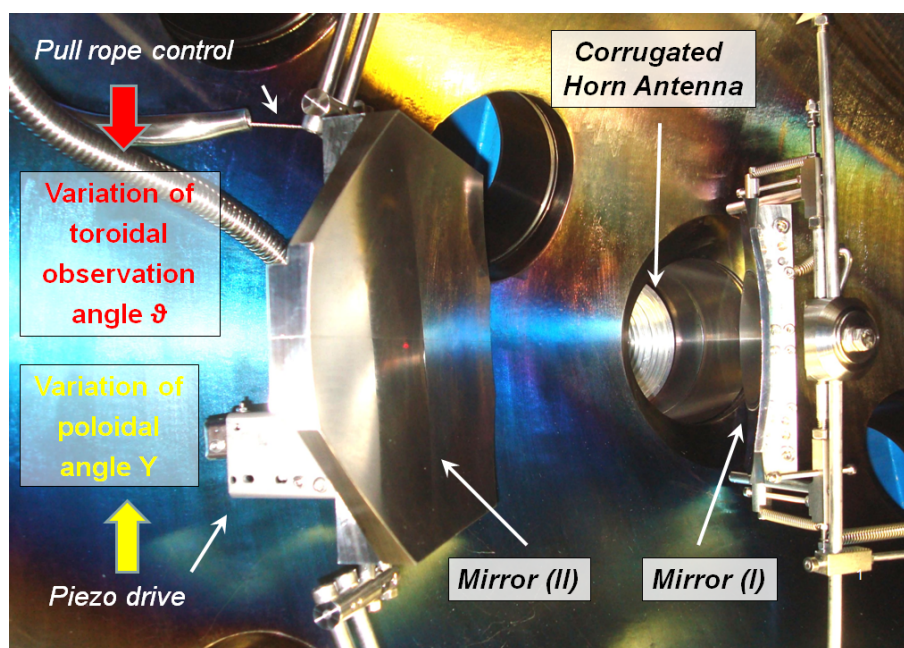


Figure 4.4: Final assembly of the mirror system within the WEGA-torus. The actual view is in propagation direction of the microwave beam emitted by the plasma.

The resultant radiation pattern of the whole quasioptic system, including the horn antenna described in the next section, was measured with a programmable xyz measurement device. For this purpose, the mirror system was installed within a mockup of the WEGA-torus so that the support structures of the two mirrors have exactly the same relation to each other as in the real WEGA-torus. Furthermore, interference effects due to reflections at the stainless wall are included in the measurement of the microwave pattern. Figure 4.5 shows five power distribution cross-sections of the resultant beam around the expected position of the cutoff layer. The width of the 86% power level (approximately  $-9$  dB) in the horizontal as well as the vertical plane is in good agreement with the desired values  $w_{\text{ver,c}} \approx 25$  mm and  $w_{\text{hor,c}} \approx 34$  mm<sup>8</sup>. The final assembly of the quasioptic antenna system within the torus is shown in Figure 4.4. The observation angle  $\vartheta$  is adjusted by a pull rope mechanism. After each change the position can be verified with the aid of a laser beam which propagates from the horn antenna along the central line of the microwave beam to a scale at the high field side wall of the torus.

<sup>8</sup>The xyz measurement device was combined with a network analyzer to measure the full frequency spectrum at each measuring point. Good imaging conditions can be obtained over the whole Ka-band frequency range, especially for the important frequency range lower than 30.0 GHz .

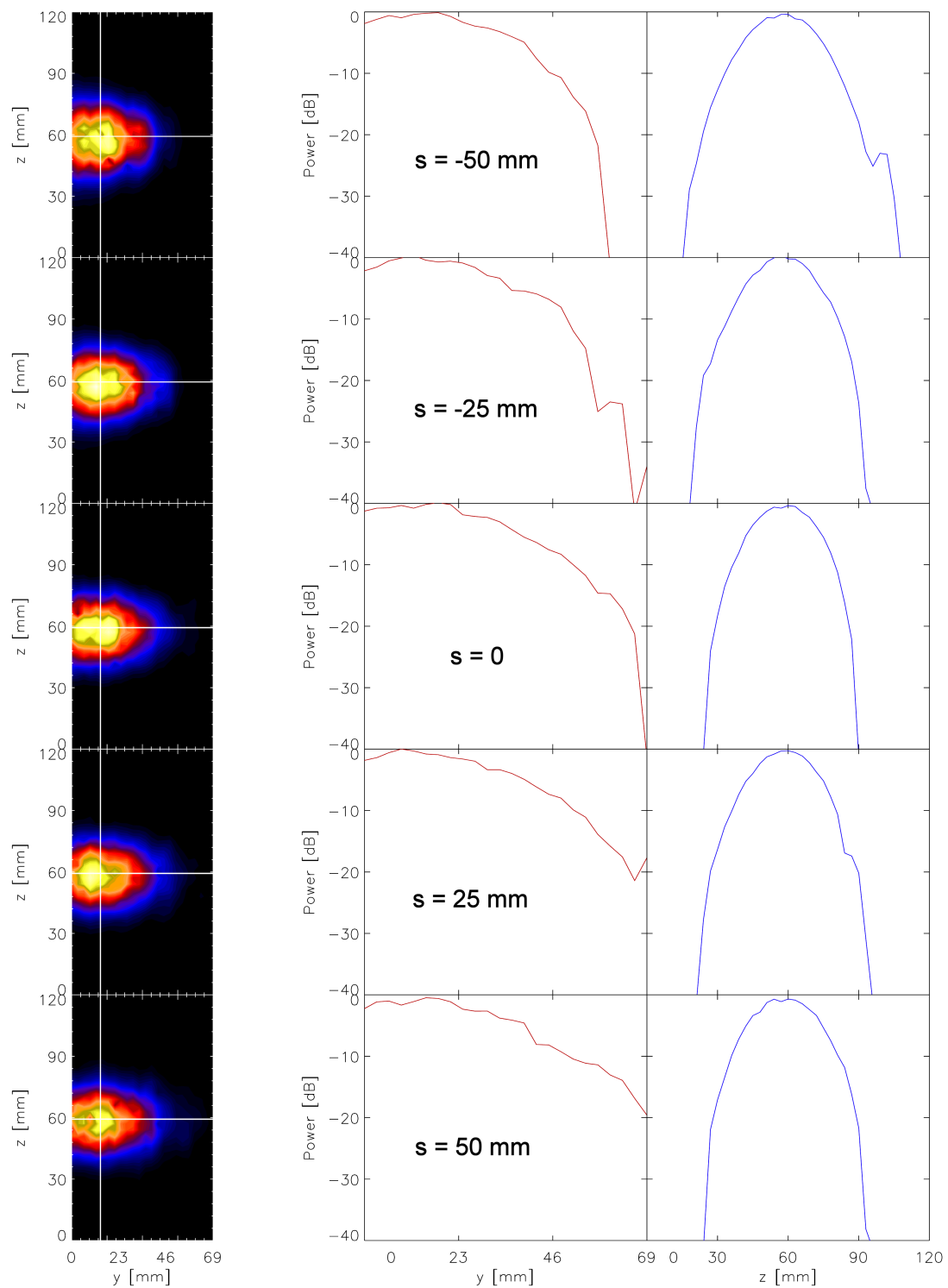


Figure 4.5: Power distribution within different cross-sections along the propagation path of the microwave beam for a frequency of 27.2 GHz (left column). The middle and the right column give the power values within the horizontal and the vertical plane. The expected position of the cutoff-layer is located around the position  $s = 0$ .

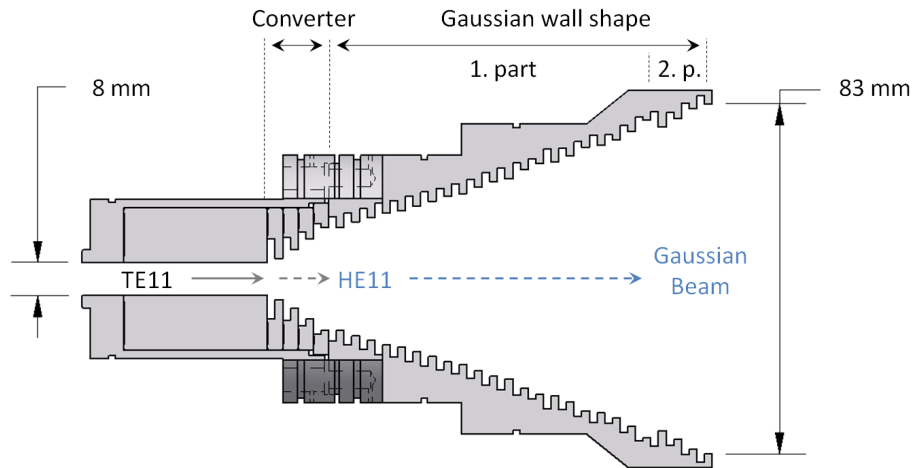


Figure 4.6: *Final cross-section of the corrugated horn antenna whose profile shape was optimized with the aid of HFSS. The expected far field pattern is shown in Figure 4.8. The horn antenna consists of two main aluminum parts. The  $TE_{11}$ - $HE_{11}$ -Converter must be build up from separately producible rings to achieve the corrugations up to a depth of a quarter wavelength.*

## 4.2 Corrugated Feed Horn

For a maximum bandwidth of the whole imaging system, the horn antenna should generate an emission spectrum whose phase front fits with the curvature radius of mirror (I) over the desired Ka-band frequency range. Furthermore, the elliptical polarization of the received plasma emission must be conserved so that a rectangular horn cannot be used.

The design of horn antennas is a very broad field and the description of the used design procedure is beyond the scope of this work. A good introduction can be found in [Gol98]. As introduced in subsection 2.3.3, the use of corrugations in the wall of a waveguide or a horn antenna allows the excitation of an  $HE_{11}$ -mode which has a coupling of 98% to the fundamental Gaussian mode  $TEM_{00}$ . Furthermore, a corrugated horn antenna can generate a symmetric beam pattern with a low cross-polarization level over a wide frequency range. The realized horn antenna, whose corrugation profile is shown in Figure 4.6, is based on the design considerations given in [GTR02; TGGR02]. As explained at the beginning of this chapter, the horn antenna is also considered as emitter which should produce a Gaussian beam. It consists of a smooth circular monomode waveguide with a diameter of  $d_{\text{horn,in}} = 8 \text{ mm}$  which feeds a very short mode converter generating the  $HE_{11}$ -mode<sup>9</sup>. The subsequent part is a corrugated taper which has a Gaussian shape and leads to a much improved Gaussian beam [GTR02]. The basic wall shape is combined with a second Gaussian shape at the end of the antenna to correct the far-field pattern of the lower frequency band and to achieve almost the same emission pattern over the desired frequency range. The software HFSS was used for the optimization of the profile shape and the corrugation depth especially within the converter. The calculated far field pattern of the final realization is shown in Figure 4.8 for different frequencies. A symmetric beam is achieved over at least a half octave. The electric field distribution within the  $-10 \text{ dB}$ -level is used for a Gaussian beam fit with good agreement up to  $-20 \text{ dB}$ . Furthermore, the antenna generates the same emission pattern over a frequency range between 26 GHz and 35 GHz with an increased width for frequencies lower than 25 GHz.

<sup>9</sup>In the technical realization the converter corrugations are composed of exchangeable rings to facilitate the manufacturing and allow modifications in the case of a poor emission pattern.

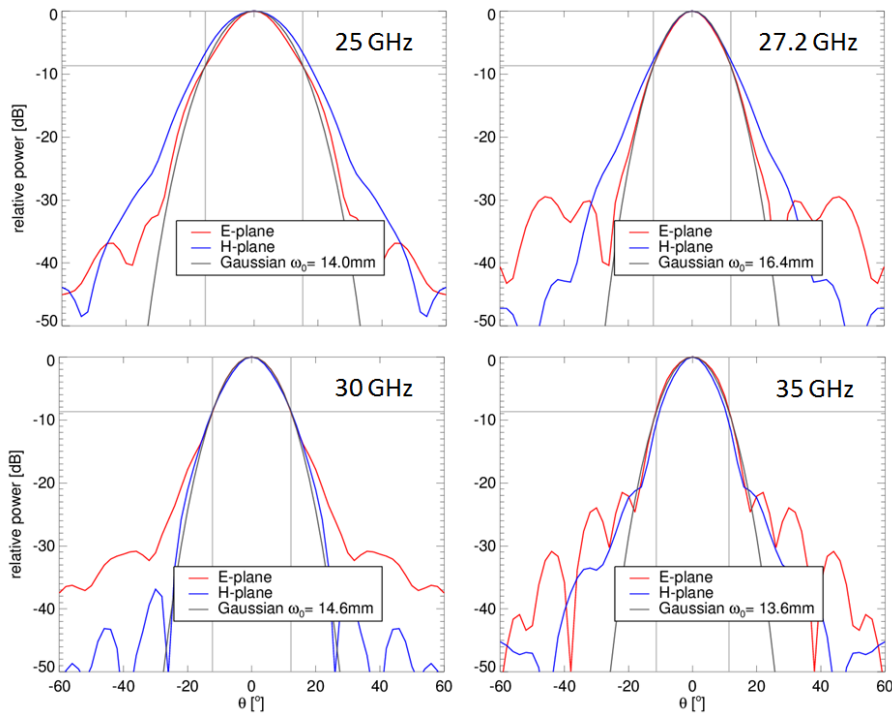


Figure 4.8: Theoretical far-field pattern of the corrugated horn antenna, shown in Figure 4.6, for a frequency range of a half octave. The profile shape was used as Perfect E boundary for the calculation with the aid of HFSS. A Gaussian beam pattern is fitted within the  $-10$  dB-level to determine a corresponding beam waist  $\omega_0$  of the emitted beam.

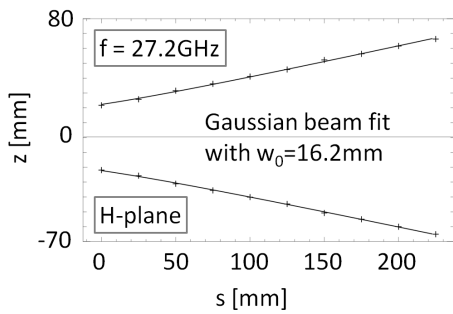


Figure 4.7: Evolution of the beam width within the H-plane of a 27.2 GHz beam emitted by the corrugated horn antenna shown in Figure 4.6.

The results were confirmed by measuring the three dimensional emission pattern<sup>10</sup>. Figure 4.7 shows the evolution of the beam width within the H-plane for 27.2 GHz which is in good agreement with the expected dependence of a Gaussian beam. The beam width in the E-plane is slightly narrower so that the fit of a Gaussian beam dependence leads to a waist of  $w_0 = 16.8$  mm. The other frequencies show the same good agreement with the calculation.

<sup>10</sup>The used programmable xyz measurement device was combined with a network analyzer to measure the full frequency spectrum at each measuring point.

### 4.3 Transmission Line

The connection between the horn antenna and the radiometer bank (see Figure 3.17) is realized by an oversized transmission line with a diameter of  $d_{\text{trans}} = 27.79$  mm to reduce the attenuation of the received plasma emission. Almost the full length of the transmission line, however, is used for the signal conditioning. An overview of the whole setup is shown in Figure 4.9.

The circular waveguide output of the horn antenna<sup>11</sup> is increased to the diameter of the transmission with the aid of an optimized taper which produces a vanishing part of higher order modes [WKL<sup>+</sup>11]. Afterwards, a 90° reflector within the oversized waveguide, which is called miter-bend, connects the taper with a vertical waveguide part. The connection can also be switched to a laser which is used for the exact adjustment of the observation angle  $\vartheta$  to the magnetic field lines after change of the steerable mirror. The vertical part of the transmission line is connected to the so called Bragg-reflector which has the function of a notch-filter and rejects the 28 GHz stray radiation [WKL<sup>+</sup>11]. This type of notch-filter is first applied at WEGA and is briefly explained in the next subsection. The Bragg-reflector is followed by a broadband circular polarizer consisting of two squeezed waveguides. The details of the design are explained in subsection 4.3.2. The output of the circular polarizer is a circular monomode waveguide with a diameter of 8 mm. It must be converted to the rectangular Ka-band waveguide of the Low-Noise-Amplifier (LNA) which is connected to the radiometer bank. Additionally, a so called Magic T is integrated between the waveguide converter and the LNA. It contains an adjustable short-circuited stub in the E- as well as the H-plane of the rectangular waveguide. Therefore, an arbitrary frequency band of a few GHz can be attenuated up to  $-20$  dB which is useful in resolving large emission differences within the detected spectrum.

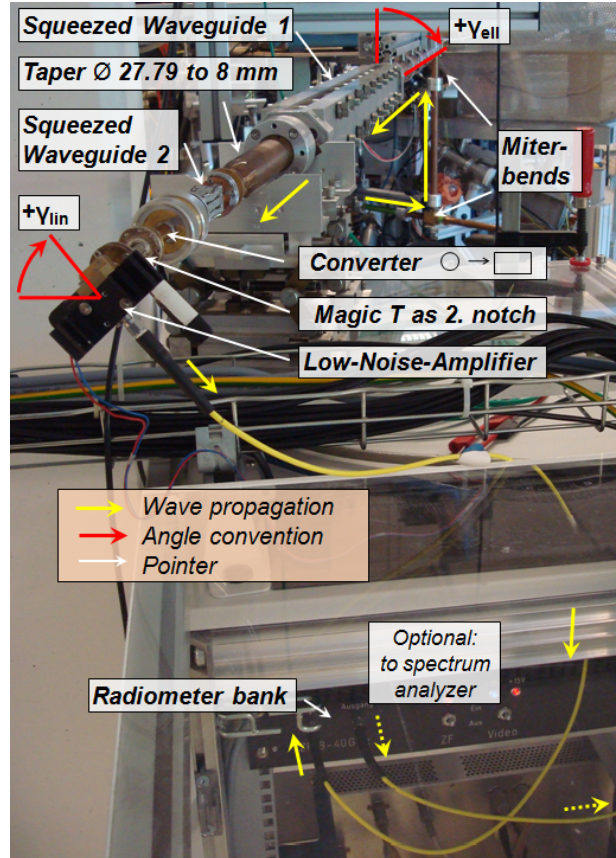


Figure 4.9: Transmission line from the horn antenna to the radiometer bank. The yellow arrow indicates the propagation direction of detected emission. The red arrows show the convention for the angle  $\gamma_{\text{ell}}$  of the circular polarizer in combination with the angle  $\gamma_{\text{lin}}$  of the linear polarization detected by the LNA.

<sup>11</sup>Diameter of  $d_{\text{horn},0} = 8$  mm

### 4.3.1 Bragg-Reflector

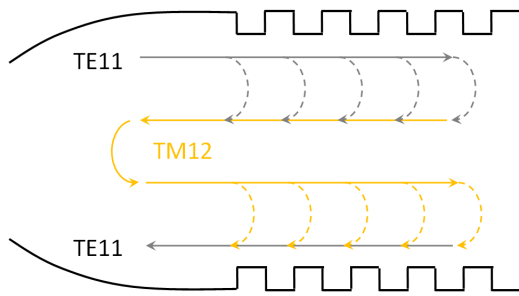


Figure 4.10: Working principle of the Bragg-reflector.

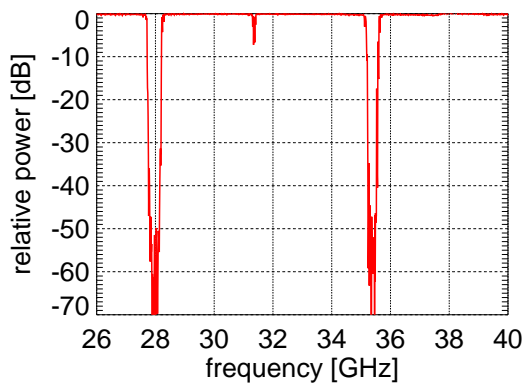


Figure 4.11: Transmission of the Bragg-reflector with the two notches at 28 GHz and 35.4 GHz.

A new notch filter design was first tested at WEGA which achieves a suppression of approximately  $-70$  dB over frequency range of a half GHz. Figure 4.10 shows a sketch of the working principle of the waveguide structure containing periodical azimuthal radial grooves in the waveguide wall. The incident  $TE_{11}$ -mode is scattered at each groove into a reflected  $TE_{11}$ -mode as well as higher order modes. If the corrugation period satisfies the Bragg condition  $p = \lambda_{Bragg} = 2\pi / (k_{z,TE_{11}} + k_{z,TM_{12}})$ , then the reflected parts of the considered  $TM_{12}$ -mode interfere constructively and the  $TE_{11}$ -mode is completely converted into the  $TM_{12}$ -mode [WKL<sup>+</sup>11]. The Bragg-reflector, however, is tapered to a monomode waveguide at the input and output so that the  $TM_{12}$ -mode propagates back to the corrugated waveguide section. Because of the satisfied Bragg condition, the  $TM_{12}$ -mode is backscattered into a  $TE_{11}$ -mode which can leave the transmission line through the horn antenna. The details of the design can be found in [WKL<sup>+</sup>11]. Figure 4.11 shows the measured transmission of the Bragg-reflector. In addition to the notch at 28 GHz, a second notch appears at 35.4 GHz which corresponds to the  $TM_{13}$ -mode but does not compromise the plasma emission measurements.

### 4.3.2 Circular Polarizer

The elliptical polarization necessary for the OX-conversion of the heating beam is achieved by a circular waveguide which is gradually squeezed to an elliptical cross section. An example was shown in Figure 3.2 which is further explained in subsection 3.1.1.1. For the case of the detection system the elliptically polarized plasma emission of the oblique observation in respect to the magnetic field lines must be converted into linear polarization because of the rectangular waveguide cross section of the Low-Noise-Amplifier (LNA). In contrast to the heating system, the necessary circular polarizer must introduce or rather reverse the  $90^\circ$  phase shift between the linear polarized partial waves along the main axes of the elliptical waveguide cross section preferably over the whole detectable frequency range of  $f = 22 - 40$  GHz. A squeezed waveguide already has the weakest frequency dependence [VL03] so that the same technique is used for the radiometer transmission line. But a too heavy tapering of the used circular oversized waveguide (diameter  $d = 27.79$  mm) can lead to a scattering of the  $TE_{11}$ -mode into spurious modes (higher order modes). This problem was already object of research almost thirty years ago when the first circular polarizers for high power transmission lines were developed.

For the numerical calculation of the corresponding power transfer, *coupling coefficients* were analytically derived for the conversion of the incident linear polarized mode to a  $90^\circ$  phase shifted, cross polarized mode as well as its scattering to the higher order modes [Doa86]. On the basis of this approach, shown in Figure 4.12, the considered incident mode with the electric field vector  $E_r^O$  and the cross polarized mode with the electric field  $E_r^X$  have the same electric field pattern because of the same waveguide shape in relation to the main polarization axis. For this reason, the both  $TE_{11}$ -modes as well as the particular higher order modes have the same phase velocity. Furthermore, the coupling coefficients for the scattering between spurious modes were derived [Doa86].

These scattering coefficients to and between higher order modes were modified in [TK89] so that the numerical calculations for the generation of spurious modes are in agreement with the fabricated squeezed waveguides at the design frequency  $f_{\text{des}} = 70$  GHz. Figure 4.13 shows the corresponding frequency dependent phase shift  $\Delta\varphi$  of the partial wave with the electric field  $E_r^b$  against the partial wave with the electric field  $E_r^a$  of an identically constructed circular polarizer with the same waveguide diameter  $d = 27.79$  mm. For other frequencies as 70 GHz the phase shift differs clearly from the design value of  $\Delta\varphi = 90^\circ$ . Within the frequency range of  $60 - 90$  GHz the variation is between  $\Delta\varphi = 103^\circ - 70^\circ$  [VL03]. The frequency dependence of  $\Delta\varphi$  can be calculated by the product of the coupling coefficient  $K$  between  $E_r^O$  and  $E_r^X$  and the integral of the change of the waveguide radius  $a_{2p} = (d_{\text{max}} - d_{\text{min}})/4 = a_0 - a_{\text{min}}$  along the waveguide axis [Doa86]

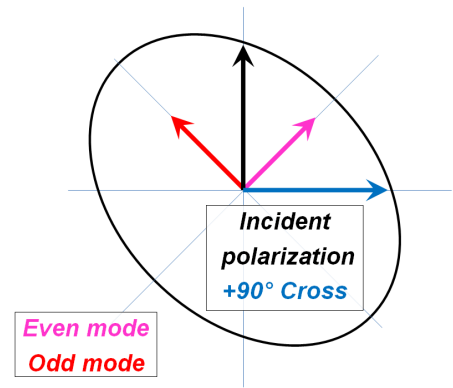


Figure 4.12: *Elliptical cross section at  $z_w = L/2$  of a gradually squeezed waveguide with the length  $L$ . The arrows  $E_r^O$  and  $E_r^X$  indicate the polarization of the considered modes by [Doa86] with  $E_r^O$  along the incident polarization. Additionally, the arrows  $E_r^a$  and  $E_r^b$  indicate the partial waves with a polarization along the main axes of the elliptical waveguide cross section.*

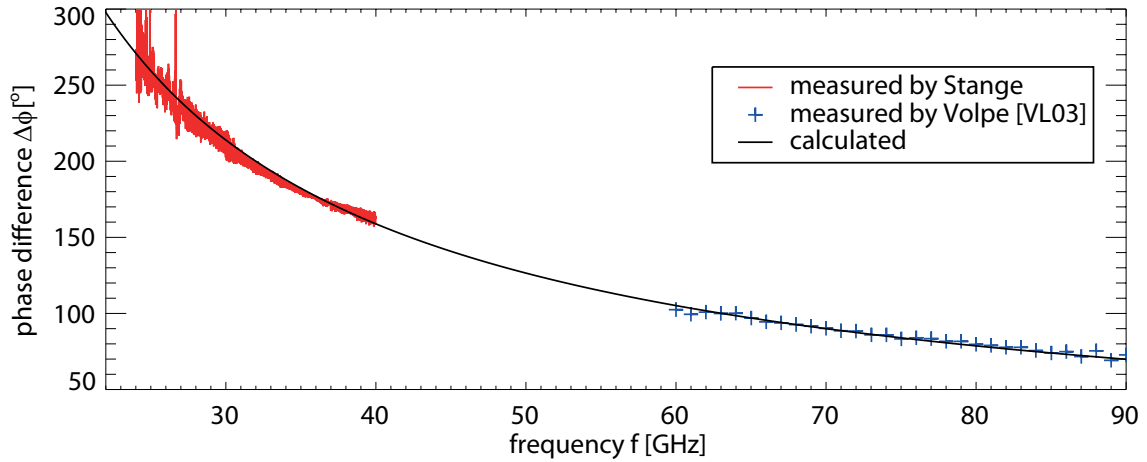


Figure 4.13: Measured and via equation (4.1) calculated phase shift of the both  $TE_{11}$ -modes with the radial electric fields  $E_r^a$  and  $E_r^b$  along the main axes of the elliptical waveguide cross section of a 70 GHz circular polarizer. The waveguide diameter is  $d = 27.79$  mm with a length of  $L = 1$  m. (The used shape function  $a_2(z_w) = a_{2,max} \sin^2(\pi z_w/L)$  has a maximum radius change of  $a_{2,max} = 1.98$  mm.)

$$\Delta\varphi = 2K \int_0^L a_{2p}(z_w) dz_w = 2K \cdot I(L, a_{2p}(z_w)). \quad (4.1)$$

The coupling coefficient  $K = K_{\text{mode}}K_w$  can be split into a constant part  $K_{\text{mode}}$  dependent on the mode type (TE or TM) and a frequency dependent part

$$K_w = \frac{1}{a_0^3 \sqrt{\left(\frac{2\pi f}{c}\right)^2 - \left(\frac{x_{\text{pm}}^{\text{TM,TE}}}{a_0}\right)^2}}. \quad (4.2)$$

For TE-modes the constant part  $K_{\text{mode}}^{\text{TE}} = (x_{\text{pm}}^{\text{TE}})^2 / [(x_{\text{pm}}^{\text{TE}})^2 + p^2] / [(x_{\text{pm}}^{\text{TE}})^2 - p^2]$  is only dependent on the zero  $x_{\text{pm}}^{\text{TE}} = \chi'_{\text{pm}}$  of the derivative of the Bessel-function  $J'_p$  and the azimuthal index  $p$ . For this reason, the frequency dependence of the phase shift  $\Delta\varphi$  can be only affected by the waveguide radius  $a_0$  and not by the shape function  $a_{2p}(z_w)$  of the squeezed waveguide. But the subtraction of the produced phase shifts of two cascaded squeezed waveguides with different waveguide radii will lead to a reduction of the occurring frequency dependence. An additional negative phase shift of  $E_r^b$  against  $E_r^a$  can be introduced by a second squeezed waveguide (number 2) whose main axis of the elliptical waveguide cross section is perpendicular to the particular main axis of the first squeezed waveguide (number 1). The total phase delay results to  $\Delta\varphi_{\text{tot}} = \Delta\varphi_1 - \Delta\varphi_2 = K_{\text{mode}}[K_{w,1}(a_{0,1})I_1 - K_{w,2}(a_{0,2})I_2]$  with  $\Delta\varphi_1 \gg 90^\circ$ . Figure 4.14 shows as example the frequency dependence of total phase delay  $\Delta\varphi_{\text{tot}}(f)$  of two squeezed waveguides for different radii  $a_{0,1}$  in combination with the respective optimal radius  $a_{0,2}$  to achieve in the shown frequency range the minimum integral deviation from the design value  $\Delta\varphi_{\text{des}} = 90^\circ$ . This is compared with the frequency dependent phase delay of a single circular polarizer with the radius of the used transmission line  $a_{0,1} = 13.895$  mm and a design frequency of  $f_{\text{des}} = 28$  GHz.

In contrast to the single polarizer with a deviation of up to  $\pm 25^\circ$ , a broadband  $90^\circ$  phase delay with a deviation of  $+6^\circ/-10^\circ$  can already be obtained with an oversized waveguide radius of  $a_{0,1} = 10$  mm. With optimization on a frequency band of only a half octave  $f = 22 - 33$  GHz, whose upper border corresponds to the expected maximum cutoff-frequency in the OXB-discharges, the deviation can be easily reduced to  $\pm 5^\circ$ .

Because of the only small improvement with  $a_{0,1} > 14$  mm, the above introduced circular polarizer for the design frequency  $f_{\text{des}} = 70$  GHz should be used as polarizer number 1 to realize a broadband circular polarizer for the frequency range of  $f = 22 - 33$  GHz. As also shown in Figure 4.13, the measured phase shift of the latter one in the measured frequency range  $f = 22 - 40$  GHz is in agreement with the theoretical prediction of equation 4.1. But the integral  $I_1(L_1, a_{2,1}(z_w))$  is greater compared to the optimized combination of Figure 4.14 so that the optimal waveguide radius of the desired second squeezed waveguide was finally determined to  $a_{0,2} = 5$  mm. The accordant integral value  $I_2$  is fixed<sup>12</sup> but a proper combination of length  $L_2$  and shape function  $a_{2,2}(z_w)$  is necessary to minimize the generation of spurious modes. For this reason, a complex  $60 \times 60$  matrix of coupled wave differential equations similar to [TK89] was implemented considering the propagation of 30 different modes in two different polarizations as well as the conversion among themselves.

The spurious mode generation by the 70 GHz circular polarizer is also in the Ka-band of the order per mille. The same shape function type<sup>13</sup> of the latter one was used for the design of the second squeezed waveguide. The same low spurious mode generation can be achieved for a length  $L_2 \geq 48$  mm. The resultant technical realization is shown in Figure 4.15 during the step by step squeezing process combined with the measurement of the single frequency characteristic<sup>14</sup>.

<sup>12</sup> $I_2 = 4.4 \cdot 10^{-5} \text{ mm}^2$

<sup>13</sup> $a_2(z_w) = a_{2,\text{max}} \sin^2(\pi z_w/L)$

<sup>14</sup>The squeezing process was divided in 4 steps. After each step the resultant frequency dependent phase shift was checked by measurement of the relative phase shift of a wave with electric field  $E_r^a$ , shown in the picture, and  $E_r^b$ , achieved by  $90^\circ$  rotation of the middle waveguide part. The linear polarization at input and output is fixed by the used waveguide converters from standard rectangular (WR-28) to circular cross section ( $d = 8$  mm). The necessary taper from  $d = 8$  mm to  $d = 10$  mm was also optimized with the above-mentioned coupled wave implementation to minimize the spurious mode generation.

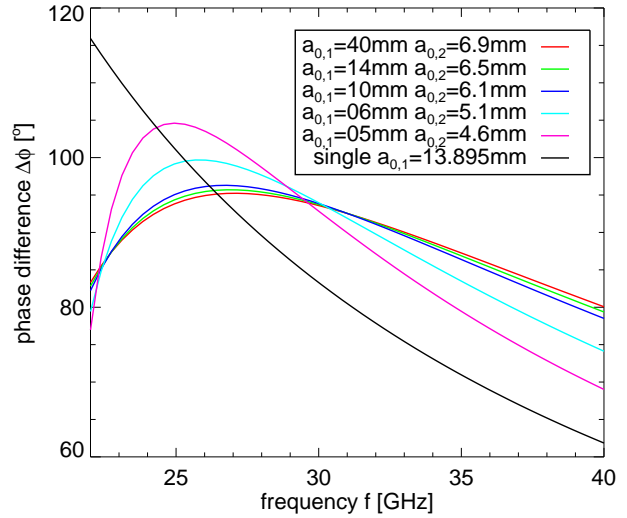


Figure 4.14: Total phase delay  $\Delta\varphi_{\text{tot}}$  versus the wave frequency of two cascaded, counteracting squeezed waveguides for different optimized combinations of the particular radii  $a_{0,1}$  and  $a_{0,2}$ . A single polarizer is shown for comparison (black).

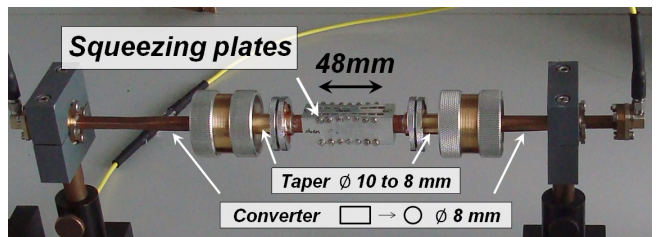


Figure 4.15: Second squeezed waveguide during fabrication and measurement.

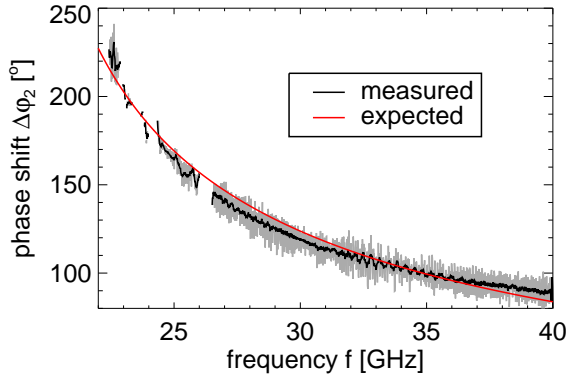


Figure 4.16: Measured and expected phase delay  $\Delta\varphi_2$  versus the wave frequency of the built squeezed waveguide shown in Figure 4.15.

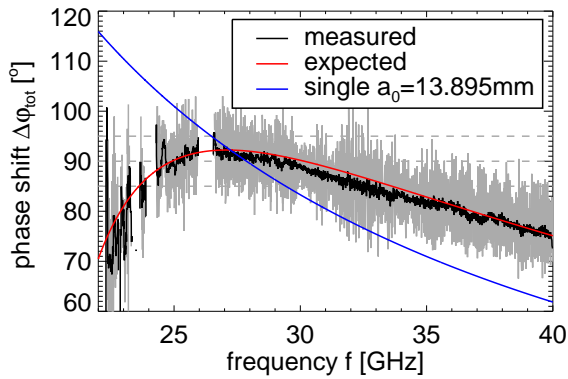


Figure 4.17: Measured and expected total phase delay  $\Delta\varphi_{tot}$  versus the wave frequency of the 70 GHz circular polarizer and the built squeezed waveguide shown in Figure 4.15. The expected phase delay of a single polarizer is shown for comparison (blue).

On the basis of the measured frequency dependence of the 70 GHz circular polarizer, the optimally achievable frequency dependent phase shift  $\Delta\varphi_2$  for  $a_{0,2} = 5$  mm is compared in Figure 4.16 with the finally measured phase shift<sup>15</sup>. Both curves are in good agreement but the measured phase shift has a stronger frequency dependence. This phenomenon is also obvious in the accordant frequency range of the 70 GHz circular polarizer whose measured phase shift is shown in Figure 4.13. It must be ascribed to the only weakly oversized waveguides<sup>16</sup> in relation to the wavelength of the order 1 cm. The resultant phase shift of the built squeezed waveguide in combination with the 70 GHz circular polarizer is shown in Figure 4.17. The frequency dependence is partially canceled out so that the deviation of the measured and expected frequency dependence is in perfect agreement. But the most important result is the obtained weaker dependence allowing the generation of a broadband circular polarization of at least a half octave.

<sup>15</sup>The measurement was accomplished with the aid of a swept frequency interferometer whose dwell time was considerably increased so that only the stable phase relation was evaluated.

<sup>16</sup>In contrast, the measured and expected phase shift within the frequency range 60 – 90 GHz are in very good agreement as apparent from Figure 4.13.

# 5 Chapter 5

---

## 5 Experimental Results

The experimental setup of WEGA, especially the possibility to combine different heating systems with different frequencies, allows the investigation and development of different heating scenarios. The main part of the following chapter focuses on the characterization of electron Bernstein wave heating via the OXB-conversion process at 28 GHz. To understand the specialty of the plasma state, a standard X2 discharge at 28 GHz heating frequency is introduced at the beginning of section 5.1. This is followed by an overview of the 2.45 GHz non-resonant heating scenario, which is used to reach the high densities, necessary for the OXB-conversion process. Despite the density in the OXB-discharges, these so called overdense plasmas are accompanied by a suprathermal electron component. The characterization of the latter one by a wide range of different diagnostics, including different X-ray detection systems, is described in section 5.2. The subsequent section 5.3 clarifies the source of the high intensity broadband microwave radiation generally appearing in the overdense discharges at frequencies corresponding to a central second harmonic electron Bernstein wave emission. With this knowledge among others it is possible to analyze in section 5.4 the OX-conversion process by means of an invasive diagnosis with the gyrotron heating beam itself and a non-invasive diagnosis with the aid of the quasioptic mirror system introduced in chapter 4.

### 5.1 Heating Scenarios in Comparison

The investigation of heating concepts in general has the goal to increase density and temperature as well as to optimize the plasma performance of magnetically confined plasmas. The amount of absorbed power or rather the heating efficiency is the most important quantity to compare different heating scenarios. For this reason, the determination of the absorbed power is a central topic. As described in subsection 3.1.1, it is not possible at WEGA to reach the OXB-threshold-density in hydrogen because of the relatively low available heating power. For this reason, the overall investigation concentrates on helium discharges with only a few comparisons to other gas types like argon and hydrogen.

### 5.1.1 X2-Heating

If helium is used as discharge gas and only the gyrotron as heating source, it is not possible to reach the cutoff-density of the ordinary 28 GHz heating wave. The overall O2-absorption, being about one magnitude less than the X2-absorption, is below the radiation and convective losses of the plasma. Therefore, the plasma is sustained by extraordinary absorption at about half the O-cutoff density. The use of ordinary polarization would also lead to a sole X2-absorption because of polarization changes by reflections at the torus wall.

#### 5.1.1.1 Discharge scenario

Figure 5.1 shows the time traces of the most important parameters of a standard X2 helium discharge. The characteristic time ranges are visualized by dotted vertical lines and numbered at the top of Figure 5.1.

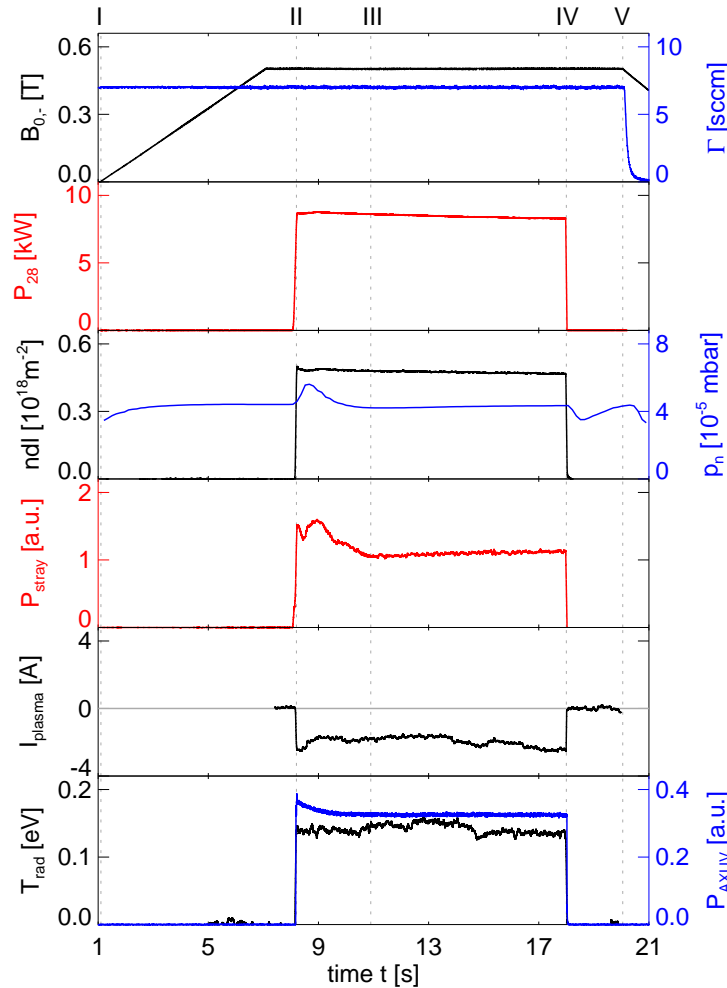


Figure 5.1: Time traces of a standard X2 helium discharge. From top to bottom: the magnetic flux density  $B_0$  on the magnetic axis & the gas flow  $\Gamma$ , the gyrotron forward power  $P_{28}$ , the line integrated electron density  $ndl$  & the neutral gas pressure  $p_n$ , the gyrotron stray radiation  $P_{stray}$ , the plasma current  $I_{plasma}$  as well as a central bolometer channel  $P_{AXUV}$  (channel B09) & the radiation temperature  $T_{rad}$  at the frequency  $f_{33.0} = 33.0 \pm 0.5$  GHz. The time points indicated by the vertical lines are described in the text.

- I Ramp up of the currents in the magnetic field coils leads to an increase of the magnetic flux density to  $B_0 = 500 \text{ mT}$  on the magnetic axis. The gas inlet is set to  $\Gamma = 7 \text{ sccm}$  resulting in a neutral gas pressure of  $p_n = 4.4 \cdot 10^{-5} \text{ mbar}$ .
- II The gyrotron forward power is increased in a time period of  $\Delta t = 100 \text{ ms}$  to the maximum of  $P_{28} = 8.7 \text{ kW}$  leading to a certain stray radiation level. After the plasma breakdown, the line integrated density is increased with the gyrotron power to  $ndl = 0.5 \cdot 10^{18} \text{ m}^{-2}$ . The plasma carries a net current of  $I_{\text{plasma}} \approx 3 \text{ A}$  directed opposite to the magnetic field.<sup>1</sup> The microwave radiation temperature  $T_{\text{rad}}$  in the frequency range  $33.0 \pm 0.5 \text{ GHz}$  reaches some per cent of the physical electron temperature because of multiple reflections. The bolometer diagnostics measure a radiated power of  $P_{\text{rad}} = 1.7 \text{ kW}$ .
- III The energy confinement is increased with decreasing neutral gas pressure and less electron collisions with neutrals. The resultant higher electron temperature and thus higher absorption leads to a decrease of the stray radiation by approximately 30%.
- IV After a discharge time of 10s, the gyrotron power is switched off in a time period  $\Delta t = 1 \text{ ms}$  so that the plasma density vanishes with a characteristic time of  $\tau \approx 10 \text{ ms}$ .
- V The gas inlet is closed and the currents of the magnetic field coils are ramped down.

The electron temperature and electron density profiles of the discharge are shown in Figure 5.2a. Typical for an X2-discharge, the electron temperature is peaked around the magnetic flux surface, where the first path of the heating beam and the resonance layer coincide. If this is not exactly at the magnetic axis or the beam does not hit the magnetic axis, a second peak will appear at the second intersection point of the probe with the same flux surface. This behavior is a clear indicator of resonant electron cyclotron absorption already at the low temperatures of WEGA plasmas. The typical averaged temperature of X2-discharges is between 5 and 10 eV, but the maximum temperature of central heated plasmas cannot be exactly measured with the Langmuir probe. On the one hand, the probe does not exactly hit the magnetic axis, and on the other hand, the probe itself disturbs the plasma parameters. For comparison, Figure 5.2b shows the density and temperature profile of an off-axis heated plasma with a magnetic flux density of  $B_0 = 460 \text{ mT}$  on the magnetic axis. The 28 GHz resonance is located at the inner side of the torus at an effective radius of  $r_{\text{eff}} = 6 \text{ cm}$  near to the last closed flux surface (LCFS).

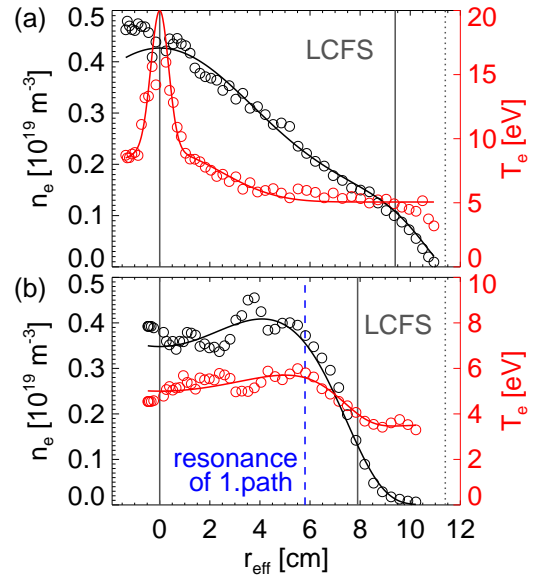


Figure 5.2: *Electron temperature and density profile of an X2-discharge with central resonance at  $B_0 = 500 \text{ mT}$  (a) and off-axis resonance with  $B_0 = 460 \text{ mT}$  (b). The fitted TRAVIS-profile is related to the LCFS given by the dotted line.*

<sup>1</sup>Because of multipath absorption, it was identified as bootstrap current rather than ECCD-current evidenced by the observed current reversal with magnetic field reversal [Chl10]. In the standard magnetic field configurations (+/+ or -/-) electrons with an energy  $> 200 \text{ keV}$  are only well confined if their velocity vector is directed opposite to the magnetic field. This effect, however, can be neglected because of no detectable suprathermal electrons.

The maximum density is typically determined by the X-cutoff density of the 28 GHz heating wave. For a magnetic field between  $B = 430$  mT and  $B = 520$  mT (lowest and highest value at  $B_0 = 460$  mT), it can be calculated to  $n_{X\text{-cut}} = (0.55 - 0.47) \cdot 10^{19} \text{ m}^{-3}$  according to the shown density profiles. To calculate the propagation of the heating beam as well as the resultant deposition, a TRAVIS profile function according to equation (2.26) is fitted to the measured data points in Figure 5.2. The determination of the total absorbed power with the aid of TRAVIS as well as other diagnostics is the topic of the next two subsections.

### 5.1.1.2 Power absorption

A direct determination of the absorbed power by comparing the stray radiation of the plasma-filled torus and the empty torus is not possible because of a high sensitivity on the resultant multimode pattern in the torus. The stray radiation can only be used for an estimation of the change of absorption during a discharge. The following evaluation process of the total absorption is depicted in Figure 5.3. The white rectangles correspond to the main calculation steps of this subsection and the green areas give the important result of each step.

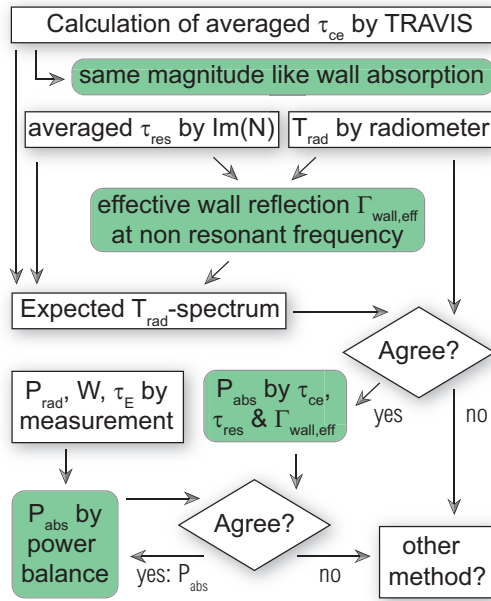


Figure 5.3: Flowchart for the determination of the absorbed power  $P_{abs}$ .

At first, the measured temperature and density profiles are used to determine the optical depth  $\tau_{ce}$  for electron cyclotron interaction with the aid of TRAVIS but the averaged absorption  $\zeta_{ce,ave} = 1 - \exp(-\tau_{ce,ave})$  over ten paths of the heating beam is of the order of the wall absorption. For this reason, the knowledge of the wall reflection coefficient  $\Gamma_{wall}$  is of great importance for the determination of the total absorption. The wall reflection coefficient  $\Gamma_{wall}$ , however, must be replaced by an effective wall reflection coefficient  $\Gamma_{wall,eff}$  because of an overall reduced reflection by ports guiding to sub volumes or areas covered with better absorbing materials. A calculation of  $\Gamma_{wall,eff}$  is difficult, but an indirect measurement is possible by the absolute calibrated radiometer. The effective wall reflection coefficient must fulfill the following relation between radiation temperature  $T_{rad}$  and electron temperature  $T_e$ :

$$T_{rad} = T_e \frac{1 - \exp(-\tau_{ce})}{1 - \Gamma_{wall,eff} \exp(-\tau_{ce})}. \quad (5.1)$$

The cyclotron absorption  $\zeta_{ce}$ , however, must be complemented with resistive absorption  $\zeta_{coll}$  caused by collisional interaction of the electrons. Especially for the frequencies corresponding to the plasma edge regions, the resistive absorption has the same magnitude like the cyclotron absorption. For this reason, the effective wall reflection coefficient can be determined for a frequency which has no cyclotron resonance within the plasma volume. If the whole spectrum of the measured radiation temperature agrees with the resultant spectrum calculated from equation (5.1) and the measured electron temperature profile, the total absorbed power  $P_{abs}$  can be determined with the aid of the calculated optical depth and the measured effective wall reflection coefficient  $\Gamma_{wall,eff}$ .

$P_{\text{abs}}$  can be validated by comparing it to the total radiated power  $P_{\text{rad}}$  and the stored energy  $W$  weighted with the energy confinement time  $\tau_E$  [Str11]:

$$\frac{dW}{dt} = P_{\text{abs}} - P_{\text{rad}} - \frac{W}{\tau_E} = P_{\text{trans}} - \frac{W}{\tau_E}. \quad (5.2)$$

The energy confinement time, however, is hard to measure in the case of the low temperature WEGA-plasmas with a stored energy of approximately 1 J. Another possibility for the determination of the absorbed power is the indirect measurement of the transported power  $P_{\text{trans}}$  across the last closed flux surface with the aid of heat waves during a modulation of the forward power. The radiated power  $P_{\text{rad}}$  is determined by the Au-bolometer.

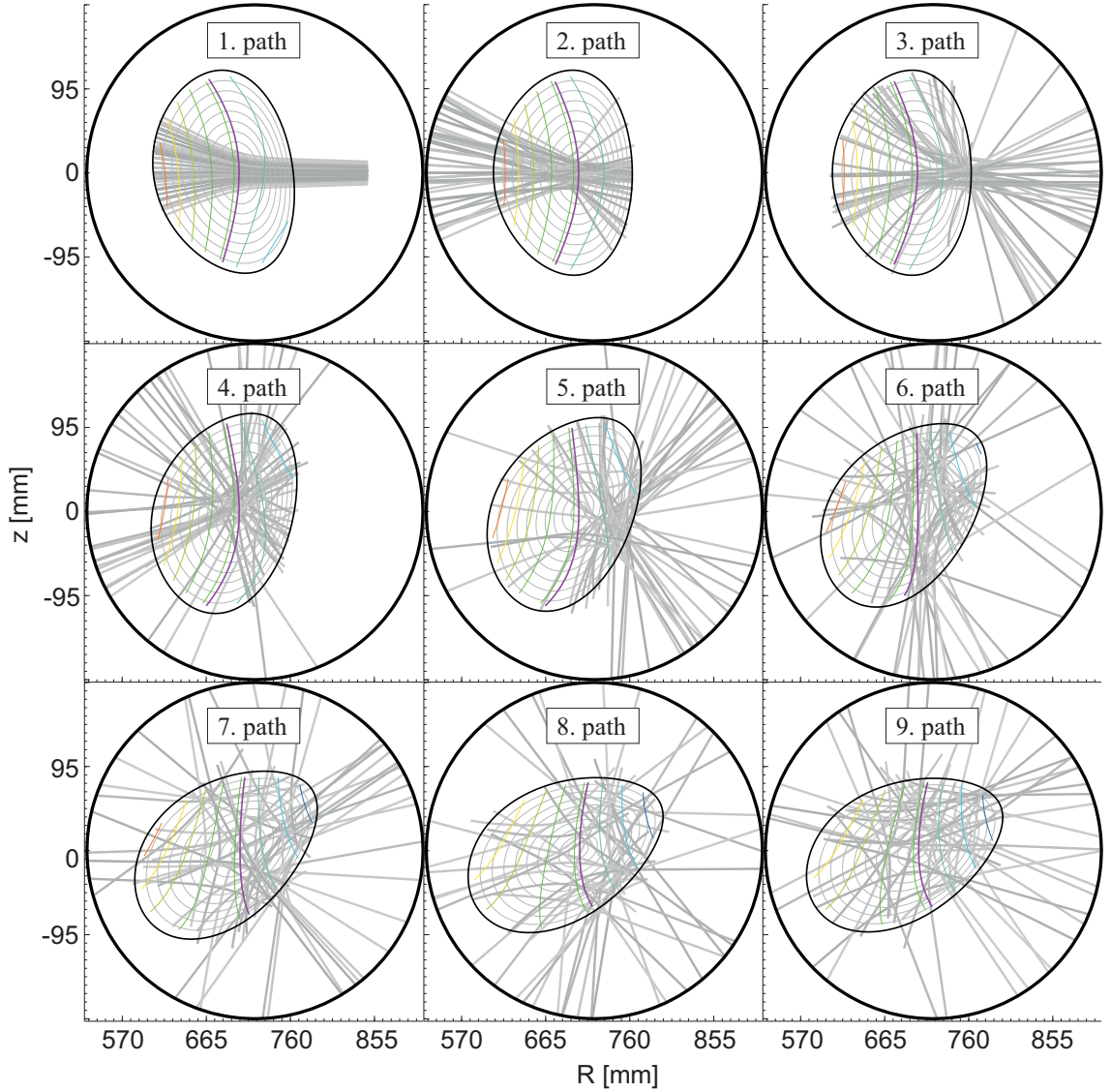


Figure 5.4: *TRAVIS* calculation of the first nine paths of an extraordinary polarized heating beam with perpendicular incidence with respect to the magnetic field lines. Shown are the poloidal cross-sections of the flux surfaces at the mean toroidal position where the particular rays propagate through the plasma. The colored lines are lines of constant magnetic field. The used temperature and density profiles are shown in Figure 5.2a with the resonance at the magnetic axis. The absorption of each path is shown in Figure 5.5.

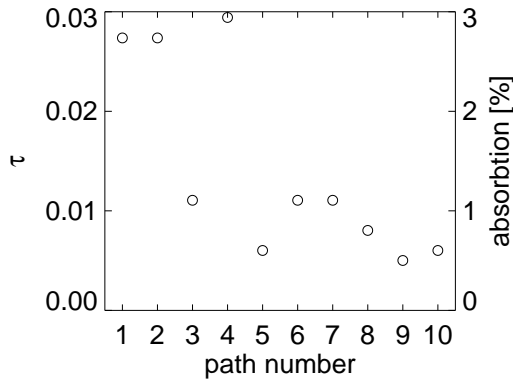


Abbildung 5.5: With TRAVIS calculated absorption depending on the paths shown in Figure 5.4.

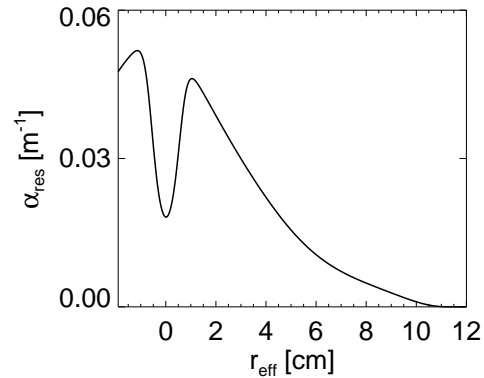


Abbildung 5.6: Resistive absorption coefficient  $\alpha_{res}$  of a 28 GHz X-wave for the plasma parameters shown in Figure 5.2a

**Calculation of Optical Depths  $\tau_{ce}$  and  $\tau_{coll}$**  The absorption during one pass of the heating beam is of the order 1%. For this reason, the beam is reflected at least 50 times because of the low absorption coefficient  $\zeta_{wall} < 1\%$  of the stainless steel wall of the torus<sup>2</sup>. Because of the complex reflection and propagation through the plasma, the absorption  $\zeta_{ce}$  or rather the optical depth  $\tau_{ce}$  must be calculated by TRAVIS. Figure 5.4 shows the first nine paths of the heating beam divided into 4 cycles with 10 rays each<sup>3</sup>. If the rays are focused on the small volume around the magnetic axis, the absorption per path is higher because of the higher temperature around the resonance. The rays uniformly permeate the whole plasma cross section after 4 reflections leading to a reduced absorption as shown in Figure 5.5. This is only valid for perpendicular incidence, however. Already small deviations of some degrees or higher density gradients can lead to a less concentrated absorption after the first path. Nevertheless, the calculated absorption of the fifth to the tenth path is used to determine an averaged value of  $\zeta_{ce,ave} = 0.8\%$  per path. This must be taken as an upper limit because of possible polarization changes during propagation and reflection that are disregarded by TRAVIS. The absorption of the first four paths is added up to an initial absorption  $\zeta_{ce,init} = 9.3\%$  which is used later in equation (5.4) without consideration of the much less wall absorption.

Because of the low average temperature in the plasma edge region, also the resistive damping must be considered as additional damping mechanism. The absolute value of resistive absorption in the volume is relatively low compared to the electron cyclotron absorption in the resonant volume. The integrated absorption coefficient along one path, however, can increase to the same magnitude which is reached by electron cyclotron absorption. For the conditions of the central heated plasma, Figure 5.6 shows the resistive absorption coefficient  $\alpha_{coll} = -2\Im(\mathbf{k})$  [Bek66] of the extraordinary wave calculated from the imaginary part of the wave vector  $\mathbf{k}$ . The low absorption in the center results from the high temperature around the cyclotron resonance. The resistive absorption  $\zeta_{coll}$  of one path depends on the path length and thus on the angle to the magnetic field lines. Ordinary and extraordinary mode are mixed by the multiple reflections so that an averaged value of  $\zeta_{coll}(28\text{ GHz}) \approx 0.2\%$  per path can be

<sup>2</sup>A value of  $\zeta_{wall} \approx 1\%$  results for an angle averaged reflection of a 140 GHz microwave beam at stainless steel [Laq13]. The skin depth is inversely proportional to the root of the wave frequency so that the wall absorption of a 28 GHz microwave beam is much smaller than 1%.

<sup>3</sup>For the calculation of the absorbed power, summarized in Figure 5.5, a higher resolution with 4 cycles and 20 rays each was used.

determined for perpendicular propagation. The overall absorbed power can be calculated by equation (3.2) after insertion of  $\tau_{\text{path}} = \tau_{\text{ce,ave}} + \tau_{\text{coll}}$  and the effective wall reflection coefficient  $\Gamma_{\text{wall,eff}}$ .

**Determination of  $\Gamma_{\text{wall,eff}}$  by comparison of measured and calculated  $T_{\text{rad}}$  spectrum** The expected radiation temperatures of 1 eV must be clearly distinguished from parasitic resonances of the gyrotron. Figure 5.8 shows the averaged time traces of all radiometer channels during a complete switch-off of the gyrotron. Especially the fourth, the fifth and the twelfth channel show too high radiation temperatures with the same sharp drop like the gyrotron forward power<sup>4</sup>. The remaining channels detect radiation levels of less than 1 eV with different noise levels dependent on the radiometer sensitivity.

A calibrated spectrum like in Figure 5.7 can only be given for the gyrotron off times. The relatively high radiation temperatures, however, must be attributed to multiple reflections. For this reason, the detection frequency was assigned to an effective radius  $r_{\text{eff}}$  by averaging over a set of sightlines in the  $z = 0$  plane which were calculated by the w7-code<sup>5</sup>. The uncertainty of  $r_{\text{eff}}$  is determined by the standard deviation as well as the frequency width of each channel. Regarding the uncertainty of the temperature, an edge in the emission can be identified in the vicinity of the LCFS at the high field side. This as well as the expected high radiation temperature of the sixth channel ( $f_{28.5} = 28.5 \pm 0.4$  GHz) shows at first that the electron cyclotron emission is responsible for the microwave emission of the plasma. The finite emission in the tenth channel ( $f_{35.0} = 35.0 \pm 0.55$  GHz) and the monotonic increasing background emission with decreasing frequency demonstrate a Bremsstrahlung part of the emission as it was predicted also for resonant heated WEGA plasmas [Sta08; SHH<sup>+</sup>09]. An explanation of the background emission by a Doppler or relativistic frequency shift can be excluded<sup>6</sup>. For this reason, the tenth channel is used to calculate the effective reflection factor by equation (5.1) assuming an averaged electron temperature  $T_{\text{coll}} = 5$  eV for the resistive emission.

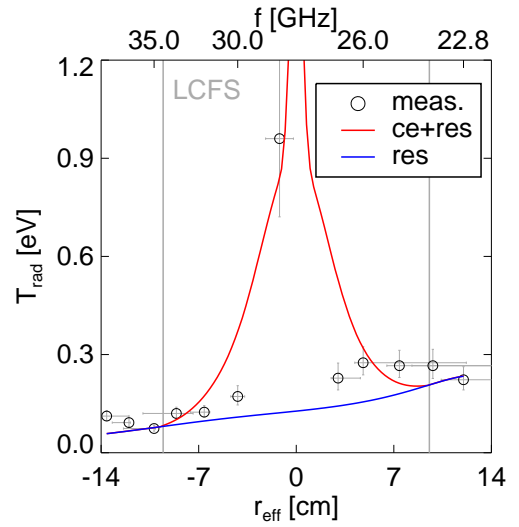


Figure 5.7: Measured radiation temperature  $T_{\text{rad}}$  of the microwave radiometer channels vs. their mid-frequency  $f_{\text{mid}}$  as well as the mean effective radius of the second harmonic resonance. Solid lines represent the expected Bremsstrahlung (resistive) and additionally combined with the X2-emission.

<sup>4</sup>Figure 5.56 in section 5.3 shows the one magnitude higher power level of parasitic resonances in the fourth and the fifth channel making the microwave measurement at such poorly absorbing and poorly emitting plasma relatively difficult. Probably the twelfth channel detects a parasitic resonance in the frequency range 40.0 – 40.3 GHz but the available equipment allows no measurement of the spectrum for frequencies between 40 GHz and 50 GHz.

<sup>5</sup>A more accurate determination can be done by averaging the volume contributions of  $r_{\text{eff}}$  on the whole resonant surface in the torus, that is proposed to include as option into MCViewer.

<sup>6</sup>Soft X-ray emission was not detected by the PHA so that the maximum energy is of the order 0.5 keV. Therefore, the generation of electrons with some hundreds eV is probable but not detectable. For very low neutral gas pressures or hydrogen as gas type soft X-ray emission is detectable indicating a suprathermal component.

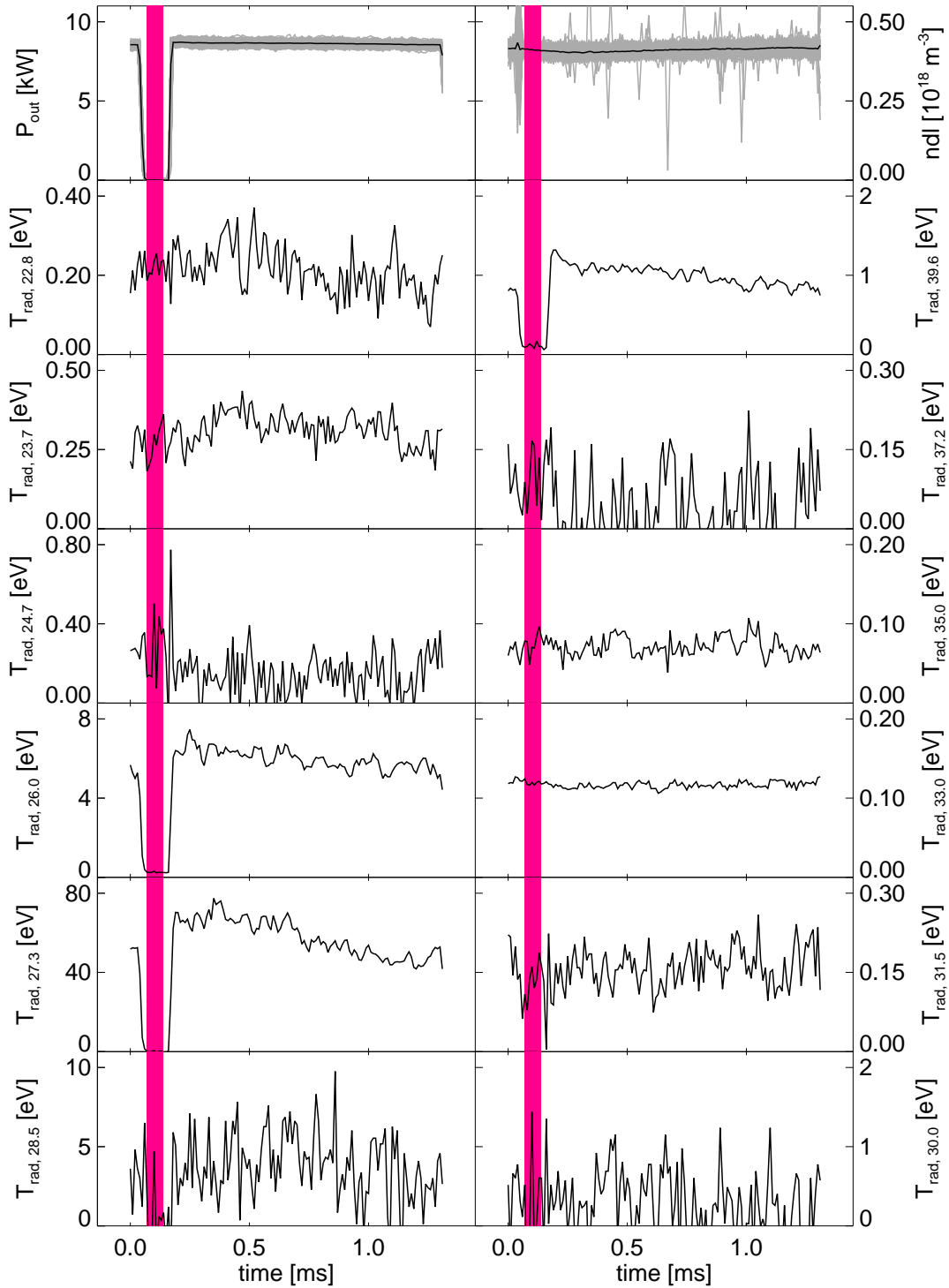


Figure 5.8: Averaged time traces of the radiometer channels during gyrotron power modulation with a frequency of  $f_{\text{mod}} = 788$  Hz and 90 % duty cycle. The helium plasma was centrally heated by X2 at a gas flux of  $\Gamma = 7$  sccm. The raw signals are shown for the gyrotron power  $P_{\text{out}}$  and the line integrated density  $\text{ndl}$ . The gyrotron was operated in an non-optimized mode with parasitic resonances in the 4. channel ( $f_{26.0} = 26.0 \pm 0.3$  GHz), the 5. channel ( $f_{27.3} = 27.3 \pm 0.3$  GHz) and the 12. channel ( $f_{39.6} = 39.6 \pm 0.7$  GHz). The marked off-times are used for the spectrum in Figure 5.7.

In contrast, the necessary averaged resistive absorption of  $\zeta_{\text{coll}}(35 \text{ GHz}) = (0.07 \pm 0.04) \%$  was calculated by a line integration of the local resistive absorption coefficient  $\alpha_{\text{coll}}$ . The uncertainty of  $\zeta_{\text{coll}}$  is defined by the different values for the ordinary and extraordinary mode and results in the same uncertainty for the effective wall reflection coefficient:

$$\Gamma_{\text{wall,eff}} = (95.5 \pm 2.5) \%$$

With this value the expected radiation temperature  $T_{\text{rad}}$  was calculated for the whole detectable frequency range under consideration of cyclotron and resistive absorption. Regarding the cascading absorption and emission of the different mechanisms as well as the wall reflection, the overall radiation temperature can be deduced to<sup>7</sup>

$$T_{\text{rad}} = \frac{T_{\text{ce}}(1 - e^{-\tau_{\text{ce}}})e^{-\tau_{\text{coll}}} + T_{\text{coll}}(1 - e^{-\tau_{\text{coll}}})}{1 - \Gamma_{\text{wall,eff}}e^{-\tau_{\text{coll}} - \tau_{\text{ce}}}}. \quad (5.3)$$

The resistive part of the spectrum, also shown in 5.7, fits approximately with the measured radiation temperatures near the LCFS on the low and high field side<sup>8</sup>. The higher radiation temperatures within the LCFS are determined by the combined resistive and electron cyclotron emission. The optical depth  $\tau_{\text{ce}}$  is also calculated by TRAVIS, but the third harmonic emission in the twelfth and eleventh channel ( $f_{37.2} = 37.2 \pm 0.7 \text{ GHz}$ ) cannot be reproduced. A reason could be a non thermalized electron component of some hundred eV. Nevertheless, the determined effective wall reflection coefficient as well as the optical depths of resistive and electron cyclotron absorption can be used to calculate the overall absorption to

$$P_{\text{abs}} = P_{28} \cdot [\zeta_{\text{ce,init}} + (1 - \zeta_{\text{ce,init}}) \zeta_{\text{multi}}] = P_{28} \cdot \begin{pmatrix} 26\% & +13\% \\ & -5\% \end{pmatrix} = \begin{pmatrix} 2.0 & +1.0 \\ & -0.4 \end{pmatrix} \text{ kW}. \quad (5.4)$$

A main source of error is the non-consideration of the non-thermalized electrons with a resultant too low calculated optical depth  $\tau_{\text{ce}}$ . For this reason, the power  $P_{\text{trans}} = P_{\text{abs}} - P_{\text{rad}}$  transported across the last closed flux surface is analyzed which intrinsically takes into account the suprathermal electron component in the plasma center<sup>9</sup>.

**Measurement of  $P_{\text{trans}}$  for the analysis of the power balance** The radiated power of the considered discharge can be determined to  $P_{\text{rad}} = (1.7 \pm 0.3) \text{ kW}$ . The radial transported power  $P_{\text{trans}}$ , being a combination of diffusive and convective transport, must be determined via [Por98]

$$P_{\text{trans}} = -n_e \chi \nabla T_e - \frac{5}{2} T_e (D \nabla n_e + n_e v). \quad (5.5)$$

The first term constitutes the thermal diffusive transport, characterized by the thermal diffusivity  $\chi$ . The second term is characterized by the radial particle diffusivity  $D$  and the particle convection velocity  $v$ , although the latter one should be ignored in the following estimate. The particle diffusivity was numerically determined to  $D = 3.5 \text{ m}^2/\text{s}$  for high density OXB-discharges [ZBG<sup>+</sup>11] treated in subsection 5.1.3. Here, a 1D particle diffusion equation was solved numerically for different radially constant values of  $D$ .

<sup>7</sup>For  $\tau \ll 1$  it does not matter if the electron cyclotron layer is in between the resistive absorption zone or in the edge region of the plasma.

<sup>8</sup>For frequencies lower 28 GHz the extraordinary wave is reflected by the plasma. Nevertheless, a resistive damping takes place, but a calculation is challenging because of the many further assumptions required.

<sup>9</sup>Section 5.2.2 will show that a suprathermal electron component with an averaged energy of some keV generated in the plasma center thermalizes with the bulk plasma before it can reach the LCFS.

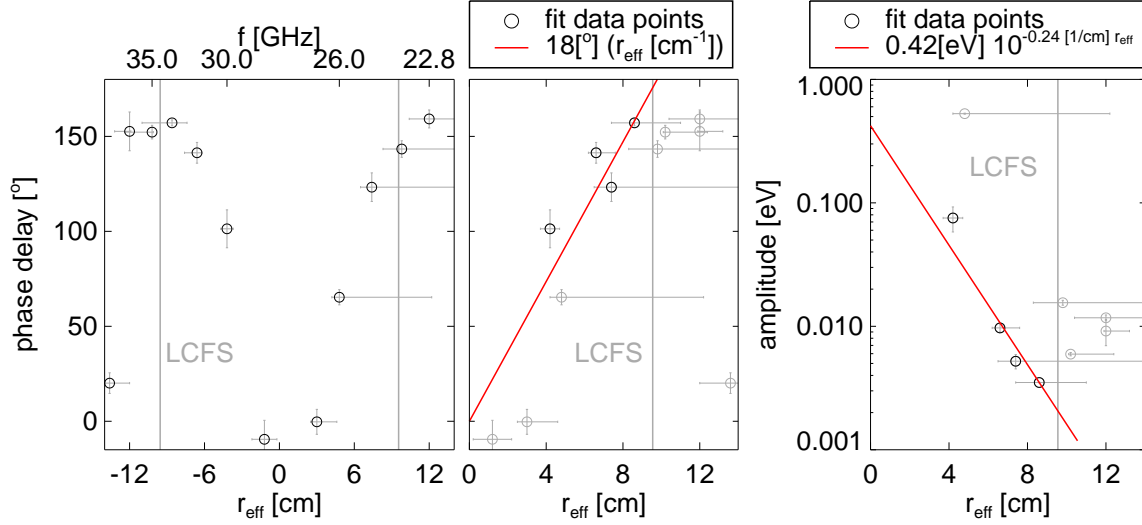


Figure 5.9: Phase delay of the radiometer channels to the forward power as well as their cross spectrum amplitude for a modulation frequency of  $f_{\text{mod}} = 788$  Hz. Both are interpolated by linear functions to determine the derivations  $\partial\varphi/\partial r_{\text{eff}}$  and  $\partial A/\partial r_{\text{eff}}$ . The gray shaded data points are not used for the fit.

The resultant density profile as well as emissivity profile were compared with the measurements [ZBG<sup>+</sup>11]. Especially in the edge region nearby the LCFS the calculated density gradient  $\nabla n_e$  fits well with the measured one, which is also similar to the edge density profile shown in Figure 5.2a. For this reason, the same  $D$ -value is taken to calculate the power  $P_{\text{trans}}$  transported through the LCFS by equation (5.5). The thermal diffusivity  $\chi$  can be determined from the phase delay and amplitude dependence of a heat pulse which propagates perpendicular to the flux surfaces during a fast modulation of the forward power<sup>10</sup>. For a simplified cylinder geometry an analytical solution for  $\chi$  can be obtained from the electron thermal transport equation [JMDG91]:

$$\chi = \frac{3\omega_{\text{mod}}}{4 \frac{\partial\varphi}{\partial r_{\text{eff}}} \left( \frac{\partial A}{A \partial r_{\text{eff}}} + \frac{1}{2r_{\text{eff}}} \right)}. \quad (5.6)$$

The electron cyclotron emission detectable, with the microwave radiometer, depends on the temperature. The measurement shows the expected dependence on the effective radius as already shown in Figure 5.7. Furthermore, the line integrated density is constant during a modulation cycle (see Figure 5.8) because of a relatively high particle confinement time of the order  $\tau_p = O(10$  ms). The phase delay of the heat pulse can be evaluated by the coherence spectrum analysis of the modulated signal time series and the forward power. Figure 5.9 shows the phase delay and cross spectrum amplitude for a modulation time of 1.6 s under optimal gyrotron conditions. The typically increasing time shift with higher effective radius reaches a maximum of  $\Delta t = 0.5$  ms at the LCFS, which cannot be identified with the confinement time  $\tau_E = W/P_{\text{trans}}$ . The phase delay and amplitude dependence versus the absolute  $r_{\text{eff}}$  is approximated with a linear function also shown in Figure 5.9. This is the most reliable approach because of the unusable data points at low  $r_{\text{eff}}$ . The central channels show untypically high cross spectrum amplitudes also under optimal gyrotron conditions

<sup>10</sup>The modulation time period should be much shorter than the energy confinement time to preserve the temperature and density gradients which determine the energy transport perpendicular to the flux surfaces.

so that the use for the fit would be doubtful. The thermal diffusivity in the vicinity of the LCFS becomes  $\chi = (2.3 \pm 0.5) \text{ m}^2/\text{s}$ . In principal, the same value was obtained giving more confidence in using the same particle diffusion coefficient  $D$ . After insertion in equation (5.5), the transported power in the edge region can be calculated to  $P_{\text{trans}} = (0.5 \pm 0.2) \text{ kW}$ . The relatively high error results from the uncertainty in the determination of the temperature and density gradient in the edge region as well as the preceding errors. The sum of radiated power and transmitted power leads to a absorbed power of  $P_{\text{abs,req}} = (2.2 \pm 0.5) \text{ kW}$ . Furthermore, the energy confinement time can be estimated to  $\tau_E \approx (1 \pm 0.5) \text{ ms}$  assuming a stored energy of  $W = (0.5 \pm 0.1) \text{ J}$  which was calculated by integration of the temperature and density profiles via equation (1.1). The determined energy confinement time is only slightly smaller than the time of a modulation period, but the numerical simulation of the electron energy transport equation for the case of WEGA showed only slightly changes of the thermal diffusivity when the modulation period is further increased [ZGL<sup>+</sup>12]<sup>11</sup>.

It becomes apparent that both methods via the direct calculation of the absorbed power and via the measurement of the transported power yield similar values. But a quantitative analysis of different X2-discharges is nearly impossible. Although  $P_{\text{abs,req}}$  lies in the uncertainty range of the calculated  $P_{\text{abs}}$ , a possibly to low calculated  $\Gamma_{\text{wall,eff}}$  or  $\tau_{\text{ce}}$  has to be discussed. The ratio of radiated and absorbed power, however, is at least  $P_{\text{rad}}/P_{\text{abs}} \approx 77\%$  so that the absorbed is mainly defined by the radiated power. For this reason, the determination of the transported power with the aid of the stored energy and an assumed energy confinement time of  $\tau_E \approx 1 \text{ ms}$  leads also to a good estimate for the absorbed power.

To sum up, the determination of the absorbed power by a calculation of the electron cyclotron absorption generates values of the right magnitude and reproduces the observed poor X2-heating efficiency at low temperature plasmas. The use of an absolutely calibrated microwave radiometer for the determination of the effective wall reflection coefficient turned out to be indispensable, even though the used orientation and polarization of gyrotron and radiometer antenna should be same. It was not possible to exactly satisfy the latter condition because of different antenna types of the ECE and the heating system. This as well as the uncertainty of the averaged resistive absorption are the main sources of error. Furthermore, the heat pulse analysis and the power balance can lead to a different transported power depending on the transport mechanism. A detailed description can be found in [Car95]. A more reliable possibility for the determination of absorbed power as well as the confinement time in the case of WEGA is described in the next subsection.

### 5.1.1.3 Improvement of analysis

The radiated power  $P_{\text{rad}}$ , part of the power balance in equation (5.2), only can be determined by the bolometer diagnostics with a relative uncertainty of at best 20% [Zha13]. A more accurate determination of the other quantities of equation (5.2) is not possible. As already estimated, the radiated power dominates the power balance, and the convective part can play at most an equivalent role. If the plasma energy can be associated with the radiated power, the time dependent equation (5.2) can be solved with the AXUV-bolometer data only. This formalism requires some simplifying estimates but has the advantage of an intrinsic consistency of the determined values.

<sup>11</sup>The measured phased delays for different modulation frequencies are compared with the simulation leading to almost the same thermal diffusivity [ZGL<sup>+</sup>12].

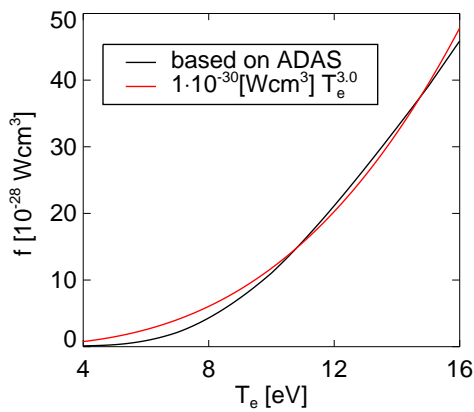


Figure 5.10: *Interpolation of the radiative power loss coefficient of He in the temperature range  $T_e = (8...16)$  eV (processed ADAS-data adapted from [Zha13])*

The critical quantities will be the initial values of plasma energy  $W_0$  and radiated power  $P_{\text{rad},0}$ . The latter one is a volume integration of the local emissivity  $\varepsilon(r_{\text{eff}}) = n_e^2(r_{\text{eff}}) \times f(T_e(r_{\text{eff}}))$  consisting of line emission from excitation (plt), radiative recombination + dielectronic stabilization + recombination cascade (pr) and Bremsstrahlung (pb) [Zha10]. As addressed in the section before, the particle diffusion equation was already solved numerically for OXB-discharges [ZBG<sup>+</sup>11]. It was shown that the radiated power of OXB-plasmas is dominated by the emissivity of the first ionization state, whose temperature dependent coefficient  $f(T_e)$  is shown in Figure 5.10. Because of the similar temperature in X2-plasmas, this result should also be applicable to the discharge of Figure 5.2a. The temperature dependence of  $f(T_e)$  in the relevant temperature range  $T_e = (8...16)$  eV can be determined to  $f(T_e) = C_{\text{rad}} T_e^\alpha$  with  $\alpha \approx 3.0$ . This leads to much higher relative radiation losses in the center compared

to the plasma edge. This in contrast to high temperature fusion plasmas, because the total radiation loss of a homogeneous plasma decreases for temperatures higher 20 eV so that almost the whole radiation is generated around the LCFS. The overproportional  $T_e$  – dependence of the coefficient  $f(T_e)$ , however, is a happenstance from the diagnostic point of view because of a high sensitivity to changes in the local plasma energy. The total plasma energy  $W$  is a summation of  $r_{\text{eff}}$ -shells with constant local temperature and density and can be expressed by means of the radiated power of a shell  $P_{\text{rad},j} = V_j n_e^2 C_{\text{rad}} T_e^\alpha$ :

$$W(t) = \frac{3}{2} k_B \sum_{j=1}^N V_j n_{e,j} T_{e,j}(t) = \frac{3}{2} k_B \sum_{j=1}^N V_j^{1-1/\alpha} n_{e,j}^{1-2/\alpha} C_{\text{rad}}^{-1/\alpha} P_{\text{rad},j}^{1/\alpha}(t). \quad (5.7)$$

The width or rather the volume  $V_j$  of each shell  $j$  can be chosen in such a way that the radiated power of each shell  $P_{\text{rad},j} = V_j n_e^2 C_{\text{rad}} T_e^\alpha$  is equal. Each of the  $N$  shells should have a constant temperature so that different shells can also have the same temperature.

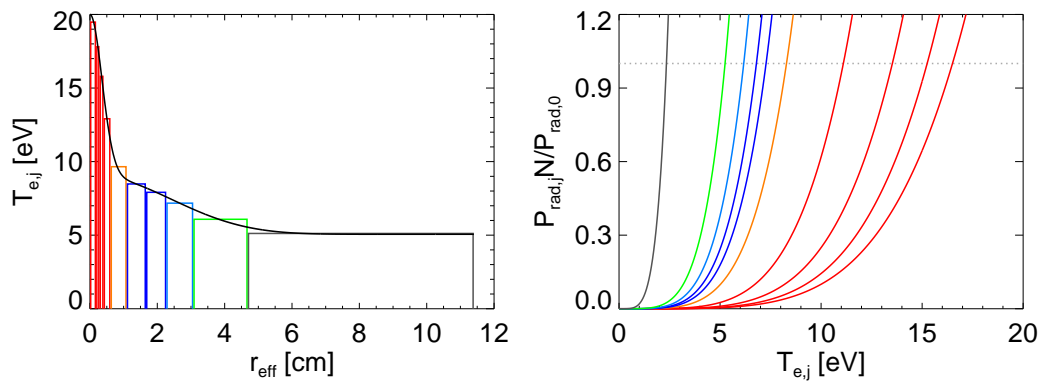


Figure 5.11: *Example of a subdivided profile with the same radiated power per shell (a) and the resultant dependence of the radiated power on the temperature (b). The sub-division into shells can be increased in any order.*

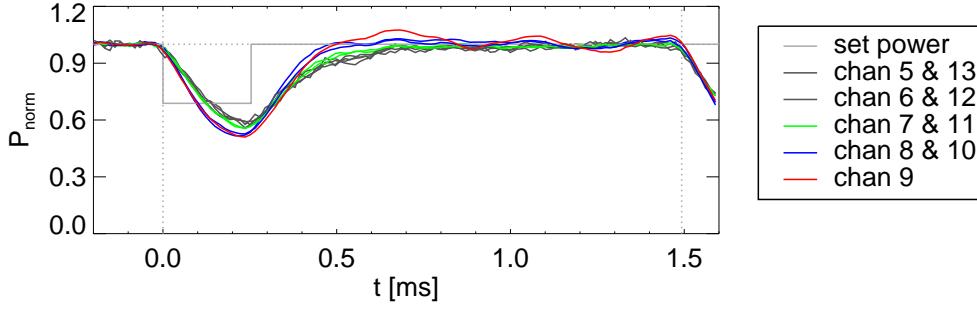


Figure 5.12:  $10\times$  averaged time traces of the AXUV-channels, looking on the plasma cross section, in the case of a modulated gyrotron power with a frequency of 672 Hz. The gyrotron set point is shown in gray with an on-off power ratio of 0.69 and an off time of 17%.

For an initial steady state plasma at  $t_0$ , equation (5.7) can be simplified to

$$W(t_0) = P_{\text{rad}}^{1/\alpha}(t_0) \frac{3k_B}{2N} \sum_{j=1}^N V_j^{1-1/\alpha} n_{e,j}^{1-2/\alpha} C_{\text{rad}}^{-1/\alpha} = P_{\text{rad}}^{1/\alpha}(t_0) \sum_{j=1}^N C_{W,j} = P_{\text{rad}}^{1/\alpha}(t_0) C_W. \quad (5.8)$$

The scaling factor  $C_W = \sum_{j=1}^N C_{W,j}$  is defined by the initial values  $W_0$  and  $P_{\text{rad},0}$ . Figure 5.11a shows a possible sub-division for the profile of the centrally heated plasma of Figure 5.2a. For each shell the temperature dependency of the coefficient  $f(T_e(r_{\text{eff}}))$  can be transformed to a temperature dependence of the radiated power  $P_{\text{rad},j}$  with the aid of the scaling factor  $C_{W,j}$  which depends on the volume  $V_j$  and the density  $n_{e,j}$ . A decrease of the radiated power in an inner shell is caused by a higher temperature decrease than in the outer shells as shown in Figure 5.11b. Qualitatively the same behavior is expected by inducing a temperature perturbation by modulation of the local absorbed heating power. For a detailed analysis of the time dependence of each shell during a modulation period, the diffusive heat transfer equation must be solved for different estimated radial dependencies of the heat diffusion coefficient  $\chi(r_{\text{eff}})$ . But for the actual case the time traces of the different AXUV-channels have approximately the same behavior as shown in Figure 5.12 for a modulation frequency of  $f_{\text{mod}} = 672$  Hz. During a modulation period the density does not change as shown in Figure 5.8 so that the variation in the radiated power is caused by the temperature. This experimental indication motivates the assumption that equation is also valid for the time evolution of the investigated modulation period. But the time dependence of the radiated power  $P_{\text{rad}}$  must be expressed by a normalized quantity in order that the radiated power  $P_{\text{rad},0}$  itself can be used as fit parameter. By using  $\bar{U} = (P_{\text{rad}}/P_{\text{rad},0})$  in equation (5.8) the plasma energy  $W$  can be substituted by the normalized radiated power  $\bar{U}$ :

$$\frac{\partial W(t)}{\partial \bar{U}} = \frac{\partial}{\partial \bar{U}} \left( \bar{U}(t)^{1/\alpha} W_0 \right) = \frac{W_0}{\alpha} \bar{U}(t)^{1/\alpha-1}. \quad (5.9)$$

After insertion in the power balance equation (5.2), the time dependence of the radiated power can be also expressed as ordinary differential equation

$$\frac{d\bar{U}}{dt} = \frac{\alpha}{W_0} \bar{U}^{1-\frac{1}{\alpha}} \left( P_{\text{abs}} - P_{\text{rad},0} \bar{U} - \frac{W_0}{\tau_E} \bar{U}^{\frac{1}{\alpha}} \right) = \frac{\alpha}{W_0} \bar{U} \left( P_{\text{abs},0} F - P_{\text{rad},0} \bar{U}^{1-\frac{1}{\alpha}} - \frac{W_0}{\tau_E} \right) \quad (5.10)$$

The time dependent function  $F(t)$  describes the step function between 1 and the modulation power ratio as indicated by the gray shaded line in Figure 5.12.

The local absorbed gyrotron power  $P_{\text{abs}}$  is approximately proportional to the electron temperature because of the low optical depth  $\tau_{\text{ce}}$ . It was assumed that the local electron temperature behaves in almost the same manner as the averaged shell temperature  $T_{\text{e},j}(t)$  leading to  $P_{\text{abs}} = P_{\text{abs},0} F \bar{U}^{1/\alpha}$ . Figure 5.13 shows the line of sight weighted summation of the 16 AXUV channels, shown in Figure 5.12, and the best fit of equation (5.10). The latter one leads to a confinement time of  $\tau_{\text{E}} \approx 0.9$  ms and  $P_{\text{rad}}/P_{\text{abs}} \approx 83\%$  reproducing the results of the preceding subsection.

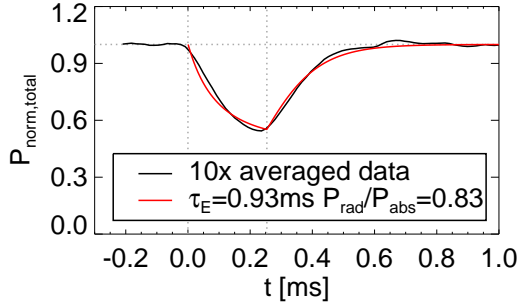


Figure 5.13: Total radiated power of the averaged AXUV-channels of Figure 5.12 fitted with equation (5.10).

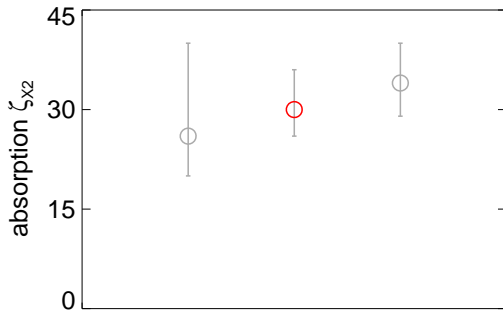


Figure 5.14: Independently determined absorption values  $\zeta_{X2}$  with the highlighted final value of about 30%.

If the radiated power is also used as fit value, the result is in accordance with the measured value in consideration of an error of at least 10%. The total absorbed power is calculated to

$$P_{\text{abs}} = P_{28} \cdot \left( \begin{array}{c} 34\% \quad +6\% \\ -5\% \end{array} \right).$$

The error results from a variation of the exponent by  $\pm 0.5$  being the most critical parameter. The main part of the radiated power is produced by the plasma regions with the highest temperature so that the method necessitates a modification of the exponent  $\alpha$  dependent on the maximum temperature. For example, the best fit of the emissivity factor  $f(T_e(r_{\text{eff}}))$  between  $T_e = (4 \dots 10)$  eV is achieved for  $\alpha \approx 4.6$ . But parametric scans with different modulation frequencies and also different power ratios should lead to a reliable determination of energy confinement time, radiated and absorbed power.

Although this method is based on the phenomenological approximation  $dP_{\text{abs}}/dt = NdP_{\text{abs},j}/dt$ , it leads to the same results as the more uncertain determination of the absorbed power corrected by the effective wall reflection coefficient. But it corroborates at least the determined values of subsection 5.1.1.2 with a reduction of the error by a factor  $1/\sqrt{2}$ . Figure 5.14 illustrates the combination of both independently determined values to a total X2-absorption of

$$\zeta_{X2} = 30\% \begin{array}{c} +8\% \\ -4\% \end{array}.$$

Further improvement of the analysis is possible by a reconstruction of the emission profile for each time point of one modulation period. This leads probably to a more accurate determination of the time dependence of the total radiated power. Additionally, the coefficient  $f(T_e)$  shown in Figure 5.10 can be used in combination with the measured equilibrium temperature profile to determine an expected emission profile. The comparison with the reconstructed emission profile can lead to a confirmation or correction of the coefficient  $f(T_e)$ .

### 5.1.2 Non-resonant Heating

As explained in the previous section it is not possible to reach the 28 GHz-O-cutoff-density in helium using only the gyrotron. For this purpose, the 2.45 GHz-magnetron is used to further increase the density and reach the overdense plasma state with the possibility of heating via electron Bernstein waves.<sup>12</sup> This heating process by the magnetron is often called non-resonant heating because of the lack of electron cyclotron resonances in the plasma volume in the case of high field operation ( $B_0 \approx 0.5$  T). Non-resonant heating can also be reached with the magnetron alone by a ramping up of the magnetic field, as shown in Figure 5.15. At WEGA as well as similar machines like the TJ-K torsatron<sup>13</sup>, this heating method has been used since 2008, but was not fully understood until now. Although it is not the central topic of this thesis, some possible coupling mechanisms are discussed here.

#### 5.1.2.1 Discharge scenario

Figure 5.15 shows the time traces of the most important parameters of a non-resonant argon discharge. This gas type is used for these explanations due to the higher availability of experimental data and further investigations concerning microwave emission [Sta08; SHH<sup>+</sup>09]. The same characteristic time traces are also achieved in helium in the case of an appropriate higher gas inlet. In the following the discharge scenario is described by means of characteristic time points visualized by gray shaded vertical lines which are numbered at the top of the Figure.

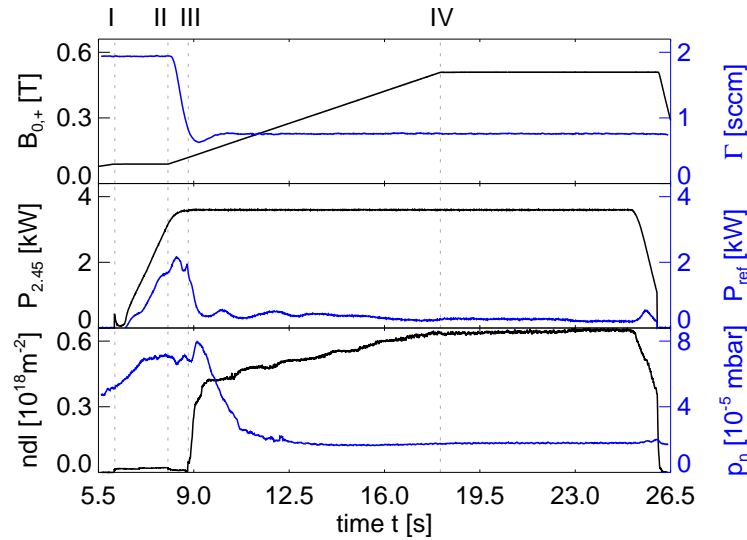


Figure 5.15: *Time traces of a standard non resonant heated argon discharge. From top to bottom: the magnetic flux density  $B_0$  on the magnetic axis & the gas flow  $\Gamma$ , the forward power  $P_{2.45}$  of the 6kW-Magnetron & their reflected power  $P_{ref}$  and the line integrated electron density  $ndl$  & the neutral gas pressure  $p_n$ . The time points indicated on the vertical lines are described in the text.*

<sup>12</sup>Figure 5.29 in subsection 5.1.3.1 shows the combined use of the resonantly heating gyrotron and the magnetron, which was switched on later.

<sup>13</sup>The TJ-K torsatron is a stellarator-like experimental device at the Institute for Plasma Research (iPF) at Stuttgart University and is slightly smaller than WEGA.

- I Start of resonant heating at the first harmonic with a magnetic flux density of  $B_0 = 87.5 \text{ mT}$  on the magnetic axis and increasing heating power to  $P_{\text{ECRH}} = 3.6 \text{ kW}$ <sup>14</sup>. The gas inlet is set to  $\Gamma = 2 \text{ sccm}$  resulting in a neutral gas pressure of up to  $p_n = 7 \cdot 10^{-5} \text{ mbar}$ . The reflected power is about half of the forward power.
- II Start of magnetic field ramp to half Tesla operation and decrease of the gas inlet to the intended level of  $\Gamma = 0.8 \text{ sccm}$ . The previous higher gas level is necessary to overcome the density drop at the beginning of the magnetic field ramp.
- III With a magnetic flux density of  $B_0 = 116 \text{ mT}$  on the axis the density starts to increase rapidly to a value of  $ndl = 0.4 \cdot 10^{18} \text{ m}^{-2}$ , 20 times that of resonant magnetron heating. At the same time the reflected power decreases to about a tenth of the forward power.
- IV Density increases continuously until the end of linear magnetic field ramp. The behavior between point II and IV is consistent with the  $B$ -dependence of the density. A discharge with constant gas pressure at  $p_n \approx 1.7 \cdot 10^{-5} \text{ mbar}$  shows the density developing in the same way.

### 5.1.2.2 Power Balance

In the previous section a multipath model was used to determine the balance between the total power absorption by the wall and the plasma. In the present case, however, the ray approximation is not valid because the wavelength is of the order of the torus dimension. Of course, the abrupt density increase indicates a fundamental change of the absorption mechanisms, but the inclusion of wall reflection and absorption is necessary to distinguish between a direct efficient conversion mechanism of the incident wave and a multipath absorption. The resonator model used is shown in Figure 5.16. Here, the torus acts as a resonator fed by the magnetron with an adjustable coupling factor. The coupling is optimized by a stub tuner transforming the waveguide impedance to the end of the transmission line. In the resonator 'Torus' there is a second resonator 'Plasma' that is coupled via tunneling or direct conversion processes in the plasma edge layer. Both resonators suffer power losses given by the ohmic dissipation in the torus wall and the damping and absorption of the converted plasma wave.

A similar model is also used to characterize the stray radiation at the Wendelstein 7-X stellarator with a heating frequency of 140 GHz [Laq10]. Here, the stray radiation is considered as a gas diffusing in all directions. In the case of electromagnetic radiation, pressure is replaced by the energy flux density  $p_T$  calculated by the Poynting vector. The equipartition of the injected power  $P_{2,45}$  is achieved through multiple reflections at the torus wall. A small part is absorbed by the wall surface  $A_T$  with the frequency dependent absorption factor  $\eta_T$ . A further loss term in the 'Torus' resonator is defined by the conversion in a plasma wave with a coupling factor  $\zeta_P$ . This leads to an energy flux  $p_T A_P \zeta_P$  through the plasma surface  $A_P$  to the 'Plasma' resonator. The 'Plasma', however, should be filled with a uniformly distributed energy flux  $P_P$  because of its lack of a specific absorption surface area. The power balance in the plasma should be given by a volume averaged absorption factor  $\langle \alpha \rangle$  and the same coupling factor  $\zeta_P$  that specifies the energy flux  $P_P \zeta_P$  back to the 'Torus' resonator. If both resonators are at equilibrium, the power balance in the 'Plasma' resonator will be given by

$$p_T A_P \zeta_P = P_P \zeta_P + P_P \langle \alpha \rangle. \quad (5.11)$$

---

<sup>14</sup>The plasma is also overdense and sustained by 2.45 GHz electron Bernstein waves even though not optimized. An extensive discussion of resonant magnetron heating at WEGA can be found in the PhD-thesis of Yurij Podoba [Pod06] as well as subsequent papers [PLW<sup>+</sup>07; LMO<sup>+</sup>09; PLU<sup>+</sup>09].

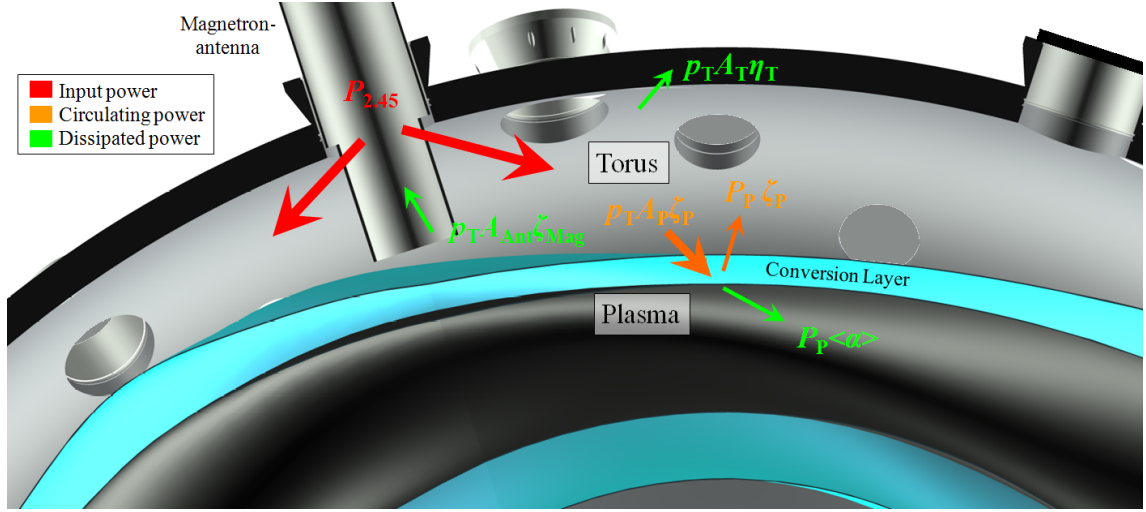


Figure 5.16: Power flow between the 'Torus' resonator, the 'Plasma' resonator and the feeding magnetron. The plasma edge area (cyan) where the conversion takes place is separated from the central plasma where the coupled power is absorbed.

In the equivalent equation of the 'torus' resonator a further loss term  $p_T A_{Ant} \zeta_{Mag}$  must be added on the right side because the energy flux density can be coupled back to the magnetron as well as to the other magnetron transmission line<sup>15</sup>:

$$P_{2.45} + P_P \zeta_P = p_T A_P \zeta_P + p_T A_T \eta_T + p_T A_{Ant} \zeta_{Mag}. \quad (5.12)$$

The effective antenna surface  $A_{Ant}$  is given by its pipe cross section. The coupling factor  $\zeta_{Mag}$  can be defined by the transmission factor  $\zeta_{Ant}$  of the antenna reduced by a factor 0.5, because of the polarization selection of the transmission line<sup>16</sup> (see section 3.1.2). By insertion of both equations into one another the energy flux density  $p_T$  and the power  $P_P \langle \alpha \rangle$  absorbed by the plasma can be separated into

$$p_T = \frac{P_{2.45}}{A_T \eta_T + A_{Ant} \zeta_{Mag} + A_P \frac{\zeta_P \langle \alpha \rangle}{\zeta_P + \langle \alpha \rangle}} = \frac{P_{2.45}}{A_T \eta_T + 0.005 + A_P \frac{\zeta_P \langle \alpha \rangle}{\zeta_P + \langle \alpha \rangle}}, \quad (5.13)$$

$$P_P \langle \alpha \rangle = \frac{P_{2.45}}{1 + \left( \frac{\zeta_P + \langle \alpha \rangle}{\zeta_P \langle \alpha \rangle} \right) \left( \frac{A_T \eta_T + A_{Ant} \zeta_{Mag}}{A_P} \right)} = \frac{P_{2.45}}{1 + \left( \frac{\zeta_P + \langle \alpha \rangle}{\zeta_P \langle \alpha \rangle} \right) \left( \frac{A_T \eta_T + 0.005}{A_P} \right)}. \quad (5.14)$$

The energy flux density  $p_T$  in the torus is defined by the injected Power  $P_{2.45}$  reduced by a damping factor which consists of the loss coefficient of the wall ( $A_T \eta_T$ ), that of the back coupling to the magnetron antenna ( $A_{Ant} \zeta_{Mag}$ ), and that of the coupling to the plasma ( $A_P \zeta_P \langle \alpha \rangle / (\zeta_P + \langle \alpha \rangle)$ ). The loss coefficient of the coupling to the plasma includes an effective absorption coefficient scaling with the plasma surface  $A_P$ . By multiplying equation (5.13) by  $A_{Ant} \zeta_{Mag}$  the back coupled power to the magnetron can be calculated and compared with the measured reflected power. The reflected power in the experiment, however, shows a strong dependence on the neutral gas density as it was observed in other experiments.

<sup>15</sup>In the standby state, both transmission lines are not short-circuited and guide the reverse power to an absorber.

<sup>16</sup> $\zeta_{Mag}$  is also changed by minimization of the reflections with the aid of the stub tuner, but the effect on the overall power balance is negligible. A further discussion of the individual  $\zeta_{Mag}$  could be interesting, if the transmission line in standby is used as stray radiation detector.

The off-axis heating between the time points II and III of Figure 5.15 leads to a change of the electron density in the plasma edge area and thus to a change in the torus impedance. For this reason, the theoretically calculated absorbed power  $P_P \langle \alpha \rangle$  of equation (5.14) is compared with the line integrated density to determine the initial coupling mechanism at time point III; an extensive discussion thereof will follow in subsection 5.1.2.4. Essential for the estimate of the absorbed power by the plasma is the determination of torus wall losses, which is discussed in the following.

### 5.1.2.3 Quality factor of the resonator torus

The power loss  $P_{\text{loss}}$  of a resonator can be represented by the unloaded quality factor  $Q_0$ , given by the ratio of stored energy  $W_{\text{res}}$  within the resonator to energy loss per angular period time  $1/\omega_{\text{res}}$  [Jac99]:

$$Q_0 = \omega_{\text{res}} \frac{W_{\text{res}}}{P_{\text{loss}}}. \quad (5.15)$$

The power loss of a cavity resonator is caused by the finite wall conductivity and the resultant finite skin depth  $\delta_T$  of the electric field. This leads to a decrease of the stored energy  $W_{\text{res}}$ , and therefore of the quality factor  $Q_0$ . Furthermore, higher skin depths lead to a relaxation of the boundary conditions and consequently reduce the sharpness of resonance. An introduction to the calculation of the quality factor can be found in Jackson's book [Jac99]. All possible field modes must be calculated analytically, which is quite challenging for the ideal torus and impossible for the plasma-filled WEGA torus. Using the example of a cylindrical cavity resonator, a calculation of the quality factor according to equation (5.15) allows the estimate of a formula containing the ratio of the electromagnetically filled storage volume  $V_T$  to the volume  $A_T \delta_T$  of the electric field interspersed cavity boundary<sup>17</sup> [Jac99]:

$$Q_0 = \frac{\mu}{\mu_T} \left( \frac{V_T}{A_T \delta_T} \right) \cdot F_{\text{geo}} \quad (5.16)$$

It has to be distinguished between the permeability  $\mu$  of the torus volume and the permeability  $\mu_T$  of the torus wall. The geometrical factor  $F_{\text{geo}}$  depends on the resonator geometry as well as on the field distribution of the resonant modes, and is of the order unity. With a stainless steel conductivity of  $\sigma_T = 1.1 \text{ MSm}^{-1}$  [Poz98] the quality factor of the ideal empty torus and the plasma-filled WEGA torus become  $Q_{\text{iT w/o P}} = 9 \cdot 10^7$  and  $Q_{\text{iT w P}} = 6 \cdot 10^7$ , respectively. In the case of the so called MISTRAL stray radiation chamber, an almost ideal aluminum cylinder resonator, a similar quality factor of  $Q = 10^6$  was measured [Ulr07]. Such high values are not expected for the WEGA torus because the electrical conductivity of stainless steel is around 25 times lower than the electrical conductivity of aluminum. Furthermore, the attenuating surface in the case of WEGA is increased by ports and in-vessel components. For this reason, the quality factor of the empty WEGA torus must be determined experimentally which was realized by the measurement of the frequency dependent reflection at the position of the magnetron in the transmission line. Minimal reflection occurs at a resonance frequency  $\omega_0$  of the 'Torus' resonator with a half width  $\Delta\omega_H$ , depending on the quality factor. Within the range of the resonance frequency resonators can be treated as parallel or as a series of LCR elements. A good introduction to this concept can be found in Heuermann's book [Heu09; Hil12]. The torus without plasma, together with the magnetron, represents a reflection resonator whose equivalent circuit diagram is shown in Figure 5.17. The matched source feeds the resonator which should have the same impedance as the transmission line. For this reason,

---

<sup>17</sup>The index 'T' is related to the 'Torus' resonator.

a further conductance  $1/Z_{\text{Mag}}$  must be considered, leading to an additional external quality factor  $Q_{\text{ext}}$  and therefore to the loaded quality factor  $Q_L$ :

$$\frac{1}{Q_L} = \frac{1}{Q_0} + \frac{1}{Q_{\text{ext}}} = \frac{1}{Q_0} + \frac{\kappa}{Q_0} \quad (5.17)$$

The external quality factor is defined only by the coupling factor  $\kappa = Z_T/(n_M^2 Z_{\text{Mag}})$ , which depends on the ratio of the resonator impedance  $Z_T$  and the transformed impedance  $Z_{\text{Mag}} n_M^2$  of the transmission line. The stub tuner acts as an impedance transformer, matching the impedance  $Z_{\text{Mag}}$  of the transmission line to the torus impedance  $Z_T$  and thus improving the power transfer. The transformation ratio  $n_M$  is defined by the position of the three stubs (.../.../...) without knowledge of the specific value for each position. The coupling must be distinguished between undercritical ( $\kappa < 1$ ), critical ( $\kappa > 1$ ) and overcritical ( $\kappa < 1$ ). Undercritical coupling can be compared with the weak coupling of a closed resonator, in which a resonance is only slightly broadened with a reduced power transfer. Critical coupling is characterized by a full power transfer to the resonator. The reflection again increases with  $\kappa > 1$  accompanied by a further increase of the half width of the resonance. Considering the conductances of resonator and transmission line, the frequency dependent scalar reflection factor  $|S_{11}(f)|$  can be deduced [Hil12]:

$$|S_{11}(f)| = \sqrt{\frac{(\kappa - 1)^2 + 4Q_0^2 (\Delta f/f_0)^2}{(\kappa + 1)^2 + 4Q_0^2 (\Delta f/f_0)^2}} \quad \text{with } |S_{11}(f)|^2 = \frac{P_{\text{ref}}}{P_{2.45}}. \quad (5.18)$$

It is important to note, that the quality factor  $Q_0$  can only be determined with the aid of this equation in the case of critical coupling. Figure 5.18 shows the measured scalar reflection factor  $S_{11}$  in the vicinity of the magnetron frequency for two different configurations of the stub tuner. In both cases many closely spaced resonances are visible, indicating the countless different possible modes in the 'Torus' resonator. The unmatched source without an impedance transformation by the stub tuner (position 00.00/00.00/00.00 with  $n_M = 1$ )<sup>18</sup> leads to an averaged reflection of 10 %. To every excitable mode a conductance or rather an impedance can be assigned, due to the differing propagation constants. In the case of vanishing reflection the transformation ratio  $n_{\text{Mag}}$  is chosen in such a way that the transformed transmission line impedance has the same value as the resonator impedance of the particular resonant mode. The optimal matching for 2.45 GHz in the case of the empty torus is achieved by the stub tuner position 00.00/03.80/8.75, whose  $S_{11}$  response is also shown in the Figure 5.18. A similar position 00.00/10.00/08.75 is used for the plasma-filled torus for the minimization of the reflection.

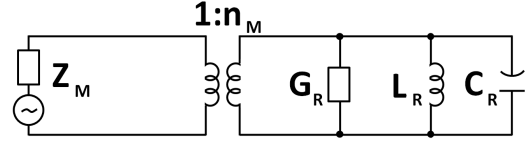
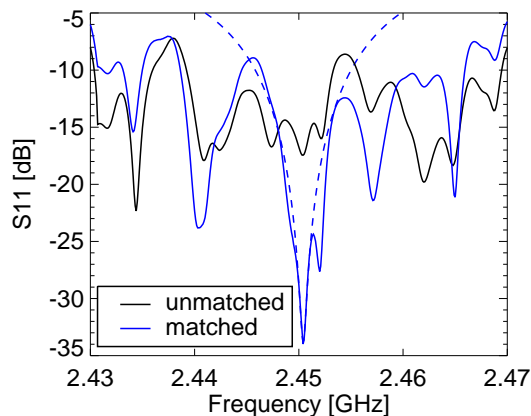


Figure 5.17: *Equivalent circuit diagram of the 'Torus' resonator working as reflection cavity to the HF-source magnetron. If the complex conductance  $G_T$  of the torus and accordingly the impedance  $Z_{\text{Mag}}$  of the transmission line are not equal, the stub tuner will be used as an impedance transformer by introducing a transformation ratio  $n_M$ .*

<sup>18</sup>The stub tuner of the 20 kW transmission line is software-controlled and its position in relation to the antenna as well as the vacuum window was not changed since more than 6 years. For this reason, the results are reproducible with the aid of the denoted stub tuner positions.

Table 5.1: *Optimal (and complementary) values for a consistent fit of the measured  $S_{11}$  parameter for the 2.434 GHz resonance in the case of different matching configurations*

Stub tuner position	$f_0$ [GHz]	$\kappa$	$Q_0$
00.00/04.15/00.00	2.4340	1.051 (0.952)	671 (639)
00.00/00.00/00.00	2.4338	0.917 (1.090)	671 (731)
00.00/03.80/08.75	2.4341	0.708 (1.412)	712 (1005)

Figure 5.18: *Scalar reflection parameter  $S_{11}$  of the loaded resonator „torus” in a frequency range of 20 MHz around the magnetron frequency of 2.45 GHz. The fit of equation (5.18) is shown for the matched configuration.*

The resonance is relatively broad and a fit of equation (5.18) would yield a small quality factor of  $Q_{0, 2.451} = 170$ . For the derivation of equation (5.18), however, an isolated resonance is assumed. In contrast, intersecting resonances lead to a broadening of the single resonance because the stored energy is distributed on different modes. Therefore, the conditions of equation (5.18) are not generally fulfilled for the measured reflection factors. The resonance at 2.434 GHz shows a relatively stable behavior in the profile shape and in the resonance position independent on the chosen stub tuner position. This resonance should be used for a determination of the quality factor. It will be assumed that the subsequent absorption factor has the same magnitude as the averaged absorption factor of the excited modes at 2.45 GHz in the case of the plasma-filled torus. Independent of the excited mode, the transformation ratio  $n_{\text{Mag}}$  can be measured, calculation of which is also

challenging, because of its dependence on the setup of the transmission line between the stub tuner and the antenna. In the case of a non-vanishing reflection the complex  $S_{11}$  must be measured or the coupling regime must be postulated. Table 5.1 shows the possible values for the coupling factor  $\kappa$  and the unloaded quality factor  $Q_0$ , which results in  $Q_{0, 2.434} = 670 \pm 50$  with the assumption of a weak overcritical coupling for the matched configuration (position 00.00/04.15/00.00) and a general undercritical coupling in other cases. The uncertainty is estimated from the complementary values.

Another possibility for the determination of the quality factor is the measurement of the decay time  $\tau_{\text{res}}$  of the stored energy  $W_{\text{res}}$  in the resonator after the source is switched off rapidly. In this case, the quality factor can be calculated by  $Q = \tau_{\text{res}}\omega_{\text{res}}$  [Jac99]. A small part of the energy flux in the torus must be coupled out by an electric probe, representing an additional load. A magnetic loop at the opposite side of the torus was used<sup>19</sup>. Figure 5.19 shows the time evolution of the detected power that was put on a level with the stored energy  $W_{\text{res}}$ . The fit of an exponential decay, shown in Figure 5.19, leads to a similar value of  $Q = 680$ . The ideal time evolution, however, seems to be distorted, as is visible in Figure 5.19. One possible explanation for this could be sub volumes with different quality factors. For example, there are two chambers with a volume of  $0.04 \text{ m}^3$  each between the torus and the pump, representing about 10 % of the whole torus volume.

<sup>19</sup>This loop is described in more detail in subsection 5.3.2, because it was originally used for the measurement of plasma waves with frequencies of approximately 100 MHz.

For the estimation of the wall absorption factor, the energy flux density  $p_T$  divided by the propagation velocity  $v_p \approx c$  can be approximated with an energy volume density in the torus. After multiplying  $p_T/c$  with the torus volume one obtains the stored energy  $W_{\text{res}}$  of equation (5.15). With a power loss of  $P_{\text{loss}} = p_T A_T \eta_T$ , a similar expression of equation (5.16) can be found for the unloaded quality factor  $Q_0$ :

$$Q_0 = \frac{2\pi f_{\text{res}} p_T \frac{1}{c} V_T}{p_T A_T \eta_T} = \frac{2\pi V_T}{\lambda_{\text{res}} A_T \eta_T} \quad (5.19)$$

The torus volume  $V_T$  is approximately twice the ideal torus volume of  $V_{T,\text{ideal}} = 0.513 \text{ m}^3$  because of ports and connection elements to the pumps. The absorption factor or rather the full absorbing part of the torus wall is calculated to  $A_T \eta_T \approx 0.08 \text{ m}^2$ , which can be directly inserted into the balance equation (5.14). The averaged absorption coefficient  $\eta_T$  can be determined by specifying of the wall surface area which is more difficult to calculate than the torus volume. If an effective torus surface of  $A_{T,\text{eff}} = 10 \text{ m}^2$  is assumed, being only twice the ideal torus surface, the effective absorption becomes  $\eta_{T,\text{eff},2.45\text{GHz}} = 0.01$ . This value scales via the  $1/\sqrt{f}$ -dependence of the skin depth with the measured effective absorption coefficient  $\eta_{T,\text{eff},28\text{GHz}} = 0.045$  of subsection 5.1.1.2<sup>20</sup>.

#### 5.1.2.4 Coupling mechanism

The main concern in the calculation of the power balance according to equation (5.14) consists of comparing the absorbed power  $P_{\text{abs,calc}} = P_P \langle \alpha \rangle$  with the line integrated density. The coupling coefficient still to be defined will be confirmed if the qualitative behavior of both quantities are in agreement. As is shown by a simple multipath model in subsection 5.1.1.2, a sufficient heating will be achieved if the effective absorption coefficient of wall and plasma have the same magnitude. At first the propagable wave modes within the plasma must be determined for the definition of a coupling factor  $\zeta_P$ . For the relevant beam directions of the slotted magnetron antenna, Figure 5.24 shows the effective radius of the 2.45 GHz resonance in dependence on the magnetic flux density  $B_0$ . The rapid increase of the line integrated density does not occur until the resonance is far from the last closed flux surface. Therefore, the vacuum wave can only couple to the relevant plasma wave for  $Y > 1$ . Figure 2.3b illustrates the solutions of the Altar-Appleton equation in dependence on the electron density for  $Y = 1.7$ . This value corresponds to the magnetic flux density in the vicinity of the O-mode-cutoff at the low field side for the indicated time point at  $t = 9.5 \text{ s}$  in Figure 5.24. Strictly speaking the graphs are not valid because the wavelength of  $\lambda \approx 12 \text{ cm}$  is much greater than the density gradient length  $L_n$ . For example, in the case of oblique incidence the wave is deflected in the density gradient area, leading to a continuous change of the propagation angle. As explained in subsection 2.2.1.3, the polarization of a fundamental mode is repositioned in the case of deflection but not for  $L_n \ll \lambda$ . For this reason, a modeling of the wave propagation is only possible with full wave calculations.

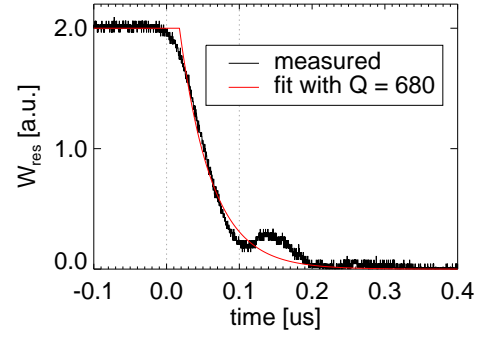


Figure 5.19: *Time evolution of the stored energy  $W_{\text{res}}$  in the resonator torus after fast generator switch off. The Wiltron 68163B function generator used has a power decay time of less than 15 ns. The fit of equation (5.18) was calculated for the time window indicated by the dotted vertical lines.*

<sup>20</sup>A direct measurement of this value by the resonator method used is probably not possible because of the more closely spaced resonances.

Nevertheless, R-like waves are able to propagate in highly overdense plasmas when the local electron cyclotron frequency is higher than the propagation frequency. This wave mode is also called a Whistler wave and must be responsible for the transport of the heating power into the plasma center. The cold dispersion relation in Figure 2.3b, however, indicates no direct coupling of the R-like branches between underdense and overdense plasma area. The physics of a Whistler wave is often investigated in linear devices where the wave can be excited parallel to the magnetic field. In the case of a plasma tube, deviations of the parallel propagation lead to a self focusing effect that has been experimentally observed [Bal80] and also theoretically explained [TW69; TAN69; KK82; SS09]. Accordingly, an excited R-like wave with a small angle between its  $\mathbf{k}$ -vector and the magnetic field lines tends towards a more parallel propagation and is prevented from leaving the plasma<sup>21</sup>. A full wave calculation of the TJ-K group shows a similar behavior for the example of an angle of  $\vartheta = 10^\circ$  [Die09]. The corresponding diploma thesis [Die09] concluded that a direct coupling to R-like waves is not possible under flat angles. Furthermore, the investigation of non-resonant heating at TJ-K was part of a PhD-thesis [Köh10] which also deals with the heating of overdense plasmas by electron Bernstein waves. A current overview can be found in [KBC<sup>+</sup>12; KBC<sup>+</sup>13] but without a final clarification of the coupling process to Whistler waves. For this reason, a variety of possible coupling mechanisms will be discussed in the following.

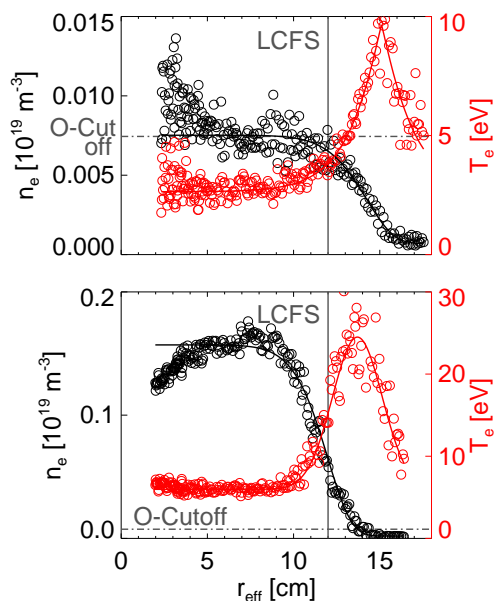


Figure 5.20: *Density and temperature profile of a non-resonant discharge before efficient resonant heating at  $B_0 = 100$  mT (a) and after the density increase at  $B_0 = 150$  mT (b).*

**Linear Transformation** In [Die09] it was attempted to explain the coupling by the so called *linear transformation* of the incident transversal electromagnetic wave to a longitudinal plasma wave and subsequent absorption at the resonance within the overdense plasma. This mechanism, studied by Golant and Piliya [GP72], occurs in finite temperature plasmas when the angle  $\alpha$  between the density gradient and the magnetic field vector is smaller than  $90^\circ$ . For a weakly inhomogeneous plasma an incident wave under the same angle  $\vartheta = \alpha$  is subjected to the same evolution of the refractive index shown in Figure 2.3b. The longitudinal plasma wave allows a direct connection between the underdense and overdense R-like branch of the dispersion relation. The occurrence of the resonance within the overdense plasma, however, depends on the maximum density for a certain propagation angle  $\vartheta$ . For this reason, the linear transformation is only possible up to a maximum angle  $\vartheta_{\max} > \vartheta \equiv \alpha$ . The densities reached at WEGA as well as TJ-K require  $\alpha \approx 50^\circ$  so that the density variation along and perpendicular to the magnetic field lines must be of the same magnitude. Even outside of the LCFS this condition cannot be fulfilled. For this reason, the linear transformation was ignored as a possible explanation.

<sup>21</sup>Examples of a leakage of Whistler waves for the case of certain density profiles and magnetic configurations will be introduced later, in connection with the proposed coupling mechanism.

**Influence of Collisions and a finite Skin Depth** On the other hand, collisions can lead to a softening of the dispersion relation around the cutoff so that a direct connection between the underdense and overdense R-like branch of the dispersion relation is possible for a low angle  $\vartheta$ . The collision frequency around the cutoff, however, is too low taking into account the measured density and temperature shown in Figure 5.20 for the time points before and after the onset of the efficient non-resonant heating. Both cases are indicated in Figure 5.24 by the vertical dotted lines. In the first case the resonances for the different  $\vartheta$  are located near to the LCFS at  $X < 1$ , explaining the high temperature at the plasma edge. The same explanation is valid for the second case with  $Y = 1.7$  around the LCFS. In this case the resonances for nearly parallel propagation are located at  $X \approx 1$ . This plasma area is accessible for the incident wave because the skin depth is of the order 1 cm for the maximum density of Figure 5.20b. Furthermore, the reflection of the incident wave at the O-cutoff-layer leads to an exaggeration of the electric field and a increased power transfer. Collisions are only important for the low temperatures in the plasma center and can be excluded as a reason for a direct coupling between the underdense and overdense R-like branch for  $Y > 1$ .

The non-resonant heating process for  $Y < 1$ , however, can be explained by collisional absorption in the plasma center. As seen in Figure 5.24, the line integrated density decreases around  $t = 8.5$  s which leads to the slightly overdense plasma shown in Figure 5.20a. The skin depth of the incident wave is on the order of one wavelength so that a finite part of the wave propagates through the plasma. The resistive absorption of one path can be estimated to be about 1%. In contrast, the skin depth for the maximum density of Figure 5.20b is on the order 1 cm. In comparison to the plasma diameter this value is quiet low, but the density increase at the O-cutoff is quite high. This can lead to a partial tunneling of the wave to the resonance in the overdense plasma area.

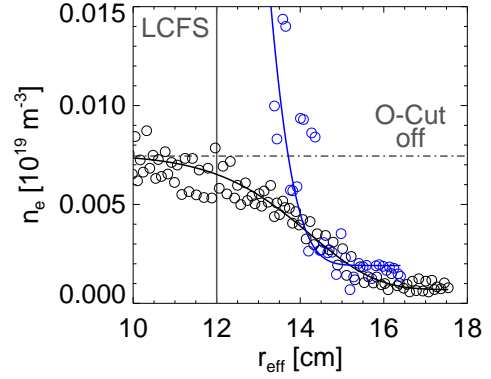


Figure 5.21: Comparison of both density profiles of Figure 5.20 in the vicinity of the cut-off density

**Tunneling** The density profile of the considered discharge at the O-cutoff is compared for  $Y < 1$  and  $Y > 1$  in Figure 5.21. At  $B_0 = 150$  mT the gradient length at the cut-off can be determined to be  $L_n = n_e / \nabla n_e = 0.6$  cm, compared to  $L_n = 2.7$  cm at the same effective radius in the case of  $B_0 = 100$  mT. Considering  $\delta \approx L_n \approx 1$  cm the extraordinary wave can enter the plasma up to twice the cut-off-density, where the resonance for the propagation angle of  $30^\circ$  is located. For oblique incidence only the refractive index  $N_\perp$  parallel to the density gradient (and perpendicular to the magnetic field) goes to zero, while  $N_\parallel$  remains constant. If the incidence angle of the wave is  $\vartheta = 80^\circ$ , for example, the skin depth will be nearly the same and near the reversal point a

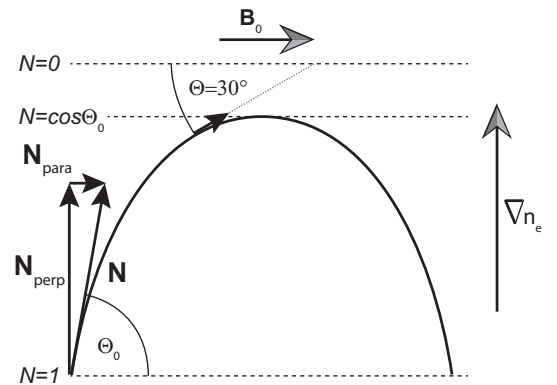


Figure 5.22: Simplified deflection of the incident  $\mathbf{k}$ -vector with reversal point at  $N = \cos \vartheta_0$  [Gek82]

part of the wave will have a propagation angle of  $30^\circ$ . The result is a partial tunneling of the wave through the O-cutoff layer while the remaining part is reflected and weakly absorbed by resistive damping dependent on the electron temperature. The transmitted power is split into absorption at the resonance as well as an excitation of a Whistler wave propagating into the plasma center [MjØ87]. The basics of tunneling through a cutoff-resonance pair are explained in subsection 2.2.3.1 for the example of the FX-SX-conversion. This process is physically related to the case of  $\sin\theta \ll 1$  in Figure 2.3b for the considered R-like wave. The first analysis of this process for nearly parallel propagation was given by Budden [Bud61; MjØ87]. For the analysis of wave propagation in the ionosphere the necessary density gradient has the same direction as the magnetic field and therefore of the propagation direction of the tunneling wave. For this reason, the wave equation can be reduced to one dimension for the wave amplitudes of the left and right hand circularly polarized fundamental modes:

$$\partial_{zz}\tilde{E}_{r,l}(z) + k_0^2 \left(1 - \frac{X(z)}{1 \pm Y}\right) \tilde{E}_{r,l}(z) = \partial_{zz}\tilde{E}_{r,l}(z) + k_0^2 N_{r,l}^2(z) \tilde{E}_{r,l}(z) = 0 \quad (5.20)$$

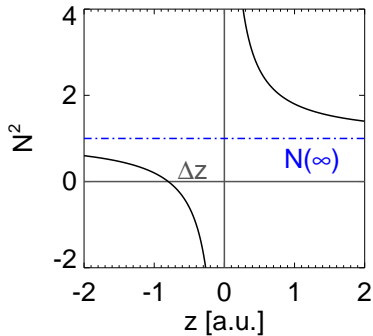


Figure 5.23: Assumed squared refractive index  $N^2(z) = 1 + \Delta z/z$  of the 'Budden equation' 5.20

In this case the dependence of the squared refractive index  $N^2$  on  $z$  is only given by straight lines, but the wave equation itself can also be taken as valid for  $\sin\theta \ll 1$ . Budden has approximated the refractive index of the latter case by  $N^2(z) = 1 + \Delta z/z$  shown in Figure 5.23 with the distance  $\Delta z$  between the cutoff and the resonance [Swa03]. With an appropriate non-linear density gradient this function complies in the range  $X = 0 - 1.3$  with the behavior of the R-like mode for  $\vartheta \leq 10^\circ$  in Figure 2.3b as well as the extraordinary mode for  $\vartheta = 90^\circ$  in Figure 2.3a. With this substitution, the solutions of the confluent hypergeometric function given by Whittaker and Watson were used by Budden for the analysis of the wave tunneling in positive and negative  $z$ -direction [Bud61]. For both cases the amplitude transmission factor can be calculated to  $|T| = \exp(-0.5\pi k_\infty \Delta z)$ . The quantity  $k_\infty = k_0 N^2(\infty)$

must be interpreted as an averaged wave vector for  $|z| = \infty$  and not necessarily as a vacuum wave vector [Sti92]. The tunneling of the R-like wave for  $X < 1$  to the R-like mode for  $X > 1$  of Figure 2.3b must be approximated for  $\sin\vartheta \ll 1$  by a function  $N^2(z)$  with an axis of symmetry along the curve  $\vartheta = 0^\circ$  and  $N^2(0) = N^2(\infty) = 2.4$ . Ginzburg has already studied this small angle problem, and predicts the access of both modes to the coupling region for  $Y > 1$  [MjØ87]. A generalized approach with oblique incidence and arbitrary direction of the density gradient to the magnetic field direction was given by Mjølhus but only applies to the small angle problem ( $\sin\vartheta \ll 1$ ) [MjØ87]. The exact transmission factor determined contains a similar  $k_\infty$  as determined for the example of Figure 2.3b<sup>22</sup>.

Another possible approach is the analysis of the containment of the R-waves in the overdense plasma. The waveguide propagation of Whistler waves is typically observed in plasma tubes with hollow density profiles where a leakage of the wave arises for the so called crests with high densities [KK81a]. The reason is a tunneling transformation whose transmission factor can reach quite high values for  $Y > 2$  and must also be valid for the reverse transformation

<sup>22</sup>The same analysis of the traditional Budden problem is possible for the vertical incidence of the extraordinary mode in the case of  $Y < 1$  [WC74], which leads to the transmission factor of the FX-SX-coupling introduced in subsection 2.2.3.1

[KK81c; KK81b]. In the case of  $B_0 = 150$  mT this condition can be fulfilled on the high field side which is also accessible for the wave because of the high quality factor of the torus.

An exact calculation of the transmission factor via the generalized Budden tunneling or the leakage of Whistlers is challenging, however, so Budden tunneling in its traditional form should be adapted to the considered problem with an evanescent layer of thickness  $\Delta r$  perpendicular to the magnetic flux surfaces

$$|T| = \exp\left(-\frac{\pi}{2}k_\infty\Delta r\right). \quad (5.21)$$

The radial distance  $\Delta r$  between the effective cutoff at  $N = \cos\vartheta_0$  and the resonance of the initial direction  $\vartheta_0$  can be approximately determined by the gradient length  $L_n$  at the cutoff and the necessary density  $n_{\text{res}}$  for the existence of the particular resonance:

$$\Delta r \approx L_n \frac{\Delta n_e}{n_e} = L_n \frac{n_{\text{res}} - n_{c,\text{eff}}}{n_c} = L_n [X_{\text{res}} - X_{c,\text{eff}}] = L_n \left[ \frac{Y^2(\cos^2\vartheta_0 - 1)}{1 - Y^2 \cos^2\vartheta_0} + \cos^2\vartheta_0 \right].$$

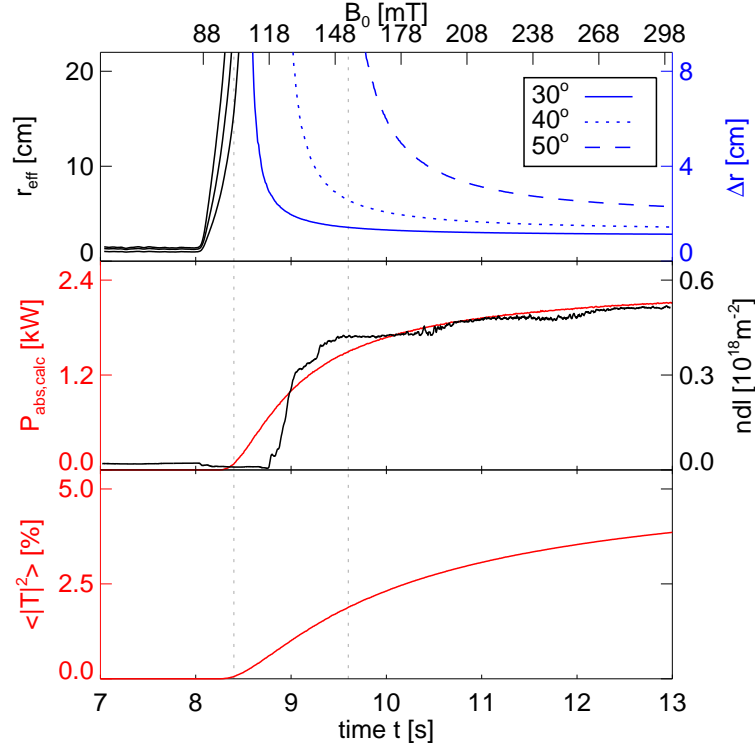


Figure 5.24: Time traces of the effective radius  $r_{\text{eff}}$  of the 2.45 GHz-resonance of the discharge shown in Figure 5.15 compared to the increase of the line integrated electron density  $ndl$  as well as the decrease of the radial distance  $\Delta r$  between the cut-off and the resonance along the main emission vectors of the magnetron. The plasma profiles for the indicated time points are shown in Figure 5.20. The onset of the  $ndl$  is in qualitative agreement with the calculated absorbed power  $P_{\text{abs,calc}}$ . The angle averaged tunneling coefficient  $\langle |T|^2 \rangle \doteq \zeta_P$  reaches some per cent being higher than the wall absorption with  $\eta_T \approx 1$  %.

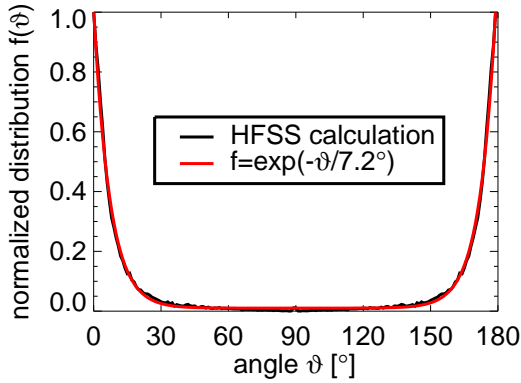


Figure 5.25: Normalized power distribution of the wave pattern in dependence on the angle  $\vartheta$  in the vicinity of the plasma boundary which is assumed as perfectly conducting layer in the HFSS-calculation shown in Figure 5.26 and 5.27.

must be given to the interference of the reflected wave with the undisturbed emission pattern leading to an effective incidence at much lower angles  $\vartheta$  with respect to the magnetic field lines ( $\cos \vartheta > 0.7$ ). Figure 5.26 shows the calculated electric field pattern in the equatorial plane within the torus when the wave emitted by the slot antenna is completely reflected at the plasma boundary. The resultant Poynting vector is shown in Figure 5.27 and indicates a more parallel propagation with respect to the magnetic field lines. A calculation of the corresponding angle  $\vartheta$  in the vicinity of the plasma boundary leads to the normalized distribution shown in Figure 5.25 which was used for the calculation of the absorbed power. For each direction the power is multiplied by the resultant transmission factor  $|T|^2$ , whose integration leads to the total coupling factor  $\langle |T|^2 \rangle \doteq \zeta_P$  as well as the coupled power.  $\langle |T|^2 \rangle$  reaches some per cent and is shown in Figure 5.24.

A further key for the modeling of the evolution of the absorbed power is up to the consideration of the resonator character of the torus. The tunneling coefficient  $|T|$  is the same for the coupling from the vacuum to the overdense plasma and reverse. As was already shown by the simple Budden problem, there is no reflection of the wave first hitting the resonance. The necessary consequence is the absorption of the remaining wave power at the resonance. The absorbed power determined by equation (5.14) is also depicted in Figure 5.24 in comparison with the line integrated density. The averaged wave vector was set to  $k_\infty = k_0 \sqrt{Y/(Y-1)}$  derived from equation (5.20) at  $X = 1$ , as was already described. The density increase is sharper than the calculated absorbed power but the overall dependence fits well. A higher gradient length of  $L_n = 0.5$  cm would lead to the same strong increase but the onset of the increase would be located at  $t = 8.4$  s. Most likely, for very small angles the wave cannot penetrate into the plasma, leading to the delayed density increase in comparison with the calculation. The qualitative agreement of the expected absorbed power with the line integrated density, however, confirms the applicability of the assumed coupling mechanism. The next subsection gives an experiment proposal to prove the tunneling as relevant coupling mechanism.

The normalized cutoff-density  $X_{c,\text{eff}}$  was estimated by the dispersion relation of the ordinary wave  $N^2 = 1 - X_{c,\text{eff}}$  leading to an overestimation of the thickness  $\Delta r$  as obvious in Figure 2.3b. The normalized resonant density  $X_{\text{res}} = (1 - Y^2)/(1 - Y^2 \cos^2 \vartheta)$  is dependent on the angle  $\vartheta$ . The actual existence of the resonance is given by the normalized magnetic field  $Y$ . The time development of the density profile being unknown, an averaged value of  $L_n = 1$  cm is used for the modeling of the coupling and the resultant absorbed power. In Figure 5.24 the resultant distance  $\Delta r$  is shown for different angles  $\vartheta$ . The density increase starts with the appearance of the 35°-resonance whose  $\mathbf{k}$ -vector is roughly the lower border of the main magnetron emission, shown in Figure 3.13b. With the appearance of the 50°-resonance the density increase stagnates in accordance with the emission maximum. Thought

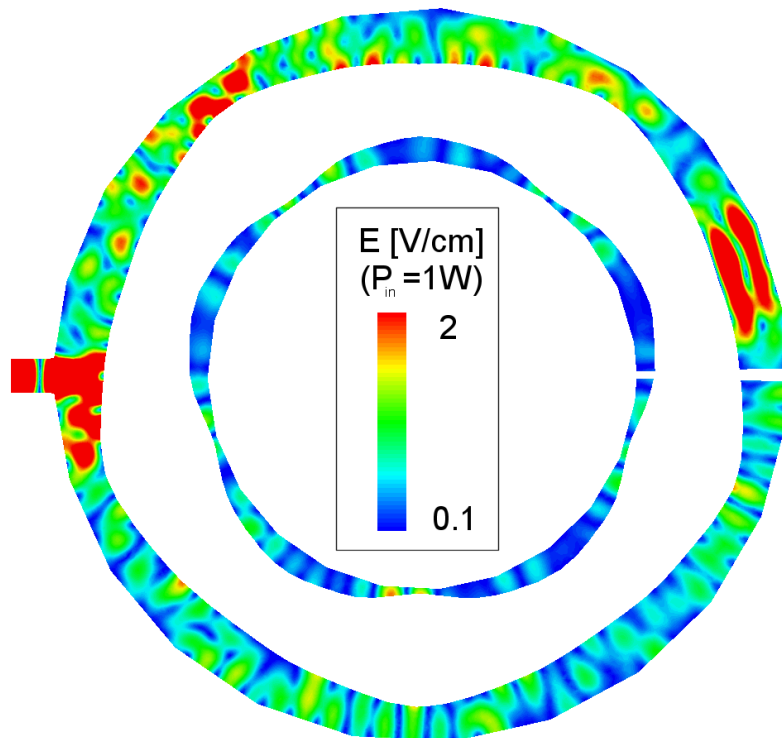


Figure 5.26: *Electric field in the resonator torus calculated with HFSS. A radiation boundary at the shown gap in the torus was used to disable the interference with the non absorbed reflected wave from the respective other side and to illustrate the conditions in the case of good absorption.*

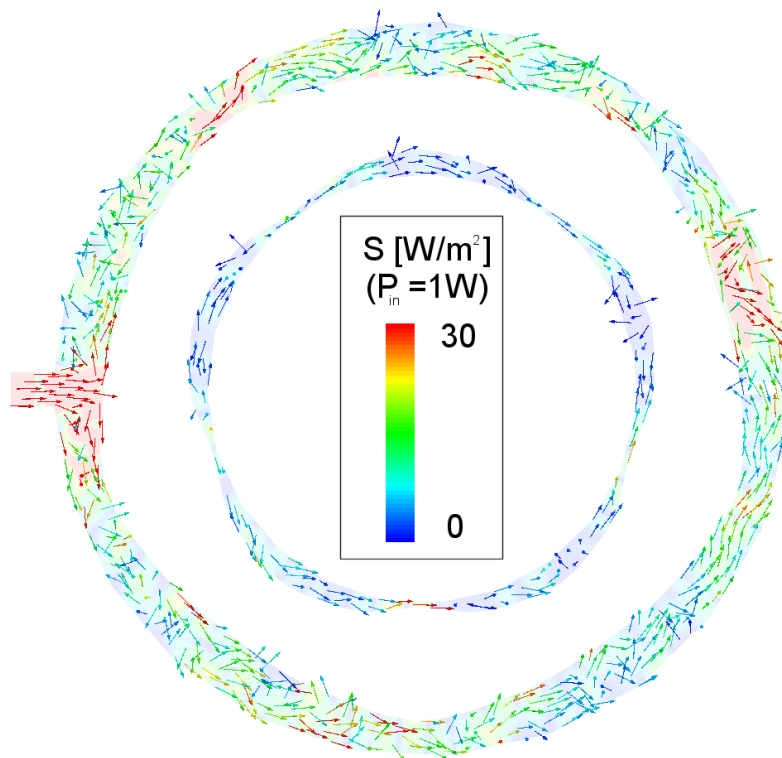


Figure 5.27: *The same as in Figure 5.26 for the Poynting vector.*

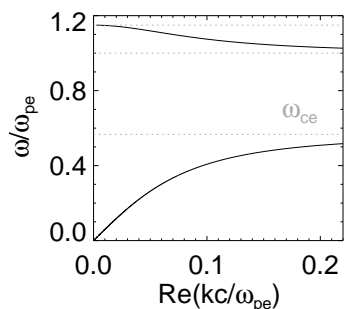


Figure 5.28: *Dispersion relation of electrostatic Trivelpiece-Gould waves of lowest order in a plasma filled conducting cylinder with axial magnetic field for  $\omega_{pe} > \omega_{ce}$*

**Trivelpiece-Gould-modes** Another possible candidate for a coupling mechanism to the propagable Whistler modes are the so called Trivelpiece-Gould-modes (TG-modes) [TG59]. Similar to a waveguide, the overdense plasma acts as a conducting wall that leads to charge separation as well as equalizing currents in the plasma. For this reason, the torus system and plasma represent a coaxial-like waveguide whose characteristic radial  $\mathbf{k}_r$ -vector is dependent on the considered mode distribution as well as on the plasma conductivity and density profile. The  $\mathbf{k}_z$ -vector arises from the dispersion function shown in Figure 5.28 for the case of  $\omega_{pe} > \omega_{ce}$ . The resultant space charge waves can propagate obliquely to the magnetic field vector and can lead to a coupling to the Whistler mode because of similar refractive indices [Str11]. The wave frequency, however, must be lower than the local electron cyclotron frequency in consistence with the observation of the coupling onset. Prior to a detailed analysis it is recommended to check the existence of the TG-modes in the WEGA torus, as is proposed in more detail in the following.

### 5.1.2.5 Experiment proposal

The density increase was generally observed at a magnetic flux density on the axis of  $B_0 = (118 - 125)$  mT. The magnetic field scan should also be accomplished in the inverse direction. In this case the density evolution is not affected by a possible delay caused by an excessively low actual density. This must be repeated for different iota values in order to shrink the plasma size and shift the cut-off position in the magnetic field. An additional radial shift of the whole plasma can be realized with the vertical field coils. A change of the threshold magnetic flux density would support the theory of Trivelpiece-Gould modes, as well as of a tunneling process that is also dependent on the incidence direction. This can be changed by a shift of the 6 kW-magnetron antenna in radial direction. If the antenna is partly submerged in the torus wall, its slot will be shorter and the emission characteristic will become more and more like a standard Gaussian profile of an open waveguide with perpendicular emission in relation to the magnetic field lines. The particular characteristic of each antenna configuration can be calculated with HFSS being in very good agreement with the real characteristic [Pod06]. Further investigation can focus on a possible gas pressure and power threshold. The change in density profile should be measured with a resolution of  $\Delta B_0 = 1$  mT for selected scenarios with an observed change in the coupling.

Study of the coupling efficiency is preferable at a low power of some hundred Watts. For this purpose, the other magnetron or the gyrotron in the case of  $B_0 \approx 0.5$  T can be used to realize a target plasma with arbitrary profile shape. Additionally a movable limiter can be used to affect the density gradient and therefore the tunneling factor. All experiments can be combined with a modulation of the heating power that was already investigated at TJ-K with a modulation frequency of 30 kHz. The density and temperature modulation was measured by means of Langmuir probes. It was not possible, however, to account for heating in the center because of high measured modulation amplitudes at the plasma edge near the L-cutoff [Die09]. The enhanced electric field reasonably leads to local heating but the influence on the global plasma sustainment by an inward particle flux is questionable in relation to a weakly

coupled R-like wave with resonances in the plasma center. At WEGA a higher modulation frequency is possible with a maximum of 50 kHz and a minimum pulse duration of 10  $\mu$ s [KG05]. The TJ-K confinement times are typically smaller than the WEGA ones [Bir08] so that further modulation studies might enable better statements about the absorption position. Small HF-loops might be used to prove the existence of 2.45 GHz waves in the central plasma. Measurements of the phase of the 2.45 GHz-heating wave outside the plasma also proved to be a useful experience. Through the use of more probes in the plasma, a detailed investigation of phase velocity and propagation angle is possible because of the known density and the resultant dispersion relation. The same strategy can be used to prove the possible coupling by Trivelpiece-Gould modes. The vacuum wavelength between the wall and plasma must be measured for different magnetic fields and compared with the calculated TG-dispersion relation shown in Figure 5.28. The necessary steerable HF-probe can be realized in a short time.

Further hardware changes depend on the remaining operation time of WEGA, which will likely end in Autumn 2013. The whole torus could be equipped with stray radiation detectors in terms of dipole antennas with a simple detector diode. This antenna type has a nearly homogenous receiving characteristic with the most simple setup. With a set of detectors in toroidal direction, a distinction of multipath absorption and direct coupling will be possible. The installed antennas can also be used for the investigation of the dispersion of the 2.45 GHz-wave in the torus. An absolute value of the stray radiation can be obtained by the particular standby transmission line whose isolator is combined with a reverse power detector. A more advanced hardware upgrade is the installation of an antenna tube guiding to a waveguide absorber partially collecting the direct reflected power of the first path and allowing an assessment of single and multipath absorption.

#### 5.1.2.6 Physics at low neutral gas density

A further effect is the generation of suprathermal particles with relativistic energies up to MeV in the case of neutral gas densities lower than  $p_n = 10^{-5}$  mbar<sup>23</sup>. Because of an intrinsic property of the WEGA magnetic field configuration, these MeV-electrons produce currents up to kilo amps. At high particle energies the magnetic confinement of stellarators and tokamaks becomes dependent on the propagation direction of the particles. Particle tracing calculations with the w7-code for  $B_0 = 0.5$  T show this behavior for electron energies higher than 200 keV. For the standard magnetic field configuration  $-/-$  the direction of the toroidal and poloidal magnetic field components are shown in Figure 1.2, whereas for  $+/+$  all directions have to be reversed. An electron with high parallel momentum in the same direction as the magnetic field encounters an additional outwardly directed centrifugal force that has the same direction as the radial Lorentz force by the poloidal magnetic field. The consequence is an enlargement of the drift surfaces. For electrons with a velocity vector oriented opposite to the magnetic field, the both forces act counter to each other and the diameter of the effective drift surface is reduced with higher energy until the border case of a so called stagnation orbit that forms a closed toroidal trajectory. This effect was predicted in [ZFG81] and further analyzed in [Fus13] because of the results achieved in WEGA. The maximum energy of the relativistic particles in WEGA is determined in section 5.2 by means of the generated synchrotron emission and with the aid of gamma rays generated after collision of the electrons with a hard target. Only a

<sup>23</sup>This pressure value is valid for Argon as gas type. In helium the pressure can be one magnitude higher. A higher power counteracts the decelerating effect of the neutral gas. Therefore, a general border is difficult to define for the acceleration process described in this section.

brief overview of the acceleration mechanism will be given here, because the overdense plasma is only indirectly sustained by collisions with the MeV-electrons. A detailed description of the results can be found in [LCOS13]. The heating process of the suprathermal electrons is not based on the above mentioned R-wave coupling, but on a stochastic acceleration of the electrons in the near field of the 2.45 GHz-antenna. The total energy gain of a test electron for many circulations in the torus and many interactions with the local RF-field would add up to zero because the electrons lose their phase information in relation to the antenna by collisions. The energy gain in a single interaction is increased with higher initial velocity, however, so that the particle makes a higher step in the energy distribution function. In connection with the circulation-time of the electron a diffusion coefficient within the energy distribution function can be defined which increases with higher energy. After temporal derivation of the total energy and insertion of a diffusion equation for the energy distribution, it can be shown that particles with higher energies and resultant higher diffusion coefficient can collect more energy in the case of a energy distribution function which monotonically decreases with increasing energy. This is in accordance with the principle of the well known Landau damping. Therefore, this scenario was called stochastic Landau acceleration (SLA) discharge.

### 5.1.3 OXB-Heating

The heating by electron Bernstein waves using OXB-mode conversion produces remarkable plasma parameters compared to X2- or non-resonant heating. The most outstanding property is the electron density of  $\geq 10^{19} \text{ m}^{-3}$ , which is necessary for the OX-conversion and also the reason that other possible heating mechanisms can be excluded with the used oblique 28 GHz launch. The other differences are the generation of mildly relativistic particles and a drastic increase of emission in the visible and microwave frequency range. How these properties are related to one another is the subject of the remainder of chapter 5.

#### 5.1.3.1 Discharge scenario

The description of the time trace of Figure 5.29 is carried out in the same way as in subsection 5.1.1.1, but in a more condensed form.

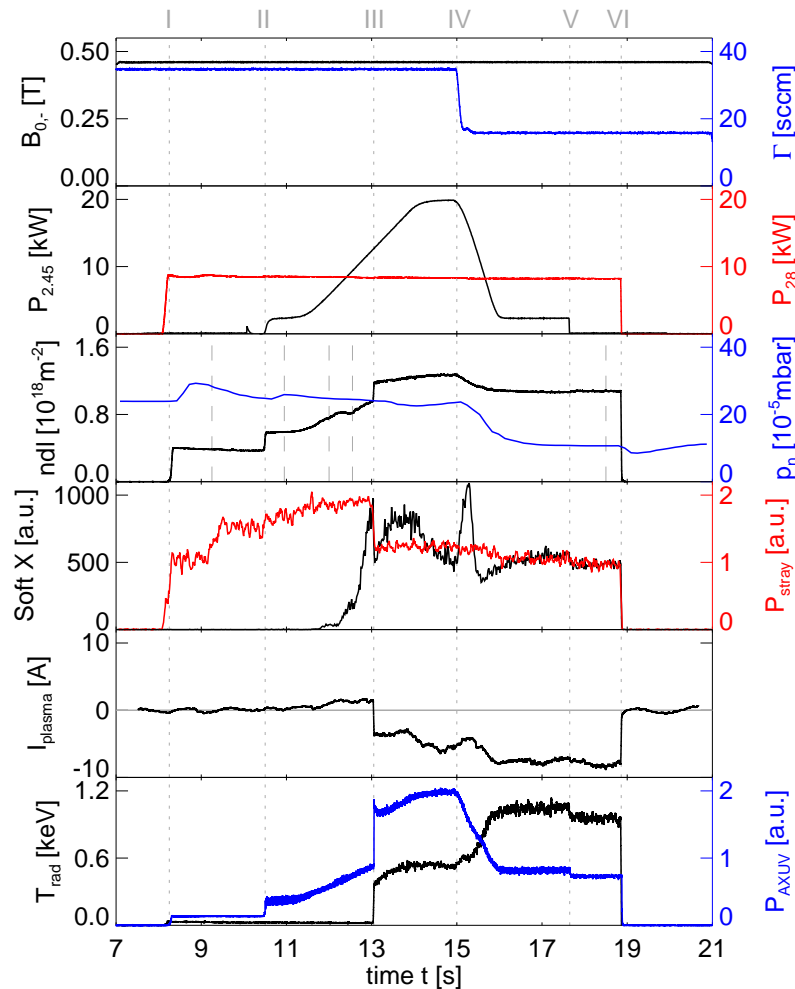


Figure 5.29: Time Traces of an OXB helium discharge (for  $-/-$  magnetic field configuration). There are shown the same plasma parameters as in Figure 5.1, as well as the soft X-ray counts combined with the gyrotron stray radiation  $P_{stray}$ . Please note the radiation temperature  $T_{rad}$  is given in keV for the frequency  $f_{27.3} = 27.3 \pm 0.3 \text{ GHz}$ . The additional vertical lines in the  $ndl$ -trace are related to the measured density profiles shown in Figures 5.30 and 5.31.

- I The magnetic field is set to  $B_0 = 460$  mT because the resonance of the later generated electron Bernstein waves is Doppler downshifted. The oblique incidence of the left hand polarized 28 GHz heating beam at  $\vartheta_{28} = 55^\circ$  is characterized by a very low single path absorption with less than 1 %<sup>24</sup>. Nevertheless, to achieve the desired high densities, the gas inlet is set to  $\Gamma = 35$  sccm resulting in a neutral gas pressure of  $p_n = 5.6 \cdot 10^{-5}$  mbar and a line integrated electron density of  $ndl = 0.4 \cdot 10^{18} \text{ m}^{-2}$ .
- II The 20 kW magnetron is switched on and ramped up to its maximum power output. With the 2 kW minimum output the line integrated density is nearly doubled by the non-resonant heating mechanism described in detail in subsection 5.1.2.4. Because of the further increased electron density and the resultant higher reflection of the 28 GHz heating beam, the stray radiation level reaches a maximum. The emission of the plasma, represented by the 8th channel of the lower AXUV-camera (see Figure 3.20), grows disproportionately with  $ndl$  as expected from the  $n_e^2$  dependence of the local emissivity  $\varepsilon$  (see subsection 5.1.1.3). With a magnetron power of about  $P_{2.45} = 11$  kW and a correspondingly high electric field in front of the magnetron antenna the soft X-ray diagnostic sees a certain amount of suprathermal electrons produced at the plasma edge by the SLA-mechanism described in subsection 5.1.2.6. The small plasma current of  $I_{\text{plasma}} \approx 1$  A in the same direction as the magnetic field vector shows the vanishing part of electrons with energies higher 200 keV<sup>25</sup>. The reason is the deceleration of the electrons by collisions with the neutral gas as well as ions suppressing a further stochastic Landau acceleration and current drive for energies higher than 200 keV. Below this value, electrons in co- and counter-direction to the magnetic field are well confined.
- III Achieving a line integrated density of  $ndl = 1.0 \cdot 10^{18} \text{ m}^{-2}$  the stray radiation level suddenly drops by a factor of two, indicating a higher absorption of the incident 28 GHz microwaves and the start of the OXB-heating phase. At this time the line integrated density increases to  $ndl = 1.2 \cdot 10^{18} \text{ m}^{-2}$  and the lower ratio of power to particle number leads to a decrease of fast particles. The plasma current, however, is reversed and considerably increased to  $I_{\text{plasma}} \approx -4$  A indicating a current drive by electron Bernstein waves. The detected emission by the AXUV-bolometer also increases with density. A temperature increase will be shown later with the evaluation of the Langmuir data. Besides the low stray radiation level, the OXB heated plasmas are characterized by extremely high microwave radiation levels in both central channels whose frequency ranges border on the 28 GHz heating frequency<sup>26</sup>. The corresponding radiation temperatures are of the order of keV being three magnitudes above the expected thermal electron Bernstein or electron cyclotron emission.
- IV The additional heating by the magnetron can be stopped and the gas inlet is set to  $\Gamma = 16$  sccm to reach higher plasma temperatures. The neutral gas pressure falls faster than the magnetron power, leading to an increase of fast particles by the SLA-mechanism and current drive in magnetic field direction. The electron density in the edge plasma is reduced by the further decreasing magnetron power so that the AXUV-bolometer detects a reduction of the plasma emission. This is accompanied by an increase of the microwave radiation indicating an increased density gradient.

---

<sup>24</sup>The absorption of the first path is nearly zero and only the extraordinary part of the heating wave, which is caused by polarization changes in the following paths, can be absorbed.

<sup>25</sup>In the standard magnetic configurations (+/+ or -/-) electrons with an energy  $> 200$  keV will only be well confined if their velocity vector is directed opposite to the toroidal magnetic field leading to a current drive in the same direction as the magnetic field.

<sup>26</sup>There is no overlap, however, as shown in subsection 3.2.4.

V With the completely turning off of the magnetron the plasma is fully sustained by electron Bernstein waves. The stray radiation level is still slightly decreased giving a further indication of a higher density gradient and a higher OX-conversion. The soft X-ray emission, however, is nearly constant, indicating the generation of a suprathermal electron component by the electrostatic waves.

VI After turning off of the gyrotron all parameters go to with the typical time constant of the order  $O(\text{ms})$ .

The control system allows for an immediate switching off of the magnetron power when reaching the OXB-phase. The line integrated density and the stray radiation level serve as indicators. The further decrease of the stray radiation and the slight increase of the line integrated density give the first evidence for the sensitive dependence of the OX-conversion on the incidence angle and on the edge density gradient. Figure 5.30 shows the evolution of the density and temperature during the ramp-up of the magnetron power. The non-resonant heating of the magnetron produces broad density profiles with a temperature maximum at the plasma edge. In comparison to the undisturbed density profile of the purely OXB-heated plasma, shown in Figure 5.31, the magnetron-heating leads to an outward shift of the OX-conversion position as well as to a flattening around its necessary density level of  $n_e = 10^{19} \text{ m}^{-3}$ . In this discharge the incidence angle of the 28 GHz heating beam was adjusted to a conversion position at  $r_{\text{eff}} = 3 \text{ cm}$ . The subsequent conversion of the slow X-waves to electron Bernstein waves (EBW) at the Upper Hybrid resonance typically has an efficiency close to 100 %. At first the main properties of the EBW-heating are compared to the previously presented discharges.

### 5.1.3.2 Power absorption

The temperature and the density profile in Figure 5.31b are centrally peaked but without a sharp absorption as is seen in the temperature profile of the centrally heated X2-plasma shown in Figure 5.2a. This is a sign of broader absorption by the thermalized plasma and can be confirmed by a calculation with the AMR-code introduced in subsection 2.2.3.3.

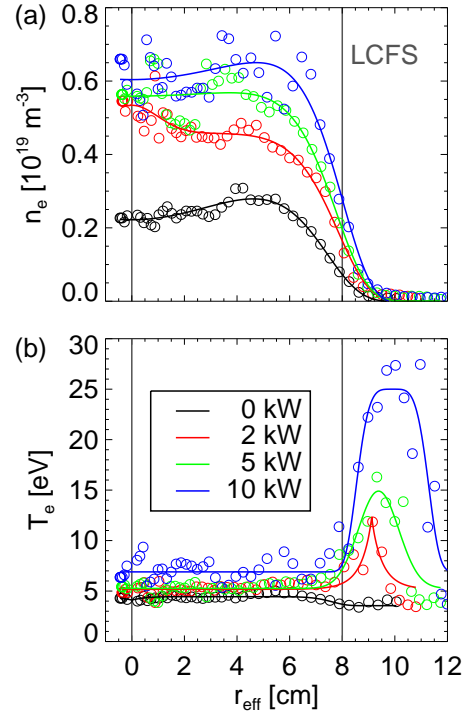


Figure 5.30: Comparison of the density (a) and temperature profile (b) during the ramp-up of the magnetron power to reach the threshold density of  $n_e = 10^{19} \text{ m}^{-3}$ . The time points of the measurement (9.2 s, 11.0 s, 12.0 s, 12.5 s) are depicted in Figure 5.29 by broken vertical lines in the *ndl*-window.

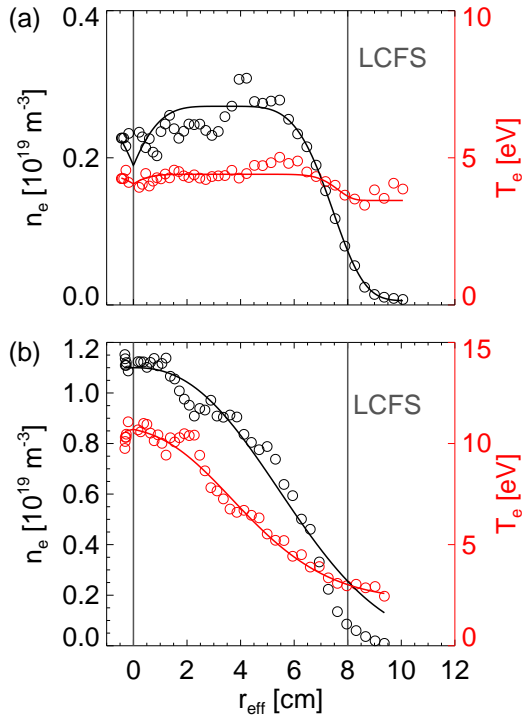


Figure 5.31: Langmuir temperature and density profile of the OXB phase at (b)  $t = 18.5$  s compared to the off-axis ECRH plasma at (a)  $t = 9.2$  s with  $B_0 = 460$  mT at the axis.

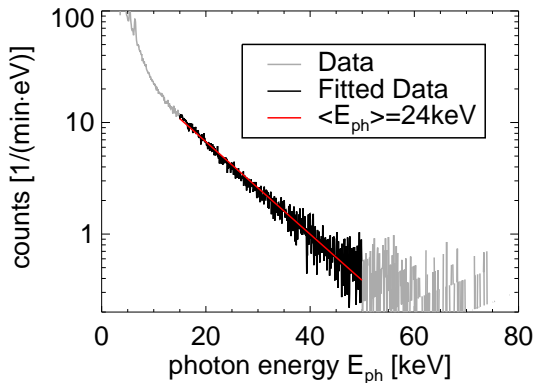


Figure 5.32: Soft X-ray spectrum of a pure EBW-heated plasma without Magnetron support. The integration was performed over a time of  $\Delta t = 20 \cdot 3$  s starting at  $t = 13.6$  s of the shown example discharge in Figure 5.34. The used modulation has no influence for a fit between  $E_{ph} = 15$  keV and 50 keV but the absolute count rate is reduced by about 40%.

Figure 2.10 shows the projections of the EBW propagation on the equatorial plane at  $z = 0$  and on the poloidal plane around the incidence position. As shown in Figure 2.12, the wave has a high parallel component to the magnetic field lines in the central plasma and therefore a high power deposition in the center, but the waves are continuously damped by collisions because of the still low temperature. The resistive absorption is estimated to be 50% as shown in Figure 2.11. All of the remaining power is absorbed near to the axis so that the absorbed power is mainly defined by the OX-conversion efficiency. Here, the acceleration mechanism of the suprathermal electrons is not important for the determination of the overall EBW-absorption. A time integrated energy resolved X-ray measurement during the EBW-heated part of the discharge leads to a spectrum shown in Figure 5.32. A Maxwellian fit results in a mean photon energy of  $\langle E_{ph} \rangle = 24$  keV that cannot be directly identified with a mean suprathermal energy. A monoenergetic electron beam in the plasma would produce a similar Bremsstrahlung spectrum but the details will be explained in 5.2.

An estimation of the total absorbed power is possible by using the power balance (5.2). With the profiles shown in Figure 5.31b the stored energy  $W_{\text{therm}}$  of the thermal plasma is  $W_{\text{therm}} = (0.85 \pm 0.1)$  J. The energy content of the OXB-plasma is nearly twice the centrally heated X2-discharges considering that the suprathermal component is not yet included. The energy confinement time is also approximately 1 ms as determined for the X2-discharge in subsection 5.1.1.3. The rotational transform is with  $t = 0.36$  slightly higher than the value  $t = 0.30$  of the regarded X2-discharge, but the collision frequency is increased by 50% because of the higher density. This results in a similar transport from the center to the plasma edge and an energy confinement time  $\tau_E \leq 1$  ms. For this reason, the transported power across the last flux surface is at least  $P_{\text{trans}} = 1$  kW. The radiated power can be determined by the Au-bolometer to  $P_{\text{rad}} = (7.3 \pm 1.4)$  kW seeming somewhat overrated in consideration of forward power of  $P_{\text{gyr}} = 8.8$  kW and 50% reduced sniffer signal compared to X2-heating.

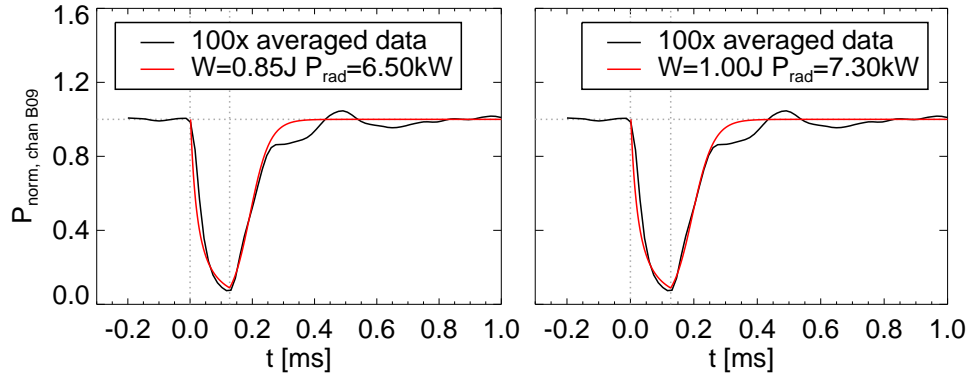


Figure 5.33: Radiated power of the central AXUV channel B09 fitted with equation (5.10) for a plasma energy of  $W = 0.85 \text{ J}$  (left) and  $W = 1.00 \text{ J}$  (right). With reference to Figure 5.10 the temperature dependence of the emissivity was assumed with  $\alpha = 4.6$ . The energy confinement time was determined to be (a)  $\tau_E = 0.9 \text{ ms}$  and (b)  $\tau_E = 0.8 \text{ ms}$ .

As a start this simple estimate indicates within the error bars of the radiated power a total absorption between 75 % and 100 %. A more accurate determination can be obtained by the power loss fitting technique recommended in subsection 5.1.1.3 in the case of a fast forward power modulation. The low confinement times and the high radiation power loss allow a switch-off of only up to 0.1 ms to sustain the EBW-heating. For this reason, the same modulation frequency  $f_{\text{mod}} = 788 \text{ Hz}$  with 90 % duty cycle was used as in the ECE-measurement of the X2-discharges. Similar to the discharge shown in Figure 5.12 all measured channels A05-A12 and B05-B12 of the tomographic AXUV-system show approximately the same behavior. Figure 5.33 shows the average of 100 modulation periods of the central AXUV channel B09 and the best fit of equation (5.10) for two different pairs of the input values of radiated power,  $P_{\text{rad}}$ , and total stored energy  $W = W_{\text{therm}}$ . The suprathermal energy  $W_{\text{supra}}$  is not included because of vanishing excitation and recombination at energies of some keV. Even if the absorption occurs only by the fast electrons, the subsequent power transfer by collisions is interpreted by the model as direct absorption. For the determined thermal energy of  $W = 0.85 \text{ J}$  the best fit leads to a radiated power of  $P_{\text{rad}} = 6.5 \text{ kW}$  and an energy confinement time of  $\tau_E = 0.9 \text{ ms}$ . The absorbed power results in  $P_{\text{abs}}/P_{28} \approx 83 \%$ . In contrast, a fixed radiated power of  $P_{\text{rad}} = 7.3 \text{ kW}$  demands  $W = 1.00 \text{ J}$  and  $\tau_E = 0.8 \text{ ms}$  with an absorption of  $P_{\text{abs}}/P_{28} \approx 95 \%$ . The minimum of the curve in Figure 5.33 is defined mainly by the energy content and the radiation loss. The energy confinement time has only a minimal effect, as the ratio of the convective losses to the total loss power is smaller than in the X2-discharges because of the disproportionately higher emissivity. Nevertheless, the total absorption can be curtailed between 83 % and 95 %. An additional important point in the AXUV time traces is the delayed hump at  $t = 0.5 \text{ ms}$  pointing to a secondary process such as the already mentioned power transfer by the suprathermal particles. A more detailed investigation will follow in section 5.2.

The determined value of absorption must be compared with the behavior of the stray radiation signal. Figure 5.34 shows the complete discharge with the performed modulation, starting at  $t = 13.6 \text{ s}$ . In this example the magnetron power is immediately shut down after achievement of the overdense OXB-phase. The stray radiation level drops from  $P_{\text{stray}} = (1.4 \pm 0.1) \text{ [a.u]}$  to  $0.8 \text{ [a.u]}$  but an absolute calibration factor for the determination of the non absorbed power is not attainable.

For instance, around  $t = 9$  s the detected stray radiation level in Figures 5.34 and 5.29 increases without change in the control parameters or the other detectable signals. For this reason, the absorption cannot be determined by means of the stray radiation signal. The relative absorption change, however, is analyzed in the following. The energy content and radiation loss of the underdense plasma phase are comparable with those of the considered X2-discharge but the energy confinement time must be lower because of its off axis power deposition. In the best case the total absorption can reach the determined X2-value of 30 %, but with this value, the total EBW-absorption reaches a maximum of 60 %. Including the large error of the X2-value a similar EBW-absorption as in the power loss fit can be obtained. Nevertheless, an accurate determination of the absorbed power with the aid of the stray radiation signal is not possible.

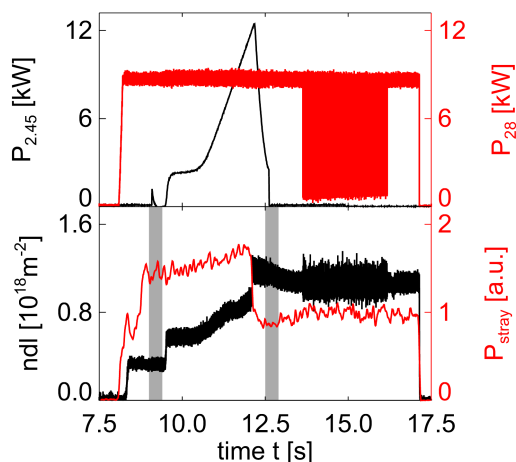


Figure 5.34: Helium discharge including a modulation period of the gyrotron forward power  $P_{2,45}$  with a modulation frequency of  $f_{mod} = 788$  Hz and 1999 periods. The full acquisition resolution of 100kHz is shown for the gyrotron and the line-integrated density  $ndl$ . Gray shaded areas are related to the considered stray radiation level  $P_{stray}$  for X2- as well as OXB-heating.

As already explained in subsection 5.1.1.2 it is not possible to obtain a precise evaluation by this method because of the uncertainties of the diffusivities and the gradients in the edge region. The calculated  $P_{trans}$ , however, agrees with to the initial estimate at the beginning of this subsection.

Another way to check the results of the overall absorption is through the determination of the thermal and particle diffusivity, as was attempted for the X2-scenario in subsection 5.1.1.2. In combination with the temperature and density gradients in the edge region the transported power  $P_{trans}$  across the last closed flux surface can be calculated by equation (5.5). An extensive description of such a calculation with the aid of the WEGA AXUV-bolometer can be found in [ZGL<sup>+</sup>12]. For three different modulation amplitudes (186 Hz, 373 Hz and 746 Hz) the measured phase delay profile was compared with a numerical computation of the electron energy transport equation. The best agreement was achieved for a central thermal diffusivity of  $\chi = (1.9 \pm 0.4) m^2/s$  [ZGL<sup>+</sup>12]. For the determination of the particle diffusivity  $D$  a similar method was used in [ZBG<sup>+</sup>11]. The 1D particle diffusion equation was solved numerically for different radially constant values of  $D$ . For  $D = 3.5 m^2/s$  the resultant density profile and emissivity profile are in accordance with the measurement [ZBG<sup>+</sup>11]. By using these values together with the temperature and density profile of Figure 5.31, the transported power can be calculated to  $P_{trans} = (1.2 \pm 0.6) kW$ . As

## 5.2 Generation of suprathermal particles

The detailed investigation of a suprathermal component generated during microwave heating is of fundamental importance for the analysis of the underlying acceleration process. The first subsection describes the general dependence of the detected energy distribution on the global parameters of OXB-heated discharges. Here, the discrimination between a monoenergetic and a thermalized component appears as a central problem. This is followed by a broader description of the spatially resolved measurement with the aid of different soft X-ray diagnostic setups. The simultaneous improvement of the detection efficiency of the soft X-ray diagnostics also enables the time resolved measurement during heat modulation experiments described in subsection 5.2.3. The last subsection is dedicated to the relativistic electrons which can be generated in the SLA-discharges briefly introduced in subsection 5.1.2.6. An answer will be given to the question of how the maximum energy can be estimated with the aid of the emitted gamma rays and microwaves.

### 5.2.1 Energy distribution in OXB-heated discharges

The main goal of the energy resolved X-ray measurement is the characterization of the energy range of the suprathermal electrons. As introduced in subsection 3.2.6, soft X-ray spectra can be used for the determination of the bulk electron temperature of fusion plasmas achieving typically some keV. In this case the main condition of a Maxwellian energy distribution function is usually fulfilled. Certain heating scenarios or a loop voltage, however, can produce suprathermal or runaway electrons with energies up to MeV because of the decreasing collision frequency with higher velocity. For this reason, the distribution function is non-Maxwellian and the suprathermal electron component is possibly characterized by a more or less discrete energy. The residual collisions within the plasma or with hard targets produce a continuous Bremsstrahlung spectrum with a local exponential dependence, but the photon energy distribution has no direct connection to the energy distribution of the suprathermal electrons. The determination of the corresponding electron energy distribution function (EEDF) is a more challenging problem and necessitates detailed calculations to reconstruct the measured Bremsstrahlung spectrum. The initial problem, however, is to distinguish between a monoenergetic electron component and independently thermalized suprathermal electrons<sup>27</sup> with the aid of the measured X-ray spectrum. For a monoenergetic electron component, the energy distribution of the primary photons due to Bremsstrahlung is available in standard libraries. Figure 5.35 shows the Bremsstrahlung spectrum for the interaction with different neutral target elements being relevant in the case of WEGA<sup>28</sup>.

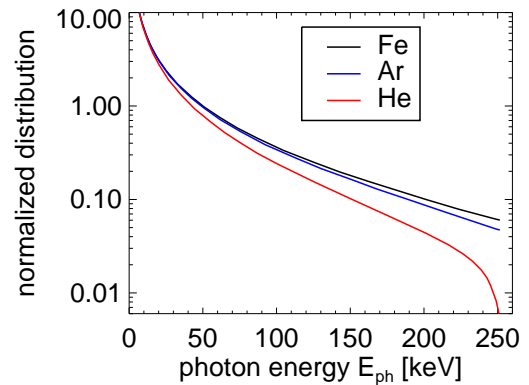


Figure 5.35: *Bremsstrahlung spectrum of a monoenergetic electron component with  $E_{mono} = 251$  keV interacting with an iron, argon or helium target. Original data of Evaluated Electron Data Library (EEDL) [CPS91].*

<sup>27</sup>Independently thermalized suprathermal electrons are characterized by a Maxwellian energy distribution function.

<sup>28</sup>Even though the plasma particles are ionized, the shown relative energy dependence will give a feeling of the emission source of the detected hard X-rays.

The walls of the torus as well as the components in the vessel consist of stainless steel, acting as limiter for a rotational transform  $t \lesssim 0.25$ . Also, with the use of higher iota, plasma particles leaving the last closed flux surface are guided along the open field lines and collide with the walls. The sputtered iron particles can be ionized in the plasma and act as additional Bremsstrahlung targets. For this reason, the detected spectrum of Figure 5.32 as well as any other X-ray spectra of WEGA contains the characteristic  $K_\alpha$  lines of iron (6.397 keV) and chromium (5.410 keV) [Att99]. Additionally the  $K_\alpha$  line of argon (2.957 keV) appears, which is routinely used. If the bulk plasma has an impurity concentration of 1 % iron, the corresponding photon emission of the electrons by ff- and fb-transitions will be more than one magnitude higher than for the interaction with the ions of the bulk plasma [Wel04]. Nevertheless, the spectrum is dominated by fb-transitions<sup>29</sup> [Wel04].

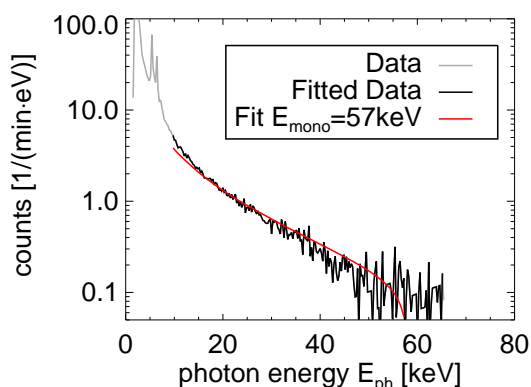


Figure 5.36: *Detected X-ray spectrum over a time of  $\Delta t = 15 \cdot 4$  s at neutral gas pressure of  $p_n = 13 \cdot 10^{-5}$  mbar fitted with the Bremsstrahlung spectrum of a monoenergetic electron component of 57 keV colliding with a helium target. The used magnetic field configuration was +/+.*

identification of the measured hard X-ray ( $> 10$  keV) spectrum with a real electron energy distribution generally must be excluded. An independent thermalization of the suprathermal electrons by collisions between themselves is not possible because of a collision time greater than the confinement time of the bulk plasma. It is more probable that such particles lose the main part of their energy via Bremsstrahlung and through collisions with the bulk electrons, as the collision frequency with ions and electrons are similar. On the other hand, the particles can be accelerated in a stochastic process generating a continuous energy distribution also in the high energy range. Nevertheless, both processes can lead to a more or less Maxwellian distribution in the soft X-ray related energy range.

The X-ray spectrum, detected with the WEGA-PHA1 during an OXB-phase with a neutral gas pressure of  $p_n = 13 \cdot 10^{-5}$  mbar<sup>30</sup>, is fitted in Figure 5.36 with the Bremsstrahlung spectrum of a monoenergetic electron component colliding with a helium target. Good agreement can be found for an energy of  $E_{\text{mono}} = (57 \pm 5)$  keV. For other targets the slope of the detected hard X-ray signal is too steep. For  $E_{\text{ph}} \leq 10$  keV the best fit is achieved for  $E_{\text{mono}} = 10$  keV, so that the spectrum can be produced by two monoenergetic components. Furthermore, the

<sup>29</sup>For this reason, the reduction of impurities in fusion plasma is one of the main goals.

<sup>30</sup>Accordant to a helium gas inlet of  $\Gamma = 20$  sccm.

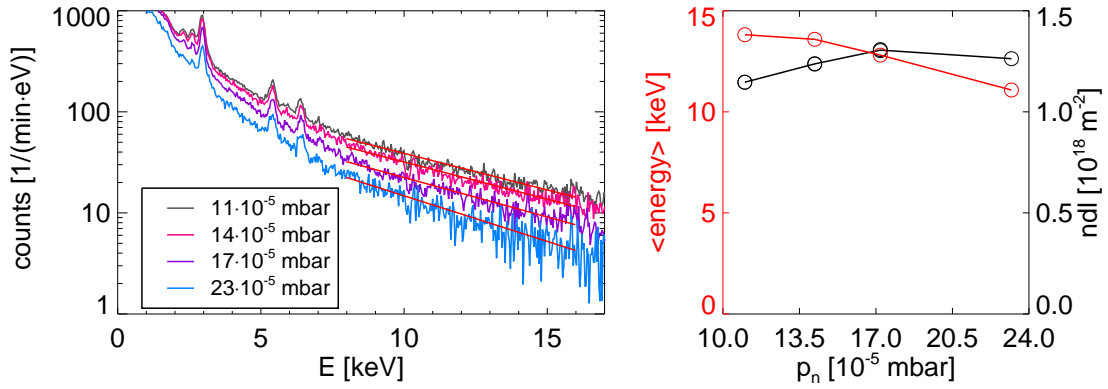


Figure 5.37: *Bremsstrahlung spectrum measured by SDD1 at different neutral gas densities  $p_n$ , with an exponential fit between 8 keV and 16 keV (left) showing an increase of the mean energy with lower neutral gas density (right). The spectrum at  $p_n = 23 \cdot 10^{-5}$  mbar is detected during an OXB-heated phase of 4.7 s length whereas the other ones are the average of two shots with the same time window. The binning is set to 16 resulting in a resolution of 512 channels (The magnetic field configuration used was +/+).*

different slopes of the soft and hard X-ray related energy ranges can be seen to be a sign for different underlying physics. However, it is unlikely that a monoenergetic electron component is the exclusive source for the whole measured X-ray spectrum. For this reason, the soft X-ray range is analyzed by means of a Maxwellian fit in the following section, even though the obtained averaged photon energy cannot be identified with the average suprathermal electron energy. In the next subsections the question is further discussed whether the suprathermal electrons are characterized by a Maxwellian energy distribution or not.

Figure 5.37 shows the energy spectrum detected by SDD1 at different neutral He gas pressures<sup>31</sup>. The relative count rate is generally higher with lower neutral gas pressure. For the examples shown the line integrated density has an almost linear dependence on the neutral gas pressure up to a value of  $11 \cdot 10^{-5}$  mbar. Regarding the overall density as a measure for the OXB-heating efficiency an optimum is achieved at  $p_n = 17 \cdot 10^{-5}$  mbar with a gas inlet around  $\Gamma = 26$  sccm. The detected averaged energy for this case is only 10% lower compared with the maximum at  $p_n = 11 \cdot 10^{-5}$  mbar, but the detected counts in the considered energy range are almost 50% lower. With higher neutral gas density the line integrated density stagnates and becomes slightly smaller indicating a decreasing heating efficiency due to a decreasing density gradient caused by collisions with neutral particles.

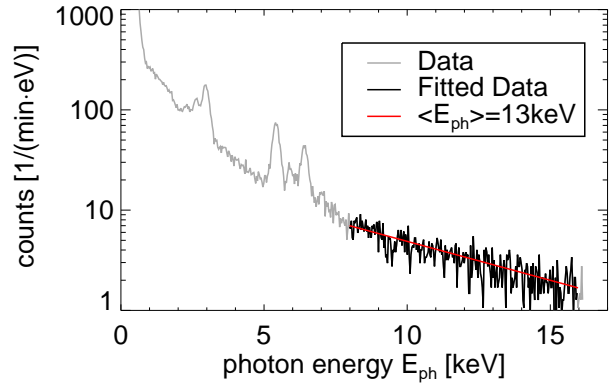


Figure 5.38: *Soft X-ray spectrum at a neutral gas pressure of  $p_n = 13 \cdot 10^{-5}$  mbar detected with the WEGA-PHA1 over a time window of  $\Delta t = 3 \cdot 3$  s. A binning of 4 channels is used to show the same resolution as Figure 5.37 with the same exponential fit between 8 keV and 16 keV (The magnetic field configuration used was +/+).*

<sup>31</sup>The accordant gas inlets were set to 17.5 sccm ( $11 \cdot 10^{-5}$  mbar), 22.0 sccm ( $14 \cdot 10^{-5}$  mbar), 26.5 sccm ( $17 \cdot 10^{-5}$  mbar) and 35.5 sccm ( $23 \cdot 10^{-5}$  mbar).

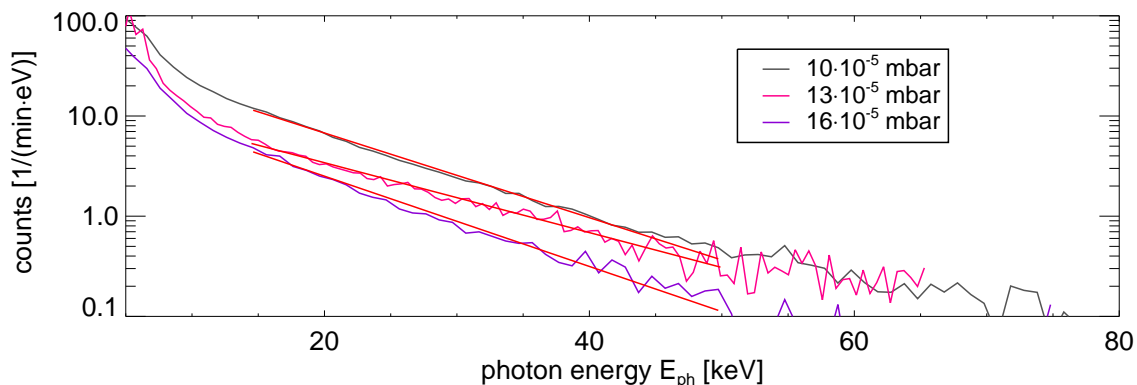


Figure 5.39: *Bremsstrahlung spectrum measured by WEGA-PHA at different neutral gas densities  $p_n$  and different magnetic field configurations, with an exponential fit between 15 keV and 50 keV showing an optimum for the production of suprathermal particles at  $p_n = 13 \cdot 10^{-5}$  mbar and  $+/+$  configuration in contrast to the other both traces with a  $-/-$  configuration. The spectrum for  $13 \cdot 10^{-5}$  mbar is divided by 1.5 for better visualization of the differences in the hard X-ray energy range.*

The expected count rate per eV and  $m^2$  can be calculated by summation of ff-, fb- and bb-transitions depending on the electron density, temperature and impurity concentration, which is implemented in the so called IONEQ-code written by Arthur Weller [Wel04]. The code takes into account the summation of profile dependent emission along the line of sight and computes the expected spectral power per eV and  $m^2$ , including the transmission of the used Be-window as well as the detector efficiency. For the detected spectrum at  $p_n = 11 \cdot 10^{-5}$  mbar a calculation by Weller shows the best agreement for a suprathermal density of 0.025 % of the bulk electron density with an averaged energy of 9 keV [Wel10]. The lower energy in comparison with the values determined in Figure 5.37 is the result of taking into account the section between 3.5 keV and 5 keV, which has a higher slope and therefore a smaller averaged energy. The impurity concentration of high-Z-elements is not known in WEGA, such that the computation was executed with only a pure helium plasma. Therefore, the determined suprathermal density is an upper estimate. Furthermore, the suprathermal particles are assumed to be homogeneously distributed in relation to the bulk electron density so that the resultant energy content of  $W_{\text{supra}} = 0.24$  J [Wel10] must also be interpreted also as an upper limit. A more exact determination of  $W_{\text{supra}}$  can be obtained with the knowledge of the spatial distribution, which is topic of the next subsection.

Comparing the results of SDD1 and the WEGA-PHA, nearly the same averaged energies are achieved for an exponential fit between 8 keV and 16 keV as shown in Figure 5.38 for a neutral gas pressure  $p_n = 13 \cdot 10^{-5}$  mbar. The determined value of  $\langle E_{\text{ph}} \rangle = 13$  keV is in very good agreement with the respective value of 13.6 keV for the gas scan shown in Figure 5.37. Furthermore, the count rates are similar taking into account the closer distance of 77 cm of SDD1 to the plasma axis. An advantage of the thicker Si(Li)-detector is the higher efficiency in the hard x-ray range. Figure 5.39 shows the comparison of different gas pressures for the energy range up to 80 keV. Furthermore, the magnetic field configuration for the intermediate pressure of  $p_n = 13 \cdot 10^{-5}$  mbar is  $+/+$ <sup>32</sup>. A difference in the maximum energy cannot be

<sup>32</sup>A spectrum in the hard X-ray related energy range necessitates at least 10 shots so that a measurement for every gas pressure was not indicated. The main focus was placed on the locally resolved measurements presented in subsection 5.2.2. Furthermore, the  $-/-$  magnetic field configuration is defined as WEGA standard configuration. A change to  $+/+$  requires a half day because of hardware modifications.

identified, but the different slopes show an optimum of fast particle production for the  $+/+$  configuration. In this case, a current twice as high as in the case of the  $-/-$  configuration is typical, which partially is the result of a higher electron energy in addition to a higher density of suprathermal electrons. To obtain a quantitative measure, an averaged energy was determined by means of an exponential fit with  $\langle E_{\text{ph}} \rangle = 29$  keV for the  $+/+$  trace compared to the outer  $-/-$  traces with  $\langle E_{\text{ph}} \rangle \approx 23$  keV. The important question, which electron component drives the current and which kind of energy distribution has the suprathermal component will be answered in the subsection after next with the determination of the spatial distribution of the suprathermal electrons. For a monoenergetic Bremsstrahlung fit as shown in Figure 5.36, a slope of  $\langle E_{\text{ph}} \rangle = 23$  keV is too steep, even though a Maxwellian energy distribution cannot be intrinsically argued.

## 5.2.2 Spatially resolved measurements during OXB-heated discharges

The spatial distribution of the suprathermal electrons inside the plasma was determined with the aid of the Langmuir probe and different soft X-ray diagnostic systems. The influence of the suprathermal component on current drive directly results from the Langmuir measurements. The question of a Maxwellian distribution can be answered with the aid of the spectral and spatial PHA-measurements.

### 5.2.2.1 Position by Langmuir perturbation

Figure 5.40 shows the time traces of the current and the detected soft X-rays during the perturbation of the suprathermal electron population by a Langmuir probe. The current goes down to zero at a minor radius of  $r = 2$  cm and the increase during outward movement appears at the same radial position. The 30 A shown for  $p_n = 10 \cdot 10^{-5}$  mbar and  $+/+$  magnetic field configuration is the maximum observed current in the OXB-discharges. At  $p_n = 13 \cdot 10^{-5}$  mbar the current decreases to 20 A, the hard X-ray spectrum of which (Figure 5.39), shows a higher averaged photon energy compared to the  $-/-$  configuration. This is interpreted as a higher suprathermal energy partially generating the higher current (see subsection 5.2.1).

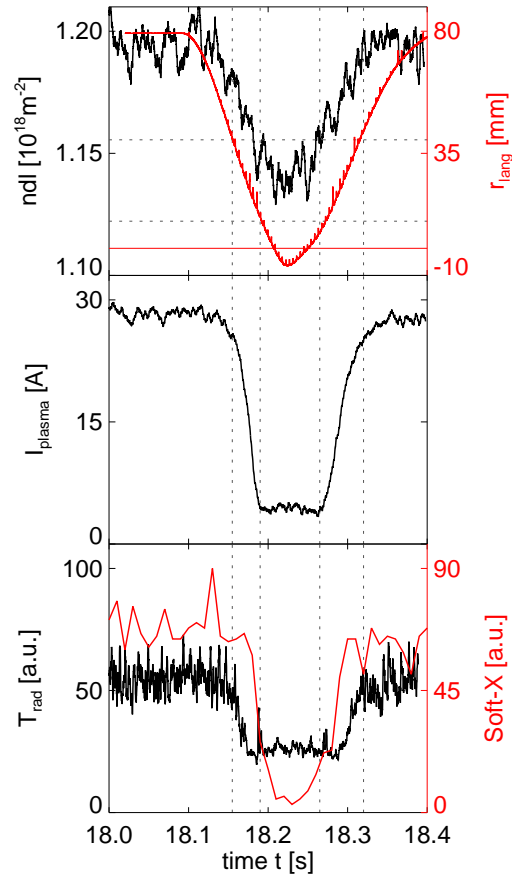


Figure 5.40: Capture of suprathermal particles by a fast reciprocating Langmuir probe ( $p_n = 10 \cdot 10^{-5}$  mbar,  $+/+$ ). The position of the probe tip is depicted as minor radius  $r$  with the plasma axis at  $r = 0$  mm. The line integrated density  $ndl$  shows only slight change but the plasma current  $I_{\text{plasma}}$ , the soft X-ray emission and the microwave radiation temperature  $T_{\text{rad}}$  ( $f_{\text{rad}} = 24.7 \pm 0.3$  GHz) are clearly distorted by the Langmuir probe.

The simultaneous decrease of the soft X-ray signal in Figure 5.40 indicates the exclusive current drive by the suprathermal electrons because the line integrated density shows at the same time a decrease of only 5%. The density gradient, however, can decrease, leading to a decrease of the OX-conversion efficiency and the electron temperature. A time dependent bulk temperature measurement is not available at WEGA, but the AXUV-bolometer has a high temperature sensitivity, as was mentioned in subsection 5.1.1.3. Considering the undisturbed temperature profile of Figure 5.31b, the emission decrease is related to a temperature decrease of about 3%. This leads to the assumption that a maximum of 5 A of the current can be caused by the bulk electrons. The radiometer channel with the frequency range  $f_{\text{rad}} = 24.7 \pm 0.3$  GHz also indicates a decrease of the detected emission, which could be electron Bernstein wave emission by the suprathermal electrons, or electron cyclotron emission by underdense plasma edge regions. The source of the emission must be investigated in detail, as will be described in section 5.3.

### 5.2.2.2 1D-resolution by WEGA-PHA

The position of the suprathermal electrons was narrowed down to within a minor radius of  $r_{\text{eff}} = 4$  cm, whereas the distortion of the heating process by the Langmuir probe indicates a fairly broad region. Furthermore, the probe can miss the plasma center or the suprathermal component can deviate from the vacuum flux surfaces. For this reason, the WEGA-PHA was upgraded with a pinhole moveable in  $z$ -direction.

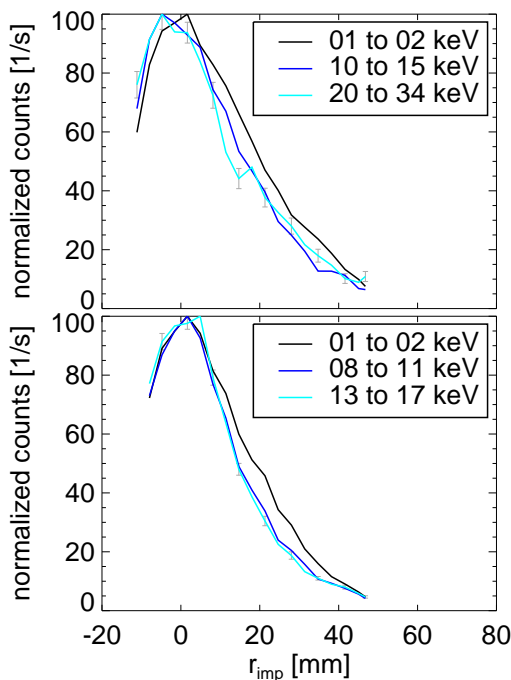


Figure 5.41: *Line integrated profile of the detected X-ray emission at a neutral gas pressure of  $p_n = 13 \cdot 10^{-5}$  mbar (top) and  $p_n = 10 \cdot 10^{-5}$  mbar (bottom) for a ++ magnetic field configuration.*

The setup of PHA1 is shown in Figure 3.25. The comparison of the spatially resolved X-ray emission at different energies will give more information on the thermalization of the suprathermal electrons and the existence of a Maxwellian energy distribution. The measurement of an X-ray profile requires almost one full experiment day because each position is related to one or two shots. Depending on the measured count rate, this number has been increased for better statistics. The cone of the viewing area captured by the whole detector area has a diameter of 7.5 mm, defining the resolution of the measurement. Figure 5.41 shows the profile of the line integrated X-ray emission for a neutral gas pressure of  $p_n = 13 \cdot 10^{-5}$  mbar. The depicted energy ranges were chosen in this way so that the total counts are of the same order of magnitude. All energies show a narrow profile centered on the magnetic axis with a 10 mm width of constant central emission. Considering the finite resolution, this value is reduced in reality to under 5 mm, which agrees with the power deposition zone. The decreasing X-ray emission with higher  $r_{\text{imp}}$  is related to transport, proven by temporally resolved measurements described in subsection 5.2.3. Both energy ranges  $E_{\text{ph}} = 20 - 34$  keV

and  $E_{\text{ph}} = 10 - 15$  keV show only marginal differences in spatial distribution, but a slightly broader line integrated profile can be identified for  $E_{\text{ph}} = 01 - 02$  keV. This is a sign of X-ray emission of different electron components. For this reason, the Bremsstrahlung emission in the soft X-ray related energy range cannot be produced exclusively by a monoenergetic electron component. A Maxwellian energy distribution, however, cannot be concluded because electrons with different start energies and different transport behavior can be generated by the electron Bernstein wave heating. A Maxwellian energy distribution over the whole energy range is improbable because the equipartition time increases with higher energy.

The analysis of the averaged energy for different energy ranges gives proof of independently thermalized electrons up to the energy of 5 keV. The interaction probability with the Bremsstrahlung target is constant for the whole profile of Figure 5.41, because the electron density profile, shown in Figure 5.31b for  $p_n = 10 \cdot 10^{-5}$  mbar, has, within the effective radius of  $r_{\text{eff}} \leq 4$  cm, nearly the same value. The suprathermal electron component thermalizes with the plasma and loses its energy completely. In the energy range  $E_{\text{ph}} = 01 - 02$  keV the averaged suprathermal energy is approximately 3 keV with only a slight decrease of 10 % to higher  $r_{\text{eff}}$ . For this reason, the suprathermal electron component must have a more or less Maxwellian energy distribution already in the center. In contrast, the inverse tendency is observable in the energy range  $E_{\text{ph}} = 08 - 16$  keV<sup>33</sup>, which is on the other hand not a sign of a monoenergetic electron component. In fact, an initial distribution function is depopulated more rapidly at lower energies and the local energy distribution function becomes flatter. For this reason, a higher averaged energy can be measured within the photon energy range  $E_{\text{ph}} = 08 - 16$  keV for higher  $r_{\text{eff}}$ .

Similar profiles of X-ray emission can be measured for lower neutral gas pressures. As shown in Figure 5.41 for a neutral gas pressure of  $p_n = 10 \cdot 10^{-5}$  mbar, the profile of the soft X-ray related energy range  $E_{\text{ph}} = 1 - 2$  keV is broader than the profiles for energies  $E_{\text{ph}} > 8$  keV. In the center, however, the profiles are slightly more peaked than is the case for  $p_n = 13 \cdot 10^{-5}$  mbar. This is accompanied by a higher averaged energy, as shown in Figure 5.37.

It has to be recalled that the shown profiles constitute a line integrated measurement with variation in  $z$ -direction. A further resolution in radial direction is necessary to investigate a deviation of the drift orbits from the vacuum flux surfaces. Furthermore, the emission could be a result of strike points at the inner wall because of the visible line emission of iron and chromium as is apparent in Figure 5.38. For this reason, an observation under a finite angle to the equatorial plane was contemplated with aid of the PHA2-setup, which is shown in Figure 3.27. By additional use of the vertical field coils the plasma could be shifted in radial direction so that a simultaneous shift of the emission would clearly indicate the plasma as the source of the emission.

The measured profiles for different radial positions of the plasma are shown in Figure 5.42 for a gas pressure of  $p_n = 15 \cdot 10^{-5}$  mbar. The illustrated expected position of the plasma center is in agreement with the measured position, confirming once again the suprathermal electrons in the plasma as source of the detected emission. The energy dependence of the profiles is similar to the measurements of PHA1 with a clear broadening in the soft X-ray related energy range. The width of the profiles are slightly broader than the profiles of Figure 5.41 at a neutral gas pressure of  $p_n = 10 \cdot 10^{-5}$  mbar and  $13 \cdot 10^{-5}$  mbar.

<sup>33</sup>The energy range  $E_{\text{ph}} = 05 - 08$  keV cannot be analyzed because of characteristic line emission as is apparent in Figure 5.38.

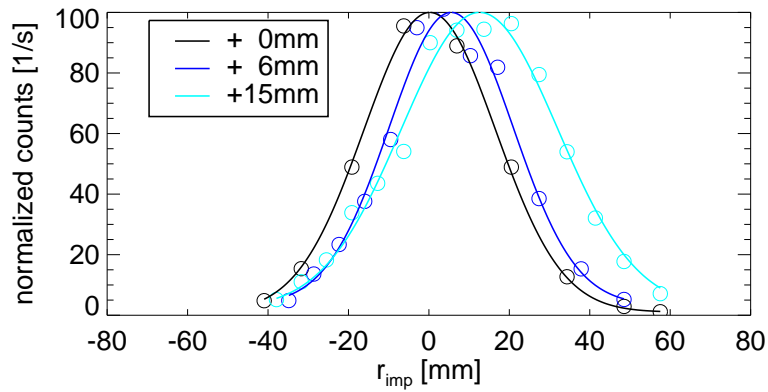


Figure 5.42: Line integrated profile of the detected X-ray emission between  $E_{ph} = 8 - 16$  keV at a neutral gas pressure of  $p_n = 15 \cdot 10^{-5}$  mbar and different plasma axis positions for a  $-/-$  magnetic field configuration. The shape of the flux surfaces is unchanged so that the same assignment is used for all profiles. The resultant shifts (0.2 mm, 5.5 mm, 12.6 mm) of the Gaussian fits are in good agreement with the expected radial shifts (0 mm, 6 mm, 15 mm).

A direct comparison of the measurements with PHA1 and PHA2 are shown in Figure 5.43 for the energy range  $E_{ph} = 13 - 17$  keV and a neutral gas pressure of  $p_n = 10 \cdot 10^{-5}$  mbar. Considering the different spatial resolutions, both profiles agree<sup>34</sup>.

As main results of the measurements of PHA1 and PHA2, it can be established that the suprathermal electrons are generated very localized in the plasma center and thermalize by collisions with the bulk plasma. A Maxwellian distribution can be assumed for photon energies up to a few keV.

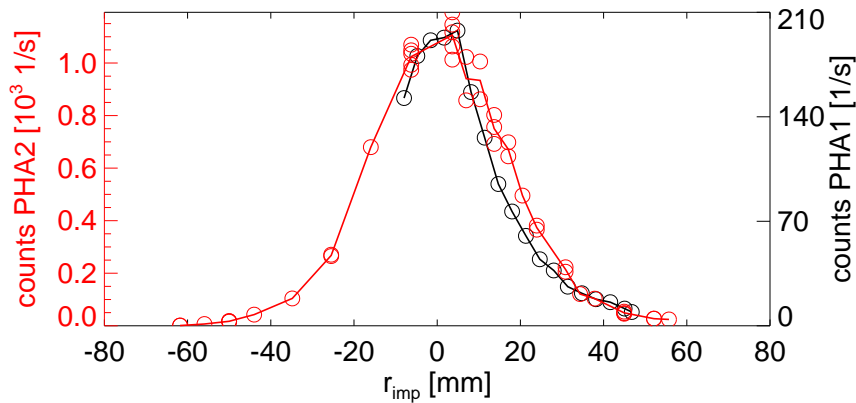


Figure 5.43: Direct comparison of the line integrated X-ray profiles measured by PHA1 and PHA2 for the energy range between  $E_{ph} = 13 - 17$  keV at  $p_n = 10 \cdot 10^{-5}$  mbar.

<sup>34</sup>For this reason, the condition to use the vacuum flux surfaces for the assignment of the PHA-sightlines to a certain impact radius was satisfied, which was explained in subsection 3.2.6.1.

### 5.2.2.3 2D-resolution by Drago detector array

The Drago detector array was originally installed for the two dimensional measurement of the relativistic electrons generated in the SLA-discharges. In the case of the OXB-discharges the system was operated without the scintillator crystal, allowing the measurement of photon energies  $E_{\text{ph}} \approx 10 - 30$  keV only<sup>35</sup>. Figure 5.44 shows the 2D image at a neutral gas pressure of  $p_n = 13 \cdot 10^{-5}$  mbar. The concentrated X-ray emission around the magnetic axis can be clearly identified. The poloidal profile is in accordance with the measurements of PHA2.

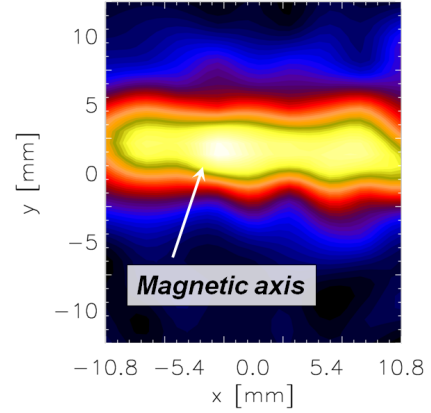


Figure 5.44: 2D X-ray emission measured with the Drago detector array.

### 5.2.3 Temporally resolved measurements during OXB-heated discharges

The measured peaked X-ray profile indicates a central absorption of the electron Bernstein waves, but the cause for the tapering off shoulders can be Doppler broadening or collisional transport of the suprathermal electrons. The answer will be given by spatially and temporally resolved measurements.

Figure 5.45 shows the calculated phase delay of the detected soft X-ray counts to the modulated gyrotron forward power during the electron Bernstein wave heated phase of a helium OXB-discharge<sup>36</sup>. The used time dependent PHA-signal contains all photon energies down to a lower edge of  $E_{\text{ph}} \approx 1$  keV so that hard X-ray photons have no influence on the phase relation. Around the centralized deposition zone the soft X-ray emission has zero phase delay to the forward power demonstrating the direct heating of electrons in the soft X-ray related energy range and the resultant energy transfer by collisions. At a higher impact radius of approximately  $|r_{\text{imp}}| = 3$  cm the phase delay is increased, indicating a transport of suprathermal electrons and no direct heating in this region. The emission around  $|r_{\text{imp}}| = 2$  cm are probably dominated by the central region because of the bad spatial resolution of the used PHA2-configuration. For this reason, a finite phase delay should be present for the data points around  $|r_{\text{imp}}| = 2$  cm.

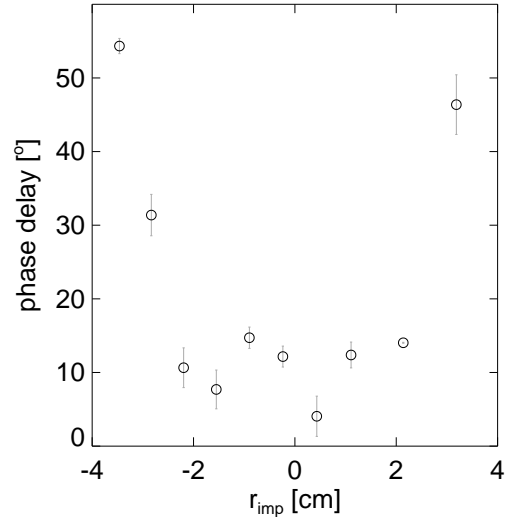


Figure 5.45: Phase delay of the detected X-ray counts to the gyrotron forward power modulated with a frequency of  $f_{\text{mod}} = 788$  Hz and 90 % duty cycle. The spatial distribution is shown in Figure 5.42 by the blue trace that is centrally peaked around the accordant  $r_{\text{imp}} = 6$  mm because of a radial shift of the magnetic field configuration. In the actual view this shift is corrected.

<sup>35</sup>The lower energy limit is given by the transmission of the vacuum quartz window

<sup>36</sup>An example of the discharge scenario is shown in Figure 5.34 for a neutral gas pressure of  $p_n = 10 \cdot 10^{-5}$  mbar.

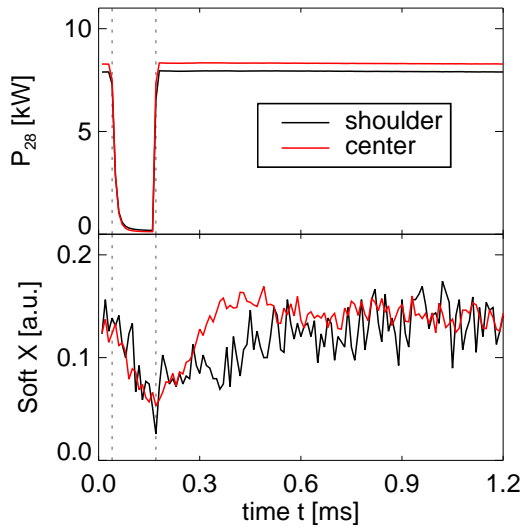


Figure 5.46: Averaged time traces of the detected X-ray photons during 1950 gyrotron power modulation periods at  $p_n = 15 \cdot 10^{-5}$  mbar with central view around  $r_{imp} = 0$  mm and  $r_{imp} = -35$  mm indicating the exclusive absorption in the center. The count rate of the trace 'shoulder' was multiplied by factor 5.

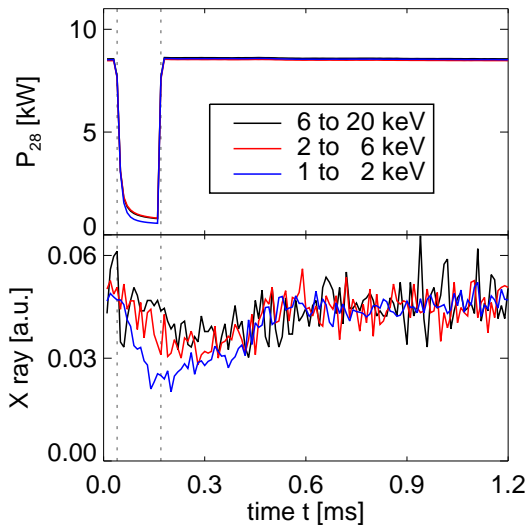


Figure 5.47: Averaged time traces of the detected X-ray photons of different energy ranges during gyrotron power modulation at  $p_n = 10 \cdot 10^{-5}$  mbar. The time window  $t = 1.1 - 1.2$  ms is used for the normalization of the black and red trace to the count rate of the energy range  $E_{ph} = 1 - 2$  keV.

The immediate response at the center can be also visualized in the time dependent count rate by averaging over the modulation periods as shown in Figure 5.46. While the decrease after switch-off is determined by the particle collisions in both cases, a direct heating after switch-on at first appears in the central region. In contrast, the measurement at  $p_n = 10 \cdot 10^{-5}$  mbar leads to an overall phase shift of approximately  $60^\circ$  independent on the radial position. This must be a result of the lower collision frequency as well as the longer acceleration time. Therefore, the centralized generation of electrons with energies  $E > 10$  keV cannot be directly proven. This is a general problem because of the intrinsic slope in the energy distribution function or rather the sink to lower electron energies. Furthermore, the detection of an electron by the emitted photon is caused by an energy loss. Especially the electrons around the lower energy edge have a higher influence on the time dependent photon signal. The probability for leaving the considered energy range after collisions and emission of a photon is also higher. A deeper study of the radial phase dependence was not conducted because of the poor spatial resolution and the relatively steep profile shoulders shown in the previous subsection.

The broad viewing area is the reason for the highest possible count rates at the central sightlines. Figure 5.47 shows the averaged time traces of one modulation period for three different photon energy windows at  $p_n = 10 \cdot 10^{-5}$  mbar. The averaging was carried out over 5850 periods. The typical count rate is between one and ten counts per period. The aforementioned phase delay of  $60^\circ$  corresponds to a time delay of 0.2 ms visible in time of the minimum of the energy range  $E_{ph} = 1 - 2$  keV. The other both energy ranges show an increased time shift and a weaker reaction on the gyrotron switch-off, indicating a decreased collision frequency with higher kinetic energy. The most important result, however, are the differing time traces itself contradicting a monoenergetic electron component. Furthermore, a slower increase of the count rate at higher photon energies after the switch-on give rise to the conclusion that the acceleration process is of diffusive nature within the phase space.

A more quantitative analysis is possible by calculating the cross-correlation. However, the results must be treated carefully because of the low count rates. The phase delay of the central X-ray emission depending on the photon energy is depicted in Figure 5.48. Characteristic changes or pronounced maxima are not obvious so that a single concentrated acceleration event is improbable. If an electron is reaccelerated after one turn around the torus, the energy gain will depend on the velocity and the phase in relation to the heating wave. Each particle would undergo a diffusion process within the energy distribution function. A finite acceleration can be achieved for an increasing step size with higher particle energy. However, the higher the energy the higher the acceleration duration, resulting in a monotonically increased phase delay depending on the particle energy as observed in the experiment. A quantitative analysis was not conducted because more data points are necessary within the high energy range. However, the results give rise to a more detailed investigation of the particle wave interaction by means of temporal resolved X-ray measurements.

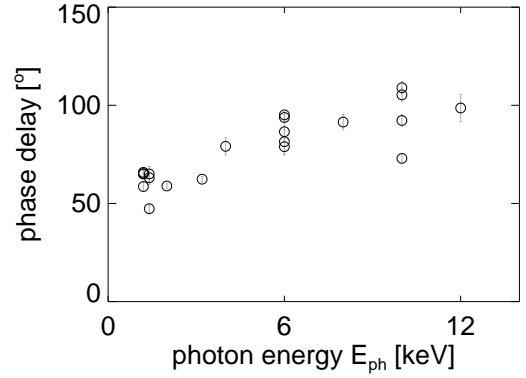


Figure 5.48: Phase delay of X-ray counts to the modulated gyrotron forward power ( $f_{mod} = 788$  Hz, 90 % duty cycle) in dependence on the lowest energy of the detected photon energy window at  $p_n = 10 \cdot 10^{-5}$  mbar.

#### 5.2.4 Maximum Energy of Relativistic Electrons in SLA-discharges

In contrast to the mildly relativistic particles, generated in the OXB-heated discharges, the additional heating with the 2.45 GHz heating system leads to much higher electron energies whose Bremsstrahlung can be detected in terms of gamma rays outside of the WEGA torus. The underlying heating process by stochastic Landau acceleration (SLA) was shortly introduced in subsection 5.1.2.6. Dose rates of the order  $\mu\text{Sv/h}$  can be measured with the used Gamma-Scout® depending on the generated plasma current. But this gives no information about the energy of the generated particles. Even though the transmission of photons around 100 keV through the 3 cm thick stainless steel torus wall is only of the order 1 %, the energy of the transmitted photons is not changed. Therefore, an increase of plasma current and gamma rays can be a result of the number of fast electrons and not of their energy. Figure 5.49 shows an energy resolved spectrum taken with PHA1. The count rate in the hard X-ray energy range is of the same order as during the OXB-discharges, but the slope of the spectrum corresponds to an averaged photon energy of  $\langle E_{ph} \rangle = 141$  keV.

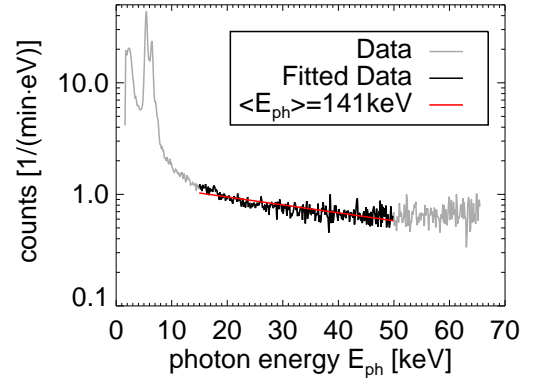


Figure 5.49: X-ray spectrum of a SLA-discharge at a neutral gas pressure of  $p_n = 2 \cdot 10^{-5}$  mbar detected with the WEGA-PHA1 over a time window of  $\Delta t = 39 \cdot 4$  s.

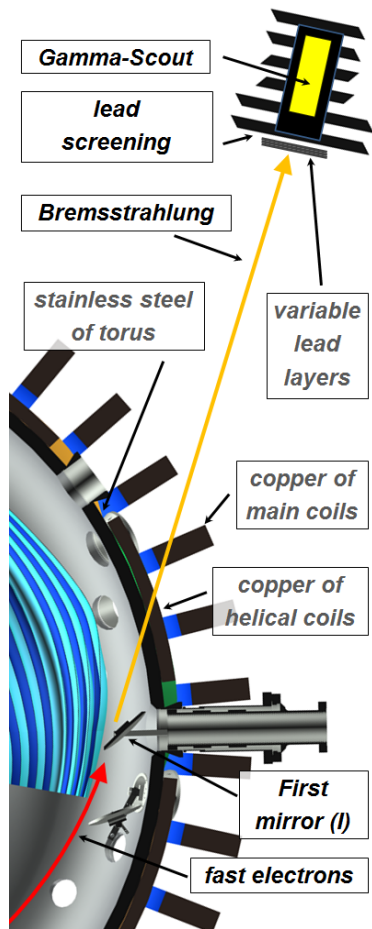


Figure 5.50: *Equatorial cut view around the gyrotron mirror system with the moving direction of the confined relativistic electrons in the  $+/+$  magnetic field configuration illustrated by a red arrow. The expected Bremsstrahlung emission after colliding with a gyrotron mirror is along the tangential sightline of the Gamma-Scout®.*

With higher energies the slope becomes smaller. However, it is not possible to detect an upper edge, because of the limited detection efficiency of the Si(Li)-detector<sup>37</sup>. As also described in subsection 5.1.2.6, electrons with energies higher than 200 keV are only well confined if their velocity vector is oriented opposite to the magnetic field vector<sup>38</sup>. Furthermore, the radial outward shift of the effective drift surface is stronger the higher the electron energy is. The highest dose rates around WEGA are detected near the gyrotron antenna whose mirrors have the lowest distance to the flux surfaces and act as Bremsstrahlung target for the electrons with the highest energies<sup>39</sup>. For this reason, a Bremsstrahlung spectrum of a monoenergetic electron component is expected<sup>40</sup>. For the investigation of the maximum electron energy, the Gamma-Scout® was screened by 10cm thick lead walls with a small entrance window looking at the expected gamma emission source. The position of the lead screening is shown in Figure 5.50. Photons with energies up to a few MeV<sup>41</sup> will only be detected if they are produced in the area around the gyrotron mirror system. The red arrow illustrates the expected moving direction of the highly relativistic electrons for the  $+/+$  magnetic field configuration. The collision with the gyrotron mirror leads to Bremsstrahlung which is mainly directed along the original velocity vector. The directivity of the Bremsstrahlung increases with increasing particle energy [VGJK<sup>+</sup>94]. For the determination of the maximum electron energy, different thicknesses of lead screening were used in front of the entrance window of the Gamma-Scout®. A first estimation of the energy of the order MeV was given in the master thesis of Chouli [Cho11]. A determination of the electron energy distribution function, however, is not possible. The measured difference of the counts for two different thicknesses of lead layers depends on the energy distribution. A detailed explanation is given in Appendix A.1. For this reason, it was preferred to model the original count rate measured with different thicknesses of the lead layers.

<sup>37</sup>These results were confirmed by the SDD3-detector, which was introduced at the end of subsection 3.2.6.2 [OBC<sup>+</sup>10]

<sup>38</sup>Direction of the resultant current and the magnetic field vector have the same orientation.

<sup>39</sup>The position of the relativistic electrons was confirmed by means of a fast reciprocating graphite probe of 5 mm diameter that leads to a current breakdown at a certain radial position because of collecting the suprathermal electrons. The radial position is in accordance with the w7-code calculations which indicate energy dependent drift surfaces [Laq13]. More details can be found in [LCC<sup>+</sup>11].

<sup>40</sup>An example is shown in Figure 5.35.

<sup>41</sup>The transmission of 2 MeV photons is of the order 1%.

The detected counts  $I_{\text{gamma}}$  depend on the lead thickness  $d_{\text{lead}}$  as follows<sup>42</sup>

$$I_{\text{gamma}}(d_{\text{lead}}) = F_{\text{gamma}} \int_{E_{\text{ph}}=0}^{E_{\text{ph}}=\infty} f_{E_{\text{mono}}}(E_n) [T_{d_{\text{lead}}}(E_n)] dE_n. \quad (5.22)$$

The fit parameters are a calibration factor  $F_{\text{gamma}}$  and the monoenergetic electron energy  $E_{\text{mono}}$  in combination with the corresponding energy distribution of the primary photons due to Bremsstrahlung that is given in the Evaluated Electron Data Library (EEDL) [CPS91] (see also Figure 5.35). The calculation of the total transmission factor of the lead layers and the torus components is described in Appendix A.1. Figure 5.51 shows the function for different monoenergetic electron energies which are characterized by a clear difference in their particular slopes in the logarithmic presentation. In comparison to the measured counts, a least squares fit with the scaling factor  $F_{\text{gamma}}$  and the monoenergetic electron energy  $E_{\text{mono}}$  as parameters allows an estimation of the maximum electron energy in the SLA-discharges. Figure 5.52 shows the result with  $E_{\text{mono}} = 0.65$  MeV. Additionally, the data are compared to the measured counts of the  $-/-$  configuration having the same current in opposite direction. Therefore, the generated Bremsstrahlung is directed in the opposite direction, as depicted in Figure 5.50, confirmed by a one magnitude lower count rate in the experiment<sup>43</sup>. Furthermore, the Figure shows the measured counts for another lead screening with perpendicular view to the magnetic field lines proven the expected less directivity as well as the confinement of MeV electrons in one direction.

The second diagnostic, allowing the investigation of electrons with energies of the order MeV, is the microwave radiometer even though the main emission is produced by synchrotron emission, caused by the movement in the toroidal magnetic field, rather than by the electron cyclotron movement around the magnetic field lines.

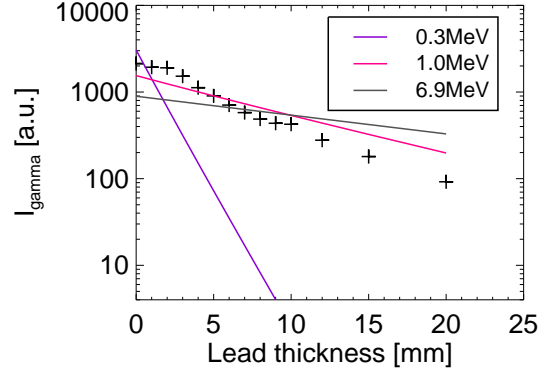


Figure 5.51: *Expected relative total count dependence with higher lead thickness for different Bremsstrahlung spectra with the given monoenergetic electron energy. Crosses are measurements with different lead layers.*

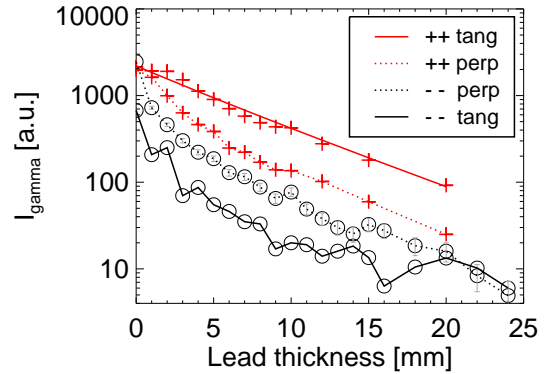


Figure 5.52: *Comparison of the measured total gamma-counts  $I_{\text{gamma}}$  in dependence on the lead thickness for different observation directions to the magnetic field lines. The tangential view for  $+/+$  configuration is shown with the least squares fit based on equation (5.22) for an monoenergetic electron energy of  $E_{\text{mono}} = 0.65$  MeV.*

<sup>42</sup>The count rate is corrected by the dark count rate  $I_{\text{gamma},0}$  that is determined by long term measurement before and after the experiment day and is not additionally mentioned in this formula.

<sup>43</sup>For this reason, the  $+/+$  magnetic field configuration is the safer operation mode under radiation protection aspects because the main gamma emission is directed to the wall of the experimental hall.

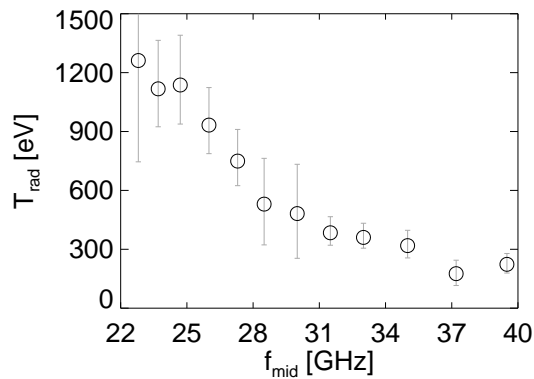


Figure 5.53: *Absolute calibrated spectrum measured with the vertical horn antenna during a SLA-discharge at a neutral gas pressure of  $p_n = 2 \cdot 10^{-5}$  mbar.*

of the gamma measurement is the estimation of a Bremsstrahlung spectrum of the primary photons. Probably the relativistic electrons interact with the target until their complete deceleration, leading to a larger slope in the emitted spectrum. For this reason, the upgrade of the radiometer system down to frequencies of 10 GHz and the intensive use of the new radiometer mirror system is recommended, allowing a more detailed determination of the maximum electron energy.

The expected broad spectrum was verified by the detection of microwave emission within the E-band (60 – 90 GHz) as well as the Ka-band (22 – 40 GHz). The Ka-band spectrum was measured with the aid of the vertical horn antenna<sup>44</sup> and is shown in Figure 5.53. No resonances can be observed but the emission maximum can be identified lower than 22 GHz. The slope of the spectrum would lead to an electron energy of approximately 2 MeV [LCOS13] being a more reliable value because of the non invasive nature of the diagnostic. The perpendicular observation used and the high reflectivity of the torus, however, result in a complicated mixing of different relativistically and Doppler shifted parts generated by different electron components with a more or less continuous energy spectrum. In contrast, the main problem

<sup>44</sup>shown in Figure 3.18

### 5.3 Source of high intensity microwave radiation during OXB-heating

The electron Bernstein wave heated discharges in general are accompanied by an intensive microwave radiation level in the both central channels whose frequency ranges borders on the 28 GHz heating frequency that was first introduced in Figure 5.29. The corresponding radiation temperatures of all radiometer channels are illustrated in Figure 5.54 showing a strongly anisotropic emission distribution over the expected frequency range of electron Bernstein wave emission. The radiation temperatures are of the order keV, being three magnitudes above the thermal electron temperature as shown in Figure 5.31b. An influence by parasitic resonances of the gyrotron can be excluded by means of simultaneous measurements of the continuous microwave spectrum that is shown in Figure 5.56 for the X2-heated plasma around  $t = 9$  s and the OXB-heated phase around  $t = 18.5$  s. During the off-axis heated X2-phase a continuous emission only can be resolved for frequencies lower than 27 GHz. Furthermore, parasitic resonances appear at the frequencies 25.94 GHz, 26.94 GHz and 28.94 GHz, which are the reason for the restricted usability of the radiometer channels with the frequency ranges  $f_{26.0} = 26.0 \pm 0.3$  GHz and  $f_{27.3} = 27.3 \pm 0.3$  GHz<sup>45</sup>. Because of the low magnetic field of  $B_0 = 460$  mT, no X2-emission is expected for frequencies higher than 29 GHz. In contrast, the emission during the OXB-phase shows a broadband frequency spectrum between 26 GHz and 30 GHz that cannot be produced by a gyrotron<sup>46</sup>. For this reason, the source must be in direct connection with the plasma, but there are a variety of different possibilities:

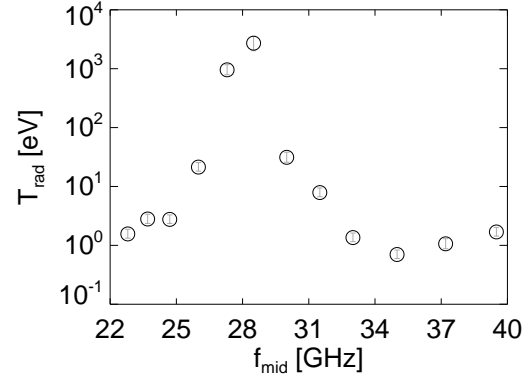


Figure 5.54: Radiation temperatures versus the mid-frequency of the radiometer channels for the OXB-heated phase around  $t = 18.5$  s of Figure 5.29. A logarithmic ordinate is used because of the two magnitudes higher power level in the both channels around 28 GHz.

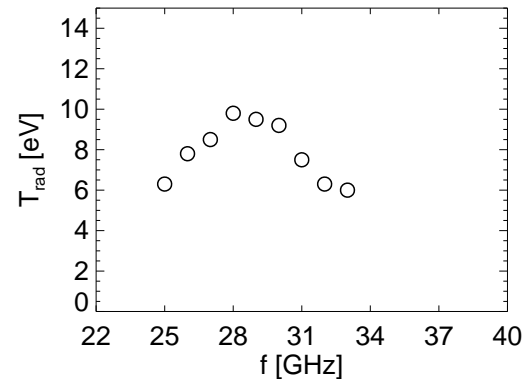


Figure 5.55: Expected electron Bernstein emission spectrum calculated with the AMR-code by use of the bulk plasma profiles shown in Figure 5.31b and a centrally distributed suprathermal electron component in accordance to the measurements shown in Figure 5.43.

<sup>45</sup>The same is assumed for the twelfth channel ( $f_{39.6} = 39.6 \pm 0.7$  GHz) but a possible parasitic resonance in the frequency range 40.0 – 40.3 GHz cannot be resolved with the available equipment.

<sup>46</sup>The spectrum is not corrected by the transmission characteristic of LNA and notch filter to illustrate also the detectable emission for frequencies higher 30 GHz that is at least partly produced by third harmonic emission. Especially the frequency range around 39 GHz corresponds to the third harmonic of the central plasma region. The following spectra with a finite emission over the whole shown frequency range are corrected in general.

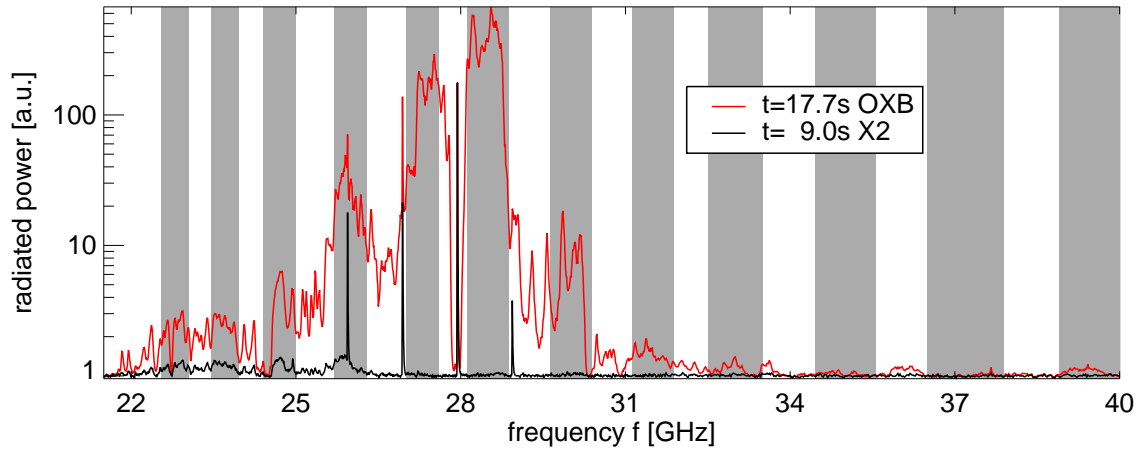


Figure 5.56: Comparison of the emission spectra during X2- and exclusive OXB-heating. The gray shaded areas indicate the frequency ranges of the radiometer channels whose radiation temperatures are shown in Figure 5.54 for the OXB-phase (see also footnote 46). A corresponding discharge is shown in Figure 5.29 and the denoted times correspond to the start points of the sweep window of 1 s length. The noise level of the used spectrum analyzer is at the power level 1 limiting the detectable power level of the emission.

#### 1. Electron Bernstein emission by suprathermal electrons

With entering the OXB-heated phase the broadband microwave as well as soft X-ray emission is observed being a hard argument for the connection of both. No other discharge type shows such high radiation temperatures corresponding to a central second harmonic electron Bernstein wave emission and has, at the same time, a centralized suprathermal electron component with an energy of the same order. But the measured continuous spectrum is sharply peaked around the heating frequency of 28 GHz as obvious in the transmission corrected spectra shown in Figure 5.61 in the next subsection. For this reason, the radiation temperatures in the frequency range 27.5 – 28.5 GHz are partly higher than the averaged photon energy of  $\langle E_{\text{ph}} \rangle \approx 23$  keV determined for the energy range 15 – 50 keV at  $p_n = 10 \cdot 10^{-5}$  mbar in Figure 5.39. Even though the real suprathermal energy distribution can be significantly different, the electron Bernstein emission by a Maxwellian distributed suprathermal electron component should be smaller than the mean energy because of the already explained reabsorption in the plasma. Furthermore, the finite XO-conversion reduces the detectable radiation temperatures. By use of the measured temperature and density profile, shown in Figure 5.31b, as well as a central Maxwellian suprathermal electron component, a calculation with the AMR-code leads to an expected EBE radiation temperature of approximately 100 eV whose spectrum is shown in Figure 5.55. Because of the cold bulk plasma, the centrally emitted EBWs are reabsorbed during their propagation to the plasma edge leading to a reduction of the detectable radiation temperature. In the frame of collaborations with the Prague IPP possible emission processes were investigated to explain the experimental observations. Urban predicted by means of AMR-calculations a radiation temperature with approximately 50% of the suprathermal mean energy if this component is located in the vicinity of the upper high resonance layer [Urb10]. However, regarding the localization of the electrons around the magnetic axis, as shown by the X-ray measurements in the previous section, this possibility can be excluded and therefore also thermal electron Bernstein waves as the source of emission.

### 2. Beam-plasma-instability

Another possible process is the formation of an instability that is not limited by reabsorption and a resultant maximum radiation temperature. An electron Bernstein wave growth would be driven by a low density hot electron component and the dispersion of the wave itself is defined by the cold plasma background. A good summary of the so called MASER-theory of the extraordinary Bernstein waves is given in [WR97]. However, the same principal problem of reabsorption and damping of the excited EBWs appears for the overdense plasma region between the center with hot electrons and the UHR-layer where the conversion to slow X-waves takes place.

### 3. Parametric Decay of the heating wave

Another possible instability is the decay of the incident heating wave with the frequency  $\omega_0$  and the wave vector  $\mathbf{k}_0$  into a plasma or ion acoustic wave with a much lower frequency  $\omega_1$  and another electromagnetic wave with a slightly lower frequency  $\omega_2$  compared to  $\omega_0$ . The condition for such an energy and impulse conserving wave decay process can be expressed as

$$\omega_0 = \omega_1 + \omega_2, \quad (5.23)$$

$$\mathbf{k}_0 = \mathbf{k}_1 + \mathbf{k}_2. \quad (5.24)$$

The appearance of the wave decay is often linked with a threshold power. It must be clearly distinguished to the beam-plasma-instability, where the energy is driven by the suprathermal electrons and not by the heating source itself. Furthermore, beam-plasma-instabilities are typically driven by a monoenergetic electron component. This could be excluded in the previous section.

The following discussion should narrow the source of emission down to the both introduced instability processes.

### 5.3.1 Distribution in the torus

A parametric decay of the heating wave primarily appears in the vicinity of the heating position in contrast to electron Bernstein emission produced by suprathermal electrons, uniformly distributed along the same flux surface in toroidal direction. For this reason, an antenna setup with two oppositely viewing horns was assembled shown in Figure 5.58. The waveguide switch allows the change of the used horn between or even during a discharge<sup>47</sup>. The setup was built in an A-Port in the equatorial plane of the torus near to the gyrotron mirror system for the view in toroidal direction in and opposite to the incidence direction of the microwave beam, launched in positive  $\phi$  direction (OXB-config 2). The position of the horn antennas is illustrated in Figure 3.14.

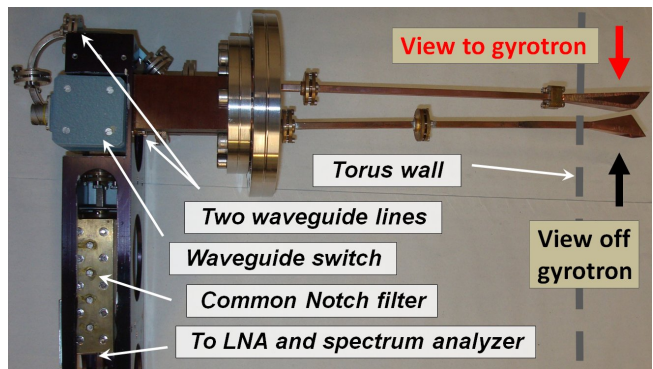


Figure 5.58: *Horn antenna setup for the investigation of an anisotropic high intensity microwave radiation within the torus.*

<sup>47</sup>Because of the limited availability of notch-filters and LNAs, two different systems would incur more expenses.

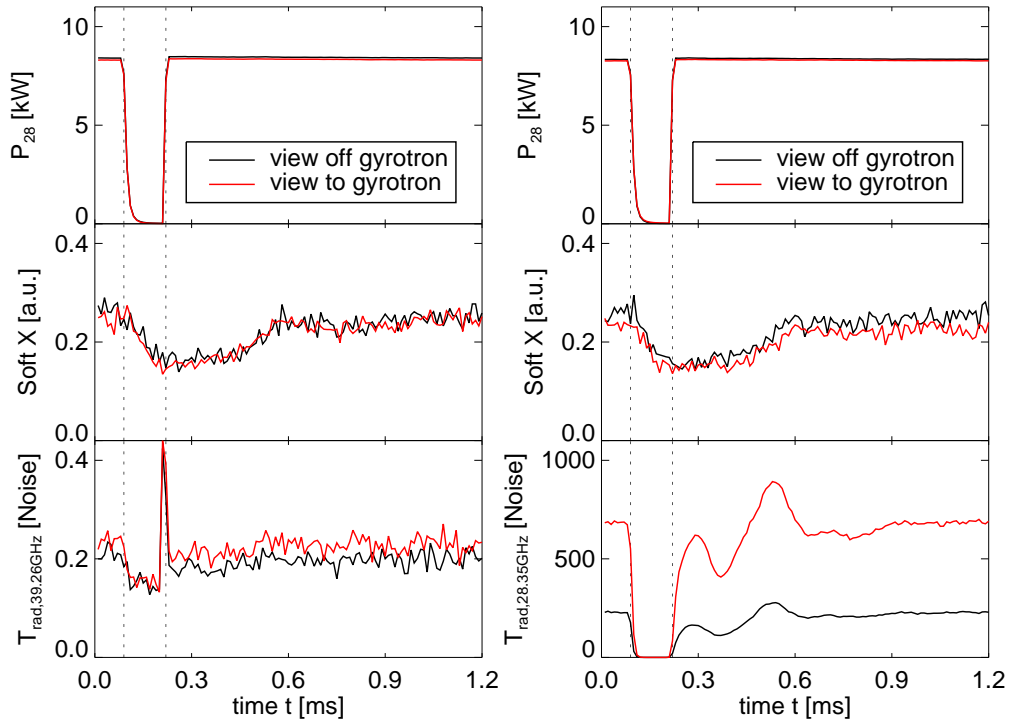


Figure 5.57: Averaged time traces over 1500 modulation periods of the gyrotron forward power  $P_{28}$ . The detected soft X-ray emission corresponds to a photon energy of  $E_{ph} = 1 - 2$  keV and is identical for all 4 shots ( $p_n = 10 \cdot 10^{-5}$  mbar). The detected microwave emission at  $f_{ECE} = 39.26$  GHz  $\pm 1.5$  MHz (left) is isotropic in toroidal direction in contrast to the high intensity emission at  $f_{ECE} = 28.35$  GHz  $\pm 1.5$  MHz (right).

The microwave emission was preamplified with the available LNA in combination with the magic T and temporally resolved with the spectrum analyzer (see section 4.3). The maximum video bandwidth is with 3 MHz much smaller than the typical frequency range of the radiometer channels and allows a detailed investigation of the relative time response within the broadband high intensity microwave emission spectrum. Figure 5.57 shows the averaged signals of both viewing directions for a frequency of  $f_{ECE} = 39.26$  GHz  $\pm 1.5$  MHz during a modulation of the forward power. The chosen frequency corresponds to the third harmonic emission and is far above the cutoff frequency of around 30 GHz. The detected power level is equal in both directions as expected from thermal plasma ECE being isotropic in the different toroidal segments of the torus. Switching off of the gyrotron leads to a slightly decrease of the signal. However, its exclusive generation by the suprathermal electrons cannot be directly proven. The shown soft X-ray signal for the energy range  $E_{ph} = 1 - 2$  keV has a slower decay time. With higher energies the phase delay is in general increased which was shown at the end of the last section. But the thermalization for lower electron energies converges to the decay time of the gyrotron which explains the small but immediate decrease of the signal after switching off of the gyrotron. In contrast, the horn antenna viewing to the gyrotron detects a three times higher power level at the frequency 28.35 GHz as the horn viewing away from the gyrotron. This indicates an anisotropic generation with a source around the incidence position of the heating beam. Furthermore, the emission breaks down to nearly zero after switch-off the gyrotron. At the same time the soft X-ray emission does not drop very much. Thus, the suprathermal electrons within the soft X-ray related energy range do not produce the high intensity microwave radiation.

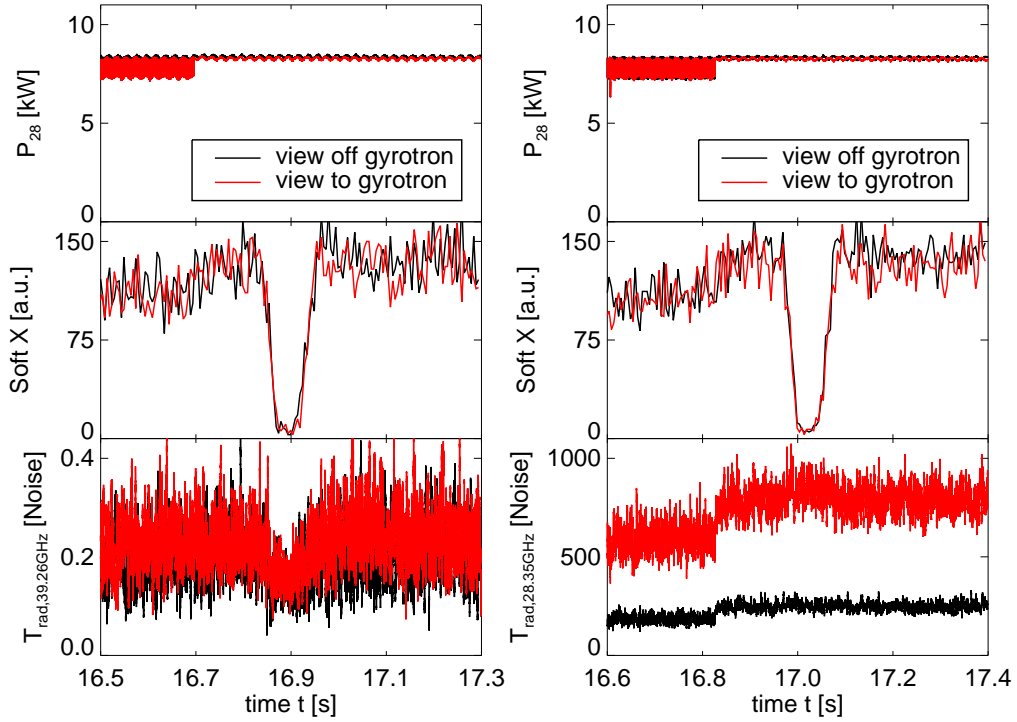


Figure 5.59: Same discharges as in Figure 5.57 at the end of the modulation period. The perturbation of the suprathermal electrons by a Langmuir probe has no influence on the high intensity microwave radiation at  $f_{ECE} = 28.35 \text{ GHz} \pm 1.5 \text{ MHz}$  (right) in contrast to the real electron cyclotron emission at  $f_{ECE} = 39.26 \text{ GHz} \pm 1.5 \text{ MHz}$  (left).

An influence of trapped fast particles can be excluded because no X-ray emission was detected at the plasma edge by PHA2. The toroidal position of the PHA2 ( $\phi_{\text{PHA2}} = 243^\circ$ ) was chosen to be between the turning points (at  $\phi = 198^\circ$  and  $\phi = 270^\circ$ ) of trapped particle orbits in the vicinity of the incidence position of the heating beam.

The inverse experiment with a disappearing soft X-ray emission is shown in Figure 5.59 where the suprathermal electrons are disturbed by a fast reciprocating Langmuir probe similar to the experiment in Figure 5.40. It can be summarized that the high intensity microwave radiation has no connection with the suprathermal electron component. On the other hand, the third harmonic emission is partly generated by the latter one because of the clear decrease with the Langmuir distortion. At the beginning of subsection 5.2.2 the almost constant bulk temperature was established so that a finite emission must remain. The observation of the time dependent Langmuir distortion at a multitude of frequencies is shown in Figure 5.60.

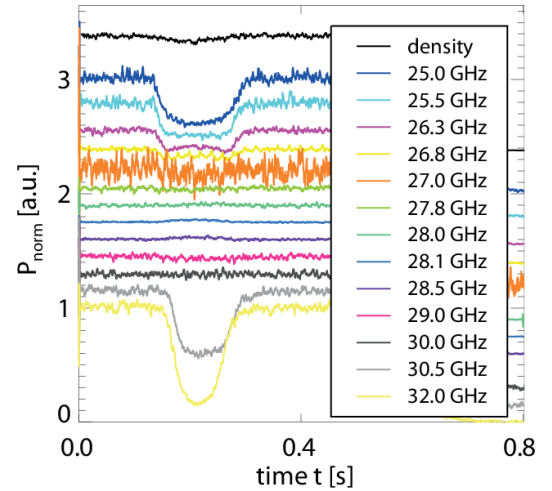


Figure 5.60: Normalized power level of the detected microwave emission during distortion by a Langmuir probe for different frequencies. Each trace is normalized to value 1 with an additional offset for better visualization.

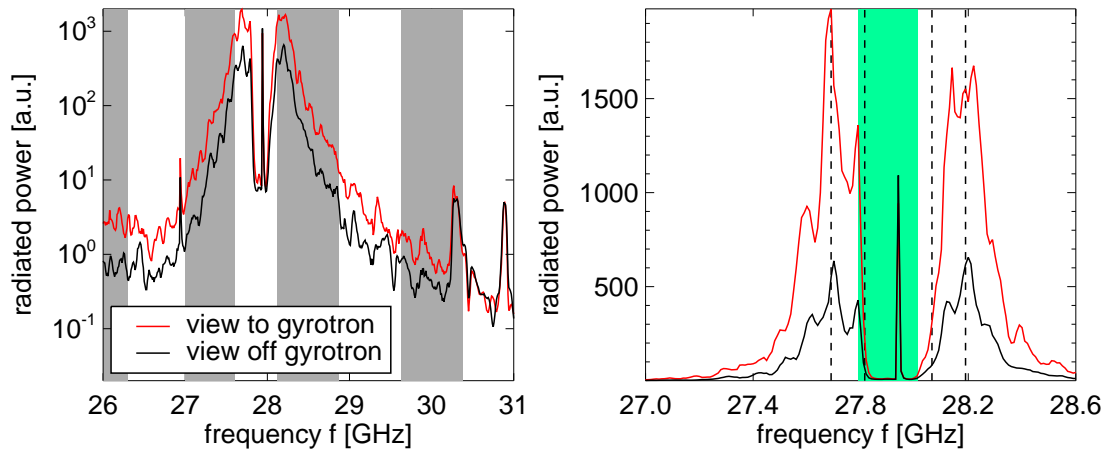


Figure 5.61: Corrected spectrum of the OXB-phase, shown in Figure 46, for the both views in opposite toroidal directions in logarithmic (left) and linear representation (right). The gray shaded areas indicate the frequency ranges of the radiometer channels and in the green shading area no relative power levels can be resolved. The vertical lines correspond to the mid frequencies of a preferred line emission complying with a frequency shift of 250 MHz in negative and positive direction to the gyrotron frequency.

The frequency spectrum between 27 GHz and 30 GHz shows no change in the level so that a beam-plasma-instability can be neglected as source for the high intensity microwave radiation. Figure 5.61 shows a comparison of the frequency ranges for both viewing directions that are corrected by the transmission characteristic of the used notch filter as well as the subsequent low noise amplifier and magic T. The logarithmic representation illustrates the continuous broadband spectrum. On the other hand, the linear representation indicates a preferred emission at certain frequencies. But in the green shaded frequency range no signal can be obtained because of the sharp notch for the rejection of the gyrotron emission. Furthermore, the additional broadband suppression by the magic T causes a further reduction so that a finite transmission cannot be determined in this frequency range, because of the limited dynamic range of the used network analyzer. Even though the transmission characteristic is strongly decreasing from 27.5 GHz to 27.8 GHz, the corrected signal also shows a decrease and a maximum around 27.7 GHz with a difference of 250 MHz to the gyrotron frequency. The same is valid for the frequency range 28.0 – 28.5 GHz with a maximum around 28.2 GHz and the same difference frequency of 250 MHz. Two additional maxima are obvious between the two main peaks, and the center frequency of the left one agrees with 125 MHz. This will be important for the discussion of the possible generation processes in the next section. The shown results give rise to the definite conclusion of a parametric decay of the heating wave.

### 5.3.2 Generation Mechanism

The decay of a pump wave  $(\omega_0, \mathbf{k}_0)$  into an idler  $(\omega_1, \mathbf{k}_1)$  and a signal wave  $(\omega_2, \mathbf{k}_2)$  corresponds to a parametric instability being a broad field with the requirement of excessive mathematical disquisitions. For this reason, only a brief overview of the basic mechanism will be given in the following. A good introduction of parametric instabilities can be found in Chen's book [Che84]. A more detailed description is given in the book of Simon and Thompson [KKLK76] or the already announced book of Swanson [Swa03]. Furthermore, certain reviews of experimental investigations can be recommended [POR76; PC78; POR78].

The basic condition for a decay or rather a parametric instability is the existence of two oscillatory systems that can be described by the equation of motion of the simple harmonic oscillator [Che84]:

$$\frac{d^2 x_i(t)}{dt^2} + \omega_i^2 x_i(t) + 2\Gamma_i \frac{dx_i(t)}{dt} = 0. \quad (5.25)$$

The amplitude  $x_i$  corresponds to the wave electric field or the density fluctuation constituting an electron plasma wave or ion acoustic wave. Each system is typically defined by a resonant frequency  $\omega_i$  and a damping rate  $\Gamma_i$  preventing the oscillation because of collisional or Landau damping. If there is an oscillating electric pump field with a frequency  $\omega_0$  in the vicinity of the resonant frequency  $\omega_2$ , being for example the electron plasma frequency  $\omega_{pe}$ , the electrons will undergo relatively large excursions in the electric field  $E_0 \cos \omega_0 t$  [POR76]. The generated oscillation  $x_2(t) = x_2 \cos \omega' t$  of the oscillator 2 will produce in combination with the pump frequency  $\omega_0$  a modulation at the beat frequency  $\omega_0 \pm \omega'$  [Swa03]. This can be in the vicinity of the resonant frequency  $\omega_1$  of the second oscillator being for example an ion acoustic oscillation with much smaller frequency. For this reason, a driving term  $F_1(t) = c_1 x_2(t) E_0 \cos \omega_0 t$  will appear on the right hand side of equation 5.25 for the oscillator 1 that is proportional to the amplitude  $x_2$  and induce a forced oscillation [Che84]. The constant  $c_1$  corresponds to the strength of the coupling and is typically determined by the particular dispersion relation. The resultant modulation of the ion density  $x_1(t) = x_1 \cos \omega t$  at the beat frequency  $\omega_0 \pm \omega$  is again in the vicinity of the resonant frequency of the oscillator 2 and results in an equivalent driving term  $F_2(t) = c_2 x_1(t) E_0 \cos \omega_0 t$ . If the condition  $\omega' = \omega_0 \pm \omega = \omega_2$  with  $\omega = \omega_1$  is exactly fulfilled, a maximum energy transfer will appear but the formation of both oscillations depends on the damping rate  $\Gamma_i$ . The resultant complex values  $\omega$  and  $\omega'$  determine an overall damping or a growth of an oscillation for the case of an instability. The combination of the particular equations 5.25 leads to a conditional equation allowing the definition of a growth rate as well as threshold power for the appearance of an decay instability. Because of the generation of waves, the already introduced condition 5.24 for the wave vectors must be fulfilled, too. An important result of the previous considerations is the principal possibility to excite waves ( $\omega' = \omega_0 \pm \omega$ ) below and above the pump frequency [Che84] which is observed in the experiment (see spectrum on the right of Figure 5.61). The frequency shift  $\omega$  in relation to the gyrotron pump frequency  $\omega_0$  allows the identification of the involved low frequency wave. Typical candidates are the ion acoustic (IA) wave or the lower hybrid wave (LH). In the limit of a small Debye length the dispersion relation of the former one is only given by the sound speed  $v_s$  in a plasma:  $\omega(k) = |k| v_s$ . But for  $|k| \rightarrow \infty$  the ion acoustic wave becomes a constant frequency wave with  $\omega$  converging to the ion plasma frequency [Che84]. Figure 5.62a shows the latter one in dependence on the effective radius for the OXB-discharge discussed in the previous subsection<sup>48</sup>.

<sup>48</sup>The plasma profiles were firstly introduced in Figure 5.29.

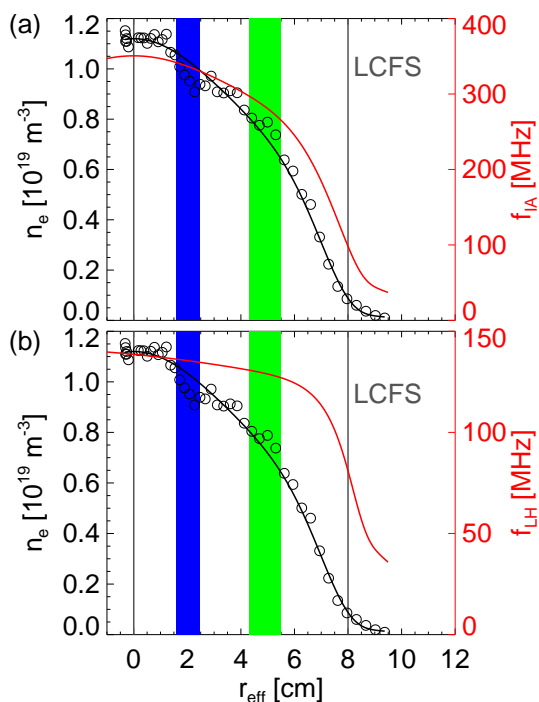


Figure 5.62: *Density profile and the resultant ion plasma frequency (a) as well as the resultant lower hybrid frequency (b) of an OXB-discharge at  $p_n = 10 \cdot 10^{-5}$  mbar, generating the high intensity microwave emission spectrum of Figure (5.61). The used sightline, necessary for the determination of the magnetic flux density at the shown effective radius  $r_{\text{eff}}$ , corresponds to the optimal propagation of the heating beam from the low field side to the O-cutoff (blue shaded). The generated slow X-wave propagates back to the UHR-layer whose relative position can be identified within the green shaded area.*

frequency the same happens for the ions superposing the oscillation by the electrons. The resultant characteristic lower hybrid resonance frequency  $\omega_{\text{LH}}$  is given by [Swa03]

$$\omega_{\text{LH}} = \sqrt{\frac{\omega_{\text{ce}}\omega_{\text{ci}}}{1 + \left(\frac{\omega_{\text{ce}}}{\omega_{\text{pe}}}\right)^2}} \quad (5.26)$$

The resultant radial dependence for the considered OXB-discharge is shown in Figure 5.62b with about 130 MHz in the vicinity of the UHR-layer. This would be in good agreement with the indicated 125 MHz and their multiples so that lower hybrid waves cannot be excluded as candidate for the decay instability.

The plasma was assumed to be singly ionized because the maximum amount of  $\text{He}^{2+}$ -ions in the plasma center is of the order 10% [ZBG<sup>+</sup>11]. Therefore, the deviation to the real ion plasma frequency is maximum a few per cent. The decay instability is a non-linear phenomenon arising from high energy densities or rather high electric fields within the plasma. During the XB-conversion at the UHR-layer the group velocity of the slow X-wave or rather the pump wave decreases to zero fulfilling the latter condition [Laq07]. The resultant decay of the pump wave depends on the local plasma parameters defining the excitable waves. The ion acoustic wave would be limited to approximately 300 MHz in the vicinity of the UHR-resonance layer being a good explanation for the observed maxima at  $f_0 \pm 250$  MHz in Figure 5.61. Depending on the necessary impulse conservation of equation (5.24), the generation of lower frequencies would be also possible. Higher frequency shifts than 300 MHz could be explained by additional cascading beat frequencies.

On the other hand, the electrostatic lower hybrid waves are caused by the collective oscillation of the electrons and the ions. For an almost perpendicular propagation to the magnetic field lines an electromagnetic slow X-wave with  $\omega \leq \omega_{\text{ce}}$  generates a longitudinal electric field because of space charges caused by the  $E \times B$ -drift of the deflected electrons in the direction of the electric field [Str11]. This leads to the already explained upper hybrid resonance where the electrons gain maximum energy by the wave leading to the conversion to electron Bernstein waves. For lower frequencies of the order of the ion cyclotron frequency the same happens for the ions superposing the oscillation by the electrons. The resultant characteristic lower hybrid resonance frequency  $\omega_{\text{LH}}$  is given by [Swa03]

However, the excited electrostatic low frequency waves can be investigated with loop antennas, sensitive to the magnetic field of the oscillating space charges, and electrostatic probes or rather monopole antennas, detecting the electric field itself. The former one was chosen because their position can be fixed at the plasma edge and not within the plasma for the case of the latter one. A loop antenna was also used for the confirmation of lower hybrid waves involved in the observed decay instability during electron Bernstein wave heating at the stellarator W7-AS [Laq07]. The detected high frequency spectrum is similar to the present case at WEGA. The used loop antenna is shown in Figure 5.63 whose position<sup>49</sup> is as close as possible to the incidence position of the heating beam (as shown in Figure 3.14). The enclosed area was maximized to increase the magnetic flux through the loop that is connected to a standard SMA-cable<sup>50</sup> guiding the signal to the used spectrum analyzer ANRITSU MS2668C. It was not possible to achieve a continuous low frequency spectrum because of the low detected power levels. Therefore, the time dependent low frequency emission at different fixed frequencies was measured during the fast modulation of the gyrotron. Figure 5.64 shows the averaged signal for  $f = 230$  MHz indicating the same fast emission decrease during the gyrotron switch-off like the high intensity microwave radiation around 28 GHz.

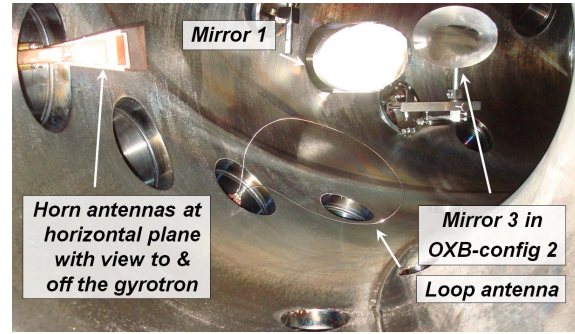


Figure 5.63: View to the gyrotron mirror system in opposite  $\phi$  – direction. Mirror 1 is only visible from behind. The two horn antennas, looking in opposite toroidal directions, are located at the low field side at the equatorial plane of the torus. The loop antenna is as close as possible to the plasma as well as the incidence position of the heating beam.

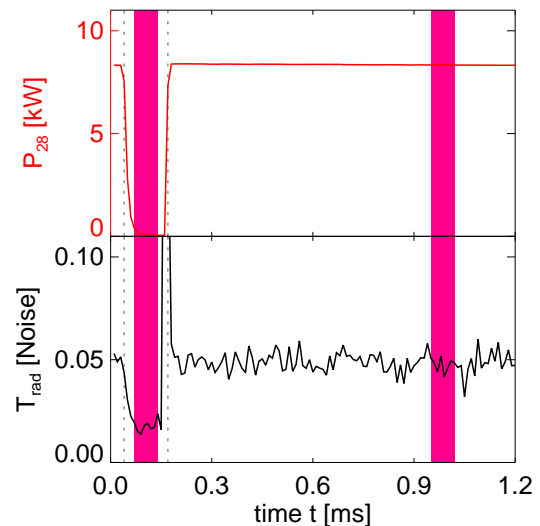


Figure 5.64: Averaged time traces over 1700 modulation periods of the gyrotron forward power  $P_{28}$ . The difference signal of the detected emission of the loop antenna during the red shaded time windows is taken as measure for the amplitude of low frequency decay waves.

<sup>49</sup>Toroidal angle of  $\phi_{loop} = 234^\circ$  compared to  $\phi_{28inc} = 208^\circ$  of OXB-config 0 (see Figure 3.14 or 3.5)

<sup>50</sup>The almost symmetric constructed loop antenna (diameter 86 mm  $\times$  180 mm) generates a balanced alternating signal without relation to ground. On the other hand, the shielding of the unbalanced coaxial line is connected to ground as reference potential. A direct connection of the loop antenna poles to the coaxial line would lead to a sheath current that partly short-circuits the source. Furthermore, the antenna system becomes sensitive to a coupling of other unwanted sources. This can be prevented by the use of a so called balun (BALANCED-UNbalanced) that can consist of an additional twisted line increasing the external inductance [MG92]. A detailed description would go beyond the scope of this work, but more details can be found in [Kri01]. The balun, used in parallel, acts as impedance transformer leading to improved coupling at certain frequencies.

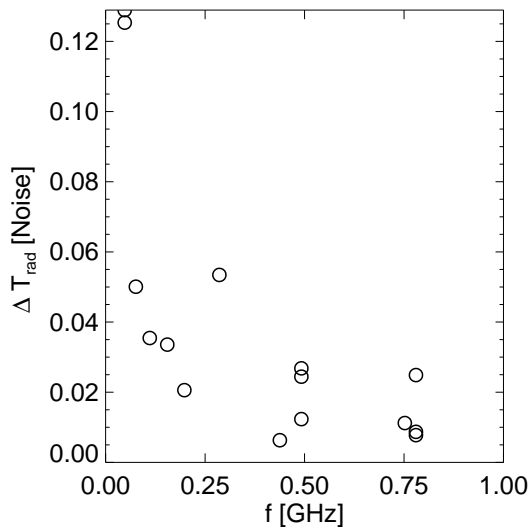


Figure 5.65: Resultant low frequency spectrum measured with loop antenna.

use of a monopole antenna should be also taken into account because good results could be achieved in other, more extensive studies regarding the decay of an helicon or rather Whistler wave into an ion acoustic wave and a Trivelpiece-Gould mode [Lor04]. Additionally, multiple antennas would allow the determination of the wave vector and a confirmation of the impulse conservation but with considerable expense.

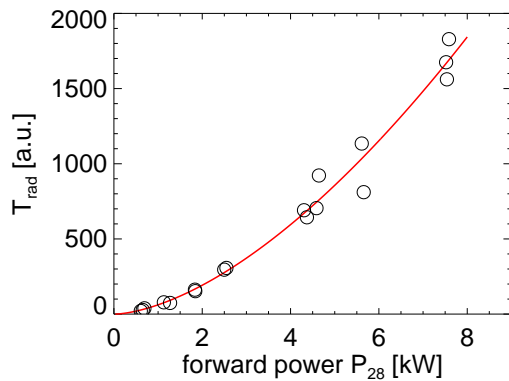


Figure 5.66: Radiation temperature of the high intensity microwave radiation within the frequency range  $f_{27.3} = 27.3 \pm 0.3$  GHz in dependence on the forward power. The fit corresponds to the power law given by equation (5.27).

The difference signal between the red shaded time windows is shown in Figure 5.65 for the optimal operating frequencies of the loop antenna<sup>51</sup>. The width and the shape of the background fits well to the high frequency spectrum shown in Figure 5.61. The increased emission at the frequency  $f = 286$  MHz indicates the expected peak around 250 MHz confirming once again the line emission character of the high intensity microwave radiation. An equivalent low frequency peak around 130 MHz is not visible so that the emission around 27.8 GHz cannot be identified as the high frequency part of a parametric decay to a lower hybrid wave. Therefore, the ion acoustic wave is the most probable candidate for the low frequency decay wave. Further investigations of the low frequency spectrum necessitates an optimization of the loop antenna to realize a more homogenous response dependent on the frequency. But the

As mentioned above the formation of the decay is a non-linear mechanism that will be defined by exponential growth if the threshold power is overcome. Typically the amplitude of the excited waves saturates at a certain level depending on a variety of parameters. If the threshold power is not achieved, the instability will not appear because of a too strong damping of the excitable waves. A power scan for the OXB-discharges can only be obtained within a fast modulation. Therefore, the lower level of the modulation amplitude of the gyrotron forward power was set to different levels by a change of the ceramic series resistor in the gyrotron high voltage power supply circuit that was described at the beginning of section 3.1.1. The radiation temperature measured in the frequency range  $f_{27.3} = 27.3 \pm 0.3$  GHz is shown in Figure 5.66 with a non-linear dependence on the forward power. An exponent of about  $b = 1.6$  results in a power law fit with:

$$T_{\text{rad}} = C_{\text{dec}}(P_{28} - P_{\text{thres}})^b + T_{\text{rad},0}. \quad (5.27)$$

<sup>51</sup>Obtained by a reflection measurement while installed in the torus.

Such a weak non-linear dependence can also be caused by changes of the plasma parameters during the modulation. Even though the line integrated electron density stays constant the density gradient around the UHR-layer can decrease during the lower power level of the modulation. Therefore, the decrease of the group velocity to zero happens during a longer propagation length leading to a less increased local electric field. Furthermore, the temperature decrease is up to 30 % for the full gyrotron switch-off<sup>52</sup> leading to a decreased ion sound velocity  $v_s$  and change of the ion acoustic dispersion relation. Nevertheless, the main result of the power scan is the unresolvable power threshold that must be of the order a few 100 W. Similar small power thresholds are observed for the already mentioned decay of an helicon wave in a laboratory plasma [Lor04], even though the heating mechanism is completely different in comparison to the OXB-discharges. However, the threshold power is defined by a decay growth rate of zero whose measurement needs much more effort. A detailed investigation necessitates a complete switch-off of the forward power with a subsequent low power pulse within one modulation period. This must be followed by the maximum gyrotron power level to sustain the electron density and the OXB-heating itself. The increase of the emission during the low power pulse defines the growth rate of the decay with time constants of the order  $O(\mu s)$ . Furthermore, an additional fast switch would be necessary to realize three different power steps during the modulation. For this reason, a deeper study of the radial phase dependency was rejected for the present. Only the source or rather the principal mechanism for the generation of the high intensity microwave radiation was important to give a proper interpretation of the emission measurements with the aid of the developed mirror system following in the next section. The only weak non linear power dependence as well as the radiation temperature of the order keV led to the initial assumption that the radiation is generated by the suprathermal electrons.

---

<sup>52</sup>This estimate results from the AXUV-bolometer system whose signal depends only on the temperature for the case of constant density.

## 5.4 Investigation of OX-Conversion Process

The efficiency of the electron Bernstein wave heating via the OXB-conversion process is almost exclusively defined by the OX-conversion efficiency as introduced in subsection 2.2.3.1. If the incident elliptically polarized ordinary wave is fully converted into a slow X-wave, the latter one will be almost 100 % converted into an electron Bernstein wave at the Upper-Hybrid-Resonance Layer (UHR). Especially in the low temperature WEGA plasmas, the EBW is strongly resistively damped, so that all of the power is absorbed by the plasma even though the resonance layer is not reached by the EBW. For this reason, this section treats the dependence of the OX-conversion on the incidence angle.

For the fast optimization of the OX-conversion the support structure of the second gyrotron mirror was modified to a remotely steerable system in September 2009. Prior to that a change in the angle was only possible by opening the vacuum vessel. In the first experiments, started in April 2009, six different incidence angles were tested to find the optimal one for the OXB-heating scenario. The angle  $\vartheta_{28}$  with respect to the magnetic field lines was varied by about  $2^\circ$ , respectively. But the expected optimal and initially adjusted angle of  $\vartheta_{28} = 56^\circ$  emerged as best configuration demonstrating the practicability of heating with the aid of the OXB-conversion process.

The following subsection will explain the more detailed investigations with the aid of the remotely steerable system which was introduced in subsection 3.1.1.2. The theoretically predicted dependence of the conversion efficiency, given by equation (2.35), can be hardly confirmed, because a change of the heating beam causes also a change of the probed plasma. For this reason, the also angle dependent electron Bernstein wave emission via the inverse OXB-conversion process (BXO) should be used as non-invasive diagnostic technique. But the broadband spectrum of the high frequency decay waves overshine the electron Bernstein wave emission around 28 GHz so that a new technique was used. The decay waves themselves were used as non-invasive diagnostic beam interacting with the plasma via OX-conversion. Because of the same angle dependence of equation (2.35), the detected angle dependent reflection allows a much better determination of the OX-conversion efficiency.

### 5.4.1 Invasive Diagnostic Technique

The dependence of the plasma parameters on the incidence angle of the heating beam was investigated for all three mirror configurations which were explained in subsection 3.1.1.2. An overdense plasma can be achieved and sustained within an angle window of  $\vartheta_{28} = 56^\circ \pm 15^\circ$  demonstrating once again the heating via the OXB-conversion process. Figure 5.67 shows as an example the radiated power of an argon discharge with OXB-config 0. The absolute value combined with about 1 kW convective losses defines the absorbed power and thereby the OX-conversion efficiency. The maximum of about 75 % absorption is achieved around the optimal incidence position of  $\vartheta_{28} = 56^\circ$  so that the principle agreement with the theory can be directly shown. But the dependence is much weaker as the expected transmission via equation (2.35). The latter one is plotted for a gradient length of  $L_n = 3$  cm which results from the measured density profile<sup>53</sup>.

---

<sup>53</sup>In the first approximation, the convective power can be assumed proportional to the radiated power so that the transmission function can be directly fitted to the measured dependence.

Because of the multiple wall reflections of the non absorbed part of the heating beam, the initial OX-conversion or rather OXB-absorption is overlaid by multiple absorption via OXB- as well as XB-conversion. A subsequent single conversion efficiency greater than the wall absorption suffices for an subsequent multipath absorption of greater than 50% as already explained for the non resonant heating. For this reason, the OXB-discharge can be sustained at for example  $\vartheta_{28} = 50^\circ$  even though the initial conversion efficiency is decreased to 25%. The stray radiation signal confirms this hypothesis with approximately the same low value of  $P_{\text{stray}} = 0.4$  [a.u] for all measured positions<sup>54</sup> but an inverse dependence to the bolometer signal could not be measured. The reason is to be found in the finite directivity of the sniffer probe as well as the instability of the argon discharges. The latter one is defined by a movement of the deposition zone from the center to the low field side because of a density profile spreading. If the absorption zone reaches the plasma edge, the density profile will collapse and the absorption zone will switch back to the center. This process on a time scale of 1 ms was already visualized via the AXUV bolometer in [Gla10].

An interesting phenomenon appears regarding the reflected power which is measured within the gyrotron transmission line. The corresponding angle dependence, shown in Figure 5.68, has a peak in the vicinity of the optimal incidence angle. The latter one can generate a steeper density gradient leading to an increased backscattering of the extraordinary part of the heating beam. The gradient length would act as substitute variable for the difference of the refractive indexes ( $N_{z,\text{opt}} - N_z$ ) in equation (2.35). The same transmission efficiency as in Figure 5.67 would be in good agreement with the measured values but a proper treatment of all included dependencies is not possible. In consideration of the uncertainties of the Langmuir probe measurement, a change of the density gradient cannot be proven within an angle change of less than  $5^\circ$ .

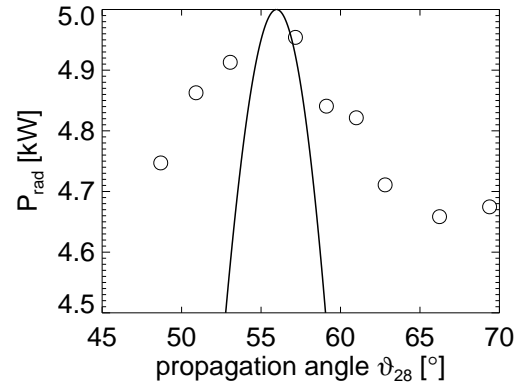


Figure 5.67: Radiated power versus the angle  $\vartheta_{28}$  between the 28 GHz heating beam and the magnetic field lines compared with the expected dependency which results from the OX-conversion efficiency (2.35) for a gradient length  $L_n = 3$  cm ( $k_0 L_n = 17.6$ ).

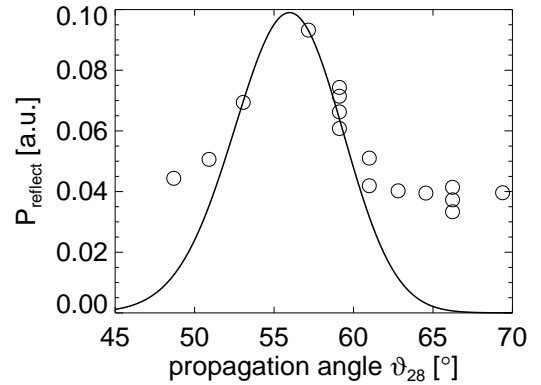


Figure 5.68: Reflected power versus the angle  $\vartheta_{28}$  between the 28 GHz heating beam and the magnetic field lines compared with the expected dependency which results from the squared OX-conversion efficiency (2.35) for a gradient length  $L_n = 3$  cm ( $k_0 L_n = 17.6$ ).

<sup>54</sup>In contrast to 0.9 of the accordant off-axis heated X2-plasma.

On the other hand, the generated broadband high frequency decay wave spectrum could be responsible for the increased reflection around the optimal incidence. The wave decay of the heating beam should be increased with higher conversion efficiency because of the resultant higher power density in the vicinity of the UHR-layer. The detected power of the high frequency decay waves is approximately proportional to the forward power as shown in Figure 5.66. For this reason, the OX-conversion efficiency should be closely connected with the generated high frequency decay waves. The latter ones leave the plasma via the inverse OX-process (XO) so that the gyrotron mirror system obtains the optimal detection efficiency. Its dependence on the incidence angle would be the square of equation (2.35) but the resultant slightly narrower profile would be also in good agreement with the measured reflected power Figure in 5.68<sup>55</sup>.

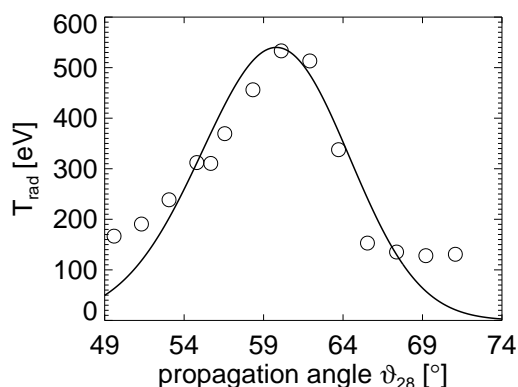


Figure 5.69: Radiated temperature of the decay wave emission within the frequency range  $f_{28.5} = 28.5 \pm 0.4$  GHz versus the angle  $\vartheta_{28}$  between the 28 GHz heating beam and the magnetic field lines. The shown fit of equation (2.35) corresponds to a gradient length  $L_n = 5$  cm ( $k_0 L_n = 29.3$ ).

cutoff layer is located at a smaller effective radius with a decreased density gradient. However, a clear discrepancy of the measured dependence is the absolute position of the maximum which is located at an incidence angle of about  $60^\circ$  in contrast to the expected  $56^\circ$ . An error of the angle assignment can be excluded but the asymmetric incidence can lead to an unexpected refraction of the heating beam. Therefore, the angle  $\vartheta_{28}$  between the 28 GHz heating beam and the magnetic field lines must be greater to compensate the additional deflection. This effect would be increased with a steeper density profile so that the measurement of the

The possibility to determine the conversion efficiency via the generated decay waves was investigated in more detail for OXB-config 1 after reinstallation of the ECE-diagnostic<sup>56</sup>. The microwave radiation is still detected with a standard horn antenna. Figure 5.69 shows the measured radiation of the frequency range  $f_{28.5} = 28.5 \pm 0.4$  GHz versus the angle  $\vartheta_{28}$ . The dependence is much more pronounced than the corresponding ones of stray radiation, line integrated density or radiated power. For this reason, the generation of decay waves should be assumed as proportional to the initial OX-conversion efficiency. A fit of equation (2.35) leads to a gradient length of  $L_n = 5$  cm. The reasons for the less steeper density profile are, on the one hand, the less compressed flux surfaces at the incidence position of the corresponding poloidal cross section. On the other hand, the absolute conversion and heating efficiency is decreased because of the oblique incidence in poloidal direction<sup>57</sup>. The result is an only slightly overdense plasma whose

<sup>55</sup> A frequency resolved measurement with the aid of a so called Inline ECE would allow a reliable differentiation between a scattered heating beam and an overlaid broadband spectrum of high frequency decay waves. Test were made with the narrow-band notch filter with about 70 dB suppression but a resolution of the side bands was not possible. However, the used directional coupler of the transmission line has a frequency independent suppression of about 80 dB so that an improvement of the measurement would necessitate much more effort.

<sup>56</sup> The diagnostic was relocated from the toroidal position  $\phi_{\text{ECE}} = 153^\circ$  to the final toroidal position at  $\phi_{\text{ECE}} = 36^\circ$ .

<sup>57</sup> The poloidal angle on the flux surface is about  $\Theta_{\text{rel, OXB-config 1}} = 67^\circ$  with a resultant  $N_y^2 = 0.15$  in equation (2.35).

angle dependence for a helium plasma shows a maximum at an incidence angle of up to  $65^\circ$ . But the corresponding angle dependence tends to the same less pronounced behavior of the measurable plasma parameter as shown in Figure 5.67 for the bolometer. The corresponding gradient length would be less than 1 cm being in contradiction with the measured density profiles. For this reason, the generation of decay waves cannot be finally identified as clear indicator for optimal conversion efficiency.

Especially for the asymmetric incidence of the OXB-configs 1 and 2, the optimal incidence angle for efficient OXB-heating must be determined by a combination of all measurable plasma parameters. The measurement of temperature and density profiles allows the determination of the optimal absorption position whichever profile is centrally peaked. Figure 5.70 shows an example for an helium discharge with OXB-config 2. The density profiles are generally peaked around the magnetic axis but the central density is increased for greater angles  $\vartheta_{28}$ . Against it, the temperature profile shows an off-axis peak so that the most efficient heating can be identified around the expected optimal incidence of  $\vartheta_{28} = 56^\circ$ .

The experimental observations are typically in good agreement with the AMR-calculations which give the motivation for the asymmetric incidence of OXB-config 1 and 2. The predicted improvement of the EBW current drive efficiency could be confirmed in the experiment by a doubling of the driven current up to 30 A as already explained in [Chl10].

#### 5.4.2 Non-invasive Diagnostic Technique

The installation of the quasioptical mirror system for the microwave radiometer had the initial goal to measure electron Bernstein wave emission of the plasma and to investigate the OX-conversion process. In the meanwhile, the broadband high intensity microwave radiation, appearing during the OXB-heating, could be identified as high frequency part of a parametric decay of the heating beam as explained in section 5.3. Nevertheless, the reabsorption of the resultant broadband stray radiation allows the investigation of the conversion efficiency.

The physical mechanism of the angle dependent reabsorption via the OXB-conversion process is explained in Figure 5.71 for the microwave detection system. The latter one is as far as possible away from the point of origin of the decay waves. For this reason, multiple reflections lead to an uniform distribution of the stray radiation in terms of the polarization as well as the direction to the magnetic field lines.

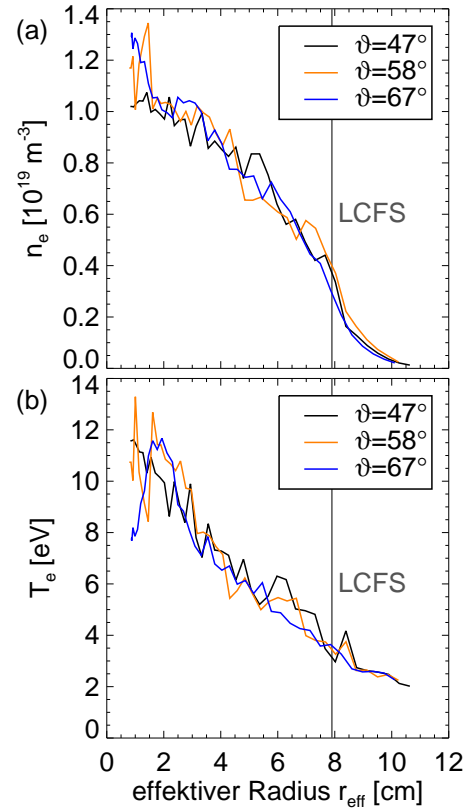


Figure 5.70: *Electron temperature and density profile of an X2-discharge with central resonance at  $B_0 = 500 \text{ mT}$  (a) and off-axis resonance with  $B_0 = 460 \text{ mT}$  (b). The fitted TRAVIS-profile is related to an extrapolated LCFS given by the dotted line.*

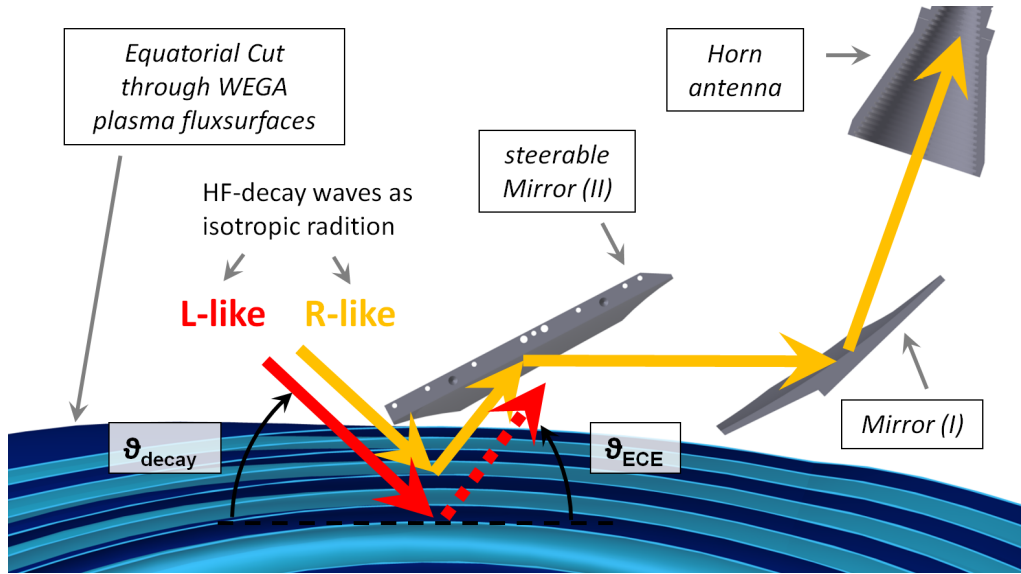


Figure 5.71: Reabsorption of the properly polarized L-like part of the high frequency (HF) decay waves by OXB-conversion leads to the detection of an R-like wave for an observation angle  $\vartheta_{ECE}$  which is equal to the optimal OXB-angle .

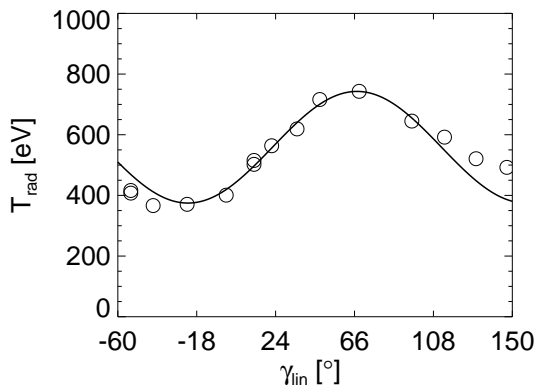


Figure 5.73: Radiation temperature for the frequency range  $f_{27.3} = 27.3 \pm 0.3$  GHz versus the linear polarization angle  $\gamma_{lin}$  for an observation angle of  $\vartheta_{ECE} \approx 56^\circ$  and an elliptical polarization angle of  $\gamma_{lin} = 0^\circ$ . A fit of a squared sine-function leads to maximum at  $\gamma_{lin,max} = +68^\circ$ .

The power of the stray radiation, incident on the flux surface in front of the second mirror, can be separated into two equal parts whose respective polarizations correspond to the extraordinary and ordinary mode of the considered direction to the magnetic field lines. For the optimal angle of approximately  $\vartheta_{decay} \approx 56^\circ$  the L-like wave (with respect to the magnetic field vector) is absorbed by the OXB-conversion process. The R-like wave is reflected around the accordant Upper X-cutoff layer without any absorption.

In contrast to a metallic mirror the polarization of the reflected wave is retained so that the expected reflection under the observation angle of  $\vartheta_{ECE} \approx 56^\circ$  would be an R-like wave (with respect to the magnetic field vector). Apart from the optimal angle  $\vartheta_{ECE} \leq 56^\circ$  no change is expected for the respective R-like wave but a finite reflection of the L-like wave occurs because of the decreased conversion efficiency. The resultant polarization of the reflected wave would be a mixture of both wave types but is reversed in relation to the expected polarization of electron Bernstein wave emission.

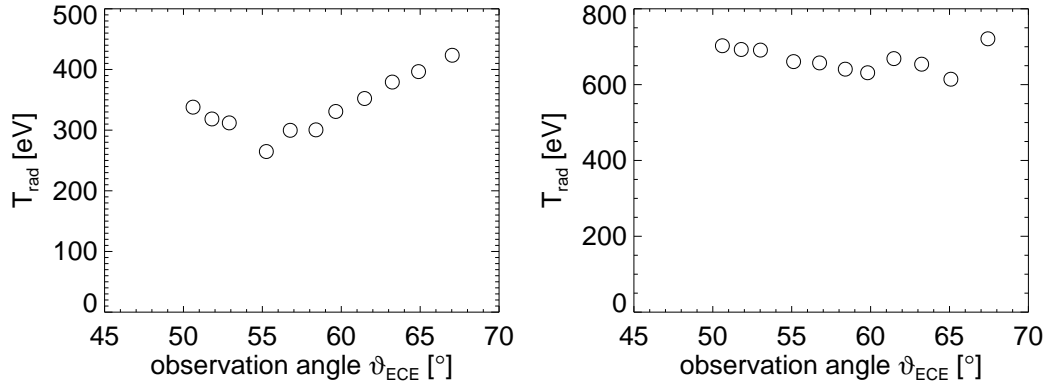


Figure 5.72: Radiation temperature for the frequency range  $f_{27.3} = 27.3 \pm 0.3$  GHz versus the observation angle  $\vartheta_{ECE}$  for the L-like (left) and the R-like (right) polarization which correspond to the detected minimum ( $\gamma_{lin,min} = 20^\circ$ ) and maximum ( $\gamma_{lin,max} = 68^\circ$ ) of the polarization scan shown in Figure 5.73.

Figure 5.73 shows the measured radiation temperature for the frequency range  $f_{28.5} = 28.5 \pm 0.4$  GHz in dependence on the linear polarization angle<sup>58</sup> for an OXB-heated helium discharge<sup>59</sup>. The used observation angle  $\vartheta_{ECE}$  corresponds to the optimal angle for OXB-conversion. The maximum emission can be detected for a R-like wave being in accordance with the expected dominant polarization of the explained reabsorption mechanism. The other radiometer channels with a frequency lower than 30 GHz show nearly the same dependence so that no clear indication of electron Bernstein wave emission exist. A scan of the observation angle  $\vartheta_{ECE}$  was carried out for the two linear polarization angles with the maximum and minimum detected radiation temperatures.

No dependence on  $\vartheta_{ECE}$  can be observed for the frequencies up to 25 GHz, even though the existence of electron Bernstein wave emission cannot be completely excluded<sup>60</sup>. For the frequencies between 25 GHz and 30 GHz, the expected inverse angle window of the decay wave reabsorption was measured, that is shown in Figure 5.72 for the fifth radiometer channel with a frequency range of  $f_{27.3} = 27.3 \pm 0.3$  GHz. The minimum of the detected L-like wave radiation is exactly located at the expected optimal conversion angle of  $\vartheta_{ECE} = 56^\circ$  that demonstrates once again the explained reabsorption process.

<sup>58</sup>It corresponds to the angle  $\gamma_{lin}$  of the detected linear polarization with respect to the equatorial plane as shown in Figure 4.9. The elliptical polarizer was adjusted to an elliptical polarization angle of  $\gamma_{ell} = 0^\circ$ .

<sup>59</sup>The discharge scenario is shown in Figure 5.29 with a neutral gas pressure of  $p_n = 10 \cdot 10^{-5}$  mbar.

<sup>60</sup>The measured radiation temperature up to 25 GHz shows no sudden decrease during the fast switch-off of the forward power that is shown in Figure 5.57 for the frequency  $f_{ECE} = 28.35$  GHz  $\pm$  1.5 MHz. It must be taken into account that the L-like wave emission can be of the same order as the reabsorbed stray radiation. For this case no dependence of the radiation on the observation angle would be measurable, even though electron Bernstein waves are emitted.

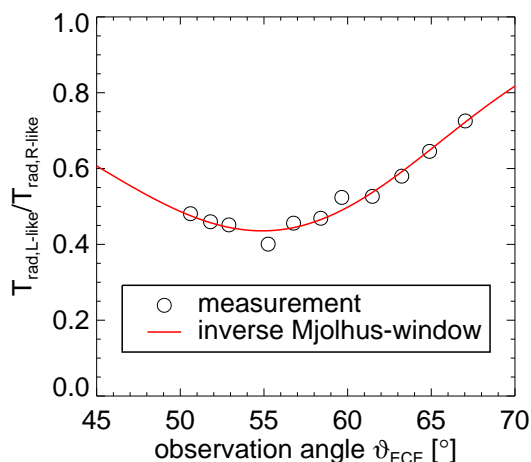


Figure 5.74: Absorption of a L-like decay wave for the frequency range  $f_{27.3} = 27.3 \pm 0.3$  GHz versus the observation angle  $\vartheta_{ECE}$ . The fit of  $1 - C_{OX}T_{Mjølhus}$  (with  $T_{Mjølhus}$  given by equation (2.35)) corresponds to density gradient length of  $L_n = 0.8$  cm and an absolute OXB-conversion factor of  $C_{OX} = 0.56$ .

position of the signal allows the investigation of particular frequency ranges. Having regard to only the low frequency part up to about 30 Hz, the efficiency can be estimated to circa 70%. This value would be in better agreement with the expected capability of the optimized mirror system.

Under the assumption that the power of the non absorbed R-like radiation constitutes the power of the absorbed L-like radiation, the measured angle dependencies can be used for the determination of the absolute OX-conversion efficiency. Figure 5.74 shows the ratio of both dependencies as well as a fit of the accordant function of an inverse transmission window  $T_{Mjølhus}$  given by equation (2.35). The corresponding density gradient length is with  $L_n = 0.8$  cm much less than the expected value of the order 2 cm which was determined with the aid of the measured Langmuir density profile. But taking account of the measurement errors of both diagnostics, the obtained values are not in principal contradiction to each other. The more important quantity of the non-invasive reflection measurement is the determined absolute OX-conversion factor of about  $C_{OX} = (56 \pm 10)$  % being a reliable value for the single conversion efficiency. Nevertheless, it must be regarded as lower limit because of a strong fluctuation of the detected decay wave power. The spectral decom-

# 6 Chapter 6

---

## Conclusions and Summary

In the thesis presented, microwave heating of overdense magnetically confined plasmas was investigated at the stellarator WEGA. The plasma frequency is higher than the heating frequency so that the propagation within such overdense plasma is generally not possible.

The main issue was the heating via electrostatic electron Bernstein waves (EBW) which can be excited under certain circumstances by an obliquely incident electromagnetic wave by means of the OXB-conversion process. The heating frequency is 28 GHz, corresponding to the second harmonic of the electron cyclotron frequency. First investigations showed a generation of a suprathermal electron component whose precise characterization was a main task. The approximately Maxwellian distributed X-ray spectrum has an averaged energy of the order of 10 keV. In collaboration with the IPP group 'Astrophysics and Laboratory-Plasma-Studies' (ALPS) in Garching, these results could be confirmed with the aid of their more sensitive X-ray detector.

For the realization of a spatially resolved measurement, the soft X-ray diagnostic at WEGA was redesigned in several optimization steps. The suprathermal electrons are distributed around the magnetic axis with a radial extension of up to  $r_{\text{eff}} = 2$  cm. In contrast, the overdense plasma region has a radial extent of at least  $r_{\text{eff}} \approx 3$  cm. Considering particle transport, the suprathermal electrons are generated within  $r_{\text{eff}} \approx 1$  cm which is in accordance with heat wave experiments. The visible emission detected with the aid of bolometers also indicates the very centralized Bernstein wave absorption [ZGL<sup>+</sup>12]. The spectrally, spatially, and time resolved X-ray measurements indicate a Maxwellian electron energy distribution up to an electron energy of around 5 keV. The corresponding averaged electron energy is on the order of a few keV. Therefore, the density of the suprathermal electrons can be narrowed down to the range  $10^{16} - 10^{17} \text{ m}^{-3}$  but the plasma current is carried almost exclusively by these particles. As a result of the collaboration with the IPP Prague, an improved EBW current drive in the plasma was predicted for an asymmetric poloidal incidence of the heating beam which was confirmed in the experiment.

Additionally in the OXB-discharges, a broadband microwave radiation appears with radiation temperatures of the order of a few keV which has, however, no connection with the suprathermal electron component. The source of the radiation could be clearly identified as a parametric decay of the heating wave. Further measurements of the low frequency spectrum up to some hundred MHz showed an increased emission around 250 MHz which suggests an ion-acoustic wave as low frequency decay wave. The simultaneous participation of a lower hybrid wave around 130 MHz, however, cannot be completely excluded and would be an explanation for the less pronounced line emission within the high frequency spectrum. In this context, an

investigation of a possible electron Bernstein wave emission via the BXO-conversion process was not possible. Electron Bernstein wave heating as well as electron Bernstein wave emission (EBE) was already the subject of intensive research at larger magnetic confinement experiments such as the stellarator Wendelstein 7-AS [LMM<sup>+</sup>03; LH98; Vol03] and the spherical tokamak MAST [SOTS10; SVFH12]. A remaining question is the experimental determination of the conversion efficiency which is important for the heating but necessary for the use of EBE as temperature measurement. Depending on the width and the divergence of the received Gaussian beam, the conversion efficiency is reduced [KCH<sup>+</sup>08]. Density fluctuations within the conversion zone cause a further reduction [Laq07]. For the investigation of the conversion efficiency, a quasioptic mirror system was built and used in combination with a microwave radiometer. To limit the decrease of the conversion efficiency, the phase front curvature of the considered beam was matched to the flux surface curvature and the beam width was maximized in the design. Furthermore, a broadband circular polarizer was developed so that an elliptically polarized emission can be measured simultaneously over at least a half octave. The high frequency decay wave spectrum shows an R-like polarization under the optimal observation angle for the OX-conversion. Assuming an isotropically distributed polarization spectrum, the L-like part can be absorbed via the OXB-conversion whereas the R-like part is reflected at the corresponding cutoff-layer. An inverse angle window can be measured for the L-like part while the R-like part shows no dependence on the observation angle. This provides the opportunity for an invasive determination of the conversion efficiency. The determined value by this method is in good agreement with the theoretically expected one given in [KCH<sup>+</sup>08].

As a further possibility for heating of overdense plasmas, the coupling to Whistler waves or rather R-like waves was investigated. This method is routinely used at WEGA as well as the torsatron TJ-K but is not yet completely understood. In both cases the used frequency is 2.45 GHz. In contrast to electron Bernstein wave heated discharges, the electron cyclotron frequency must be lower than the heating frequency. For this reason, the process was referred to as non-resonant heating because of no cyclotron resonances within the plasma. The coupling of the vacuum wave to a R-like wave within the overdense plasma is the most probable candidate. In the previous works of the TJ-K group [Die09; Köh10], however, the coupling mechanism could not be exactly clarified. The coupling in the case of WEGA was analyzed with a model which treats the torus and the plasma as two resonators coupled to each other through the cutoff-layer. The ratio of the coupling factor and the wall absorption is the most critical value determining the absorbed power by the plasma. The wall absorption was determined by a measurement of the quality factor of the WEGA-torus. For the specification of the coupling factor, different coupling mechanisms were discussed. The measured density gradient lengths in the vicinity of the cutoff-layer are generally less than one tenth of the free space wavelength of the heating wave. For this reason, the tunneling of the incident wave emerged as the most probable candidate. Assuming a fully reflective plasma edge layer, the resultant microwave pattern within the torus was simulated with the software HFSS. The averaged angle distribution of the Poynting vector with respect to the cutoff-layer was used for the calculation of an angle dependent coupling, which is defined by the density gradient length and the electron cyclotron frequency at the cutoff-layer. The dependence of the calculated absorbed power on the magnetic flux density is in good agreement with the evolution of the line integrated density in the experiment. The density gradient length mainly defines the increase of incipient power coupling with increase of the magnetic flux density. Further experiments are suggested to prove that the tunneling is the relevant coupling mechanism.

---

With regard to the heating efficiency, electron Bernstein wave heating and non-resonant heating were compared with an underdense X2-heated WEGA-plasma. The determination of the absorbed power, however, poses a challenge especially in the case of X2-heating. The sniffer probe, which measures the microwave stray radiation, can provide only a rough indication because the stray radiation within the torus is not homogeneously distributed. Small changes in the multipath propagation of the heating beam can cause a change of the microwave pattern within the torus and therefore a change of the coupled power into the sniffer sphere. For this reason, the overall absorbed power of the considered X2-discharge was determined indirectly by determination of the single path absorption and an effective reflection factor of the torus wall. The single path absorption was calculated with the aid of the ray-tracing code TRAVIS taking into account the measured electron density and temperature profiles. With the aid of the passively detected electron cyclotron emission, the effective wall reflection factor was determined by comparing the measured and calculated spectrum of the corresponding radiation temperature. As predicted in [Sta08], a small part of resistive emission could be identified which was also taken into account in the calculation of the absorbed power in the case of X2-heating.

A second possibility for the determination of the absorbed power is given by the overall power balance. For this purpose, the power  $P_{\text{trans}}$  transported across the last closed fluxsurface was measured by means of power modulation experiments. A Fourier analysis of the radially dependent electron cyclotron emission leads to a value of  $\chi = (2.3 \pm 0.5) \text{ m}^2/\text{s}$  for the thermal diffusivity which agrees with the measurement of the thermal diffusivity in OXB-discharges using the bolometer. A characteristic of the low temperature WEGA-plasmas is the minor role of  $P_{\text{trans}}$ . The radiated power is generally more than twice as high as  $P_{\text{trans}}$  so that a basic condition for the determination of the absorbed power is the exact measurement of the radiated power. This circumstance is even more relevant in the case of OXB-heated plasmas due to the overproportional dependence of the emissivity coefficient on the temperature. Here, a radiated power of the order of 90 % of the input power can be measured so that the absorption can be determined only with the aid of the radiated power and the measured plasma profiles. A more detailed analysis leads to the same value for the overall absorption of OXB-heated plasmas in comparison to about 30 % of the considered X2-discharge. The absorbed power for non-resonant heated discharges is of the order of 50 %.

For the fast evaluation of the absorbed power, especially for the case of low absorption, a model was suggested which determines the relevant quantities of the overall power balance only with the aid of the bolometer. A modified power balance equation is fitted to the time dependent radiated power during a modulation of the forward power. The analysis for a central power deposition leads to consistent values in comparison to the determination with the aid of  $P_{\text{trans}}$ .



# A

## Appendix A

---

# Appendices

### A.1 Lead Filter Method

The averaged energy of a Maxwellian distributed photon spectrum can be determined with the so called filter method, which is used in fusion research for the measurement of the electron temperature via the soft X-ray emission of the plasma [Hut94]. If two highpass transmission filters with different cutoff frequencies are used for the detection of the spectrally integrated intensity, the ratio of both measured intensities allows the determination of the electron temperature. For relativistic photon energies, there are no sharp highpass filters so that the definition of a minimum transmitted photon frequency is not possible. Furthermore, the measured photon spectrum of, for instance, a monoenergetic electron component is not Maxwellian so that an averaged energy is not defined. For this reason, the transmission properties must be analyzed in detail for the investigation of an unknown photon energy distribution function.

For the determination of the maximum electron energy in the SLA-discharges, different thicknesses of lead screening were used in front of the Gamma-Scout® detector. The setup for the tangential view on the moving direction of the relativistic electrons is shown in Figure 5.50. The corresponding transfer factor defined by equation (3.5) is shown in Figure A.1 for the used lead layers. Even without additional lead the considered attenuation by 55 mm of stainless steel and about 117 mm of copper of the helical and toroidal field coils along the sightline of the Gamma-Scout® allows only a transmission of the order per mill. In the logarithmic representation there seems to be an edge in dependence on the energy but this is conditioned on the existence of photons around 1 MeV and higher. The absolute value of the radial outward shift of the drift surfaces of relativistic electrons is dependent on the electron energy so that a more or less monoenergetic electron component hit the mirror with a resultant Bremsstrahlung spectrum similar to Figure 5.35. For energies around 1 MeV and higher the emitted counts for iron also converge asymptotically in the vicinity of the maximum energy as obvious for the shown spectrum of helium.

Figure A.2 shows the expected energy dependent counts for different initial electron energies that were computed by the product of their Bremsstrahlung distribution function  $f(E_{\text{ph}})$  and the transfer factor  $T_{\text{tang}}(E_{\text{ph}})$  of Figure A.1. The result is also compared with the case for perpendicular observation without the influence of the toroidal field coils and a shorter sightline through the torus materials. Because of the high intrinsic attenuation by the torus and the copper coils, the Gamma-Scout® would detect for the tangential view, in general, the maximum photon energies for the case of MeV or less. For higher energies or a perpendicular

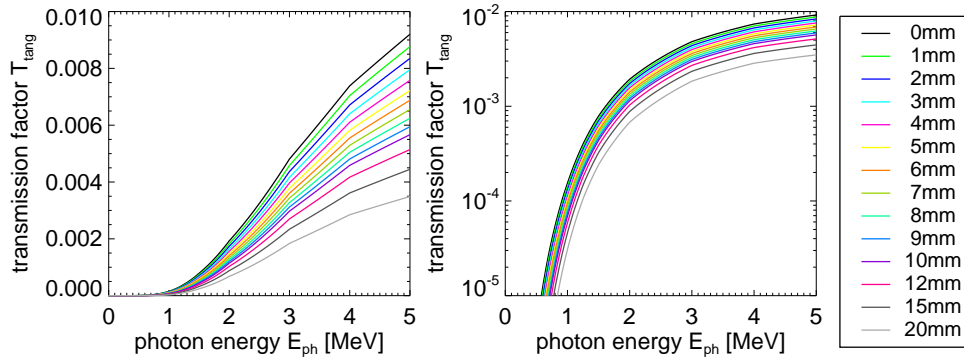


Figure A.1: Energy dependent transfer factor of photons along a tangential sightline through the WEGA torus that is shown for an equatorial cut view in Figure 5.50. The summation of the attenuation by 55 mm stainless steel, 117 mm copper and different thicknesses of lead layers results in the shown transfer factor  $T_{tang}$  in linear (left) as well as logarithmic representation (right).

observation a maximum in the photon energy can be identified but still with a dependence on the energy of the colliding electron component. As obvious in Figure 5.35 the Bremsstrahlung spectrum can be locally defined by an exponential distribution function. For this reason, the transmission can also be analyzed analytically with the latter one as emitted photon energy distribution function within the torus. As shown in Figure A.3 the Bremsstrahlung emission for photon energies lower than 50 keV has no influence on the overall transmission so that the intrinsic deviation in the hard X-ray energy range is not important for the expected maximum electron energy of much more than 100 keV. By using different thicknesses of lead layers, the difference of the expected counts can be expressed as

$$\Delta N \propto \int_{E_{ph}=0}^{E_{ph}=\infty} f(E_{ph}) [T_i(E_{ph}) - T_j(E_{ph})] dE_{ph} = \int_{E_{ph}=0}^{E_{ph}=\infty} 10^{a_{\Delta counts}} dE_{ph}. \quad (\text{A.1})$$

The assumed exponential distribution function  $f(E_{ph}) = \exp(-E_{ph}/\langle E_{ph} \rangle)$  will be expressed by means of base 10 to get a better appraisalment of the magnitudes in Figure A.3 where the resultant energy dependent exponent  $a_{\Delta counts} = \log(T_i - T_j) - \log(e) \cdot E_{ph}/\langle E_{ph} \rangle$  of equation (A.1) is shown for different mean photon energies and views to the magnetic field lines. By changing the thickness of the lead layers, the energy of the maximum of the spectrum dependent exponent in equation (A.1) is also changed. Since the absolute position is dependent on the mean photon energy, the determination of an energy distribution is not possible. The shown examples  $\langle E_{ph} \rangle = 80$  keV and  $\langle E_{ph} \rangle = 250$  keV can be related in the energy between circa 100 keV and the maximum photon energy to a Bremsstrahlung spectrum generated by monoenergetic electrons of  $E_{mono} = 250$  keV and  $E_{mono} = 1$  MeV colliding with an iron target. In Figure 5.49 the mean photon energy in the hard X-ray energy range was determined to a similar value of  $\langle E_{ph} \rangle = 141$  keV but the slope seems to become more shallow. Even though a reliable determination would be possible, this spectrum results not from the hard iron target, but rather from the collisions with ions and neutrals in the plasma. Therefore, the emission results not from a monoenergetic electron component and a direct comparison is difficult.

Because of the performed analysis, it was preferred to model the original count rate measured with different thicknesses of the lead layers as explained in subsection 5.2.4.

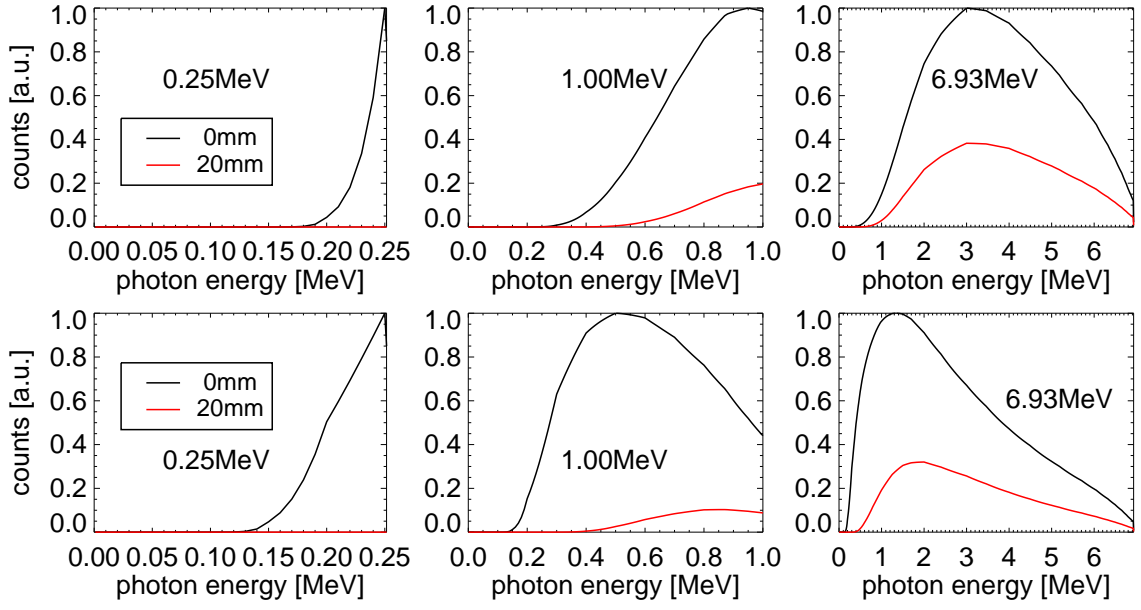


Figure A.2: Transmitted Bremsstrahlung spectrum of a monoenergetic electron component of different energies  $E_{mono}$  and different thickness of the lead layers used for tangential (top) and perpendicular view.

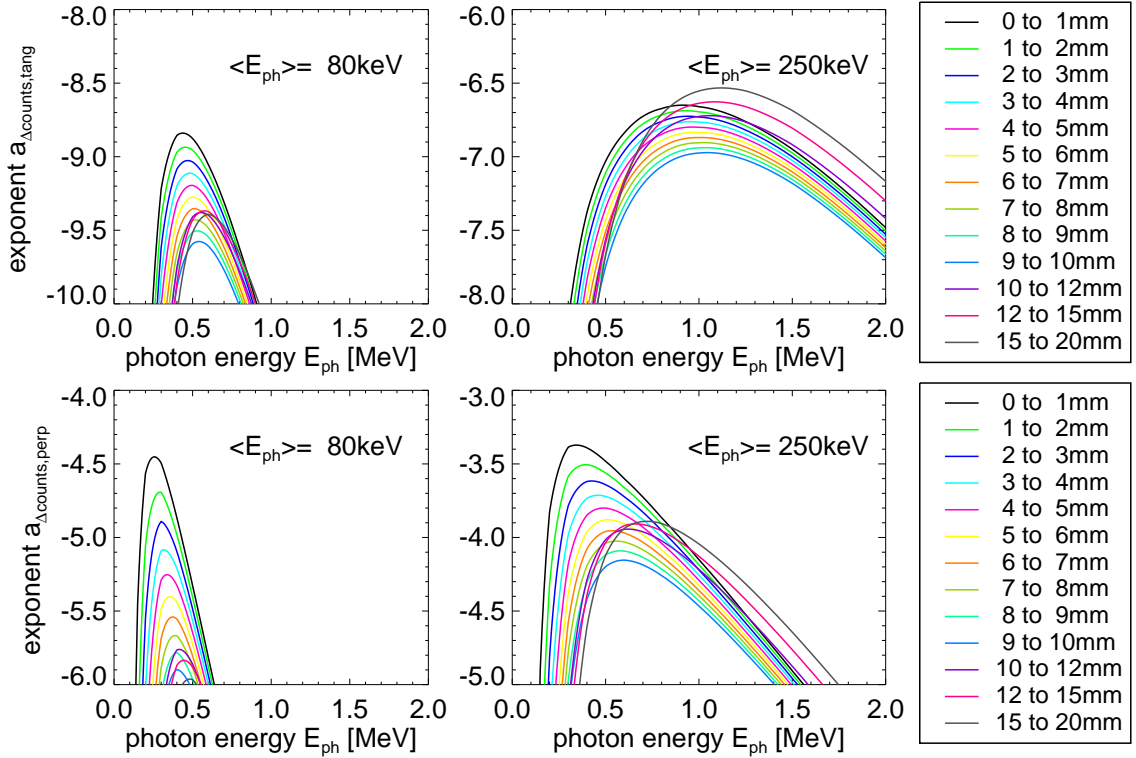


Figure A.3: Comparison of the exponent  $a_{\Delta counts} = \log(T_i - T_j) - \log(e) \cdot E_{ph} / \langle E_{ph} \rangle$  of equation (A.1) for the mean energies  $\langle E_{ph} \rangle = 50 \text{ keV}$  and  $\langle E_{ph} \rangle = 200 \text{ keV}$  in the case of tangential (top) and perpendicular view (bottom) to the magnetic field lines. (Please note the different scales of the ordinate.)



## Bibliography

- [Att99] ATTWOOD, David: *Soft X-rays and Extreme Ultraviolet Radiation - Principles and Applications*. Cambridge University Press, 1999
- [Bal80] BALMASHNOV, A. A.: On the Self-focusing of Whistler Waves In A Radial Inhomogeneous-plasma. In: *Physics Letters A* 79 (1980), Nr. 5-6, S. 402–404
- [BCDBE83] BORNATICI, M. ; CANO, R. ; DE BARBIERI, O. ; ENGELMANN, F.: Electron Cyclotron Emission And Absorption In Fusion Plasmas. In: *Nuclear Fusion* 23 (1983), Nr. 9, S. 1153–1257
- [Beh13] BEHLKE: *Technical Data of Fast High Voltage Transistor Switches HTS 331-03-LC, HTS 501-03-LC, HTS 651-03-LC*. 61476 Kronberg, Germany: Behlke Electronic GmbH, 2013
- [Bek66] BEKEFI, G.: *Radiation Processes in Plasmas*. John Wiley And Sons, Inc., New York, London, Sydney, 1966
- [Bel10] BELAPURE, Jaydeep. *WEGA campaign : experiment summary - 26th Apr - 7th May 2010*. May 2010
- [Bel13] BELAPURE, Jaydeep S.: *Non-thermal electron populations in microwave heated plasmas investigated with X-ray detectors*, Technische Universität München, Diss., 2013
- [BF79] BADEN FULLER, A. J.: *Microwaves - An introduction to microwave theory and techniques*. Second Edition. Pergamon Press Ltd., Oxford, 1979
- [BH10] BELAPURE, Jaydeep ; HUBER, Bernhard. *Private Communications*. May 2010
- [Bir08] BIRKENMEIER: *Experiments and Modeling of Transport Processes in Toroidal Plasmas*, Universität Stuttgart, Diplomarbeit, 2008
- [Bud61] BUDDEN, K. G.: *Radio Waves in the Ionosphere*. Cambridge University Press, 1961
- [Car95] CARDOZO, N. J. L.: Perturbative Transport Studies In Fusion Plasmas. In: *Plasma Physics and Controlled Fusion* 37 (1995), August, Nr. 8, S. 799–852
- [CCTF08] CASTEJON, F. ; CAPPA, A. ; TERESHCHENKO, M. ; FERNANDEZ, A.: Computation of EBW heating in the TJ-II stellarator. In: *Nuclear Fusion* 48 (2008), Nr. 7, S. 075011 (14pp)
- [Che84] CHEN, F. F.: *Introduction to Plasma Physics and Controlled Fusion*. Bd. Vol. 1. 2nd Ed. Plenum Press, 1984
- [Chl10] CHLECHOWITZ, Enrico: *Plasma Current and Pressure Measurements at the WEGA Stellarator*, Ernst-Moritz-Arndt Universität Greifswald, Diplomarbeit, April 2010
- [Cho11] CHOULI, Billal: *Lower Hybrid Heating and Current Drive in the WEGA Stellarator*, Diplomarbeit, September 2011

- [CPS91] CULLEN, D.E. ; PERKINS, S.T. ; SELTZER, S.M.: Tables and Graphs of Electron Interaction Cross 10 eV to 100 GeV Derived from the LLNL Evaluated Electron Data Library (EEDL),  $Z = 1 - 100$  / Lawrence Livermore National Laboratory. 1991 ( UCRL-50400, Vol. 31). – Forschungsbericht
- [DGLR94] DIU, Bernard ; GUTHMANN, Claudine ; LEDERER, Danielle ; ROULET, Bernard ; MARSCHNER, Freimut (Hrsg.): *Grundlagen der Statistischen Physik*. Walter de Gruyter & Co., Berlin, New York, 1994. – 1283 S
- [Die09] DIEZ, Peter: *Non-Resonant Heating of Toroidal Overdense Plasma*, Universität Stuttgart, Diplomarbeit, October 2009
- [Doa86] DOANE, J. L.: Polarization Converters For Circular Waveguide Modes. In: *International Journal of Electronics* 61 (1986), Dezember, Nr. 6, S. 1109–1133
- [Edg93] EDGCOMBE, C. J.: *Gyrotron Oscillators*. Taylor and Francis Ltd., 1993
- [FGP<sup>+</sup>10] FIORINI, C. ; GOLA, A. ; PELOSO, R. ; LONGONI, A. ; LECHNER, P. ; SOLTAU, H. ; STRUDER, L. ; OTTOBRINI, L. ; MARTELLI, C. ; LUI, R. ; MADASCHI, L. ; BELLOLI, S.: The DRAGO gamma camera. In: *Review of Scientific Instruments* 81 (2010), April, Nr. 4, S. 044301
- [FH01a] FUCHS, Ch. ; HARTFUSS, H. J.: Extreme broadband multichannel ECE radiometer with "zoom" device. In: *Review of Scientific Instruments* 72 (2001), Nr. 1, S. 383–386
- [FH01b] FUCHS, Ch. ; HARTFUSS, H. J.: Technology of the new W7-AS broadband radiometer system. In: *Fusion Engineering and Design* 53 (2001), S. 451–456
- [FRS<sup>+</sup>95] FUCHS, V. ; RAM, A. K. ; SCHULTZ, S. D. ; BERS, A. ; LASH-MOREDAVIES, C. N.: Mode Conversion and Electron Damping of the Fast Alfvén-wave In A Tokamak At the Ion-ion Hybrid Frequency. In: *Physics of Plasmas* 2 (1995), Mai, Nr. 5, S. 1637–1647
- [Fus13] FUSSMANN, G.: Toroidal runaway beams. In: *Physical Review E* 87 (2013), Januar, Nr. 1, S. 013105
- [GCH<sup>+</sup>01] GANDINI, F. ; CIRANT, S. ; HIRSCH, M. ; LAQUA, H. P. ; NOWAK, S. ; BRUSCHI, A. ; GRANUCCI, G. ; ERCKMANN, V. ; MELLERA, V. ; MUZZINI, V. ; NARDONE, A. ; SIMONETTO, A. ; SOZZI, C. ; SPINICCHIA, N.: The detection of the non-absorbed millimeterwave power during EC heating and current drive. In: *Fusion Engineering and Design* 56-57 (2001), Oktober, S. 975–979
- [Gek82] GEKKER, I. R.: *Interaction of strong magnetic fields with plasmas*. Oxford University Press, New York, 1982. – Translated by J. B. Sykes and R. N. Franklin
- [Gla10] GLAUBITZ, Michael: *Bolometer-Optimierung und -Anwendung auf WEGA-Plasmen*, Ernst-Moritz-Arndt-Universität Greifswald, Diplomarbeit, Januar 2010
- [Gol98] GOLDSMITH, Paul F.: *Quasioptical Systems : Gaussian Beam, Quasioptical Propagation and Applications*. IEEE Computer Soc Press, 1998
- [GP72] GOLANT, V. E. ; PILIYA, A. D.: Linear Transformation and Absorption of Waves In A Plasma. In: *Soviet Physics Uspekhi-ussr* 14 (1972), Nr. 4, S. 413–37

- [Göt05] GÖTT, Gregor: *Untersuchung suprathemischer Elektronen mittels Detektion von weichen Röntgenstrahlen*, Ernst-Moritz-Arndt-Universität Greifswald, Diplomarbeit, 2005
- [GTR02] GONZALO, R. ; TENIENTE, J. ; DEL RIO, C.: Improved radiation pattern performance of Gaussian profiled horn antennas. In: *Ieee Transactions On Antennas and Propagation* 50 (2002), November, Nr. 11, S. 1505–1513
- [GW97] GEIST, Thomas ; WÜRSCHING, H.-J.: Handbuch zum 160GHz Interferometer an W7-AS / Max-Planck-Institut für Plasmaphysik. 1997 ( IPP III/221). – Forschungsbericht
- [GWH97] GEIST, T. ; WURSCHING, E. ; HARTFUSS, H. J.: Multichannel millimeter wave interferometer for W7-AS. In: *Review of Scientific Instruments* 68 (1997), Februar, Nr. 2, S. 1162–1167
- [Heu09] HEUERMANN, Holger: *Hochfrequenztechnik*. 2., durchgesehene und erweiterte Auflage. Vieweg+Teubner, 2009
- [HG13] HARTFUSS, Hans-Jürgen ; GEIST, Thomas: *Fusion Plasma Diagnostics with mm-Waves - An Introduction*. John Wiley And Sons, Inc., 2013
- [Hil12] HILLERT, W. *E106 - Hohlraumresonatoren / Cavities - Ergänzende Informationen zur Versuchsdurchführung*. 2012
- [HS04] HUBBELL, J.H. ; SELTZER, S.M.: *Tables of X-Ray Mass Attenuation Coefficients and Mass Energy-Absorption Coefficients*. Online. 2004. – (version 1.4)
- [Hut94] HUTCHINSON, I. H.: *Principles of Plasma Diagnostics*. Second edition. Cambridge University Press, 1994
- [HW65] HEALD, M. A. ; WHARTON, C. B.: *Plasma Diagnostics with Microwaves*. John Wiley & Sons, Inc., 1965
- [IRD13] INTERNATIONAL RADIATION DETECTORS, Inc. <http://www.ird-inc.com/axuvarrays/axuvarr.html>. 2013
- [Jac99] JACKSON, John D.: *Classical electrodynamics*. 3rd. John Wiley And Sons, Inc., 1999
- [Jah01] JAHNS, Jürgen: *Photonik : Grundlagen, Komponenten und Systeme*. Oldenbourg Wissenschaftsverlag GmbH, 2001. – S. 81-88
- [JMDG91] JACCHIA, A. ; MANTICA, P. ; DELUCA, F. ; GORINI, G.: Determination of Diffusive and Nondiffusive Transport In Modulation Experiments In Plasmas. In: *Physics of Fluids B-plasma Physics* 3 (1991), November, Nr. 11, S. 3033–3040
- [KBC<sup>+</sup>12] KÖHN, Alf ; BIRKENMEIER, G. ; CHUSOV, A. ; DIEZ, P. ; FEUER, A. ; HÖFEL, U. ; HÖHNLE, H. ; HOLZHAUER, E. ; RAMISCH, M. ; SEIFERT, J. ; WOLF, S. ; STROTH, U.: Investigations of Microwave Heating Scenarios of Overdense Plasmas in the Stellarator TJ-K. In: *18th International Stellarator/Heliotron Workshop*. Australian National University & Murramarang Beachfront Nature Resort, 2012
- [KBC<sup>+</sup>13] KOEHN, Alf ; BIRKENMEIER, Gregor ; CHUSOV, A ; DIEZ, P ; FEUER, A ; HÖFEL, U ; HÖHNLE, H ; HOLZHAUER, Eberhard ; KASPAREK, W ; MERLI, S ; RAMISCH, Mirko ; SEIFERT, J ; WOLF, S ; STROTH, Ulrich:

- Schemes of microwave heating of overdense plasmas in the stellarator TJ-K. In: *Plasma Physics and Controlled Fusion* (2013), January. – Accepted
- [KCH<sup>+</sup>08] KOEHN, A. ; CAPPA, A. ; HOLZHAUER, E. ; CASTEJON, F. ; FERNANDEZ, A. ; STROTH, U.: Full-wave calculation of the O-X-B mode conversion of Gaussian beams in a cylindrical plasma. In: *Plasma Physics and Controlled Fusion* 50 (2008), August, Nr. 8, S. 085018
- [KG05] KG, IBF Electronic GmbH & C.: *PGEN6KW2450/400*. 0.1, April 2005
- [Köh10] KÖHN, Alf: *Investigation of microwave heating scenarios in the magnetically confined low-temperature plasma of the stellarator TJ-K*, Universität Stuttgart, Diss., May 2010
- [KK81a] KARPMAN, V. I. ; KAUFMAN, R. N.: Leakage of whistlers from plasma waveguides. In: *Pis'ma v Zhurnal Eksperimental'noi i Teoreticheskoi Fiziki* 33 (1981), Mai, Nr. 5, S. 266–70
- [KK81b] KARPMAN, V. I. ; KAUFMAN, R. N.: Tunnel Transformation of Whistler Waves In An Inhomogeneous-plasma. In: *Zhurnal Eksperimentalnoi I Teoreticheskoi Fiziki* 80 (1981), Nr. 5, S. 1845–1858
- [KK81c] KARPMAN, V. I. ; KAUFMAN, R. N.: Whistler Detrapping From A Density Crest Duct. In: *Physics Letters A* 84 (1981), Nr. 1, S. 9–12
- [KK82] KARPMAN, V. I. ; KAUFMAN, R. N.: The Self-focusing of Whistler Waves. In: *Zhurnal Eksperimentalnoi I Teoreticheskoi Fiziki* 83 (1982), Nr. 1, S. 149–160
- [KKLK76] KAW, P. K. ; KRUEER, W. L. ; LIU, C. S. ; KYOJI, Nishikawa ; SIMON, A. (Hrsg.) ; THOMPSON, W. B. (Hrsg.): *Advances in Plasma Physics*. Bd. Vol. 6. Wiley, 1976. – pp 1–269
- [KM08] KÄMPFER, Niklaus ; MURK, Axel. *Microwavephysics and Quasioptics*. 2008
- [Kri01] KRISCHKE, Alois: *Rothammels Antennenbuch*. DARC, 2001
- [LAM<sup>+</sup>08] LAQUA, H.P. ; ANDRUCZYK, D. ; MARSEN, S. ; OTTE, M. ; PODOBA, Y. Y. ; PREINHEALTER, J. ; URBAN, J. ; WARR, G. ; ZHANG, D.: Fully Electron Bernstein Wave Sustained Overdense Plasma Operation With 28 GHz ECRH at the WEGA Stellarator. In: *Proceedings of the 22nd IAEA Fusion Energy Conference, Geneva, 13-18 October 2008* International Atomic Energy Agency, 2008
- [Laq07] LAQUA, H. P.: Electron Bernstein wave heating and diagnostic. In: *Plasma Physics and Controlled Fusion* 49 (2007), April, Nr. 4, S. R1–R42
- [Laq10] LAQUA, Heinrich: Spezifikation für die erwartete Mikrowellenstreustrahlung in W7-X / Max-Planck-Institut für Plasmaphysik, Teilinstitut Greifswald. 2010 ( KKS-Nr.: 1-CBD20, Dok-Kennz.: S0001.4). – PLM
- [Laq13] LAQUA, Heinrich P. *Private communications*. 2013
- [LCC<sup>+</sup>11] LAQUA, H.P. ; CHLECHOWITZ, E. ; CHOULI, B. ; MARSEN, S. ; STANGE, T. ; OTTE, M. ; PREINHAELTER, J. ; J., Urban.: Multi-Frequency Microwave Heating and Current Drive in over-dense Plasmas at the WEGA Stellarator. In: *38th EPS Conference on Plasma Physics, Strasbourg, France, 2011*
- [LCOS13] LAQUA, H. P. ; CHLECHOWITZ, E. ; OTTE, M. ; STANGE, T.: Stochastic Landau Like Acceleration of Relativistic Electrons and Plasma Heating and Current Drive at the WEGA Stellarator. In: *Submitted to PPCF* (2013)

- [LH98] LAQUA, H. P. ; HARTFUSS, H. J.: Electron Bernstein wave emission from an overdense plasma at the W7-AS stellarator. In: *Physical Review Letters* 81 (1998), September, Nr. 10, S. 2060–2063
- [LMM<sup>+</sup>03] LAQUA, H. R. ; MAASSBERG, H. ; MARUSHCHENKO, N. B. ; VOLPE, F. ; WELLER, A. ; KASPAREK, W.: Electron-Bernstein-wave current drive in an overdense plasma at the Wendelstein 7-AS stellarator. In: *Physical Review Letters* 90 (2003), Nr. 7, S. 075003/1–4
- [LMO<sup>+</sup>09] LAQUA, H. P. ; MARSEN, S. ; OTTE, M. ; PODOBA, Y. ; PREINHEALTER, J. ; STANGE, T. ; URBAN, J. ; ZHANG, D.: Electron Bernstein Wave Experiments at the WEGA Stellarator. In: *AIP Conference Proceedings* 1187 (2009), Nr. 1, S. 441–448
- [Lor04] LORENZ, Bernd: *Anomale Helikonwellenabsorption und parametrische Anregung elektrostatischer Fluktuationen in einer Helikonenladung*, Ruhr-Universität Bochum, Diss., 2004
- [Mar08] MARSEN, Stefan: *The Spatio-temporal Structure of Electrostatic Turbulence in the WEGA Stellarator*, Ernst-Moritz-Arndt-Universität Greifswald, Diss., 2008
- [MEH<sup>+</sup>06] MARUSHCHENKO, Nikolai B. ; ERCKMANN, Volker ; HARTFUSS, Hans J. ; HIRSCH, Matthias ; LAQUA, Heinrich P. ; MAASSBERG, Henning ; TURKIN, Yuri: Ray-Tracing Calculations for the W7-X Stellarator by BRT code. In: *Joint Workshop on Electron Cyclotron Emission and Electron Cyclotron Resonance Heating (EC-14)*, Santorini, Greece, 9-12 May 2006, 2006
- [MG92] MEINKE ; GRUNDLACH: *Taschenbuch der Hochfrequenztechnik*. Springer-Verlag, Berlin/Heidelberg, 1992
- [Mic98] MICHEL, Georg: *Feldprofilanalyse und -synthese im Millimeterwellenbereich*, Universität Karlsruhe, Diss., 1998
- [Mic10] MICHEL, Georg. *Private communications*. 2010
- [Mir10] MIROW, Dr.: *Bedienungsanleitung des GAMMA-SCOUT mit Installationsanleitung und Beschreibung der GAMMA-TOOLBOX Software*. Postfach / P.O. Box 1346, Abtsweg 15, D-69198 Schriesheim: GAMMA-SCOUT GmbH & Co. KG, Dezember 2010
- [Mjøl84] MJØLHUS, E.: Coupling To Z-mode Near Critical Angle. In: *Journal of Plasma Physics* 31 (1984), Nr. FEB, S. 7–28
- [Mjøl87] MJØLHUS, Einar: Generalized Budden resonance tunnelling, with application to linear conversion nearly parallel to magnetic field. In: *Journal of Plasma Physics* 38 (1987), 7, S. 1–26. – ISSN 1469–7807
- [OBC<sup>+</sup>10] OTTE, M. ; BELAPURE, J. ; CHLECHOWITZ, E. ; GLAUBITZ, M. ; HASINGER, G. ; HUBER, B. ; KRYCHOWIAK, M. ; LAQUA, H. P. ; MARSEN, S. ; MÜLLER, E. ; SCHLOSSER, D. M. ; STANGE, T. ; WAGNER, F. ; WELLER, A. ; WOLF, R. ; ZHANG, D.: Diagnostic Development for Wendelstein 7-X at the WEGA Stellarator. In: *37th EPS Conference on Plasma Physics, Dublin, Ireland, 21 - 25 June, 2010*, 2010
- [OLM<sup>+</sup>06] OTTE, M. ; LISCHTSCHENKO, O. ; MARSEN, S. ; SCHUBERT, M. ; PODOBA, Y. Y. ; WAGNER, F. ; WARR, G. B.: Five Years of WEGA operation at IPP Greifswald. In: *Stellarator News* 106 (2006), November, S. 4–9

- [ORT10] ORTEC: Review of the Physics of Semiconductor Detectors / AMETEK, Inc. 2010. – Forschungsbericht
- [PC78] PORKOLAB, M. ; CHANG, R. P. H.: Non-linear Wave Effects In Laboratory Plasmas - Comparison Between Theory and Experiment. In: *Reviews of Modern Physics* 50 (1978), Nr. 4, S. 745–795
- [Pea11] PEARLSTEIN, Robert D.: *Calibration Report/Certificate No 111378 (Model: Mazur PRM-8000)*. Online [Access 29.12.2011]. August 2011. – (using a NIST traceable radiation field source)
- [PFE02] PFEIFFER VACUUM: *Operating manual - Compact FullRange Gauge (All-metal) PKR 261*. BG 805 157 BE / A (0206) PKR 261. June 2002
- [PK73] PREINHAELTER, J. ; KOPECKY, V.: Penetration of High-frequency Waves Into A Weakly Inhomogeneous Magnetized Plasma At Oblique-incidence and Their Transformation To Bernstein Modes. In: *Journal of Plasma Physics* 10 (1973), Nr. AUG, S. 1–12
- [PLU<sup>+</sup>09] PREINHAELTER, Josef ; LAQUA, Heinrich P. ; URBAN, Jakub ; VAHALA, Linda ; VAHALA, George: EBW power deposition and current drive in WEGA - comparison of simulation with experiment. In: *Plasma Physics and Controlled Fusion* 51 (2009), Nr. 12, S. 125008
- [PLW<sup>+</sup>07] PODOBA, Y. Y. ; LAQUA, H. P. ; WARR, G. B. ; SCHUBERT, M. ; OTTE, M. ; MARSEN, S. ; WAGNER, F. ; HOLZHAUER, E.: Direct Observation of Electron-Bernstein Wave Heating by *O-X-B-Mode* Conversion at Low Magnetic Field in the WEGA Stellarator. In: *Phys. Rev. Lett.* 98 (2007), Jun, S. 255003
- [Pod06] PODOBA, Yuriy: *Radio frequency heating on the WEGA stellarator*, Ernst-Moritz-Arndt-Universität Greifswald, Diss., 2006
- [POR76] PORKOLAB, M.: High-frequency Parametric Wave Phenomena and Plasma-heating - Review. In: *Physica B & C* 82 (1976), Nr. 1, S. 86–110
- [POR78] PORKOLAB, M.: Parametric Processes In Magnetically Confined CTR Plasmas. In: *Nuclear Fusion* 18 (1978), Nr. 3, S. 367–413
- [Por98] PORTER, G. D.: The role of radial particle flow on power balance in DIII-D. In: *Physics of Plasmas* 5 (1998), Dezember, Nr. 12, S. 4311–4320
- [Poz98] POZAR, David M.: *Microwave Engineering*. 2. John Wiley And Sons, Inc., New York, Chichester, Weinheim, Brisbane, Singapore, Toronto, 1998
- [RS00] RAM, A. K. ; SCHULTZ, S. D.: Excitation, propagation, and damping of electron Bernstein waves in tokamaks. In: *Physics of Plasmas* 7 (2000), Oktober, Nr. 10, S. 4084–4094
- [SAS11] SAS IP Inc.: *HFSS Online Help*. 2011
- [SDBF<sup>+</sup>11] SHEVCHENKO, V. F. ; DE BOCK, M. ; FREETHY, S. J. ; SAVALIEV, A. N. ; VANN, R. G. L.: Two-dimensional Studies of Electron Bernstein Wave Emission In Mast. In: *Fusion Science and Technology* 59 (2011), Mai, Nr. 4, S. 663–669
- [SHH<sup>+</sup>09] STANGE, T. ; HARTFUSS, H.-J. ; HIRSCH, M. ; OTTE, M. ; S., Marsen ; S., Schmuck: Electron Cyclotron Emission from the WEGA stellarator. In: *Stellarator News* Issue 120 (2009), June, S. 4–6

- 
- [SL10] SCHMID-LORCH, Dominik G.: *Mikrowellen-Streustrahlung am Tokamak AS-DEX Upgrade*, Universität Ulm, Diplomarbeit, May 2010. – IPP Report 1/345
- [SOTS10] SHEVCHENKO, V. F. ; O'BRIEN, M. R. ; TAYLOR, D. ; SVELIEV, A. N.: Electron Bernstein wave assisted plasma current start-up in MAST. In: *Nuclear Fusion* 50 (2010), Februar, Nr. 2, S. 022004
- [SS09] SINGH, R. ; SHARMA, A. K.: Self-focusing of a whistler propagating at an angle to the magnetic field in a plasma. In: *Physica Scripta* 79 (2009), Juni, Nr. 6, S. 065502
- [Sta08] STANGE, Torsten: *Aufbau einer Elektron-Zyklotron-Emissions-Diagnostik am Stellarator WEGA und erste Messungen*, Ernst-Moritz-Arndt-Universität Greifswald, Diplomarbeit, November 2008
- [Ste13] STEMMER, Christian: *Wiedereintrittsaerodynamik*. 2013. – Skript der TU München, Lehrstuhl für Aerodynamik
- [Sti92] STIX, Thomas H.: *Waves in Plasmas*. Springer-Verlag New York, Inc., 1992
- [Str11] STROTH, Ulrich: *Plasmaphysik - Phänomene, Grundlagen, Anwendungen*. Vieweg+Teubner, 2011
- [SVFH12] SHEVCHENKO, V. F. ; VANN, R. G. L. ; FREETHY, S. J. ; HUANG, B. K.: Synthetic aperture microwave imaging with active probing for fusion plasma diagnostics. In: *Journal of Instrumentation* 7 (2012), Oktober, S. P10016
- [Swa03] SWANSON, Gary D.: *Plasma Waves*. 2nd. IOP Publishing Ltd, 2003
- [TAN69] TANIUTI, T.: Corrections. In: *Physical Review Letters* 22 (1969), Nr. 14, S. 752–&
- [TG59] TRIVELPIECE, A. W. ; GOULD, R. W.: Space Charge Waves In Cylindrical Plasma Columns. In: *Journal of Applied Physics* 30 (1959), Nr. 11, S. 1784–1793
- [TGGR02] TENIENTE, Jorge ; GONI, David ; GONZALO, Ramon ; DEL RIO, Carlos: Choked Gaussian Antenna: Extremely Low Sidelobe Compact Antenna Design. In: *IEEE Antennas and Wireless Propagation Letters* 1 (2002), S. 200–202
- [TK89] THUMM, M. ; KUMRIC, H.: High-power TE<sub>11</sub> and TM<sub>11</sub> Circular Polarizers In Oversized Waveguides At 70 Ghz. In: *International Journal of Infrared and Millimeter Waves* 10 (1989), September, Nr. 9, S. 1059–1075
- [TRM<sup>+</sup>09] THOMA, C. ; ROSE, D. V. ; MILLER, C. L. ; CLARK, R. E. ; HUGHES, T. P.: Electromagnetic wave propagation through an overdense magnetized collisional plasma layer. In: *Journal of Applied Physics* 106 (2009), August, Nr. 4, S. 043301
- [TW69] TANIUTI, T. ; WASHIMI, H.: Self-focusing of A Plasma Wave Along A Magnetic Field. In: *Physical Review Letters* 22 (1969), Nr. 10, S. 454–&
- [Ulr07] ULRICH, Stefan: *Charakterisierung einer Mikrowellenstreustrahlkammer*, Ernst-Moritz-Arndt-Universität Greifswald, Diplomarbeit, 2007
- [Urb08] URBAN, Jakub: *Electron Bernstein Wave Emission Simulations for Spherical Tokamaks*, Czech Technical University in Prague, Diss., 2008
- [Urb10] URBAN, Jakub. *Private communications*. 2010

- [VGJK<sup>+</sup>94] VON GOELER, S. ; JONES, S. ; KAITA, R. ; BERNABEI, S. ; DAVIS, W. ; FISHMAN, H. ; GETTELFINGER, G. ; IGNAT, D. ; PAOLETTI, F. ; PETRAVICH, G. ; RIMINI, F. ; RONEY, P. ; STEVENS, J. ; STODIEK, W.: Camera For Imaging Hard X-rays From Suprathermal Electrons During Lower-hybrid Current Drive On PBX-M. In: *Review of Scientific Instruments* 65 (1994), Mai, Nr. 5, S. 1621–1630
- [VL03] VOLPE, F. ; LAQUA, H. P.: BXO mode-converted electron Bernstein emission diagnostic (invited). In: *Review of Scientific Instruments* 74 (2003), März, Nr. 3, S. 1409–1413
- [Vol03] VOLPE, Francesco: *Electron Bernstein emission diagnostic of electron temperature profile at W7-AS Stellarator*, Ernst-Moritz-Arndt-Universität Greifswald, Diss., 2003
- [Vow88] VOWINKEL, Bernd: *Passive Mikrowellenradiometrie*. Friedr. Vieweg & Sohn, Braunschweig / Wiesbaden, 1988
- [Wag96] WAGNER, Dietmar: *Entwurf und Analyse von korrigierten überdimensionierten Hohlleiterstrukturen für Hochleistungsmillimeterwellensysteme*, Universität Stuttgart, Diss., 1996
- [Wag10] WAGNER, Dietmar. *Private communications*. 2010
- [WC74] WHITE, R. B. ; CHEN, F. F.: Amplification and Absorption of Electromagnetic-waves In Overdense Plasmas. In: *Plasma Physics and Controlled Fusion* 16 (1974), Nr. 7, S. 565–587
- [Wel04] WELLER, Arthur: Soft X-Ray Emission Diagnostics of magnetically confined hot Plasmas. In: *2nd German-Polish Conference on Plasma Diagnostics for Fusion and Applications (GPPD-2004), Cracow, Poland, September 8-10, 2004*, 2004. – or JET Report JET-IR 10 (1987)
- [Wel10] WELLER, Arthur. *Private communications*. october 2010
- [Wer08] WERNER, Andreas: 2008. – Private Mitteilungen
- [WGGPR07] WAGNER-GENTNER, A. ; GRAF, U. U. ; PHILIPP, M. ; RABANUS, D.: A simple method to design astigmatic off-axis mirrors. In: *Infrared Physics & Technology* 50 (2007), März, Nr. 1, S. 42–46
- [WHB<sup>+</sup>11] WELLER, A. ; HUBER, B. ; BELAPURE, J. ; PÜTTERICH, T. ; SERTOLI, M. ; GUDE, A. ; NEU, R. ; DUX, R. ; SUTTROP, W. ; THE ASDEX UPGRADE TEAM: X-Ray Pulse Height Analysis on ASDEX Upgrade. In: *38th EPS Conference on Plasma Physics, Strasbourg, France, 2011*
- [WKL<sup>+</sup>11] WAGNER, D. ; KASPAREK, W. ; LEUTERER, F. ; MONACO, F. ; MUNICH, M. ; SCHUTZ, H. ; STANGE, T. ; STOBBER, J. ; THUMM, M.: Bragg Reflection Band Stop Filter for ECE on Wega. In: *Journal of Infrared Millimeter and Terahertz Waves* 32 (2011), Dezember, Nr. 12, S. 1424–1433
- [WLA<sup>+</sup>06] WARR, G. B. ; LAQUA, H. P. ; ASSMUS, D. ; KASPAREK, W. ; KEIL, D. ; LISCHTSCHENKO, O. ; MARSEN, S. ; OTTE, M. ; SCHUBERT, M. ; WAGNER, F.: New 28 GHz Plasma ECR Heating System for the WEGA Stellarator. In: *33rd EPS Conference on Plasma Physics, Rome, 19 - 23 June 2006 ECA Vol.30I*, 2006

- 
- [WR97] WILLES, A. J. ; ROBINSON, P. A.: Electron-cyclotron maser theory for extraordinary Bernstein waves. In: *Journal of Plasma Physics* 58 (1997), Nr. 01, S. 171–191
- [ZBG<sup>+</sup>11] ZHANG, D. ; BURHENN, R. ; GLAUBITZ, M. ; KÖNIG, R. ; LAQUA, H.P. ; MARSEN, S. ; STANGE, T. ; OTTE, M. ; THE WEGA-TEAM: Simulation of the spectrally-resolved plasma radiation in the WEGA stellarator and comparison with bolometer measurements. In: *38th EPS Conference on Plasma Physics, Strasbourg, France, 2011*
- [Zei13] ZEIDLER, Eberhard: *Springer-Taschenbuch der Mathematik*. Third. Springer Fachmedien Wiesbaden, 2013
- [ZFG81] ZEHRFELD, H. P. ; FUSSMANN, G. ; GREEN, B. J.: Electric-field Effects On Relativistic Charged-particle Motion In Tokamaks. In: *Plasma Physics and Controlled Fusion* 23 (1981), Nr. 5, S. 473–489
- [ZGL<sup>+</sup>12] ZHANG, D. ; GLAUBITZ, M. ; LAQUA, H.P. ; MARSEN, S. ; OTTE, M. ; STANGE, T.: Determination of electron thermal diffusivity at the WEGA stellarator. In: *Nuclear Fusion* 52 (2012), Nr. 4, S. 043002
- [Zha10] ZHANG, Daihong: *Estimation of the Diffusivities of the WEGA-Plasma*. W7 seminar, IPP Greifswald. March 2010. – p. 29
- [Zha13] ZHANG, Daihong. *Private Communications*. 2013



# Danksagung

Zu aller erst möchte ich meiner Freundin Kathrin und meiner Mutter Christa danken, die während meiner Promotionszeit sicher am meisten unter meinem chronischen Zeitmangel zu leiden hatten, und mich trotz alledem immer in allen Belangen nach allen Kräften unterstützt haben. Dies gilt natürlich gleichermaßen für meine ganze Familie und Freunde, die während dieser Zeit alle in Gedanken bei mir waren. Ich habe diese Worte bereits nach meiner Diplomarbeit gewählt, aber ich verspreche, dass die Arbeit wieder ein gesundes Maß einnimmt. Besonders möchte ich hierbei an meine Oma Helene erinnern, die den Abschluss dieser Arbeit leider nicht mehr mit erleben konnte.

Besonderer Dank geht an meine Betreuer Dr. Heinrich Peter Laqua und Prof. Robert Wolf für die Annahme als Doktorand sowie die fachliche Unterstützung während der Doktorarbeit.

Vielen Dank an Dieter Assmuß, der mir immer mit Rat und Tat in allen WEGA-Belangen zur Seite stand und mit dem ich zusammengerechnet viele Wochen vor der Prototypensteuerung verbrachte. In diesem Zusammenhang möchte ich auch den Mitarbeitern von der CODAC danken, die mitunter genervte Anrufe erdulden mussten. Ebenfalls Vielen Dank an Ralf Gerhardt und Matthias Otte für die Unterstützung beim Aufbau der Diagnostiken sowie in allen anderen Belangen. In diesem Zusammenhang möchte auf keinen Fall die technischen Dienste vergessen zu nennen, die so einige Späne fliegen lassen mussten zur Realisierung dieser Arbeit.

Vielen Dank an die Diplomanden vor und während meiner Zeit als Doktorand, die mit ihrer Arbeit die knappe Diagnostikausstattung ausbauten oder es zumindest versuchten. Besonders zu nennen ist hier Enrico Chlechowicz, der mit dem Aufbau der Strommessung eine nahezu wartungsfreie Diagnostik zur Verfügung stellte, und Peter Drewelow, der die erste Version des WEGA-Torus in Inventor implementierte.

Zu guter letzt möcht ich allen anderen Personen danken, die in irgendeiner Weise zum Gelingen dieser Arbeit beigetragen haben.



### **Selbständigkeitserklärung**

Ich versichere an Eides statt, dass ich die von mir am heutigen Tage der Fakultät Physik eingereichte Dissertation vollkommen selbstständig verfasst und keine anderen als die angegebenen Quellen und Hilfsmittel benutzt sowie Zitate kenntlich gemacht habe.

(Ort), den (Datum)

Unterschrift